The Gas-Phase Ligand Exchange of Trivalent Metal β-Diketonates

by

James Kole Gasior

Submitted in Partial Fulfillment of the Requirements

for the Degree of

Master of Science

in the

Chemistry

Program

YOUNGSTOWN STATE UNIVERSITY

May 2017

The Gas-Phase Ligand Exchange of Trivalent Metal β-Diketonates

James Kole Gasior

I hereby release this thesis to the public. I understand that this thesis will be made available from the OhioLINK ETD Center and the Maag Library Circulation Desk for public access. I also authorize the University or other individuals to make copies of this thesis as needed for scholarly research.

Signature:

James K. Gasior, Student Date

Approvals:

Dr. Brian D. Leskiw, Thesis Advisor Date

Dr. Howard D. Mettee, Committee Member Date

Dr. Sherri R. Lovelace-Cameron, Committee Member Date

Dr. Salvatore A. Sanders, Dean of Graduate Studies Date

Abstract

The gas-phase ligand exchange reactions incorporating main group and transition metal β-diketonate complexes were investigated using a Finnigan TSQ 7000 triple quadrupole electron impact mass spectrometer. Specifically, trivalent iron and aluminum complexes were reacted with a variety of other metal β-diketonates during mass spectrometric analysis, and the ensuing gas-phase reactions were shown to generate a variety of products. Relative peak heights of parent ions in the resultant co-sublimation spectra were compared to the reactants' baseline spectra to discern the relative reactivity of each parent ion, and subsequently, propose reaction mechanisms accounting for the production of mixed ligand products. To attain a more complete understanding of certain gas-phase reactions, tandem mass spectrometry was implemented to study selective reactions between specific parent ions and a neutral gas species. Analysis and interpretation of the resulting spectra allowed for the formulation of specific reaction mechanisms for each product detected. Finally, for the first time, the mechanism of partial ligand exchange was proposed and modeled using the PM3 semi-empirical method to elucidate general features thought to be employed during the simultaneous mass analysis of homo-metal β-diketonates.

Acknowledgements

I cannot express enough gratitude to my committee for their guidance and supervision: Dr. Brian D. Leskiw, my research advisor; Dr. Howard D. Mettee; and Dr. Sherri R. Lovelace Cameron. To my committee and former instructors at Youngstown State University: thank you for the knowledge and wisdom you have imparted that has not only benefitted this study, but also molded me into the skilled and competent chemist I am today.

To my family, friends, and co-workers: without your support, either morally or financially, the completion of this project would have not been possible; you have my sincere appreciation.

Lastly, to my beautiful and loving fiancé, Abby: you have my deepest heartfelt appreciation. I am truly thankful for the encouragement, patience, and love that you have provided over the past couple of years. You are my haven; my light in the dark. I am yours, forever and always.

Table of Contents

Chapters

List of Figures

List of Tables

List of Equations

Chapter 1

Literature Review

1.1 Introduction

Metal β-diketonates are coordination compounds that are of particular interest owing to their intrinsic properties and technological applications which includes catalysis,[1-4] organic light-emitting diodes,[5] carbon-nanotube structures,[6] chemical vapor deposition,[7] and more recently, anticancer agents.[8,9] Myriad mass spectrometry studies have elucidated gas-phase ligand exchange,[10-13] fragmentation,[11-19] reaction mechanisms,[11,12] ionization energies,[14,19] structure,[19] volatility,[20] preparation and tunability.[21-24] In addition, a wide variety of mass spectrometry techniques have been employed to investigate metal β-diketonates; including, electron impact (EI),[10-18] secondary-ion mass spectrometry (SIMS),[25] electrospray ionization (ESI),[26] tandem mass spectrometry (MS/MS),[11,12,26] and matrix-assisted laser desorption/ionization (MALDI).[27]

1.2 Mechanism of Ionization

Experimental results of the reports described herein have been acquired by EI mass spectrometry. Using this method, the analyte ($M(L)_n$, n = 2, 3) is subjected to an electron beam (70 eV) in the ion source of the mass spectrometer which induces large fluctuations in the electric field around the neutral molecules, resulting in both

ionization and fragmentation.[28] A general equation for the ionization of these complexes is expressed in Equation (1.1).

$$M(L)_n + e^- \longrightarrow [ML_n]^+ + 2e^- \qquad \text{(Eqn 1.1)}$$

The degree of radical character in the resultant ion varies with the identity of the central metal as shown in Figure 1.1.[19] Radical delocalization across the conjugated π-system of the ligand is more prominent in complexes containing metals that resist oxidation. Conversely, complexes containing readily oxidized metals possess the capability to donate d_π electrons across the electron deficient ligand orbitals to gain additional stability.

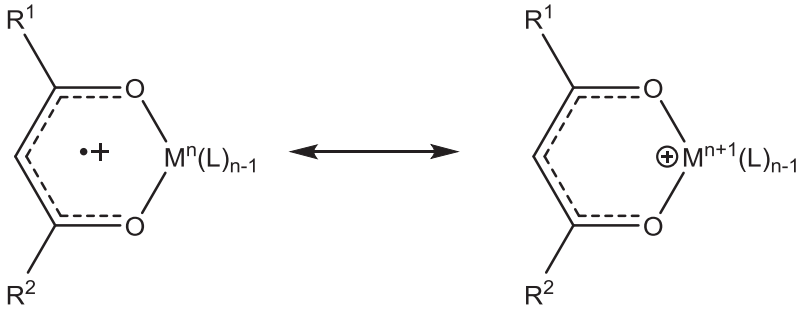

Figure 1.1: Structure of the ionized metal chelate $M(L)_n$ (n = 2,3).[19]

1.3 Fragmentation Pathways

Earlier studies of metal β-diketonate complexes focused on formulating possible fragmentation pathways that occur during mass spectrometric analysis.[13,15-18] In their report, MacDonald and Shannon evaluated metal acetylacetonates ($M(acac)_n$) and noted multiple fragmentation patterns that were generally consistent across a range of complexes.[13] Bancroft *et al*. were able to reproduce their work in addition to generating

a cationic spectrum for $Mn(acac)_3$ which was previously unobtainable.[14] In a review composed by Westmore, the findings of Shannon and coworkers were organized into three extended proposals.[19] First, M^+ will be stabilized if the central metal is easily oxidized and metal to ligand π electron donation occurs readily. As a result, M^+ in the mass spectra will be relatively abundant, and the loss of even electron neutral fragments will be enhanced. As an example, $[Ti(acac)_3]^+$ consecutively loses two even electron fragments, *m/z* 82 and *m/z* 18, as shown in Equation (1.2).

$$[Ti^{III}(acac)_3]^{+\bullet} \rightarrow [Ti^{IV}(acac)_3]^+ \rightarrow$$
$$[Ti^{IV}(acac)_2OH]^+ + CH_3COCHCH_2 \rightarrow$$
$$[Ti^{IV}(acac)(acac\text{-}H)]^+ + H_2O \qquad \text{(Eqn 1.2)}$$

Secondly, if the metal center is not readily oxidized or reduced, M^+ may be of low abundance due to the resultant instability, and fragmentation will usually proceed through the loss of an odd electron fragment followed by a loss of an even electron fragment. For example, $[La(acac)_3]^+$ has been observed to undergo a loss of *m/z* 99 followed by a loss of *m/z* 82 as outlined in Equation (1.3).

$$[La^{III}(acac)_3]^{+\bullet} \rightarrow [La^{III}(acac)_2]^+ + acac^\bullet \rightarrow$$
$$[La^{III}(acac)OH]^+ + CH_3COCHCH_2 \qquad \text{(Eqn 1.3)}$$

The loss of an odd electron fragment such as CH_3 or (acac) from $[M^{III}(acac)_2]^+$ occurs following a reduction of valency, and occurs more readily for metals having a stable +2 oxidation state such as presented in Equation (1.4).

$$[Co^{III}(acac)_2]^+ \rightarrow [Co^{II}(acac)_2]^{+\bullet} \rightarrow$$
$$[Co^{II}(acac)(acac\text{-}CH_3)]^+ + CH_3^{\bullet} \qquad \text{(Eqn 1.4)}$$

Finally, when the metal center exhibits some propensity to undergo reduction, M^+ may be of low abundance, and fragmentation typically occurs through two successive losses of odd electron fragments as shown in Equation (1.5).

$$[Cu^{II}(acac)_2]^{+\bullet} \rightarrow [Cu^{II}(acac)(acac\text{-}CH_3)]^+ + CH_3^{\bullet} \rightarrow$$
$$[Cu^{I}(acac)(acac\text{-}CH_3)]^{+\bullet} \rightarrow [Cu^{I}(acac\text{-}CH_3)_2]^+ + CH_3^{\bullet} \qquad \text{(Eqn 1.5)}$$

Common fragmentation pathways of $M(acac)_n$, adapted from Shannon, are presented in Figure 1.2.[13] Fragmentation commences with either the preferential loss of *m/z* 99 or *m/z* 15, corresponding to an acetylacetonate ligand or a methyl group, respectively. Following methyl fragmentation, the fragmented ligand may then dissociate from the metal for a total loss of *m/z* 99. Alternatively, $[M(acac)(acac\text{-}CH_3)]^+$ may undergo a loss of *m/z* 42 through ketene fragmentation. Less common fragmentation pathways include the loss of *m/z* 18, which corresponds to water, or the loss of ketene from the molecular ion.

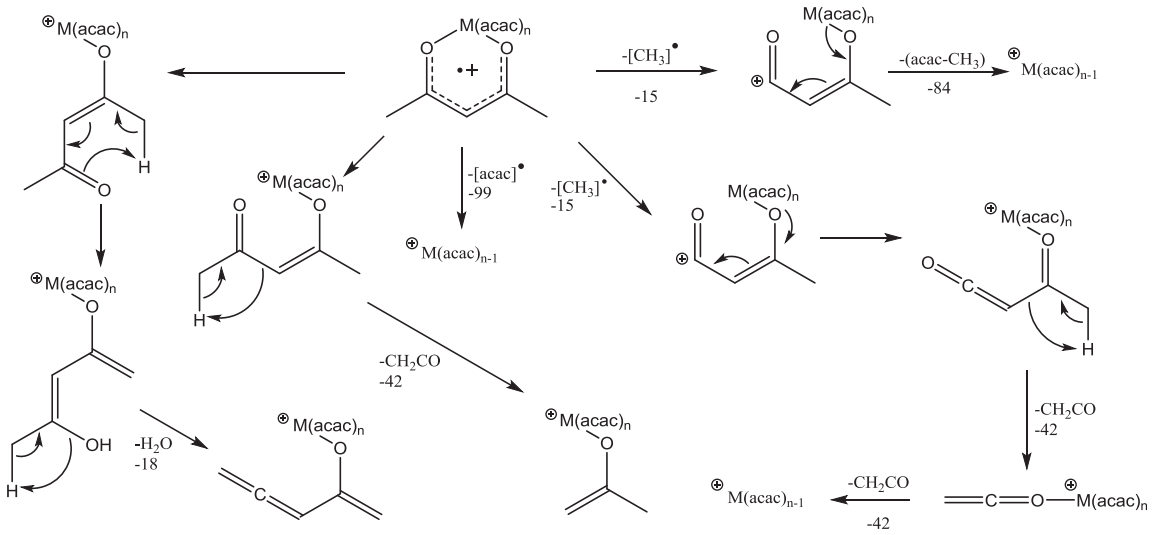

Figure 1.2: Fragmentation pathways of $M(acac)_n$ (n = 2, 3).[13]

As previously shown in Equation (1.5), $Cu(acac)_2$ undergoes additional fragmentation pathways which can be attributed to the stable d^{10} electron configuration acquired by the ensuing Cu(I) fragments. An adapted mechanism illustrating the fragmentation pathway of $Cu(acac)_2$ is presented in Figure 1.3. Following the initial loss of methyl, the resulting fragment simultaneously undergoes reduction at the metal center and structural rearrangement in a process later referred to as reductive rearrangement. The formation of the β-keto ester complex presumably enables the loss of an additional methyl group—a fragmentation event exclusive to $Cu(acac)_2$. Fragmentation of the demethylated β-keto ester results in the loss of (acac-CH_3) to form $[Cu(acac\text{-}CH_3)]^+$.

In regards to the activation energies (E_A) associated with fragmentation, Westmore states that if E_A is low for the loss of (acac), $[M_n(acac)_{n-1}]^+$ (n = 2, 3) will readily form.[19] Conversely, when E_A is high for the loss of (acac), the rate in which $[M_n(acac)_{n-1}]^+$ is formed will be impeded. The excess internal energy from the ionization

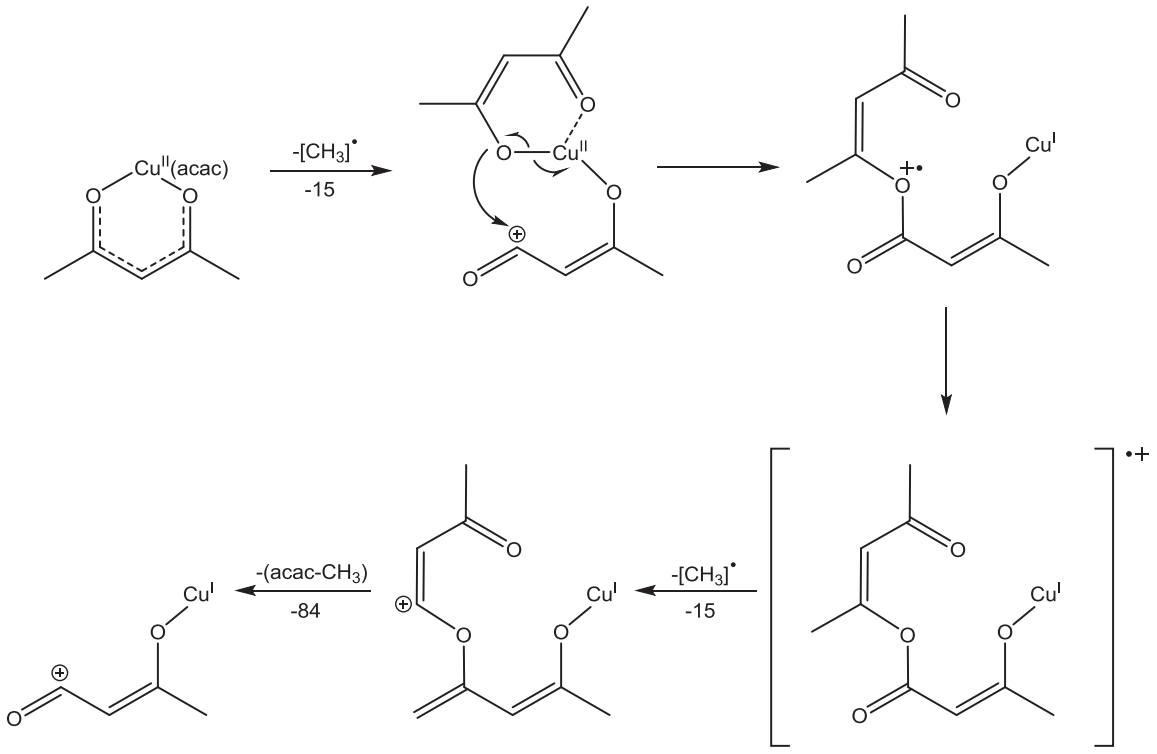

Figure 1.3: Fragmentation pathway of $Cu(acac)_2$.[13]

process is instead focused into vibrational modes leading to the loss of other stable fragments such as a methyl group.

Later studies investigated the mass spectrometric analysis of fluorinated acetylacetonates, which became of interest due to their enhanced volatility and applications.[11,12,15-18,20] Figure 1.4 shows possible fragmentation pathways of fluorinated complexes based on the studies conducted by Clobes.[16] Complexes containing either trifluoroacetylacetonate (tfac) or hexafluoroacetylacetonate (hfac) were shown to undergo fragmentation resulting in the loss of *m/z* 69 or *m/z* 50, corresponding to CF_3 and CF_2, respectively. Apparent one step losses of an intact ligand were proposed to occur via consecutive fragmentation events based on the observation of peaks that correspond to metastable transitions.[15,17] As an example, the loss of CF_3 from $Al(hfac)_3$

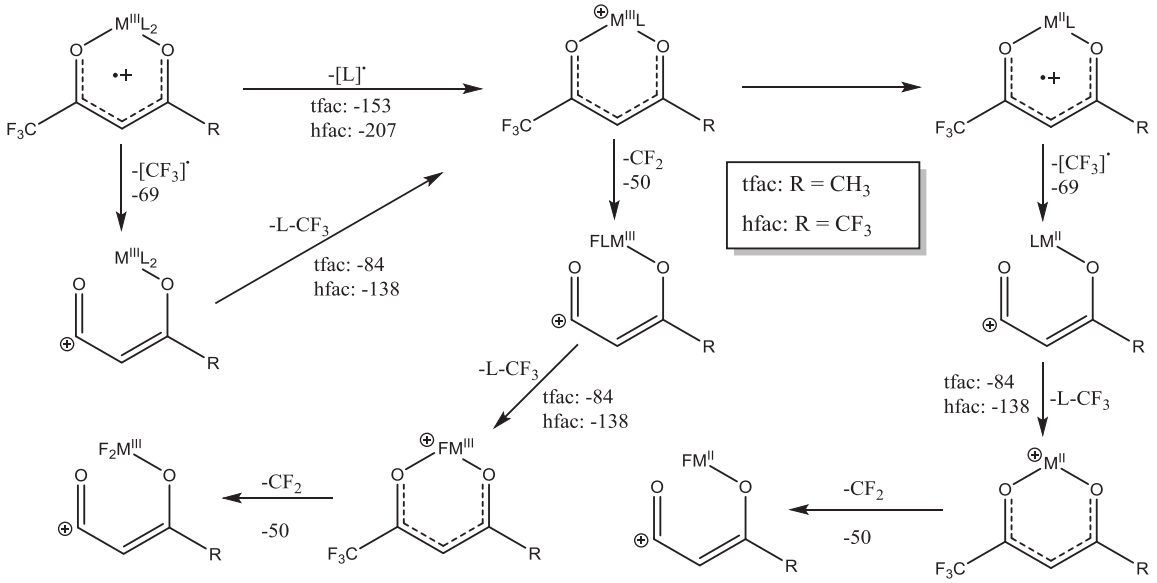

Figure 1.4: Fragmentation pathways of $M(hfac)_n$ and $M(tfac)_n$ (n = 2, 3).[16]

may facilitate the net loss of (hfac) since the fragmented ligand can dissociate as a stable neutral fragment from the resulting $[Al(hfac)_2(hfac\text{-}CF_3)]^+$ species.

Complexes containing asymmetric fluorinated ligands have been shown to undergo variable fragmentation pathways depending upon the nature of the ligand as well as the metal. For instance, $M(tfac)_n$ (n = 2, 3) preferentially undergoes the loss of CF_3 over CH_3. However, if the methyl substituent in (tfac) is exchanged for another alkyl group, the loss of that substituent becomes more prevalent with increasing radical stability.[16] Loss of CF_3 with concurrent fluorine migration to the metal center equates to the loss of the even electron fragment, CF_2. This phenomenon is supported by spectra containing ion signals indicating the formation of metal fluorides, MF_n (n = 2, 3).[16-18] Previous studies demonstrate that fluorine migration is most prominent in complexes containing metals that resist oxidation since it allows for the retention of valency.[16-18]

For example, aluminum in $Al(tfac)_3$ retains the +3-oxidation state throughout the fragmentation pathway shown in Equation (1.6).[16]

$$[Al^{III}(tfac)_3]^{+\bullet} \rightarrow [Al^{III}(tfac)_2]^{+} + tfac^{\bullet} \rightarrow$$
$$[Al^{III}F(tfac)(tfac\text{-}CF_3)]^{+} + CF_2 \rightarrow [Al^{III}F(tfac)]^{+} + (tfac\text{-}CF_3) \rightarrow$$
$$[Al^{III}F_2(tfac\text{-}CF_3)]^{+} + CF_2 \qquad \text{(Eqn 1.6)}$$

In addition, fluorinated complexes tend to undergo fluorine migration to varying degrees depending upon the nature of the ligand.[18] In a study conducted by Morris and Koob, hard/soft acid/base (HSAB) theory was shown to accurately explain the prominence of fluorine migration in a variety of fluorinated metal complexes. In general, complexes containing asymmetric fluorinated ligands were shown to have decreasing affinity for fluorine as the electron-donating nature, or softness, of the fluorine-free substituent increased.

Later studies of metal complexes containing trifluorotrimethylacetoacetonate (tftm) revealed a preferential loss of *m/z* 57 which is indicative of *tert*-butyl fragmentation.[11,12] The preferential loss of *t*Bu over CF_3 is to be expected considering the difference in radical stability.[16] However, unlike the loss of neutral CH_3 or CF_3, *tert*-butyl fragmentation may generate cationic or neutral *t*Bu. Mass spectrometric studies of (tftm) complexes conducted by Lerach and Hunter reveal tBu^+ to be in signficant

abundance which, according to Stevenson's Rule, suggests that *t*Bu has a relatively low ionization energy compared to other branching substituents of metal β-diketonates.[11,12]

1.4 Reaction Mechanisms

Earlier studies on metal β-diketonates have shown that when two different metal complexes are simultaneously mass analyzed, new metal chelates are produced and detected. This phenomenon was originally reported by MacDonald and Shannon where the co-sublimation of $Fe(acac)_3$ and $Fe(bzac)_3$ (bzac = benzoylacetonate) produced $[Fe(acac)_2(bzac)]^{+\cdot}$.[13] They referred to this reaction as ligand or metal scrambling and even noted that the exchange occurred when the two metal chelates were introduced through separate containers in the ion source. A few years later, Majer and Perry reported a similar occurrence between alkali- and rare earth metal β-diketonates.[7] Product formation was either attributed to association or ligand interchange reactions wherein the alkali- and rare earth metal derivatives either merge into one complex or undergo a metathesis reaction, respectively.

The gas-phase reactions of metal β-diketonates were further investigated by the Leskiw research group at Youngstown State University.[11,12] Various combinations of metal β-diketonate complexes were shown to produce spectral signals corresponding to new metal chelate products during mass spectrometric analysis. To ensure exchange was exclusively occurring within the gas-phase, these samples were physically isolated within the ion source prior to mass analysis. Reaction pathways were then formulated by comparing the resulting spectra to reference spectra of the individual complexes.

During co-sublimation of $M(acac)_2$ and $M(tftm)_2$, the more volatile fluorinated complex is the first to sublime according to the early appearance of its characteristic mass spectrometric distribution.[12] Prior research has established that the degree of fluorination is directly proportional to volatility which is not surprising when considering the weak C-F···F-C van der Waals interactions between fluorinated complexes.[20] As the mass spectrometric distribution of the less volatile complex begins to appear, peaks corresponding to mixed ligand products form while the ion intensities of the original fluorinated complex begin to drastically decrease.[12] This suggests that the more volatile complex becomes ionized and then consumed during a ligand exchange reaction with the less volatile, neutral gas complex.

Results obtained from collision-cell gas experimentation further suggest that the formation of mixed ligand products typically occurs when the less volatile complex is introduced as the neutral gas while the more volatile complex presents the positively charged species.[12] In addition, by mass-selecting the most abundant parent ions present in the reference spectra it was possible to discern their respective roles in ligand exchange processes. The evidence gathered from these studies provides a strong indication that gas-phase ligand exchange processes are responsible for product formation.[12] Further investigation into the scope of this research is worth pursuing, and will hopefully lead to further mechanistic insight and the establishment of periodic trends.

Chapter 2

Instrumentation

2.1 Introduction

Mass spectrometry is an analytical technique that is routinely utilized to identify the molecular weight of an unknown sample. In general, this technique can be broken down into three parts, the source, mass analyzer, and detector. First, the sample is transferred under vacuum to the source region where it is ionized and accelerated in the mass analyzer. Within the mass analyzer, resulting ions are separated according to their mass-to-charge ratio (*m/z*) and are subsequently detected.[28,29]

2.2 Sample Introduction

The method of sample introduction depends on the nature of the material being loaded into the instrument. A direct insertion probe is typically employed for the mass spectrometric analysis of low vapor pressure liquids and solids. The sample can either be loaded in a small capillary tube at the end of a heated sleeve, or alternatively as in the research described here, onto a wire filament. Once the sample is applied, the probe is inserted into a vacuum lock and then allowed to move forward into the source region where the sample is introduced via sublimation or direct evaporation.

2.3 Ionization and Fragmentation

Electron impact ionization (EI) is the most common method to ionize the sample. This ionization technique bombards the sample with high-energy electrons which carry 70 eV of energy. Accelerated electrons from the filament approach the gaseous compound, and consequently, distort the electron cloud of the molecule. This distortion results in the transference of kinetic energy from the accelerated electron to the electron cloud, and if enough energy is passed along, it causes an electron to be ejected from the valence shell of the compound. The resulting radical cation is often of great interest, and is also called the molecular ion $[M]^+$. Fragmentation of the molecular ion typically generates a cationic and radical fragment. Myriad fragmentation pathways are possible under the high-energy conditions of a mass spectrometer, but the most favored fragmentation events usually result from the formation of the most stable cation from the dissociation of the most stable radical. The distribution and abundances of the resulting fragments are dependent upon the kinetics of the fragmentation pathways and the ionization energy. Interpreting this distribution is important in regards to the elucidation of molecular structure.

Following ionization, the resultant ions are accelerated by an electric field into the mass analyzer where each ion is separated according to the corresponding mass-to-charge ratio, *m/*z. Since the charge, *z*, is typically +1, *m/*z is essentially a measure of mass, *m*. The abundances of the detected cations are plotted as a function of *m/z* on a mass spectrum. Abundance is measured on a relative scale rather than an absolute scale

where peak intensities are recorded relative to the most intense peak, commonly known as the base peak, which is designated a value of 100%. Furthermore, the natural (isotopic) abundance of all constituent atoms within a sample is reflected in the mass spectrum. For example, the mass spectrum of an iron-containing species would have a representative pattern of four peaks with relative abundances of 5.845%, 91.754%, 2.119% and 0.282% which is consistent with the naturally occurring abundance of isotopes, ^{54}Fe, ^{56}Fe, ^{57}Fe, and ^{58}Fe, respectively. Simply stated, each resultant iron-containing fragment will have a set of corresponding peaks with a peak-to-peak ratio of approximately 6:92:2:0. Recognition of such patterns readily aids in the interpretation of a mass spectrum by providing information on elemental composition.

2.4 Mass Analyzer

Mass analyzers are components of mass spectrometers that separate ions based on their *m/z* value. Quadrupole filters are the most common type of analyzer, and are composed of two pairs of parallel rods (electrodes). They are also classified as continuous analyzers, and function by only transmitting mass-selected ions to the detector. The analyzer is scanned across a range of *m/z* so that all ions within that range can be detected. Two types of voltages are applied to the electrodes in order to filter and transfer a single *m/z* value ion: Radio Frequency (RF) and Direct Current (DC) voltages.

In regards to the RF voltage, both a positive and negative potential are alternately applied to the two pairs of electrodes during analysis. One half of the cycle

involves the application of a positive potential to the vertical pair of electrodes while a negative potential is applied to the horizontal pair. Consequently, this focuses the incoming ions in a horizontal plane. The second half of the cycles reverses the potential across the electrodes causing the ions to focus into a vertical plane. Overall, the alternating fields forces the ions to move in a three-dimensional oscillation where the amplitude of the wave is dependent upon the RF frequency, voltage, and *m/z* value of the ions. Selection and transmittance of specific *m/z* values is accomplished by the use of a certain RF frequency and voltage. Species with *m/z* values below the selected value have a greater acceleration rate and thus greater amplitude. With a high enough amplitude, these lower *m/z* ions are directed off axis and fail to reach the detector.

Ions with a *m/z* value greater than the selected value are filtered out via the DC voltage. The DC current does not affect the species with a *m/z* value less than the selected value because they are quickly refocused in response to the alternating RF potential. In contrast, those with a high *m/z* value do not refocus fast enough and the DC voltage alters their trajectory, and in effect causes them to drift away from the center of the quadrupole and not reach the detector.

By adjusting the RF and DC voltages, only ions pertaining to the selected *m/z* value are transmitted through the mass analyzer to the detector. RF and DC fields are continually scanned by either varying RF or DC potentials to detect all ions within a specified mass range, thereby producing a complete mass spectrum.

2.5 Triple Quadrupole Mass Analyzer

Triple quadrupole mass analyzers, as the name suggests, consists of three quadrupoles in tandem which are utilized to study the fragmentation of specific mass-selected ions; otherwise known as Tandem Mass Spectrometry (MS/MS). The first and third quadrupole are subjected to RF and DC potentials, while the second is only controlled by RF potential. The first quadrupole (Q1) in this series functions as a *m/z* filter, allowing passage for ions of a selected *m/z* value while rejecting all others for the entirety of mass spectrometric analysis. These ions are accelerated into the second quadrupole (Q2), also known as the collision cell, which typically contains an inert gas when conducting such experiments. Once the ions collide with the inert gas, kinetic energy is converted into internal energy which induces fragmentation in a process known as Collision-Induced Dissociation (CID). The resulting daughter fragments exit the collision cell and enter the third quadrupole (Q3) to undergo mass analysis followed by detection.

Chapter 3

Experimental

3.1 Introduction

Metal trimethyltrimethylacetylacetonates ($M(tmtm)_n$, n = 2, 3) were synthesized on site. Most metal trifluorotrimethylacetylacetonates ($M(tftm)_2$), aside from $Fe(tftm)_3$, were available from previous syntheses conducted by former Leskiw group members. The ligands used to synthesize these complexes were purchased from Sigma-Aldrich (St. Louis, MO, USA) and were incorporated without further purification. The resulting compounds were also not purified prior to mass spectrometric analysis. All metal acetylacetonates were purchased commercially from Roc/Ric Corp. (Sun Valley, CA, USA). Prior to loading into the mass spectrometer, all samples were dissolved in 5.0 mL of methanol at a concentration of 0.025 M, an efficient and effective concentration proven in previous studies conducted by Hunter.[12]

3.2 $Al(tmtm)_3$ Synthesis

0.6120 g of aluminum isopropoxide and 2.08 mL of 2,2,6,6-tetramethyl-3,5-heptanedione were added to 50.0 mL of toluene. The reaction mixture was allowed to stir for four hours under reflux, and then was left to stir overnight at room temperature. The solvent was removed from the resulting solution via rotary evaporation, and the resulting white solid was prepared for mass spectrometric analysis by dissolving in methanol to a concentration of 0.025 M. Product confirmation was achieved via mass spectrometric analysis as shown in Figure 7.1.[30]

3.3 $Fe(tmtm)_3$ Synthesis

0.2220 g of ferric chloride and 343 µL of 2,2,6,6-tetramethyl-3,5-heptanedione were added to 100.0 mL of deionized water followed by the dropwise addition of 20.0 mL of 1:1 (*v/v*) NH_4OH:H_2O. The reaction mixture was allowed to stir overnight at room temperature, and the resulting brown precipitate was isolated using vacuum filtration, dried overnight in a desiccator, and then prepared for mass spectrometric analysis by dissolving in methanol to a concentration of 0.025 M. Product confirmation was achieved via mass spectrometric analysis as shown in Figure 4.1.[31]

3.4 $Co(tmtm)_2$ Synthesis

0.4176 g of cobaltous chloride and 0.1026 g of sodium chloride were added to 10.0 mL of methanol and allowed to stir overnight at room temperature. The resulting solution was filtered into an Erlenmeyer flask and diluted with 20.0 mL of methanol followed by the addition of 732 µL of 2,2,6,6-tetramethyl-3,5-heptanedione and 0.1860 g of sodium carbonate. The solution stirred overnight at room temperature where the resulting green precipitate was isolated using vacuum filtration, dried overnight in a desiccator, and then prepared for mass spectrometric analysis by dissolving in methanol to a concentration of 0.025 M. Product confirmation was achieved via mass spectrometric analysis as shown in Figure A1.[32]

3.5 $Ni(tmtm)_2$ Synthesis

0.1517 g of nickel (II) chloride and 488 µL of 2,2,6,6-tetramethyl-3,5-heptanedione were added to 100.0 mL of deionized water followed by the dropwise addition of 15.0 mL of 1:1 (*v/v*) NH_4OH:H_2O. The reaction mixture was allowed to stir overnight at room temperature, and the resulting green precipitate was isolated using vacuum filtration, dried overnight in a desiccator, and then prepared for mass spectrometric analysis by dissolving in methanol to a concentration of 0.025 M. Product confirmation was achieved via mass spectrometric analysis as shown in Figure A2.[31]

3.6 $Cu(tmtm)_2$ Synthesis

0.1556 g of cupric chloride and 483 µL of 2,2,6,6-tetramethyl-3,5-heptanedione were added to 100.0 mL of deionized water followed by the dropwise addition of 15.0 mL of 1:1 (*v/v*) NH_4OH:H_2O. The reaction mixture was allowed to stir overnight at room temperature, and the resulting indigo precipitate was isolated using vacuum filtration, dried overnight in a desiccator, and then prepared for mass spectrometric analysis by dissolving in methanol to a concentration of 0.025 M. Product confirmation was achieved via mass spectrometric analysis as shown in Figure A3.[31]

3.7 $Zn(tmtm)_2$ Synthesis

0.2380 g of zinc chloride and 567 µL of 2,2,6,6-tetramethyl-3,5-heptanedione were added to 100.0 mL of deionized water followed by the dropwise addition of 15.0 mL of 1:1 (*v/v*) NH_4OH:H_2O. The reaction mixture was allowed to stir overnight at room temperature, and the resulting white precipitate was isolated using vacuum filtration, dried overnight in a desiccator, and then prepared for mass spectrometric analysis by dissolving in methanol to a concentration of 0.025 M. Product confirmation was achieved via mass spectrometric analysis as shown in Figure A4.[31]

3.8 $Fe(tftm)_3$ Synthesis

0.2097 g of ferric chloride and 2.70×10^2 µL of 1,1,1-trifluoro-5,5-dimethyl-2,4-hexanedione were added to 15 mL of methanol followed by the addition of 20.0 mL of 1:1 (*v/v*) NH_4OH:H_2O. The reaction mixture was allowed to stir for three hours at room

temperature. The solvent was evaporated under vacuum for approximately 30 minutes at 50.0 °C, and the resulting brown solid was collected. The sample for mass spectrometric analysis was prepared by dissolving the product in methanol to a concentration of 0.025 M. Product confirmation was achieved via mass spectrometric analysis as shown in Figure A5.[31]

3.9 Mass Spectrometric Parameters

All experimentation incorporating mass spectrometric analysis was performed using a Finnigan TSQ 7000 triple quadrupole electron impact mass spectrometer. Sample introduction was accomplished using a direct insertion probe fitted with a Re filament. Approximately 1.0 µL aliquots of the 0.025 M samples were added to a custom made double-loop filament which was evaporated to dryness within the vacuum chamber of the mass spectrometer prior to ionization. All mass spectra were produced using an electron energy of 70 eV, and were scanned within the range of *m/z* 50 to *m/z* 650. System calibration was performed with perfluorotributylamine (PFTBA) calibration gas. The source pressure was maintained at pressures between 10^{-5} to 10^{-6} Torr while the temperature of the source and manifold were held at 160.0 °C and 80.0 °C, respectively. In regards to the probe, it was set to ramp from ambient temperature to 1000.0 °C over a span of 10 minutes. The recorded peaks reflect the relative percentages of naturally occurring isotopes.

Chapter 4

The Gas-Phase Ligand Exchange Reactions of Iron (III) Trimethyltrimethylacetylacetonate ($Fe(tmtm)_3$) with Copper (II) Acetylacetonate ($Cu(acac)_2$)

4.1 Introduction

The data presented herein discusses evidence pertaining to the gas-phase ligand exchange reactions between $Fe(tmtm)_3$ and copper (II) acetylacetonate ($Cu(acac)_2$). Past studies have exclusively focused on divalent complexes while the co-sublimation reactions investigated in this study were performed using both divalent and trivalent complexes. For the first time, this study incorporates trimethyltrimethylaceylacetonate (tmtm) to further expand the scope of gas-phase ligand exchange reactions. These complexes were shown to behave very similarly to complexes in previous studies, as well as showing evidence for the formation of novel trivalent products.[11,12] Aside from interpreting the products stemming from ligand exchange processes, this study is also concerned with how these processes may be occurring. Relative intensities between the parent ions from the co-sublimation spectra were analyzed and compared back to the baseline spectra of the two separate reacting species. The differences between the two spectra were then used to suggest the relative reactivity of parent ions.

4.2 Iron (III) Trimethyltrimethylacetylacetonate ($Fe(tmtm)_3$)

$Fe(tmtm)_3$ is a seventeen-electron complex wherein three equivalents of (tmtm) are chelated to trivalent iron. The synthesis of this complex is outlined in Chapter 3. The EI mass spectrum is displayed in Figure 4.1 for the first time with tabulated data describing the relative abundance featured in Table 4.1. A mass range of *m/z* 225 to 615 was selected to highlight the natural isotopic pattern of iron, and to provide a closer view of the fragmentation pattern specific for $Fe(tmtm)_3$. The parent ion $[Fe(tmtm)_2]^+$, found at *m/z* 422, corresponds to the base peak of this spectrum, and subsequently, was used as the reference species when normalizing the spectrum. Another prominent peak can be found at *m/*z 365 which is consistent with the loss of a *tert*-butyl group to form $[Fe(tmtm)(tmtm\text{-}t\text{Bu})]^+$. The ion signal at *m/z* 239 represents the loss of an intact ligand to form $[Fe(tmtm)]^+$. The peak observed at *m/z* 605 corresponds to the molecular

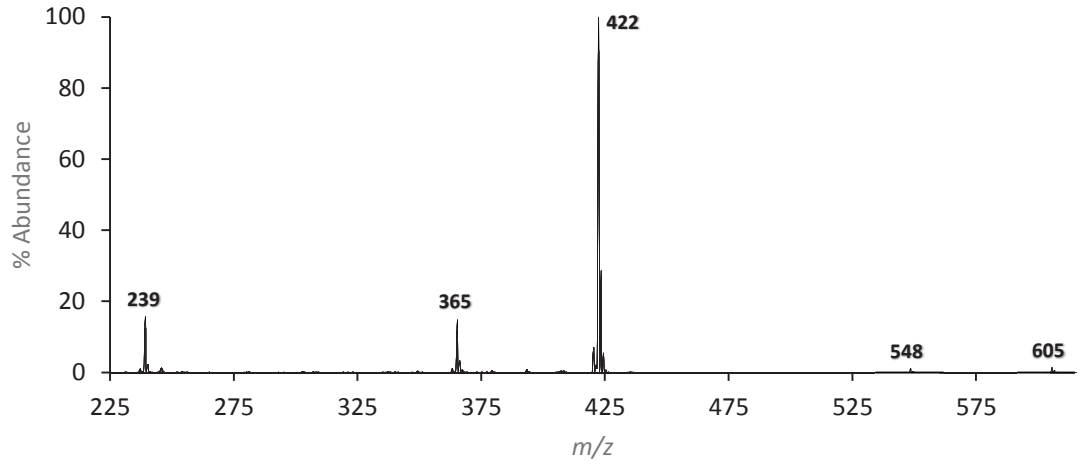

Figure 4.1: The 70 eV positive EI mass spectrum of $Fe(tmtm)_3$.

ion $[Fe(tmtm)_3]^+$ while the peak at *m/z* 548 is indicative of the fragmented species $[Fe(tmtm)_2(tmtm\text{-}t\text{Bu})]^+$.

The fragmentation pattern shown in Figure 4.1 is similar to that of $M(tftm)_3$ (M = an arbitrary metal-center), as discussed by Clobes.[16] An adapted fragmentation pathway for $Fe(tmtm)_3$ is presented in Figure 4.2. The low abundance associated with the molecular ion and $[Fe(tmtm)_2(tmtm\text{-}t\text{Bu})]^+$ can be attributed to the inability to delocalize positive charge across the metal and the high degree of steric repulsion between the bulky (tmtm) ligands.[19] The resulting instability provides a low kinetic barrier to facilitate the net loss of (tmtm).

Species	*m/z*	Relative Abundances
$[Fe(tmtm)_3]^+$	605	1
$[Fe(tmtm)_2(tmtm\text{-}t\text{Bu})]^+$	548	1
$[Fe(tmtm)_2]^+$	422	100
$[Fe(tmtm)(tmtm\text{-}t\text{Bu})]^+$	365	15
$[Fe(tmtm)]^+$	239	16

Table 4.1 The fragmentation species and corresponding relative abundances of the mass spectrometric analysis of $Fe(tmtm)_3$ as presented in Figure 4.1.

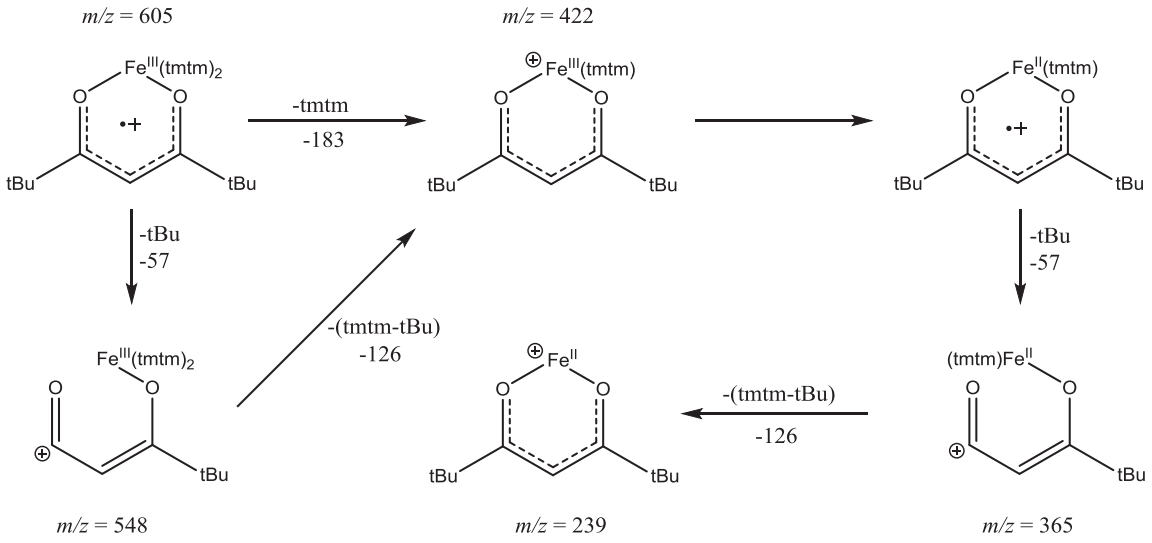

Figure 4.2: Fragmentation pathway of $Fe(tmtm)_3$.

4.3 Copper (II) Acetylacetonate ($Cu(acac)_2$)

For more information regarding $Cu(acac)_2$ and its fragmentation behavior please refer back to Chapter 1, Lerach, Hunter, or Shannon.[11-13] The base spectrum and corresponding tabulated data of $Cu(acac)_2$ may be found in Figure 4.3a and Table 4.2.

4.4 The Co-sublimation of $Fe(tmtm)_3$ & $Cu(acac)_2$

To investigate the gas-phase reactivity of $Fe(tmtm)_3$, a series of co-sublimation reactions were performed with other metal β-diketonates. The co-sublimation mass spectrum of $Fe(tmtm)_3$ and $Cu(acac)_2$ is displayed in Figure 4.3c wherein a series of gas-phase iron and copper product species are observed for the first time. Figure 4.3c is stacked beneath the individual sublimation spectra in Figure 4.3a and Figure 4.3b in an effort to emphasize the appearance of novel peaks in the co-sublimation spectrum which result from gas-phase ligand exchange. The corresponding masses with their respective abundances are provided in Table 4.2.

Upon inspection of the co-sublimation spectrum, the complete ligand exchange product $[Fe(acac)_2]^+$ is observed at *m/z* 254 while $[Fe(acac)(acac\text{-}CH_3)]^+$ can be found at *m/z* 239. Additionally, the singly-ligate product $[Fe(acac)]^+$ makes an appearance at *m/z* 155. Although not formed in substantial abundances, the formation of the hexacoordinate mixed ligand products should also be noted due to their novelty. The peak observed at *m/z* 521 suggests the formation of $[Fe(acac)(tmtm)_2]^+$ while the peak at *m/z* 464 is consistent with the formation of the fragmented species $[Fe(acac)(tmtm)(tmtm\text{-}t\text{Bu})]^+$. Detection of the intact mixed ligand product

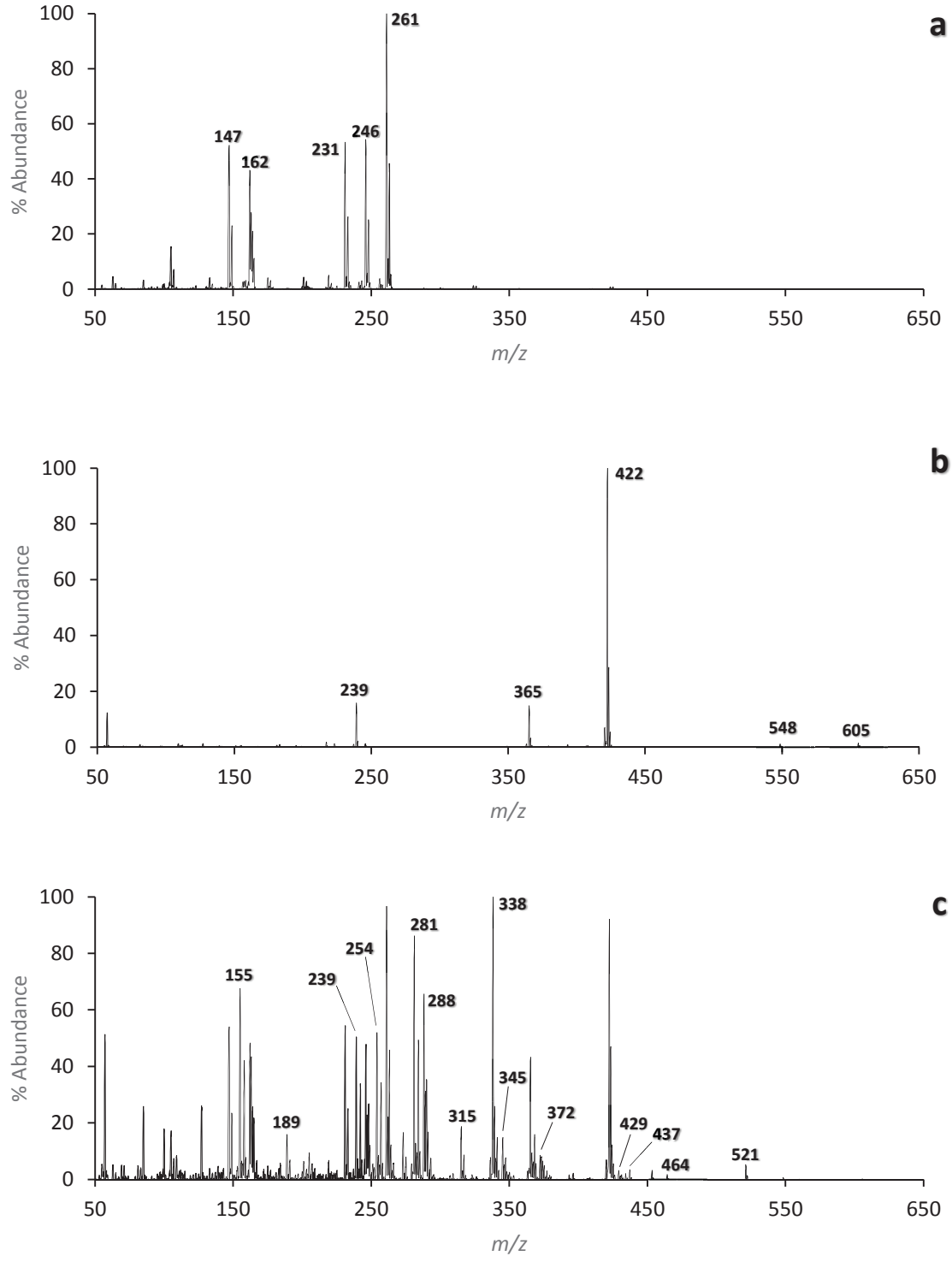

Figure 4.3: The 70eV positive EI mass spectra for a) $Cu(acac)_2$, b) $Fe(tmtm)_3$, and c) the gas-phase reactions of $Cu(acac)_2$ and $Fe(tmtm)_3$.

	Mass	Mass	FeL_3	CuL_2	FeL'_3	CuL'_2	FeL'_3 & CuL_2	
Species	Fe	Cu	Fe	Cu	Fe	Cu	Fe	Cu
$[ML_3]^+$	353	360	22	<1			1	<1
$[ML_2]^+$	254	261	100	100 (2.33)			**52**	97 (2.02)
$[ML_2\text{-}CH_3]^+$	239	246	20	54 (1.26)			***50***	48 (1.00)
$[ML_2\text{-}2CH_3]^+$	224	231	<1	53 (1.23)			**2**	54 (1.13)
$[ML]^+$	155	162	21	43 (1.00)			**68**	48 (1.00)
$[ML\text{-}CH_3]^+$	140	147	2**	52 (1.21)			**5****	54 (1.13)
$[ML'_3]^+$	605	612			1	<1	<1	<1
$[ML'_3\text{-}t\text{Bu}]^+$	548	555			1 (0.07)	<1	1 (0.02)	<1
$[ML'_2]^+$	422	429			100 (6.67)	26	92 (2.14)	**3**
$[ML'_2\text{-}t\text{Bu}]^+$	365	372			15 (1.00)	59	43 (1.00)	**9**
$[ML'_2\text{-}2t\text{Bu}]^+$	308	315			<1	100	<1	**19**
$[ML']^+$	239	246			16 (1.07)	9*	*50* (1.16)	**23***
$[ML'\text{-}t\text{Bu}]^+$	182	189			<1	28	<1	**16**
$[MLL'_2]^+$	521	528					**5**	<1
$[MLL'_2\text{-}t\text{Bu}]^+$	464	471					**2**	<1
$[ML_2L']^+$	437	444					**3**	<1
$[MLL']^+$	338	345					**100**	**15**
$[MLL'\text{-}t\text{Bu}]^+$	281	288					**86**	**66**
$[MLL'\text{-}CH_3\text{-}t\text{Bu}]^+$	266	273					**6**	**17**

Table 4.2 Relative positive ion intensities (% abundance) of hetero-metal species to their respective base peaks as presented in Figure 4.3. L = (acac), L' = (tmtm), *Protonated: observed at one mass unit higher than expected, **Deprotonated: observed at one mass unit lower than expected, *Italics:* Isobaric, **Bold**: Ligand exchange product, (Parentheses): Relative Ratio

$[Fe(acac)_2(tmtm)]^+$ can also be inferred from the peak at *m/z* 437, although the corresponding ion signal is, again, in relatively low abundance.

Conversely, the tetracoordinate mixed ligand products were formed in significantly greater abundance. In fact, the intact mixed ligand product $[Fe(acac)(tmtm)]^+$ at *m/z* 338 is the base peak of the co-sublimation spectrum. Loss of *tert*-butyl generates the fragmented species $[Fe(acac)(tmtm\text{-}t\text{Bu})]^+$ at *m/z* 281. Additionally, a minor peak appears at *m/z* 266 which is consistent with the loss of both *tert*-butyl and a methyl group to form the Fe(I) complex $[Fe(acac\text{-}CH_3)(tmtm\text{-}t\text{Bu})]^+$.

Also present in Figure 4.3c is a peak corresponding to the complete ligand exchange product $[Cu(tmtm)_2]^+$ at *m/z* 429. Ion signals at *m/z* 372 and 315 indicate the formation of $[Cu(tmtm)(tmtm\text{-}t\text{Bu})]^+$ and $[Cu(tmtm\text{-}t\text{Bu})_2]^+$, respectively. The product $[Cu(tmtm)H]^+$ is found at *m/z* 247 while the Cu(I) complex $[Cu(tmtm\text{-}t\text{Bu})]^+$ is observed

to form at *m/z* 189. Formation of the mixed ligand product $[Cu(acac)(tmtm)]^+$ can be inferred from the peak at *m/z* 345. Loss of *tert*-butyl generates the mixed ligand fragment $[Cu(acac)(tmtm\text{-}t\text{Bu})]^+$ at *m/z* 288. Additional fragmentation yields $[Cu(acac\text{-}CH_3)(tmtm\text{-}t\text{Bu})]^+$ as suggested by the ion signal at *m/z* 273.

The formation of Cu(I) products is consistent with prior experimentation and literature, and can be attributed to the acquisition of a stable d^{10} electron configuration following redox dependent fragmentation as shown in Figure 1.3.[11-13,19] Another notable feature consistent with the literature is the preferential formation of $[Cu(acac)(tmtm\text{-}t\text{Bu})]^+$ at *m/z* 288 over $[Cu(acac)(tmtm)]^+$ at *m/z* 345. Loss of *tert*-butyl is likely facilitated by the inability to delocalize positive charge across the metal center from the ligand orbitals to stabilize the intact product. The iron-containing mixed ligand product $[Fe(acac)(tmtm)]^+$ at *m/z* 338, on the other hand, is in greater abundance than $[Fe(acac)(tmtm\text{-}t\text{Bu})]^+$ at *m/z* 281. Unlike the copper-containing mixed ligand product, $[Fe(acac)(tmtm)]^+$ is stabilized via the localization of positive charge onto the metal center.

The relative ion intensities of parent fragments appearing in the baseline spectra were compared to their respective abundances in the co-sublimation spectrum in order to probe the mechanistic framework of the reaction and identify potential reactants. A facile method to perform such a comparison relies on the calculation of relative ratio values which quantify relative peak heights with respect to a frame of reference. Relative ratios of $Fe(tmtm)_3$ fragments can be determined by dividing the normalized

abundance of each $Fe(tmtm)_3$ parent ion contained in either Figure 4.3b or 4.3c by the normalized abundance of another fragment, otherwise referred to as the reference species. Once selected, the same fragment is maintained as the reference species for each relative ratio calculation. The resulting values are placed in parentheses next to the corresponding normalized abundance in Tables 4.2, 4.3, and 4.4. Any fragment that is isobaric with a ligand exchange product is automatically disregarded as a viable reference species since such peaks can have additive abundances and therefore may not accurately represent fragment consumption.

In order to elucidate the gas-phase mechanism that is contributing to the formation of the mixed ligand species, a careful analysis of the relative ratios must be

a

	Mass	**Mass**	**FeL'_3**	**CuL'_2**	**FeL'_3 & CuL_2**	
Species	Fe	Cu	Fe	Cu	Fe	Cu
$[ML'_3]^+$	605	612	1	<1	<1	<1
$[ML'_3$-*t*Bu$]^+$	548	555	1 (0.01)	<1	1 (0.01)	<1
$[ML'_2]^+$	422	429	100 (1.00)	26	92 (1.00)	**3**
$[ML'_2$-*t*Bu$]^+$	365	372	15 (0.15)	59	43 (0.46)	**9**
$[ML'_2$-2*t*Bu$]^+$	308	315	<1	100	<1	**19**
$[ML']^+$	239	246	16 (0.16)	9	*50* (0.54)	**23***
$[ML'$-*t*Bu$]^+$	182	189	<1	28	<1	**16**

b

	Mass	**Mass**	**FeL'_3**	**CuL'_2**	**FeL'_3 & CuL_2**	
Species	Fe	Cu	Fe	Cu	Fe	Cu
$[ML'_3]^+$	605	612	1	<1	<1	<1
$[ML'_3$-*t*Bu$]^+$	548	555	1 (0.07)	<1	1 (0.02)	<1
$[ML'_2]^+$	422	429	100 (6.67)	26	92 (2.14)	**3**
$[ML'_2$-*t*Bu$]^+$	365	372	15 (1.00)	59	43 (1.00)	**9**
$[ML'_2$-2*t*Bu$]^+$	308	315	<1	100	<1	**19**
$[ML']^+$	239	246	16 (1.07)	9	*50* (1.16)	**23***
$[ML'$-*t*Bu$]^+$	182	189	<1	28	<1	**24**

Table 4.3 Relative positive ion intensities (% abundance) of hetero-metal species to their respective base peaks as presented in Figure 4.3. Relative ratios (shown in parentheses) were calculated using a) $[Fe(tmtm)_2]^+$ as the reference species and b) $[Fe(tmtm)(tmtm\text{-}t\text{Bu})]^+$ as the reference species. L = (acac), L' = (tmtm) *Italics:* Isobaric, **Bold**: Ligand exchange product, (Parenthesis): Relative Ratio

considered to make a sensible inference based on the data. Consider, for example, the data presented in Table 4.3a, which reproduces the middle right data set in Table 4.2, where $[Fe(tmtm)_2]^+$ at *m/z* 422 is assigned as the reference species. Presented in parenthesis are the relative ratios of both $[Fe(tmtm)(tmtm\text{-}t\text{Bu})]^+$ at *m/z* 365 and $[Fe(tmtm)]^+$ at *m/z* 239 which show some variable increase in intensity. In the baseline spectrum, $[Fe(tmtm)(tmtm\text{-}t\text{Bu})]^+$ has a relative ratio of 0.15 with respect to the intact species, but when in the presence of $Cu(acac)_2$, the relative ratio increases to 0.46. Likewise, $[Fe(tmtm)]^+$ has a relative ratio of 0.16 in the baseline spectrum that increases to a relative ratio of 0.54 in the co-sublimation spectrum. The relative peak growth exhibited by both parent ions reflects the decreasing abundance of the reference species $[Fe(tmtm)_2]^+$ upon exposure to $Cu(acac)_2$, which in turn suggests the consumption of $[Fe(tmtm)_2]^+$ in a reaction with $Cu(acac)_2$.

When changing the reference species to either $[Fe(tmtm)(tmtm\text{-}t\text{Bu})]^+$ or $[Fe(tmtm)]^+$, a similar conclusion can be attained. Consider, for example, Table 4.3b where $[Fe(tmtm)(tmtm\text{-}t\text{Bu})]^+$ is selected as the reference species. The relative ratio of the intact species $[Fe(tmtm)_2]^+$ is clearly lower in the presence of $Cu(acac)_2$ with respect to the baseline spectrum. Peak attenuation of the corresponding ion signal reflects the decreasing abundance of $[Fe(tmtm)_2]^+$, and again suggests the consumption of $[Fe(tmtm)_2]^+$ in a reaction with $Cu(acac)_2$. Thus, the relative ratios presented in both Table 4.3a and 4.3b indicate the preferential reactivity of $Cu(acac)_2$ with $[Fe(tmtm)_2]^+$ rather than with $[Fe(tmtm)(tmtm\text{-}t\text{Bu})]^+$ and $[Fe(tmtm)]^+$ which appear to be relatively inert. Such a conclusion operates on the presumption that the magnitude of relative

peak growth or attenuation correlates to fragment reactivity. Additional experiments, namely collision-induced reactions, are used to support this analysis and are presented in detail following this discussion.

In considering the fragments of $Cu(acac)_2$, a similar analysis can be implemented to gain further insight into the reaction pathway. To accurately assess the reactivity of each fragment, the corresponding relative ratios must again be calculated. Shown in Table 4.4a, which reproduces the upper left data set in Table 4.2, are the resulting relative ratios of $Cu(acac)_2$ fragments if $[Cu(acac)_2]^+$ at *m/z* 261 is selected as the reference species. Given that the relative ratios do not change substantially, the extent to which each species is consumed in a reaction is not as evident.

a

	Mass	**Mass**	**FeL_3**	**CuL_2**	**FeL'_3 & CuL_2**	
Species	Fe	Cu	Fe	Cu	Fe	Cu
$[ML_3]^+$	353	360	22	<1	1	<1
$[ML_2]^+$	254	261	100	100 (1.00)	**52**	97 (1.00)
$[ML_2\text{-}CH_3]^+$	239	246	20	54 (0.54)	***50***	48 (0.49)
$[ML_2\text{-}2CH_3]^+$	224	231	<1	53 (0.53)	**2**	54 (0.56)
$[ML]^+$	155	162	21	43 (0.43)	**68**	48 (0.49)
$[ML\text{-}CH_3]^+$	140	147	<1	52 (0.52)	**2**	54 (0.56)

b

	Mass	**Mass**	**FeL_3**	**CuL_2**	**FeL'_3 & CuL_2**	
Species	Fe	Cu	Fe	Cu	Fe	Cu
$[ML_3]^+$	353	360	22	<1	1	<1
$[ML_2]^+$	254	261	100	100 (2.33)	**52**	97 (2.02)
$[ML_2\text{-}CH_3]^+$	239	246	20	54 (1.26)	***50***	48 (1.00)
$[ML_2\text{-}2CH_3]^+$	244	231	<1	53 (1.23)	**2**	54 (1.13)
$[ML]^+$	155	162	21	43 (1.00)	**68**	48 (1.00)
$[ML\text{-}CH_3]^+$	140	147	<1	52 (1.21)	**2**	54 (1.13)

Table 4.4 Relative positive ion intensities (% abundance) of hetero-metal species to their respective base peaks as presented in Figure 4.3. Relative ratios (shown in parentheses) were calculated using a) $[Cu(acac)_2]^+$ as the reference species and b) $[Cu(acac)]^+$ as the reference species. L = (acac), L' = (tmtm) *Italics:* Isobaric, **Bold**: Ligand exchange product, (Parenthesis): Relative Ratio

If instead $[Cu(acac)]^+$ at *m/z* 162 is selected as the reference species, the resulting relative ratios presented in Table 4.4b prove more useful towards the interpretation of fragment reactivity. The peak corresponding to $[Cu(acac)_2]^+$ becomes attenuated from a relative ratio of 2.33 to a relative ratio of 2.02 following co-sublimation which would suggest its involvement in ligand exchange processes. The same conclusion can be made for the remaining fragments when compared to the reference species $[Cu(acac)]^+$. However, unlike for the relative ratio analysis of $Fe(tmtm)_3$, a clear preference for one fragment to react over another is not demonstrated for the $Cu(acac)_2$ species. The collision-induced reactions of mass-selected $Cu(acac)_2$ fragments and neutral $Fe(tmtm)_3$ attempt to resolve this uncertainty in fragment reactivity and are presented in detail in the following section.

4.5 Selective Reactions of $Fe(tmtm)_3$ & $Cu(acac)_2$

Although not routinely employed, tandem mass spectrometry (MS/MS) is an appropriate technique to ascertain specific reaction pathways that likely occur within the mass spectrometer. A triple quadrupole mass analyzer consists of two mass analyzers with a collision cell between the two scanning quadrupoles. MS/MS exclusively allows the passage of a mass-selected ion from the first quadrupole into the collision cell which traditionally contains an inert gas species in order to induce further fragmentation from that specific ion. The resulting fragments are then collected and processed by the third quadrupole. Identified fragments can subsequently be used to

validate or determine molecular structure. This process as a whole is known as collision-induced dissociation (CID).

Alternatively, as described herein, a metal β-diketonate compound of interest is loaded into the collision cell chamber rather than an inert species. This modification allows the chamber to act as a reaction vessel for the selected ion and neutral compound. Having a highly volatile nature, the neutral complex of interest readily enters the gas phase under the reduced pressure of the instrument. As an illustration of this concept, consider the cation and neutral gas species, $[Fe(tmtm)_2]^+$ and $Cu(acac)_2$, as the reactants of interest. To investigate possible reaction pathways between them, the first quadrupole of the mass spectrometer is set to mass-select $[Fe(tmtm)_2]^+$ at *m/z* 422 with $Cu(acac)_2$ loaded into the collision cell chamber, and the third quadrupole is scanned to detect the resulting products. In interpreting these spectra, it becomes possible to propose gas-phase reaction pathways stemming from the particular ion of interest to account for product detection.

The selective reactions presented in this section are performed through the use of MS/MS, and for this study will include $[Fe(tmtm)_2]^+$, $[Fe(tmtm)(tmtm\text{-}t\text{Bu})]^+$, $[Fe(tmtm)]^+$, $[Cu(acac)_2]^+$, $[Cu(acac)(acac\text{-}CH_3)]^+$, $[Cu(acac\text{-}CH_3)_2]^+$, $[Cu(acac)]^+$, and $[Cu(acac\text{-}CH_3)]^+$. Note that the selected ion will be the only species allowed to enter the collision cell, causing the resulting spectra to be devoid of all other ions emerging from the ion source. The third quadrupole will scan the mass range from *m/z* 50 to *m/z* 650 for all products from the selective reaction. All reactions were performed over a span of

ten minutes with a source temperature of 160 °C, manifold temperature of 80 °C, electron energy of 70 eV, and the electron multiplier held at 1200 V.

Shown in Figure 4.4 is the mass spectrum of the ligand exchange product resulting from the reaction between mass-selected $[Fe(tmtm)_2]^+$ at *m/z* 422 and neutral $Cu(acac)_2$ which specifically corresponds to the formation of the mixed ligand product $[Fe(acac)(tmtm)_2]^+$ at *m/z* 521.

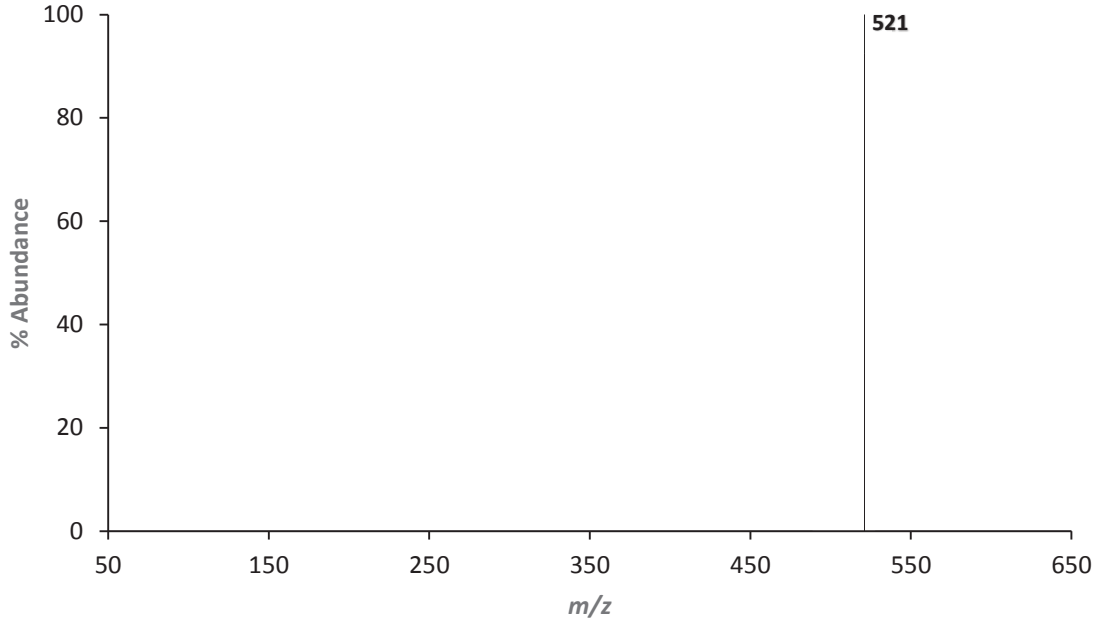

Figure 4.4: The 70eV positive EI mass spectrum EI mass spectrum obtained by scanning the third quadrupole after the selective reaction of *m/z* 422 ($[Fe(tmtm)_2]^+$) with neutral $Cu(acac)_2$ to produce the mixed ligand product at *m/z* 521 ($[Fe(acac)(tmtm)_2]^+$).

Equation (4.1) provides a mechanism to help account for the gas-phase formation of the triply-ligated product.

$$[Fe^{III}(tmtm)_2]^+ + Cu^{II}(acac)_2 \rightarrow$$

$$[Fe^{III}(acac)(tmtm)_2]^{+\bullet} + Cu^{I}(acac) \qquad \text{(Eqn 4.1)}$$

The spectrum displayed in Figure 4.5 features a peak at *m/z* 428 resulting from the reaction between mass-selected $[Fe(tmtm)_2]^+$ at *m/*z 422 and neutral $Cu(acac)_2$. The observed ion signal is indicative of the complete ligand exchange product $[Cu(tmtm)_2]^+$, albeit at one mass unit lower than expected.

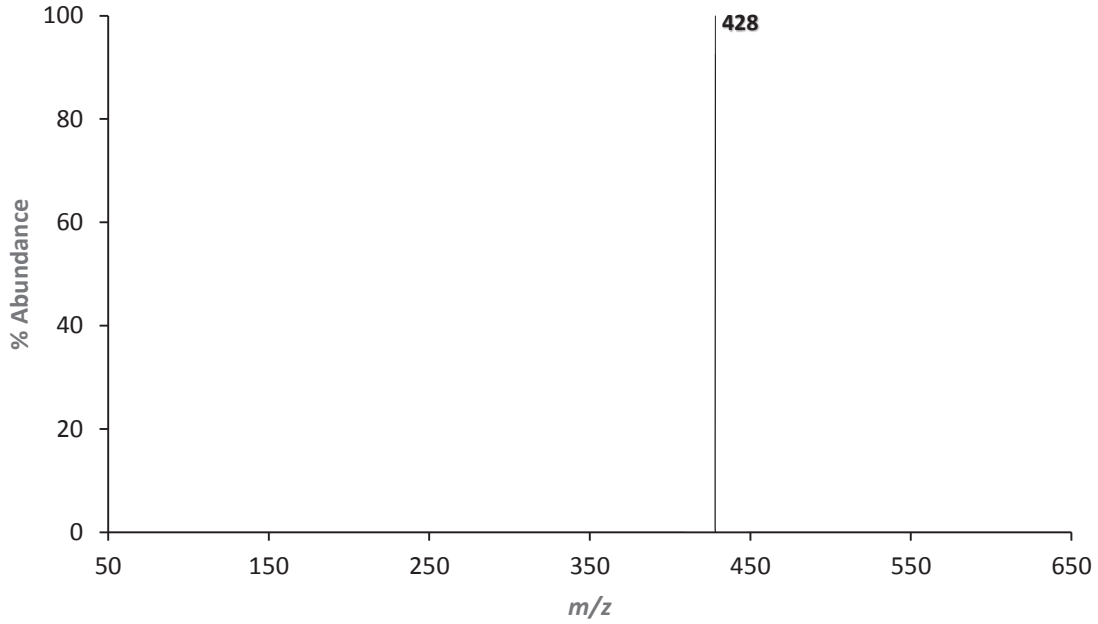

Figure 4.5: The 70eV positive EI mass spectrum obtained by scanning the third quadrupole after the selective reaction of *m/z* 422 ($[Fe(tmtm)_2]^+$) with neutral $Cu(acac)_2$ to produce the product at m/z 428 ($[Cu(tmtm)_2]^+$).

The following expression in Equation (4.2) incorporates complete ligand exchange to generate the cupric product.

$$[Fe^{III}(tmtm)_2]^+ + Cu^{II}(acac)_2 \rightarrow$$

$$[Cu^{II}(tmtm)_2]^{+\bullet} + Fe^{II}(acac)_2 \qquad \text{(Eqn 4.2)}$$

Another product generated by the collision-induced reaction of mass-selected $[Fe(tmtm)_2]^+$ at *m/z* 422 and neutral $Cu(acac)_2$ is the product species $[Cu(tmtm)(tmtm\text{-}t\text{Bu})]^+$ at *m/z* 372 as shown in Figure 4.6.

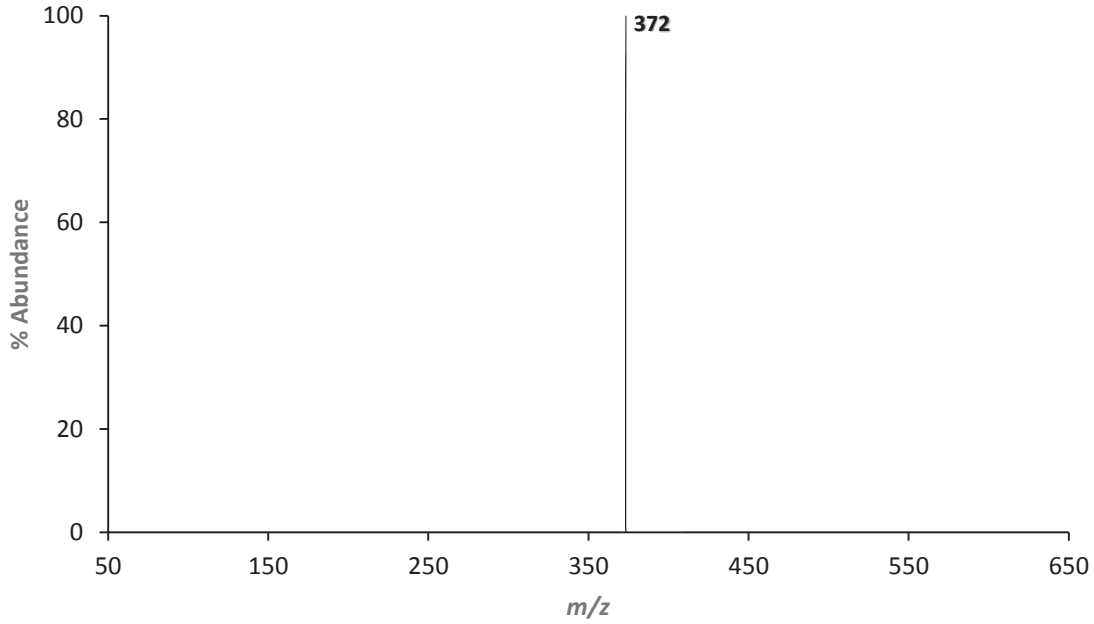

Figure 4.6: The 70eV positive EI mass spectrum mass spectrum obtained by scanning the third quadrupole after the selective reaction of *m/z* 422 ($[Fe(tmtm)_2]^+$) with neutral $Cu(acac)_2$ to produce the product at m/z 372 ($[Cu(tmtm)(tmtm\text{-}tBu)]^+$).

As shown in Equation (4.3), the proposed product is generated by complete ligand exchange and *tert*-butyl fragmentation.

$$[Fe^{III}(tmtm)_2]^+ + Cu^{II}(acac)_2 \rightarrow$$

$$[Cu^{II}(tmtm)(tmtm\text{-}t\text{Bu})]^+ + Fe^{II}(acac)_2 + t\text{Bu}^{\bullet} \qquad \text{(Eqn 4.3)}$$

The mixed ligand product $[Cu(acac)(tmtm)]^+$ at *m/z* 344 presented in Figure 4.7 also appears to form following the selective reaction of $[Fe(tmtm)_2]^+$ at *m/z* 422 and neutral $Cu(acac)_2$. Production of the mixed ligand species occurs at one mass unit lower than expected.

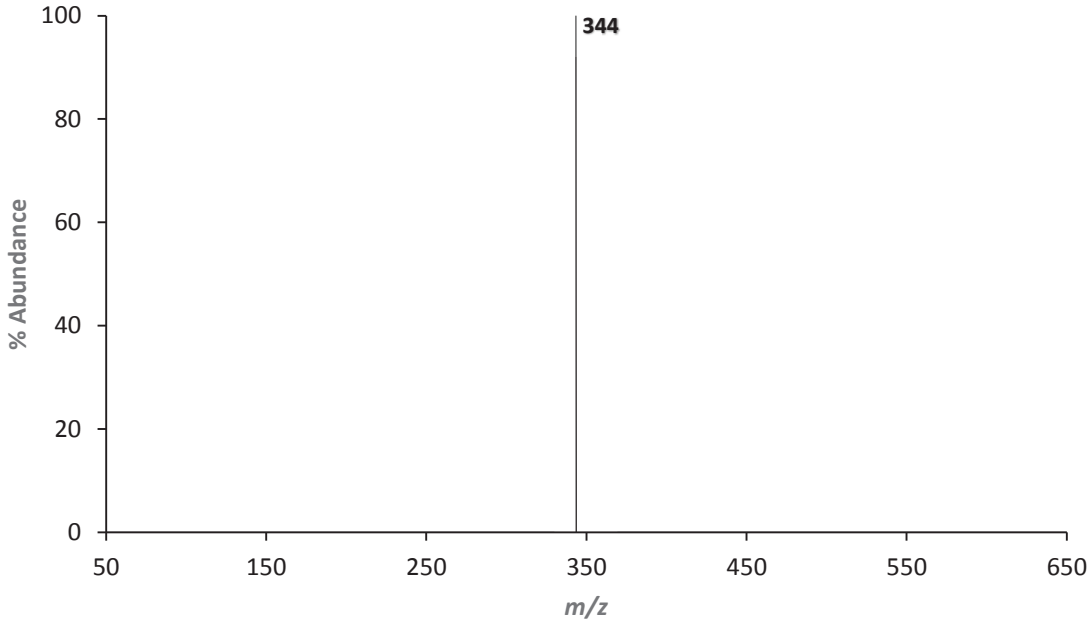

Figure 4.7: The 70eV positive EI mass spectrum obtained by scanning the third quadrupole after the selective reaction of *m/z* 422 ($[Fe(tmtm)_2]^+$) with neutral $Cu(acac)_2$ to produce the mixed ligand product at m/z 344 ($[Cu(acac)(tmtm)]^+$).

Equation (4.4) provides a mechanism featuring partial ligand exchange to form the mixed ligand product.

$$[Fe^{III}(tmtm)_2]^+ + Cu^{II}(acac)_2 \rightarrow$$

$$[Cu^{II}(acac)(tmtm)]^{+\bullet} + Fe^{II}(acac)(tmtm) \qquad \text{(Eqn 4.4)}$$

Additionally, the iron mixed ligand product $[Fe(acac)(tmtm)]^+$ forms following the reaction of mass-selected $[Fe(tmtm)_2]^+$ and neutral $Cu(acac)_2$ based on the presence of the peak at *m/z* 338 in Figure 4.8. Also shown in this spectrum is an ion signal at *m/z* 422 which is representative of the parent ion $[Fe(tmtm)_2]^+$.

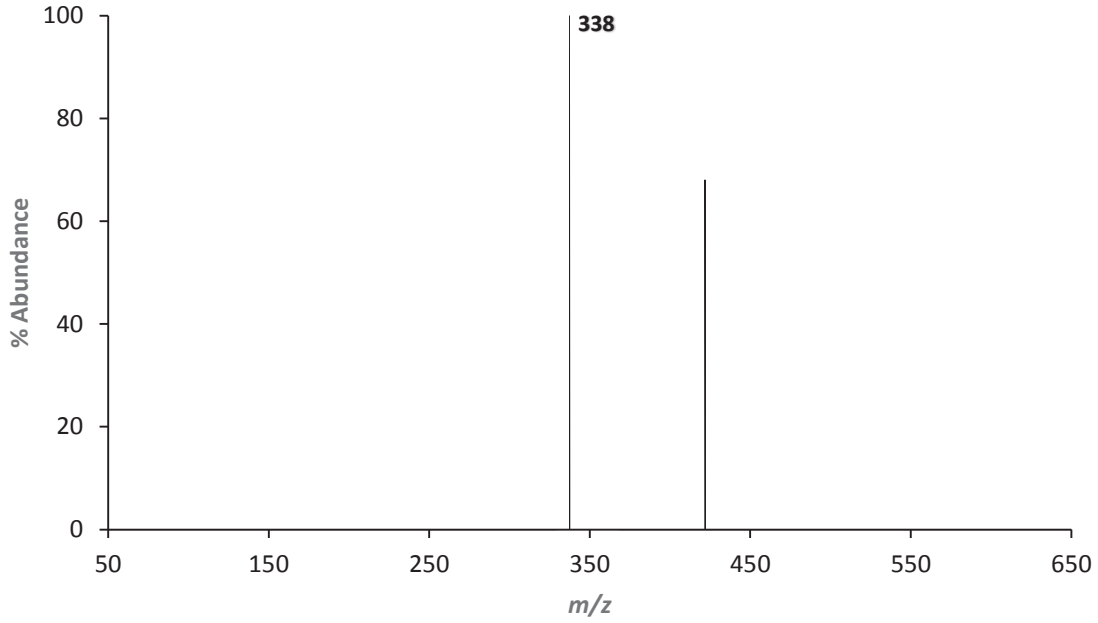

Figure 4.8: The 70eV positive EI mass spectrum obtained by scanning the third quadrupole after the selective reaction of *m/z* 422 ($[Fe(tmtm)_2]^+$) with neutral $Cu(acac)_2$ to produce the mixed ligand product at m/z 338 ($[Fe(acac)(tmtm)]^+$).

Product formation likely occurs via partial ligand exchange between the ferric and cupric reactants as outlined in Equation (4.5).

$$[Fe^{III}(tmtm)_2]^+ + Cu^{II}(acac)_2 \rightarrow$$

$$[Fe^{III}(acac)(tmtm)]^+ + Cu^{II}(acac)(tmtm) \qquad \text{(Eqn 4.5)}$$

The appearance of a peak at *m/z* 315 in Figure 4.9 corresponds to the formation of the cuprous fragment $[Cu(tmtm\text{-}t\text{Bu})_2]^+$ from the collision-induced reaction of mass-selected $[Fe(tmtm)_2]^+$ with neutral $Cu(acac)_2$. The peak at *m/z* 378 does not correlate to any species of interest, while the base peak at *m/z* 422 corresponds to $[Fe(tmtm)_2]^+$.

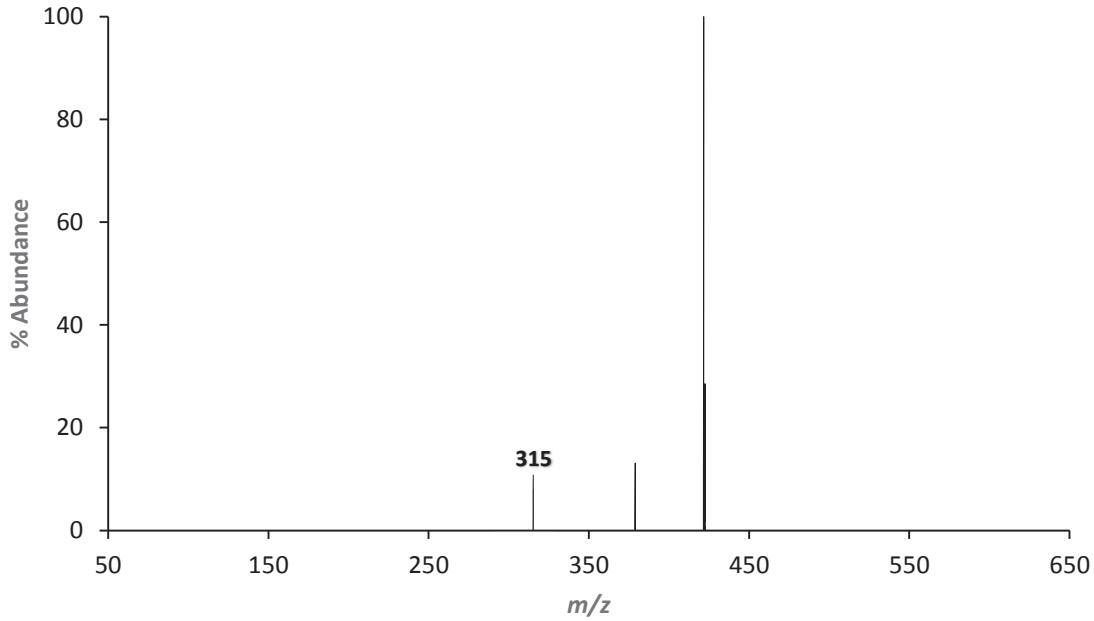

Figure 4.9*:* The 70eV positive EI mass spectrum obtained by scanning the third quadrupole after the selective reaction of *m/z* 422 ($[Fe(tmtm)_2]^+$) with neutral $Cu(acac)_2$ to produce the product at m/z 315 ($[Cu(tmtm\text{-}t\text{Bu})_2]^+$).

Mechanistically, the generation of $[Cu(tmtm\text{-}t\text{Bu})_2]^+$ likely occurs according to Equation (4.6) through a process of complete ligand exchange, reductive rearrangement, and *tert*-butyl fragmentation.

$$[Fe^{III}(tmtm)_2]^+ + Cu^{II}(acac)_2 \rightarrow$$

$$[Cu^{I}(tmtm\text{-}t\text{Bu})_2]^+ + Fe^{II}(acac)_2 + 2t\text{Bu}^{\bullet} \qquad \text{(Eqn 4.6)}$$

The mixed ligand fragment $[Cu(acac)(tmtm\text{-}t\text{Bu})]^+$ at *m/z* 289 was also observed to form from the collision-induced reactions of mass-selected $[Fe(tmtm)_2]^+$ at *m/z* 422 and neutral $Cu(acac)_2$, and is presented in Figure 4.10. Product formation occurs at one mass unit higher than expected.

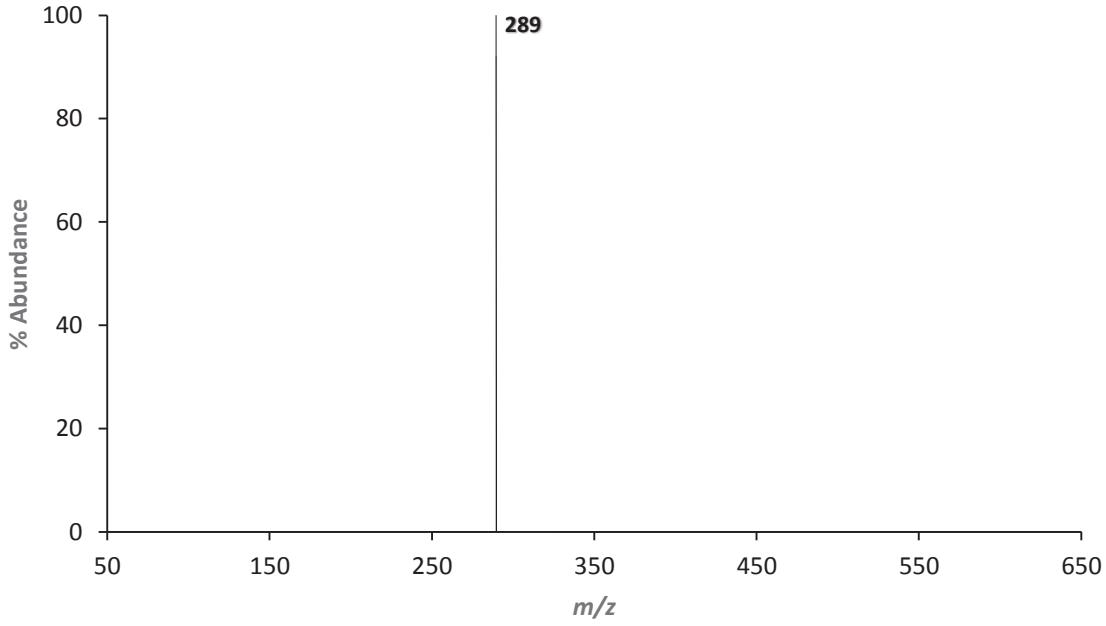

Figure 4.10: The 70eV positive EI mass spectrum obtained by scanning the third quadrupole after the selective reaction of *m/z* 422 ($[Fe(tmtm)_2]^+$) with neutral $Cu(acac)_2$ to produce the mixed ligand fragment at m/z 289 ($[Cu(acac)(tmtm\text{-}t\text{Bu})]^+$).

The proposed mechanism provided in Equation (4.7) entails partial ligand exchange and *tert*-butyl fragmentation to generate $[Cu(acac)(tmtm\text{-}t\text{Bu})]^+$.

$$[Fe^{III}(tmtm)_2]^+ + Cu^{II}(acac)_2 \rightarrow$$

$$[Cu^{II}(acac)(tmtm\text{-}t\text{Bu})]^+ + Fe^{II}(acac)(tmtm) + t\text{Bu}^{\bullet} \qquad \text{(Eqn 4.7)}$$

The mixed ligand fragment $[Fe(acac)(tmtm\text{-}tBu)]^+$ at *m/z* 281 in Figure 4.11 is observed to form following the reaction of mass-selected $[Fe(tmtm)_2]^+$ at *m/z* 422 with neutral $Cu(acac)_2$.

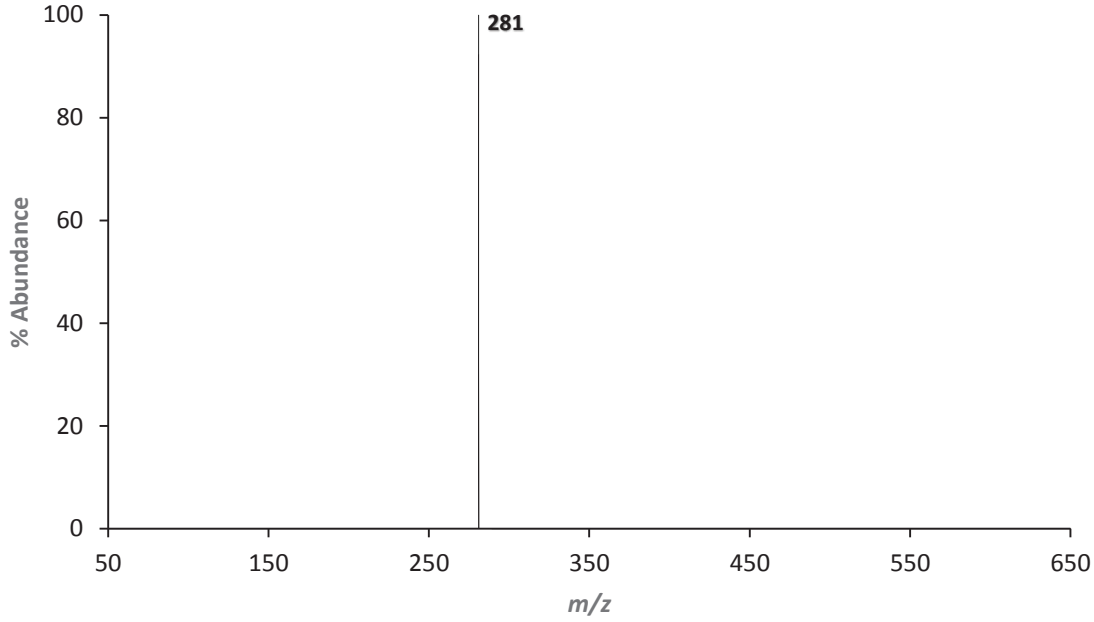

Figure 4.11: The 70eV positive EI mass spectrum obtained by scanning the third quadrupole after the selective reaction of *m/z* 422 ($[Fe(tmtm)_2]^+$) with neutral $Cu(acac)_2$ to produce the mixed ligand fragment at m/z 281 ($[Fe(acac)(tmtm\text{-}tBu)]^+$).

To generate the mixed ligand product $[Fe(acac)(tmtm\text{-}tBu)]^+$, *tert*-butyl fragmentation is coupled with partial ligand as shown in Equation (4.8)

$$[Fe^{III}(tmtm)_2]^+ + Cu^{II}(acac)_2 \rightarrow$$

$$[Fe^{II}(acac)(tmtm\text{-}tBu)]^+ + Cu^{II}(acac)(tmtm) + tBu^{\bullet} \qquad \text{(Eqn 4.8)}$$

Shown in Figure 4.12 is a peak corresponding to the generation of the cuprous mixed ligand fragment $[Cu(acac\text{-}CH_3)(tmtm\text{-}t\text{Bu})]^+$ at *m/z* 274 from the collision-induced reaction between $[Fe(tmtm)_2]^+$ and neutral $Cu(acac)_2$. Generation of the mixed ligand fragment occurs at one mass unit higher than expected.

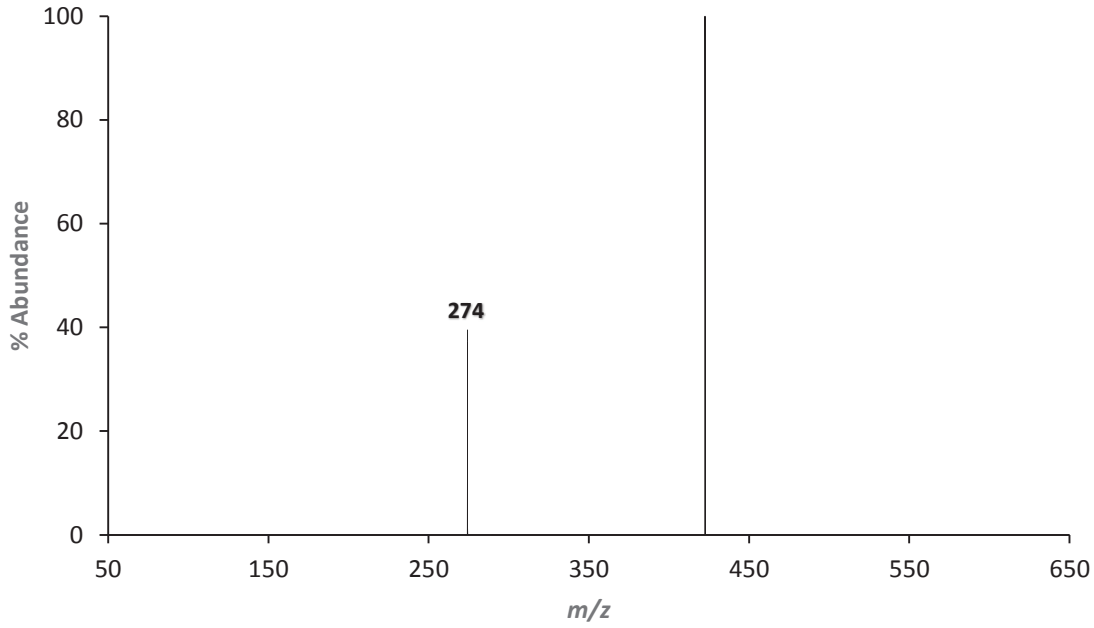

Figure 4.12: The 70eV positive EI mass spectrum obtained by scanning the third quadrupole after the selective reaction of *m/z* 422 ($[Fe(tmtm)_2]^+$) with neutral $Cu(acac)_2$ to produce the mixed ligand fragment at m/z 274 ($[Cu(acac\text{-}CH_3)(tmtm\text{-}t\text{Bu})]^+$).

Formation of the mixed ligand fragment is proposed to occur through partial ligand exchange, reductive rearrangement, and fragmentation as shown in Equation (4.9).

$$[Fe^{III}(tmtm)_2]^+ + Cu^{II}(acac)_2 \rightarrow$$

$$[Cu^{I}(acac\text{-}CH_3)(tmtm\text{-}t\text{Bu})]^+ + Fe^{II}(acac)(tmtm)$$

$$+ t\text{Bu}^{\bullet} + CH_3^{\bullet} \qquad \text{(Eqn 4.9)}$$

The final product observed for collision-induced reactions between mass-selected $[Fe(tmtm)_2]^+$ at *m/z* 422 and neutral $Cu(acac)_2$ corresponds to the ion signal observed at *m/z* 189 in Figure 4.13.

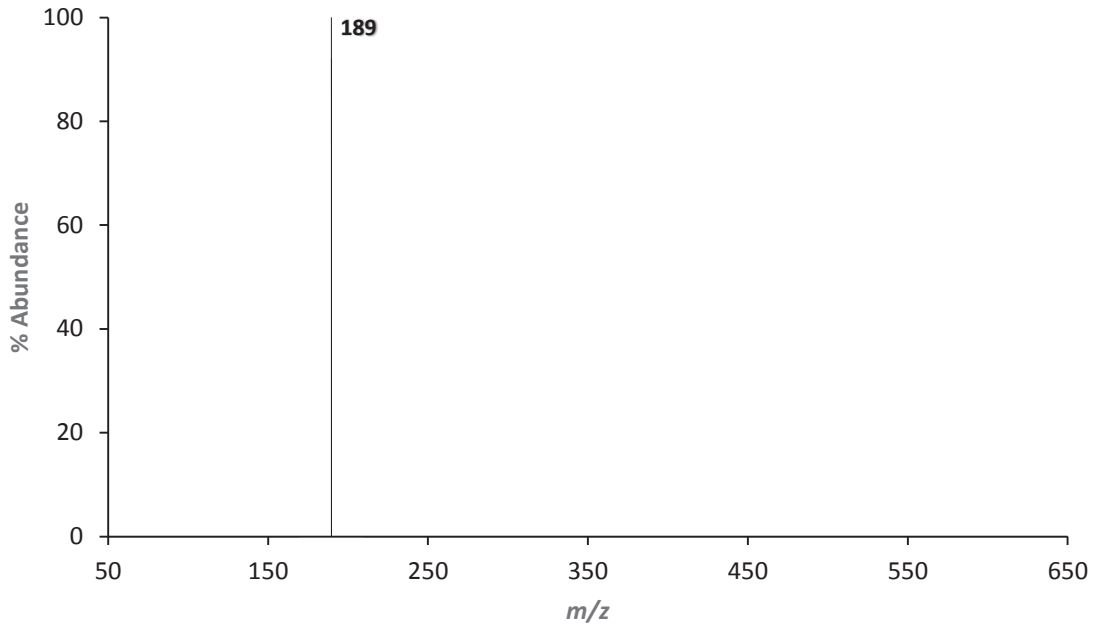

Figure 4.13: The 70eV positive EI mass spectrum obtained by scanning the third quadrupole after the selective reaction of *m/z* 422 ($[Fe(tmtm)_2]^+$) with neutral $Cu(acac)_2$ to produce the product at m/z 189 ($[Cu(tmtm\text{-}t\text{Bu})]^+$).

The observed ions signal is indicative of $[Cu(tmtm\text{-}t\text{Bu})]^+$ formation which likely occurs through a process of complete ligand exchange and fragmentation as expressed in Equation (4.10).

$$[Fe^{III}(tmtm)_2]^+ + Cu^{II}(acac)_2 \rightarrow$$

$$[Cu^{I}(tmtm\text{-}t\text{Bu})]^+ + Fe^{II}(acac)_2 + tmtm^{\bullet} + t\text{Bu}^{\bullet} \qquad \text{(Eqn 4.10)}$$

The next set of selective reactions involves the mass-selection of $[Fe(tmtm)(tmtm\text{-}t\text{Bu})]^+$ at *m/*z 365 while maintaining $Cu(acac)_2$ as the neutral gas-phase complex in the collision chamber. The two peaks observed in Figure 4.14 correspond to $[Fe(acac)(tmtm)_2]^+$ at *m/*z 522 and the mass-selected ion. Formation of the mixed ligand product occurs at one mass unit higher than expected.

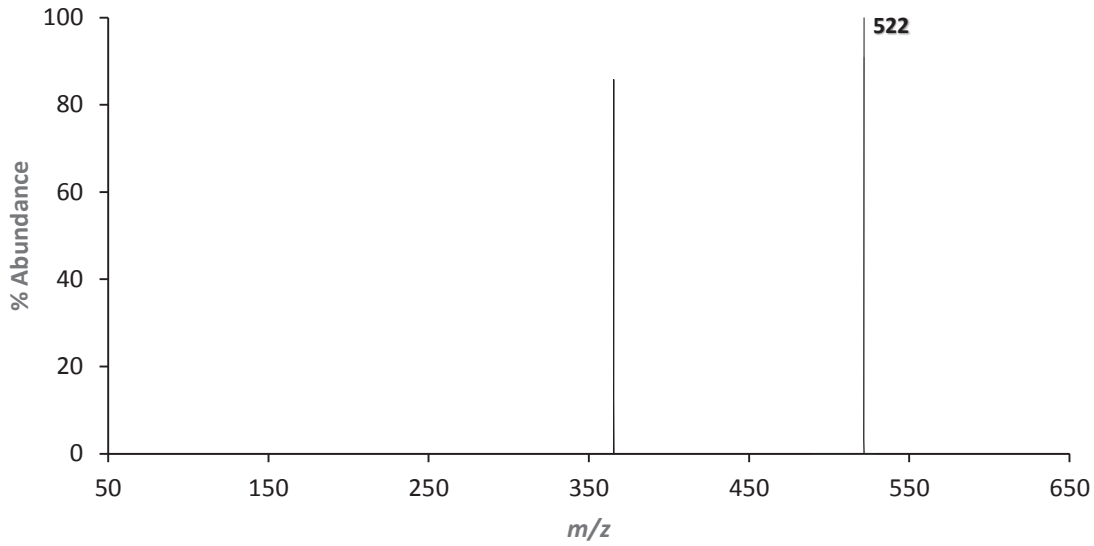

Figure 4.14: The 70eV positive EI mass spectrum obtained by scanning the third quadrupole after the selective reaction of *m/z* 365 ($[Fe(tmtm)(tmtm\text{-}tBu)]^+$) with neutral $Cu(acac)_2$ to produce the mixed ligand product at *m/z* 522 ($[Fe(acac)(tmtm)_2]^+$).

In addition to partial ligand exchange, product formation seemingly results from the donation of (tmtm) from a second equivalent of $[Fe(tmtm)(tmtm\text{-}t\text{Bu})]^+$, as expressed in Equation (4.11).

$$2[Fe^{II}(tmtm)(tmtm\text{-}t\text{Bu})]^+ + Cu^{II}(acac)_2 \rightarrow$$

$$[Fe^{III}(acac)(tmtm)_2]^{+\bullet} + [Fe^{I}(tmtm\text{-}tBu)]^+$$

$$+ Cu^{I}(acac)(tmtm\text{-}t\text{Bu}) \qquad \text{(Eqn 4.11)}$$

Figure 4.15 features a spectrum with two peaks at *m/z* 365 and *m/z* 346 following the reaction between mass-selected $[Fe(tmtm)(tmtm\text{-}tBu)]^+$ at *m/z* 365 and neutral $Cu(acac)_2$. The latter peak indicates the formation of the mixed ligand product $[Cu(acac)(tmtm)]^+$ at one mass unit higher than expected.

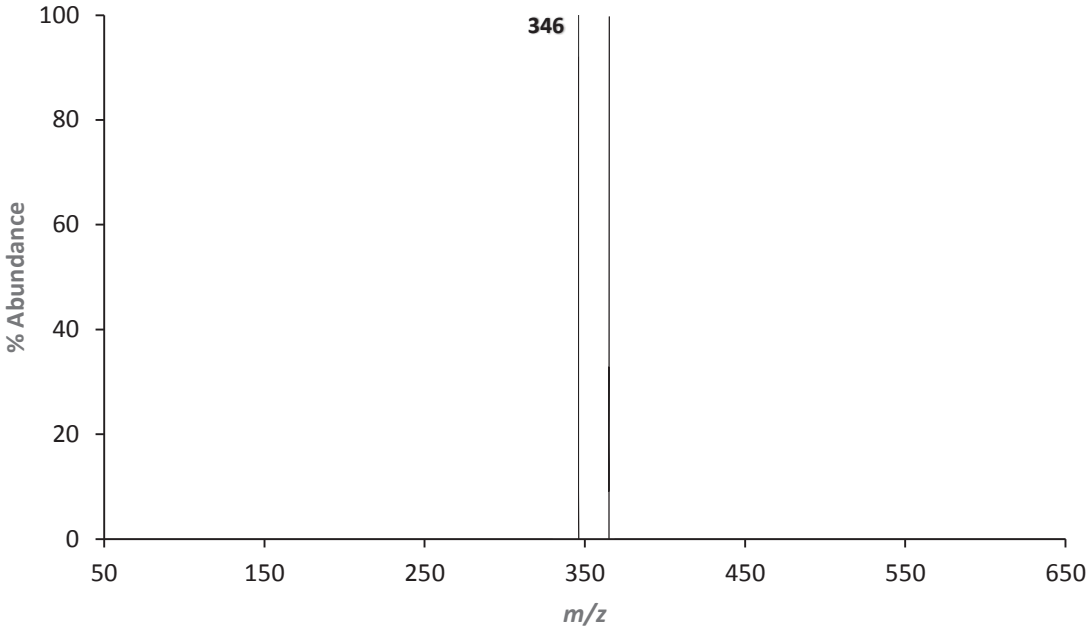

Figure 4.15: The 70eV positive EI mass spectrum obtained by scanning the third quadrupole after the selective reaction of *m/z* 365 ($[Fe(tmtm)(tmtm\text{-}tBu)]^+$) with neutral $Cu(acac)_2$ to produce the mixed ligand product at *m/z* 346 ($[Cu(acac)(tmtm)]^+$).

Given this finding, it was possible to propose the following mechanism in Equation (4.12) which features partial ligand exchange to form the mixed ligand product.

$$[Fe^{II}(tmtm)(tmtm\text{-}tBu)]^+ + Cu^{II}(acac)_2 \rightarrow$$

$$[Cu^{II}(acac)(tmtm)]^{\bullet+} + Fe^{I}(acac)(tmtm\text{-}tBu) \qquad \text{(Eqn 4.12)}$$

The spectrum shown in Figure 4.16 features a peak at *m/z* 281, indicating the formation of the mixed ligand product $[Fe(acac)(tmtm\text{-}tBu)]^+$ from the reaction between mass-selected $[Fe(tmtm)(tmtm\text{-}tBu)]^+$ at *m/z* 365 and neutral $Cu(acac)_2$. Additional peaks are present that correspond to the generation of $[Fe(tmtm)_2(tmtm\text{-}tBu)]^+$, $[Fe(tmtm)]^+$, and $[tBu]^+$ at *m/z* 549, 239, and 57, respectively.

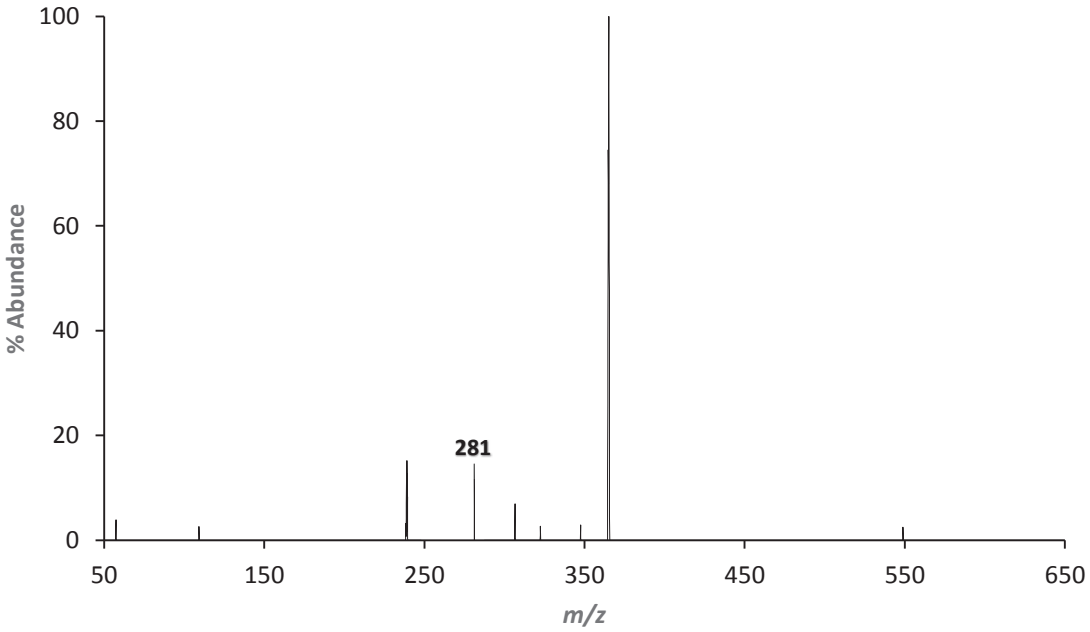

Figure 4.16: The 70eV positive EI mass spectrum obtained by scanning the third quadrupole after the selective reaction of *m/z* 365 ($[Fe(tmtm)(tmtm\text{-}tBu)]^+$) with neutral $Cu(acac)_2$ to produce the mixed ligand fragment at *m/z* 281 ($[Fe(acac)(tmtm\text{-}tBu)]^+$).

The observation of the mixed ligand fragment is consistent with the occurrence of partial ligand exchange as proposed in Equation (4.13).

$$[Fe^{II}(tmtm)(tmtm\text{-}tBu)]^+ + Cu^{II}(acac)_2 \rightarrow$$

$$[Fe^{II}(acac)(tmtm\text{-}tBu)]^+ + Cu^{II}(acac)(tmtm) \qquad \text{(Eqn 4.13)}$$

Two additional products are generated from the collision-induced reactions of mass-selected $[Fe(tmtm)(tmtm\text{-}t\text{Bu})]^+$ at *m/z* 365 and neutral $Cu(acac)_2$ as shown in Figure 4.17. The peak at *m/z* 254 is indicative of the complete ligand exchange product $[Fe(acac)_2]^+$ while the peak at *m/z* 246 is consistent with the formation of $[Cu(tmtm)]^+$.

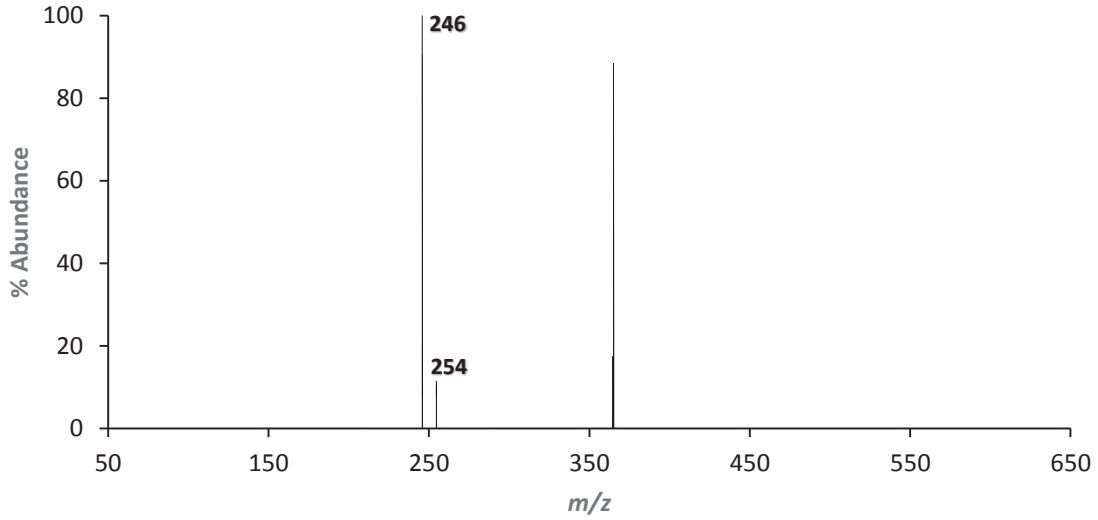

Figure 4.17: The 70eV positive EI mass spectrum obtained by scanning the third quadrupole after the selective reaction of *m/z* 365 ($[Fe(tmtm)(tmtm\text{-}tBu)]^+$) with neutral $Cu(acac)_2$ to produce the products at *m/z* 254 and *m/z* 246 ($[Fe(acac)_2]^+$ and $[Cu(tmtm)]^+$, respectively).

The two equations listed in Equations (4.14) and (4.15) express the formation of the complete ligand exchange products.

$$[Fe^{II}(tmtm)(tmtm\text{-}t\text{Bu})]^+ + Cu^{II}(acac)_2 \rightarrow$$

$$[Fe^{III}(acac)_2]^+ + Cu^{I}(tmtm)(tmtm\text{-}t\text{Bu}) \qquad \text{(Eqn 4.14)}$$

$$[Fe^{II}(tmtm)(tmtm\text{-}t\text{Bu})]^+ + Cu^{II}(acac)_2 \rightarrow$$

$$[Cu^{II}(tmtm)]^+ + Fe^{II}(acac)_2(tmtm\text{-}t\text{Bu}) \qquad \text{(Eqn 4.15)}$$

The species $[Fe(tmtm)]^+$ at *m/z* 239 was the last mass-selected fragment of $Fe(tmtm)_3$ to be incorporated into a collision-induced reaction with neutral $Cu(acac)_2$. Of the four peaks that appear in Figure 4.18, only those shown at *m/z* 345 and *m/z* 239 can be identified as the mixed ligand product $[Cu(acac)(tmtm)]^+$ and the mass-selected parent ion $[Fe(tmtm)]^+$, respectively. The remaining peaks at *m/z* 211 and *m/z* 195 could not be identified as products of interest and were not further investigated.

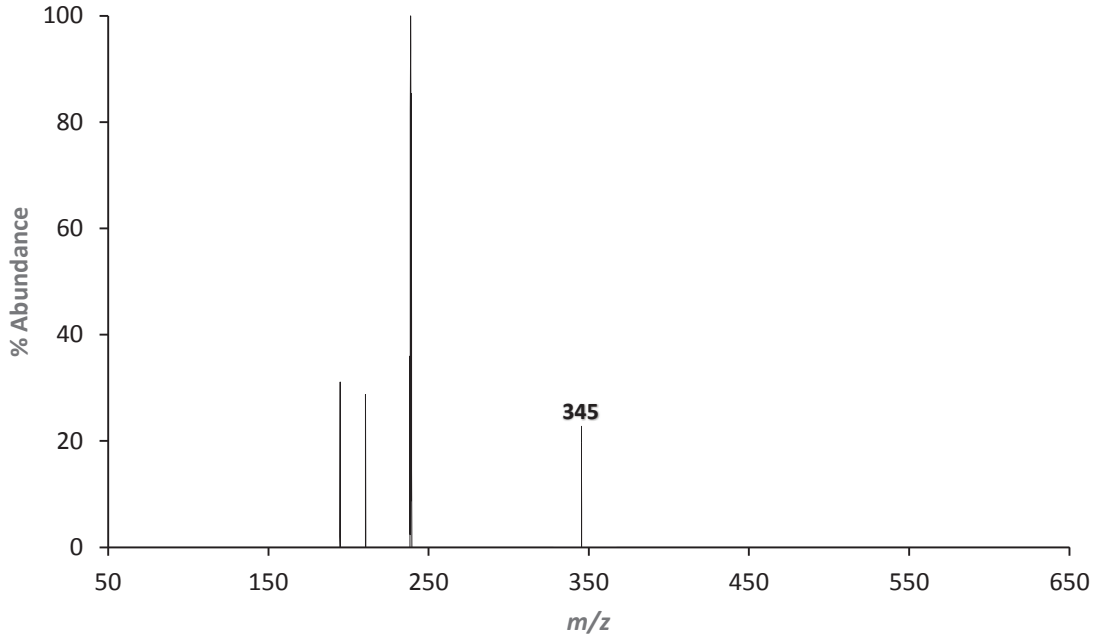

Figure 4.18: The 70eV positive EI mass spectrum obtained by scanning the third quadrupole after the selective reaction of *m/z* 239 ($[Fe(tmtm)]^+$) with neutral $Cu(acac)_2$ to produce the mixed ligand product at *m/z* 345 ($[Cu(acac)(tmtm)]^+$).

The formation of the mixed ligand product is proposed to result from a partial ligand exchange process between the reacting complexes as shown in Equation (4.16).

$$[Fe^{II}(tmtm)]^+ + Cu^{II}(acac)_2 \rightarrow$$

$$[Cu^{II}(acac)(tmtm)]^{\bullet+} + Fe^{I}(acac) \qquad \text{(Eqn 4.16)}$$

Another product observed to form from the reaction between mass-selected $[Fe(tmtm)]^+$ at *m/z* 239 and neutral $Cu(acac)_2$ is the mixed ligand product $[Fe(acac)(tmtm)]^+$ at *m/z* 339 in Figure 4.19. Formation of the mixed ligand product occurs at one mass unit higher than expected.

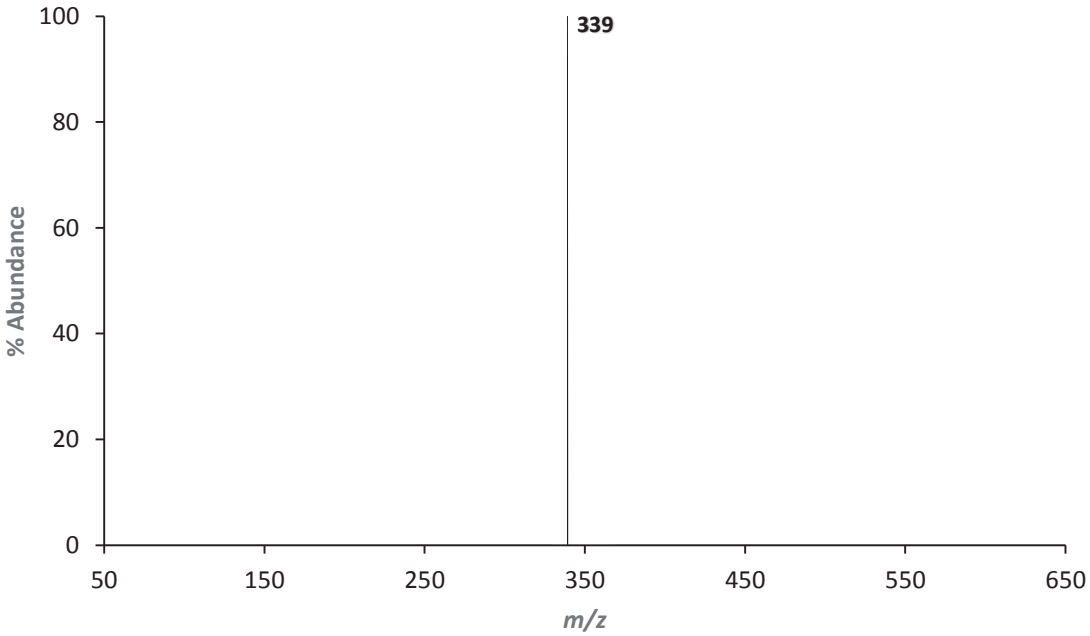

Figure 4.19: The 70eV positive EI mass spectrum obtained by scanning the third quadrupole after the selective reaction of *m/z* 239 ($[Fe(tmtm)]^+$) with neutral $Cu(acac)_2$ to produce the mixed ligand product at *m/z* 339 ($[Fe(acac)(tmtm)]^+$).

In the mechanistic proposal outlined in Equation (4.17), $[Fe(tmtm)]^+$ acquires (acac) from $Cu(acac)_2$ to form the mixed ligand product.

$$[Fe^{II}(tmtm)]^+ + Cu^{II}(acac)_2 \rightarrow$$

$$[Fe^{III}(acac)(tmtm)]^+ + Cu^{I}(acac) \qquad \text{(Eqn 4.17)}$$

The peak displayed at *m/z* 315 in Figure 4.20 indicates the formation of $[Cu(tmtm\text{-}tBu)_2]^+$ from the reaction between mass-selected $[Fe(tmtm)]^+$ at *m/z* 239 and neutral $Cu(acac)_2$. Additional peaks are shown to form at *m/*z 239 and *m/*z 181 which correspond to the mass-selected parent ion and an unidentifiable species, respectively. Similar to Equation (4.11), two equivalents of the parent ion are required for the production of $[Cu(tmtm\text{-}tBu)_2]^+$.

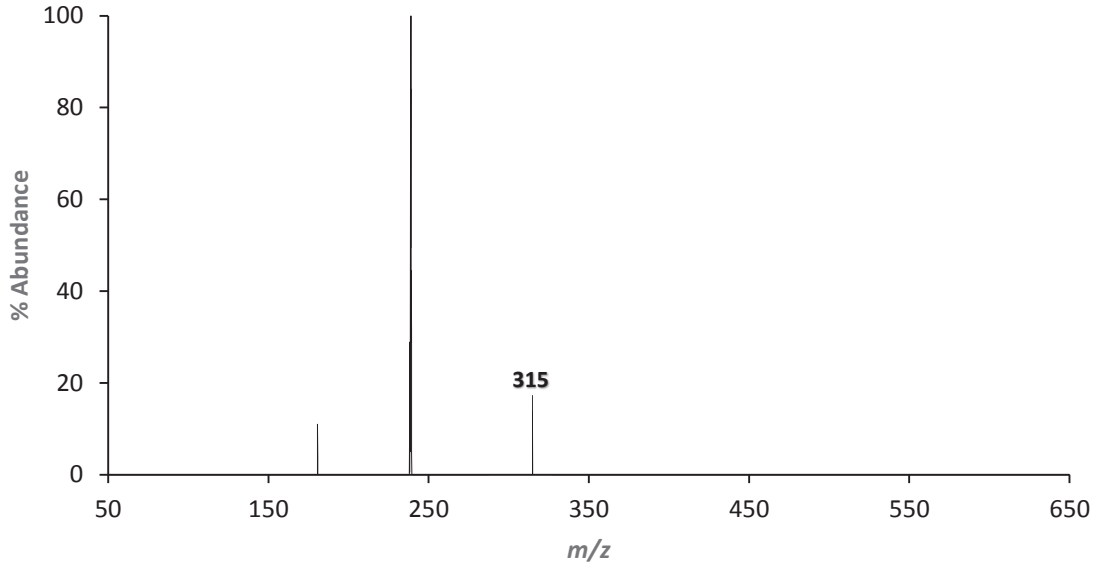

Figure 4.20: The 70eV positive EI mass spectrum obtained by scanning the third quadrupole after the selective reaction of *m/z* 239 ($[Fe(tmtm)]^+$) with neutral $Cu(acac)_2$ to produce the product at *m/z* 315 ($[Cu(tmtm\text{-}tBu)_2]^+$).

An appropriate expression for the formation of this ligand exchange product is provided in Equation (4.18).

$$2[Fe^{II}(tmtm)]^+ + Cu^{II}(acac)_2 \rightarrow$$

$$[Cu^{I}(tmtm\text{-}tBu)_2]^+ + [Fe^{II}(acac)]^+ + Fe^{I}(acac)$$

$$+ 2tBu^{\bullet} \qquad \text{(Eqn 4.18)}$$

The following series of collision-induced reactions examine the ligand exchange processes that occur between neutral $Fe(tmtm)_3$ and the mass-selected ions of $Cu(acac)_2$. In mass-selecting the molecular ion $[Cu(acac)_2]^+$ at *m/z* 261, a total of three product peaks were observed. The first product is displayed at *m/z* 371 in Figure 4.21 which corresponds to $[Cu(tmtm)(tmtm\text{-}t\text{Bu})]^+$ at one mass unit lower than expected.

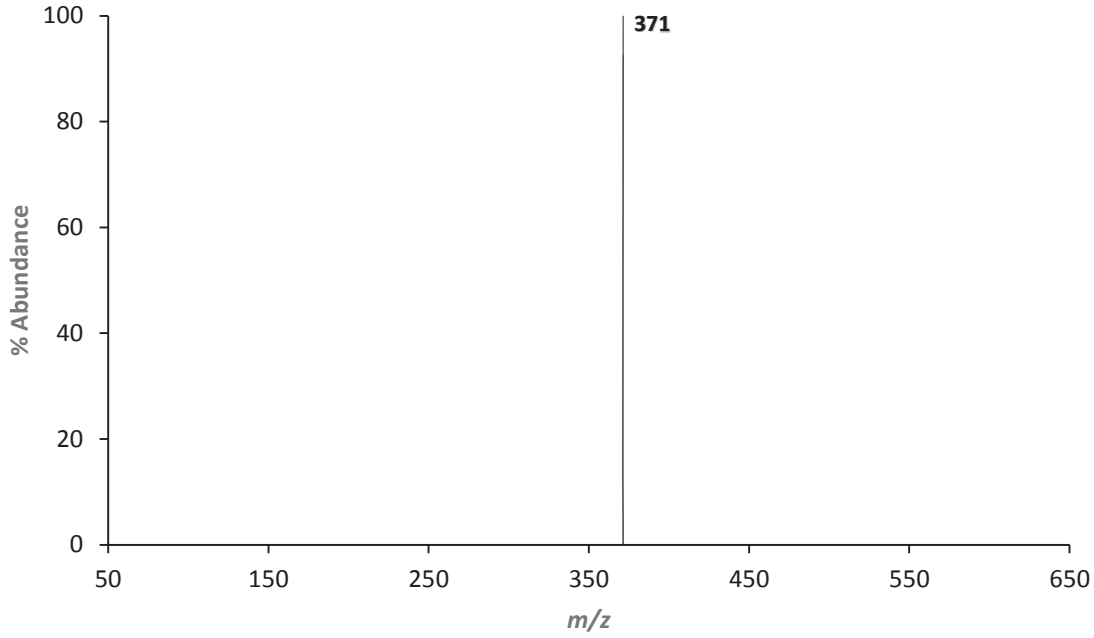

Figure 4.21: The 70eV positive EI mass spectrum obtained by scanning the third quadrupole after the selective reaction of *m/z* 261 ($[Cu(acac)_2]^+$) with neutral $Fe(tmtm)_3$ to produce the product at *m/z* 371 ($[Cu(tmtm)(tmtm\text{-}t\text{Bu})]^+$).

This observation is consistent with a mechanism that incorporates both complete ligand exchange and *tert*-butyl fragmentation as shown in Equation (4.19).

$$[Cu^{II}(acac)_2]^{+\bullet} + Fe^{III}(tmtm)_3 \rightarrow$$

$$[Cu^{II}(tmtm)(tmtm\text{-}t\text{Bu})]^+ + Fe^{III}(acac)_2(tmtm) + t\text{Bu}^{\bullet} \qquad \text{(Eqn 4.19)}$$

The ion signal observed at *m/z* 340 in Figure 4.22 results from a reaction between mass-selected $[Cu(acac)_2]^+$ at *m/z* 261 and neutral $Fe(tmtm)_3$, and is consistent with the formation of the mixed ligand product $[Fe(acac)(tmtm)]^+$ at *m/z* 338, albeit at two mass units higher than expected.

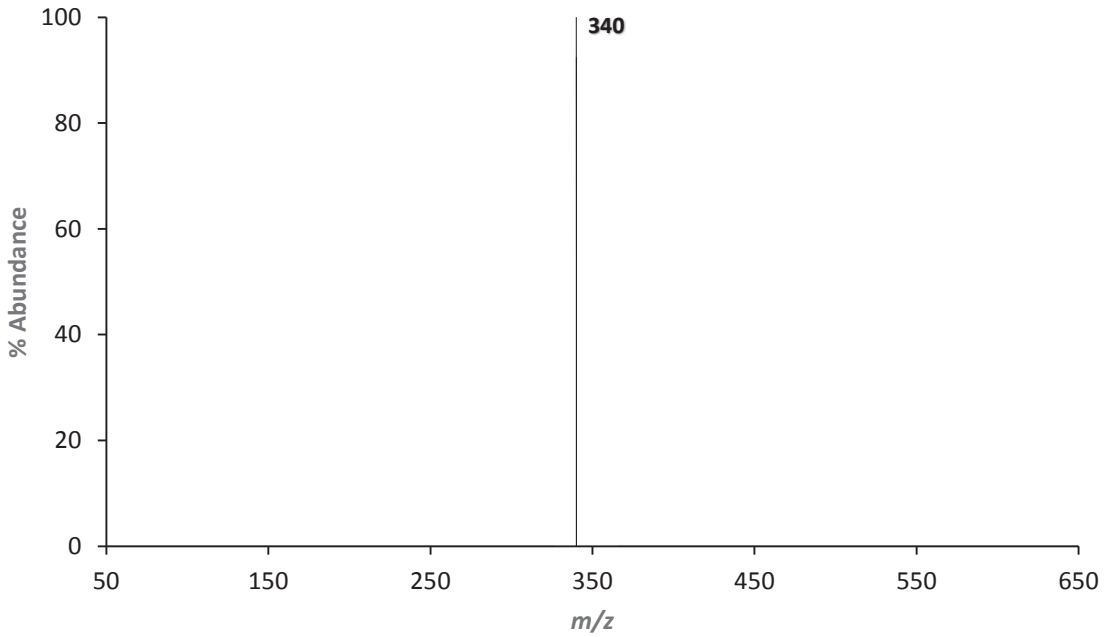

Figure 4.22: The 70eV positive EI mass spectrum obtained by scanning the third quadrupole after the selective reaction of *m/z* 261 ($[Cu(acac)_2]^+$) with neutral $Fe(tmtm)_3$ to produce the mixed ligand product at *m/z* 340 ($[Fe(acac)(tmtm)]^+$).

A mechanism that accounts for the mixed ligand product is expressed in Equation (4.20) which entails a process of partial ligand exchange between the cationic and neutral reactants.

$$[Cu^{II}(acac)_2]^{+\bullet} + Fe^{III}(tmtm)_3 \rightarrow$$

$$[Fe^{III}(acac)(tmtm)]^+ + Cu^{II}(acac)(tmtm) + tmtm^{\bullet} \qquad \text{(Eqn 4.20)}$$

Collision-induced reactions between mass-selected $[Cu(acac)_2]^+$ at *m/z* 261 and neutral $Fe(tmtm)_3$ were also found to produce $[Fe(acac)(acac\text{-}CH_3)]^+$ at *m/z* 239 in Figure 4.23. The ion signal appearing at *m/z* 261 corresponds to the mass-selected parent ion.

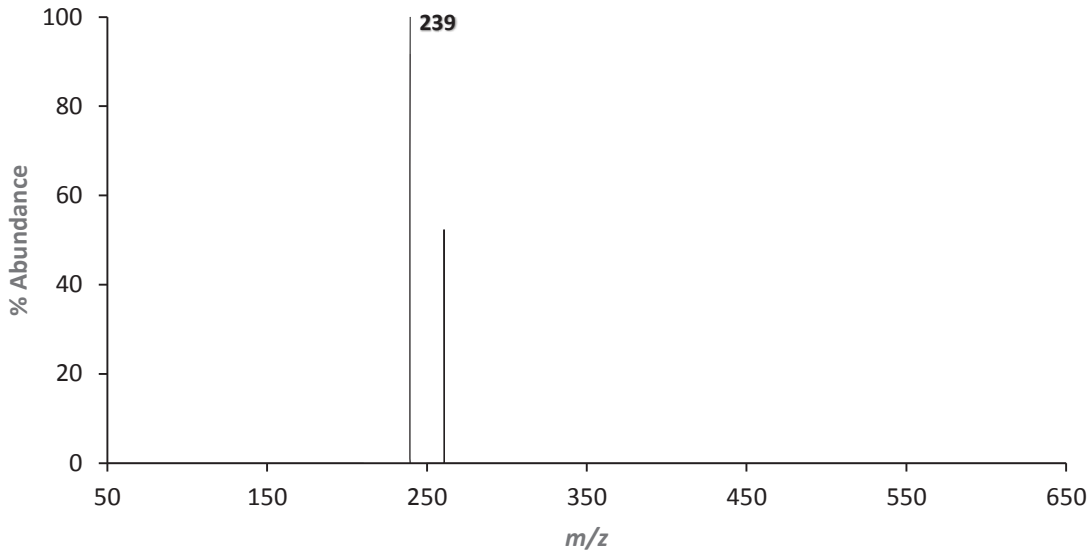

Figure 4.23: The 70eV positive EI mass spectrum obtained by scanning the third quadrupole after the selective reaction of *m/z* 261 ($[Cu(acac)_2]^+$) with neutral $Fe(tmtm)_3$ to produce the product at *m/z* 239 ($[Fe(acac)(acac\text{-}CH_3)]^+$).

A mechanistic proposal consistent with this result is outlined in Equation (4.21) wherein the mass-selected ion undergoes a complete ligand exchange process with $Fe(tmtm)_3$ to produce $[Fe(acac)(acac\text{-}CH_3)]^+$.

$$[Cu^{II}(acac)_2]^{+\bullet} + Fe^{III}(tmtm)_3 \rightarrow$$

$$[Fe^{II}(acac)(acac\text{-}CH_3)]^+ + Cu^{II}(tmtm)_2 + tmtm^{\bullet} + CH_3^{\bullet} \qquad \text{(Eqn 4.21)}$$

The mass-selection of $[Cu(acac)(acac\text{-}CH_3)]^+$ at *m/z* 246 was found to be fairly conducive towards the gas-phase formation of ligand exchange products. The ion signal appearing at *m/z* 522 in Figure 4.24 corresponds to the formation of $[Fe(acac)(tmtm)_2]^+$ at one mass unit higher than expected. The other peaks apparent in this spectrum indicate the presence of the mass-selected parent ion $[Cu(acac)(acac\text{-}CH_3)]^+$ and an unidentified species at *m/z* 231.

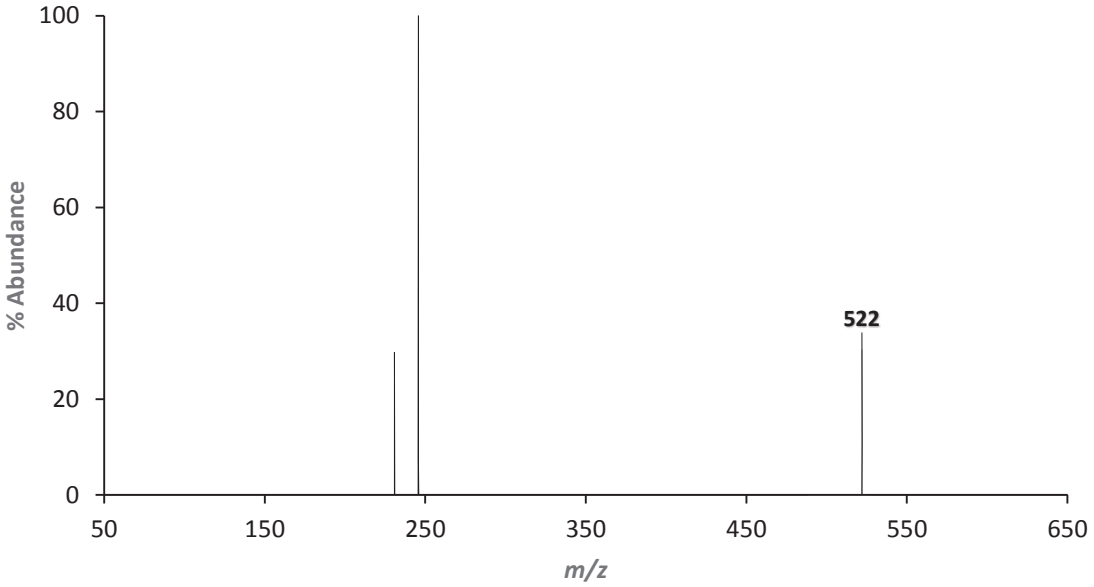

Figure 4.24: The 70eV positive EI mass spectrum obtained by scanning the third quadrupole after the selective reaction of *m/z* 246 ($[Cu(acac)(acac\text{-}CH_3)]^+$) with neutral $Fe(tmtm)_3$ to produce the mixed ligand product at *m/z* 522 ($[Fe(acac)(tmtm)_2]^+$).

Unlike Equation (4.11), this gas-phase reaction does not require two equivalents of either reactant, and would presumably occur according to Equation (4.22) via partial ligand exchange.

$$[Cu^{II}(acac)(acac\text{-}CH_3)]^+ + Fe^{III}(tmtm)_3 \rightarrow$$

$$[Fe^{III}(acac)(tmtm)_2]^{+\bullet} + Cu^{I}(acac\text{-}CH_3)(tmtm) \qquad \text{(Eqn 4.22)}$$

An ion signal at *m/z* 465 in Figure 4.25 indicates the formation of the triply-ligated product $[Fe(acac)(tmtm)(tmtm\text{-}tBu)]^+$ from the collision-induced reaction of mass-selected $[Cu(acac)(acac\text{-}CH_3)]^+$ at *m/z* 246 with neutral $Fe(tmtm)_3$. Formation of the mixed ligand fragment occurs at one mass unit higher than expected. The peak at *m/z* 246 corresponds to the mass-selected parent ion.

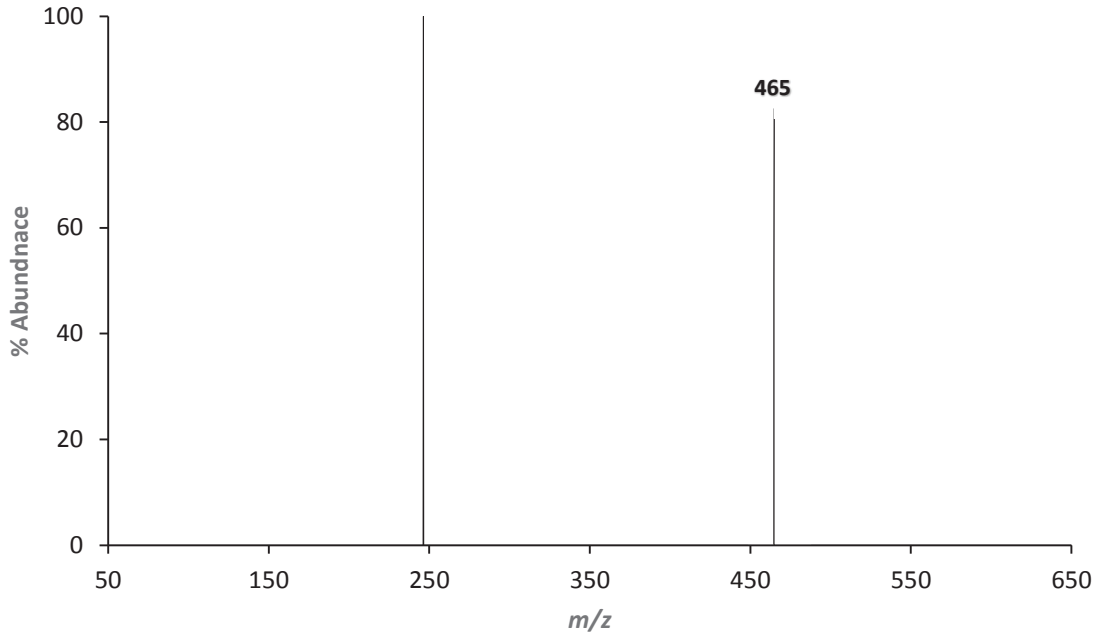

Figure 4.25: The 70eV positive EI mass spectrum obtained by scanning the third quadrupole after the selective reaction of *m/z* 246 ($[Cu(acac)(acac\text{-}CH_3)]^+$) with neutral $Fe(tmtm)_3$ to produce the mixed ligand fragment at *m/z* 465 ($[Fe(acac)(tmtm)(tmtm\text{-}tBu)]^+$).

Equation (4.23) entails a reaction pathway that incorporates both partial ligand exchange and *tert*-butyl fragmentation to generate the observed product.

$$[Cu^{II}(acac)(acac\text{-}CH_3)]^+ + Fe^{III}(tmtm)_3 \rightarrow$$

$$[Fe^{III}(acac)(tmtm)(tmtm\text{-}tBu)]^+$$

$$+ Cu^{I}(acac\text{-}CH_3)(tmtm) + tBu^{\bullet} \qquad \text{(Eqn 4.23)}$$

The ion signal appearing at *m/z* 372 in Figure 4.26 indicates the formation of $[Cu(tmtm)(tmtm\text{-}tBu)]^+$ from the collision-induced reaction between mass-selected $[Cu(acac)(acac\text{-}CH_3)]^+$ at *m/z* 246 and neutral $Fe(tmtm)_3$.

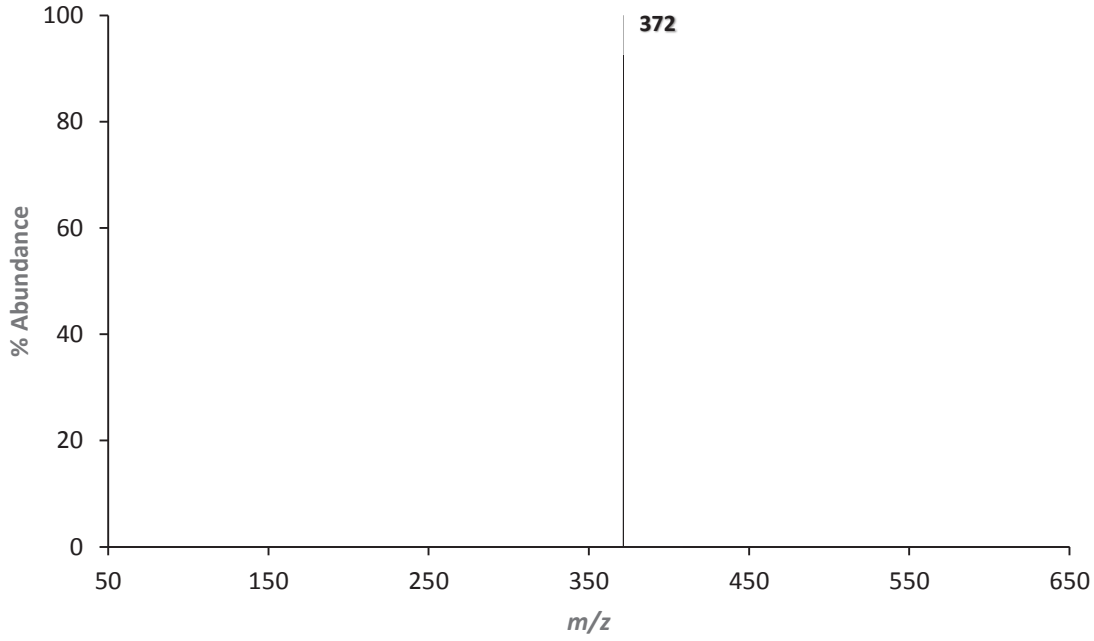

Figure 4.26: The 70eV positive EI mass spectrum obtained by scanning the third quadrupole after the selective reaction of *m/z* 246 ($[Cu(acac)(acac\text{-}CH_3)]^+$) with neutral $Fe(tmtm)_3$ to produce the product at *m/z* 372 ($[Cu(tmtm)(tmtm\text{-}tBu)]^+$).

Product formation presumptively occurs via a complete ligand exchange process coupled with *tert*-butyl fragmentation as shown in Equation (4.24).

$$[Cu^{II}(acac)(acac\text{-}CH_3)]^+ + Fe^{III}(tmtm)_3 \rightarrow$$

$$[Cu^{II}(tmtm)(tmtm\text{-}tBu)]^+ + Fe^{II}(acac)(acac\text{-}CH_3)(tmtm)$$

$$+ tBu^{\bullet} \qquad \text{(Eqn 4.24)}$$

Another product stemming from the selective reactions of $[Cu(acac)(acac\text{-}CH_3)]^+$ at *m/z* 246 and neutral $Fe(tmtm)_3$ corresponds to the peak at *m/z* 338 in Figure 4.27 which can be identified as the mixed ligand product $[Fe(acac)(tmtm)]^+$.

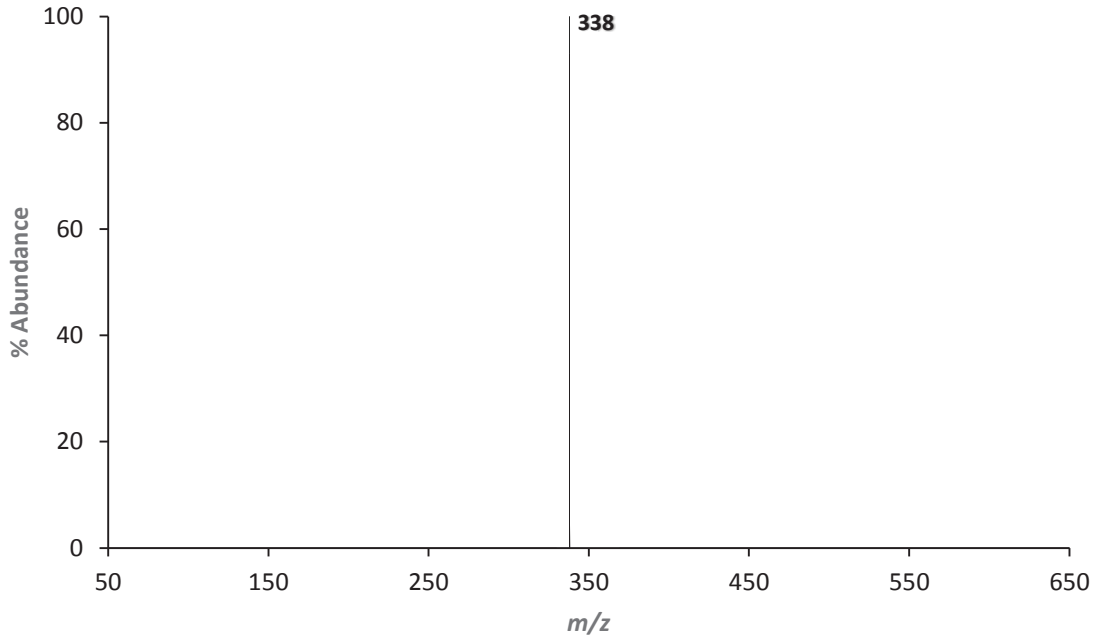

Figure 4.27: The 70eV positive EI mass spectrum obtained by scanning the third quadrupole after the selective reaction of *m/z* 246 ($[Cu(acac)(acac\text{-}CH_3)]^+$) with neutral $Fe(tmtm)_3$ to produce the mixed ligand product at *m/z* 338 ($[Fe(acac)(tmtm)]^+$).

Product formation likely occurs via partial ligand exchange between the reactant complexes as expressed in Equation (4.25).

$$[Cu^{II}(acac)(acac\text{-}CH_3)]^+ + Fe^{III}(tmtm)_3 \rightarrow$$

$$[Fe^{III}(acac)(tmtm)]^+ + Cu^{I}(acac\text{-}CH_3)(tmtm) + tmtm^{\bullet} \qquad \text{(Eqn 4.25)}$$

The peak displayed at *m/z* 289 in Figure 4.28 indicates the production of the mixed ligand fragment $[Cu(acac)(tmtm\text{-}t\text{Bu})]^+$ from the reaction between mass-selected $[Cu(acac)(acac\text{-}CH_3)]^+$ at *m/z* 246 and neutral $Fe(tmtm)_3$. Product formation occurs at one mass unit higher than expected.

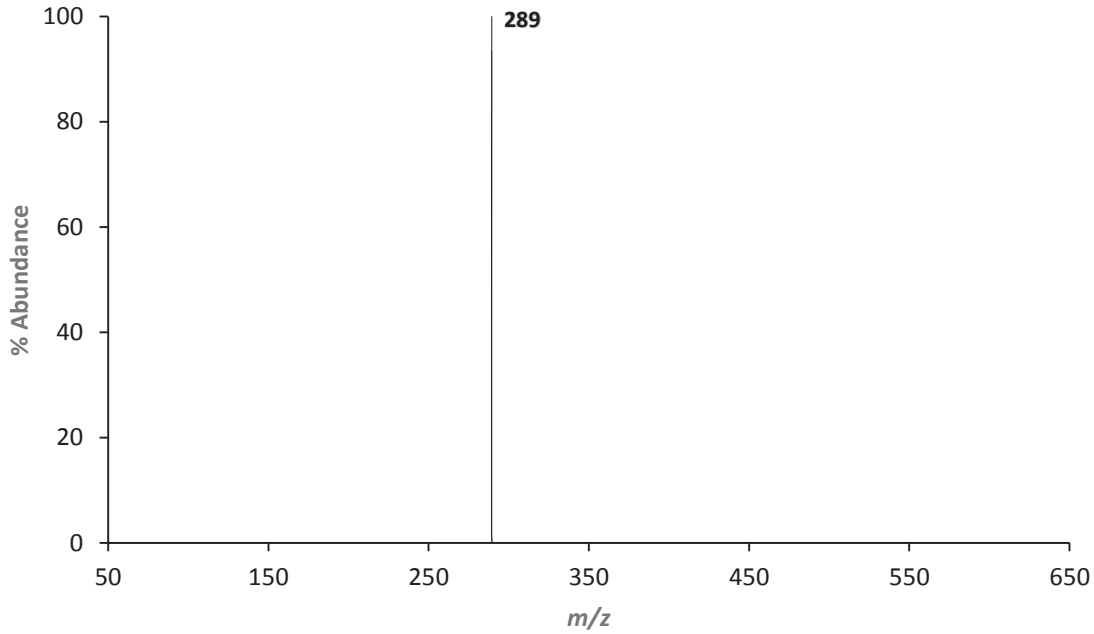

Figure 4.28: The 70eV positive EI mass spectrum obtained by scanning the third quadrupole after the selective reaction of *m/z* 246 ($[Cu(acac)(acac\text{-}CH_3)]^+$) with neutral $Fe(tmtm)_3$ to produce the mixed ligand fragment at *m/z* 289 ($[Cu(acac)(tmtm\text{-}t\text{Bu})]^+$).

A mechanistic interpretation consistent with this finding is given by Equation (4.26) wherein partial exchange and *tert*-butyl fragmentation generate the mixed ligand product.

$$[Cu^{II}(acac)(acac\text{-}CH_3)]^+ + Fe^{III}(tmtm)_3 \rightarrow$$

$$[Cu^{II}(acac)(tmtm\text{-}t\text{Bu})]^+ + Fe^{II}(acac\text{-}CH_3)(tmtm)_2 + t\text{Bu}^{\bullet} \qquad \text{(Eqn 4.26)}$$

The final peak observed from the collision-induced reactions between mass-selected $[Cu(acac)(acac\text{-}CH_3)]^+$ at *m/z* 246 and neutral $Fe(tmtm)_3$ is shown in Figure 4.29 at *m/z* 282 which corresponds to $[Fe(acac)(tmtm\text{-}t\text{Bu})]^+$. Product formation occurs at one mass unit higher than expected.

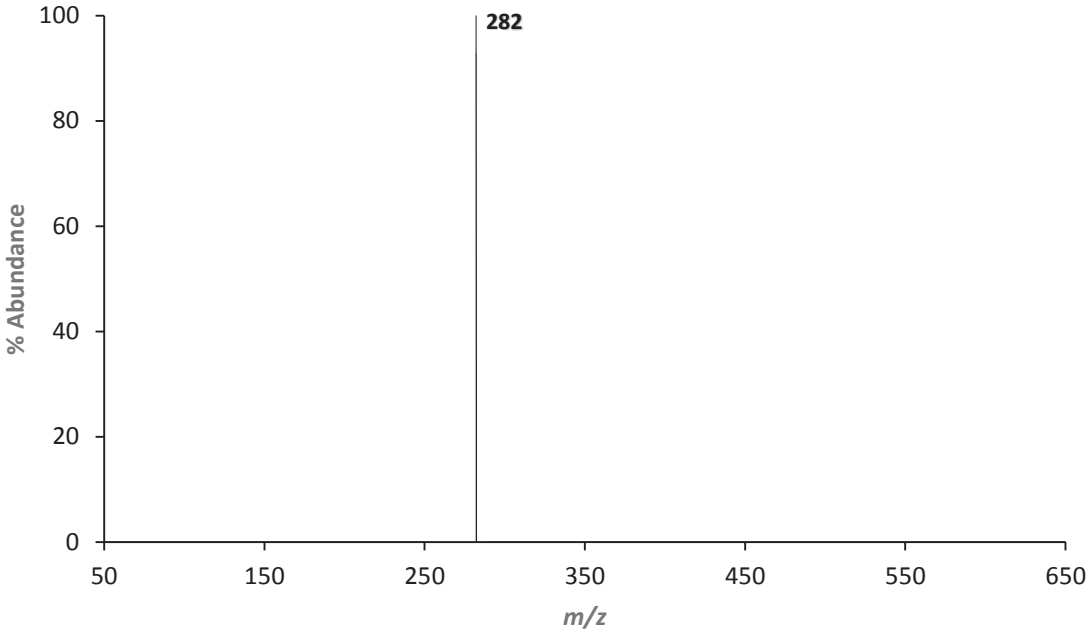

Figure 4.29: The 70eV positive EI mass spectrum obtained by scanning the third quadrupole after the selective reaction of *m/z* 246 ($[Cu(acac)(acac\text{-}CH_3)]^+$) with neutral $Fe(tmtm)_3$ to produce the mixed ligand fragment at *m/z* 282 ($[Fe(acac)(tmtm\text{-}t\text{Bu})]^+$).

According to the proposed mechanism in Equation (4.27), the mass-selected cation undergoes a ligand exchange process with the neutral complex to form the mixed ligand fragment.

$$[Cu^{II}(acac)(acac\text{-}CH_3)]^+ + Fe^{III}(tmtm)_3 \rightarrow$$

$$[Fe^{II}(acac)(tmtm\text{-}t\text{Bu})]^+ + Cu^{I}(acac\text{-}CH_3)(tmtm)$$

$$+ tmtm^{\bullet} + t\text{Bu}^{\bullet} \qquad \text{(Eqn 4.27)}$$

In continuing the investigation on the collision-induced reactions of $Cu(acac)_2$ fragments, $[Cu(acac\text{-}CH_3)_2]^+$ at *m/z* 231 was mass-selected to react with neutral $Fe(tmtm)_3$. Three products were shown to form from the resulting reactions, such as the one presented in Figure 4.30 at *m/z* 374 which indicates the formation of $[Cu(tmtm)(tmtm\text{-}t\text{Bu})]^+$ at two mass units higher than expected.

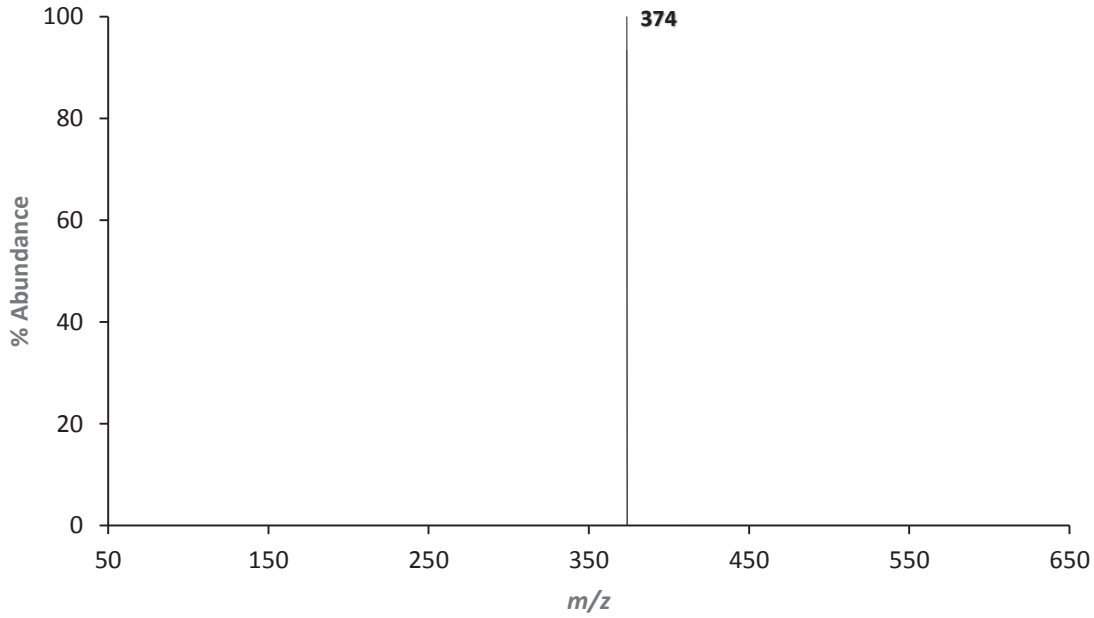

Figure 4.30: The 70eV positive EI mass spectrum obtained by scanning the third quadrupole after the selective reaction of *m/z* 231 ($[Cu(acac\text{-}CH_3)_2]^+$) with neutral $Fe(tmtm)_3$ to produce the product at *m/z* 374 ($[Cu(tmtm)(tmtm\text{-}t\text{Bu})]^+$).

The proposed mechanism presented in Equation (4.28) is representative of the ligand exchange process responsible for the production of this species.

$$[Cu^{I}(acac\text{-}CH_3)_2]^+ + Fe^{III}(tmtm)_3 \rightarrow$$

$$[Cu^{II}(tmtm)(tmtm\text{-}t\text{Bu})]^+ + Fe^{I}(acac\text{-}CH_3)_2(tmtm) + t\text{Bu}^{\bullet} \qquad \text{(Eqn 4.28)}$$

An additional product generated from the reaction between mass-selected $[Cu(acac\text{-}CH_3)_2]^+$ at *m/z* 231 and neutral $Fe(tmtm)_3$ corresponds to the complete ligand exchange fragment $[Cu(tmtm\text{-}t\text{Bu})_2]^+$ at *m/z* 314 in Figure 3.31. Product formation occurs at one mass unit lower than expected.

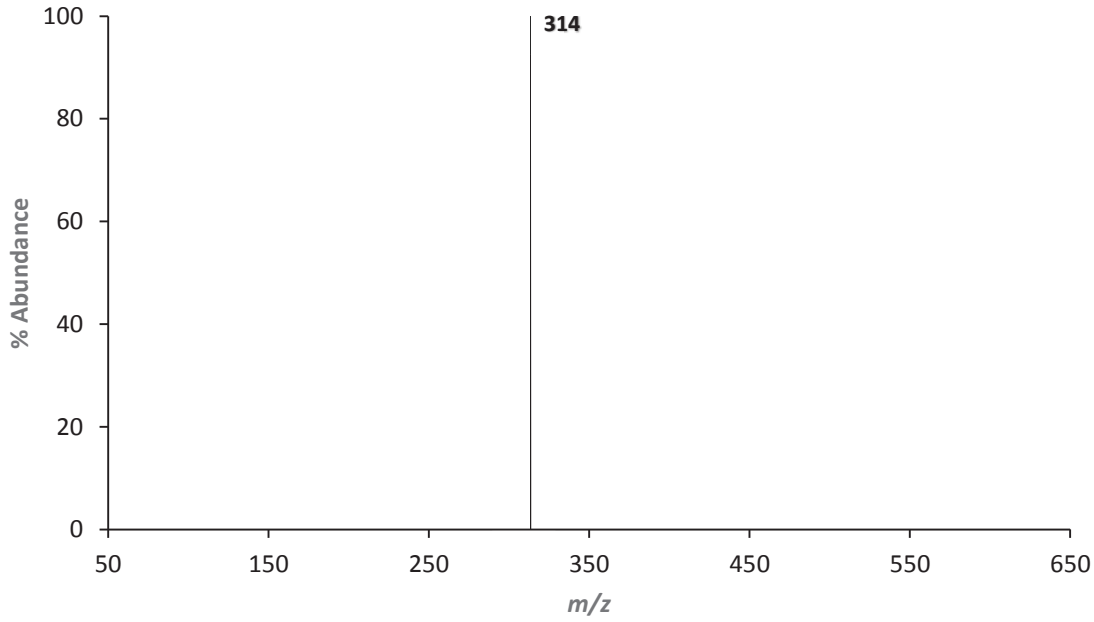

Figure 4.31: The 70eV positive EI mass spectrum obtained by scanning the third quadrupole after the selective reaction of *m/z* 231 ($[Cu(acac\text{-}CH_3)_2]^+$) with neutral $Fe(tmtm)_3$ to produce the product at m/z 314 ($[Cu(tmtm\text{-}tBu)_2]^+$).

The formation of this product is consistent with Equation (4.29) wherein the cuprous complex undergoes complete ligand exchange, reductive rearrangement, and *tert*-butyl fragmentation.

$$[Cu^{I}(acac\text{-}CH_3)_2]^+ + Fe^{III}(tmtm)_3 \rightarrow$$

$$[Cu^{I}(tmtm\text{-}t\text{Bu})_2]^+ + Fe^{I}(acac\text{-}CH_3)_2(tmtm) + 2t\text{Bu}^{\bullet} \qquad \text{(Eqn 4.29)}$$

The last species generated from the gas-phase reaction between mass-selected $[Cu(acac\text{-}CH_3)_2]^+$ at *m/z* 231 and neutral $Fe(tmtm)_3$ is shown at *m/z* 141 in Figure 4.32, and indicates the formation of $[Fe(acac\text{-}CH_3)]^+$ at one mass unit higher than expected.

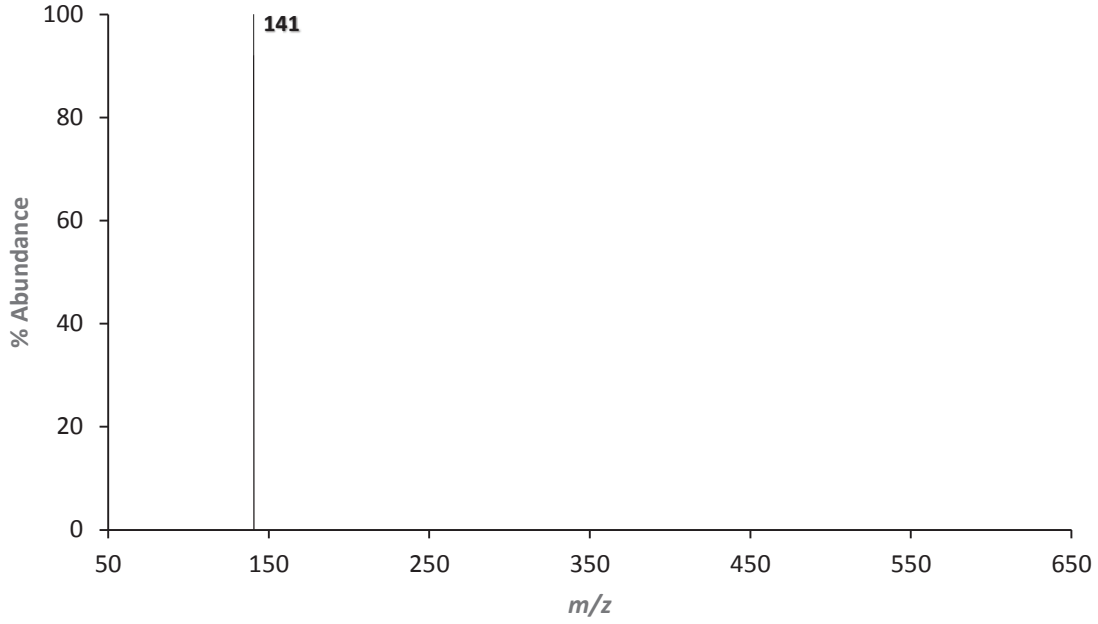

Figure 4.32: The 70eV positive EI mass spectrum obtained by scanning the third quadrupole after the selective reaction of *m/z* 231 ($[Cu(acac\text{-}CH_3)_2]^+$) with neutral $Fe(tmtm)_3$ to produce the product at *m/z* 141 ($[Fe(acac\text{-}CH_3)]^+$).

Product formation likely occurs through a process of complete ligand exchange coupled with extensive fragmentation, as expressed in Equation (4.30).

$$[Cu^{I}(acac\text{-}CH_3)_2]^+ + Fe^{III}(tmtm)_3 \rightarrow$$

$$[Fe^{I}(acac\text{-}CH_3)]^+ + Cu^{I}(acac\text{-}CH_3)(tmtm) + 2tmtm^{\bullet} \qquad \text{(Eqn 4.30)}$$

To investigate potential gas-phase reactions between $[Cu(acac)]^+$ and $Fe(tmtm)_3$, the first quadrupole was setup to selectively introduce $[Cu(acac)]^+$ at *m/z* 162 to the collision chamber. The ensuing gas-phase interactions resulted in a multitude of ligand exchange products such as the one shown below in Figure 4.33 at *m/z* 521.

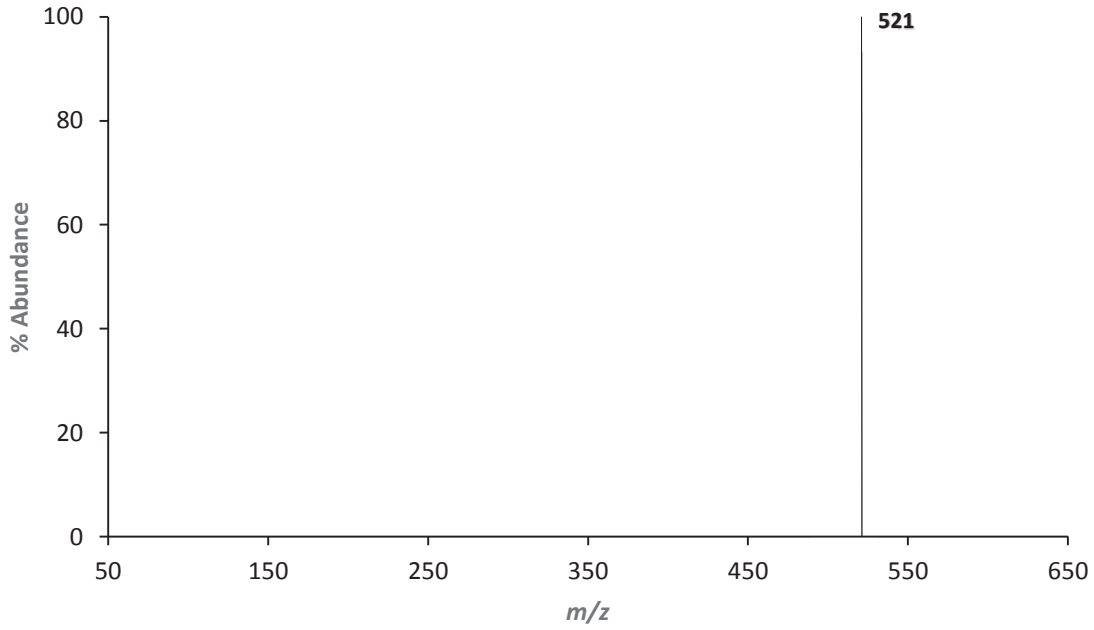

Figure 4.33: The 70eV positive EI mass spectrum obtained by scanning the third quadrupole after the selective reaction of *m/z* 162 ($[Cu(acac)]^+$) with neutral $Fe(tmtm)_3$ to produce the mixed ligand product at *m/z* 521 ($[Fe(acac)(tmtm)_2]^+$).

As previously demonstrated, this mass value corresponds to the mixed ligand product $[Fe(acac)(tmtm)_2]^+$ which could be formed through a process of partial ligand exchange as shown in Equation (4.31).

$$[Cu^{II}(acac)]^+ + Fe^{III}(tmtm)_3 \rightarrow$$

$$[Fe^{III}(acac)(tmtm)_2]^{+\bullet} + Cu^{I}(tmtm) \qquad \text{(Eqn 4.31)}$$

The formation of the complete ligand exchange product $[Cu(tmtm)_2]^+$ from the collision-induced reaction of mass-selected $[Cu(acac)]^+$ at *m/z* 162 and neutral $Fe(tmtm)_3$ can be inferred from the peak observed at *m/z* 428 in Figure 4.34. Formation of the product occurs at one mass unit lower than expected. In contrast, peaks at *m/z* 331 and *m/z* 107 do not correspond to any of the products of interest and were not further investigated.

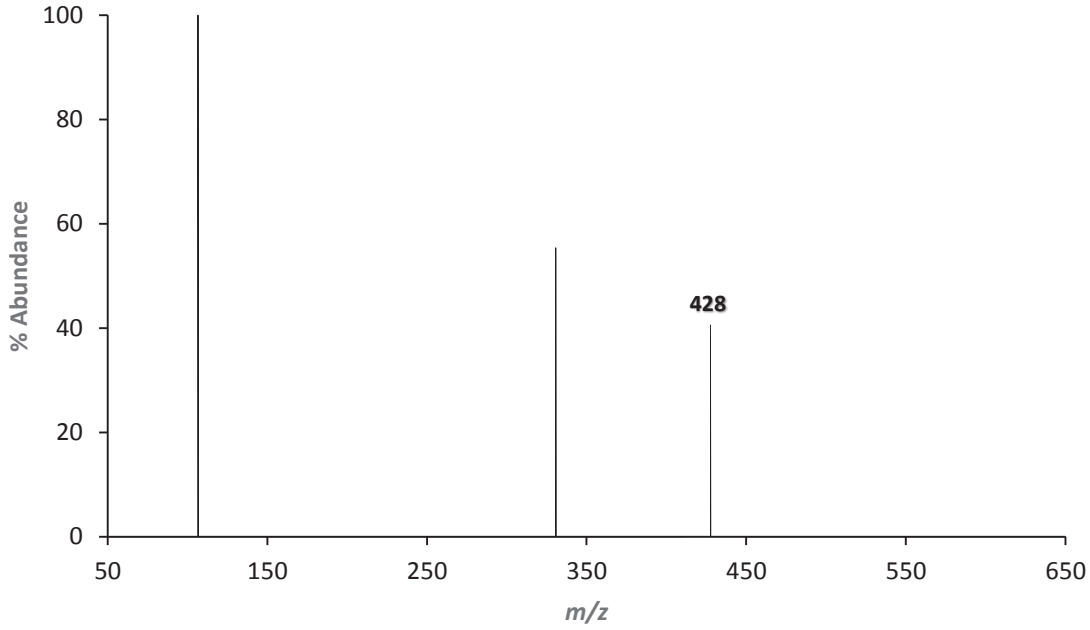

Figure 4.34: The 70eV positive EI mass spectrum obtained by scanning the third quadrupole after the selective reaction of *m/z* 162 ($[Cu(acac)]^+$) with neutral $Fe(tmtm)_3$ to produce the product at *m/z* 428 ($[Cu(tmtm)_2]^+$).

Provided in Equation (4.32) is a proposed reaction scheme consistent with the gas-phase formation of $[Cu(tmtm)_2]^+$ via complete ligand exchange.

$$[Cu^{II}(acac)]^+ + Fe^{III}(tmtm)_3 \rightarrow$$

$$[Cu^{II}(tmtm)_2]^{+\bullet} + Fe^{II}(acac)(tmtm) \qquad \text{(Eqn 4.32)}$$

The appearance of a peak at *m/z* 373 in Figure 4.35 suggests the formation of $[Cu(tmtm)(tmtm\text{-}t\text{Bu})]^+$ from reacting mass-selected $[Cu(acac)]^+$ at *m/z* 162 with neutral $Fe(tmtm)_3$. Product formation occurs at one mass unit higher than expected. The peak observed at *m/z* 119 does not correspond to any product of interest.

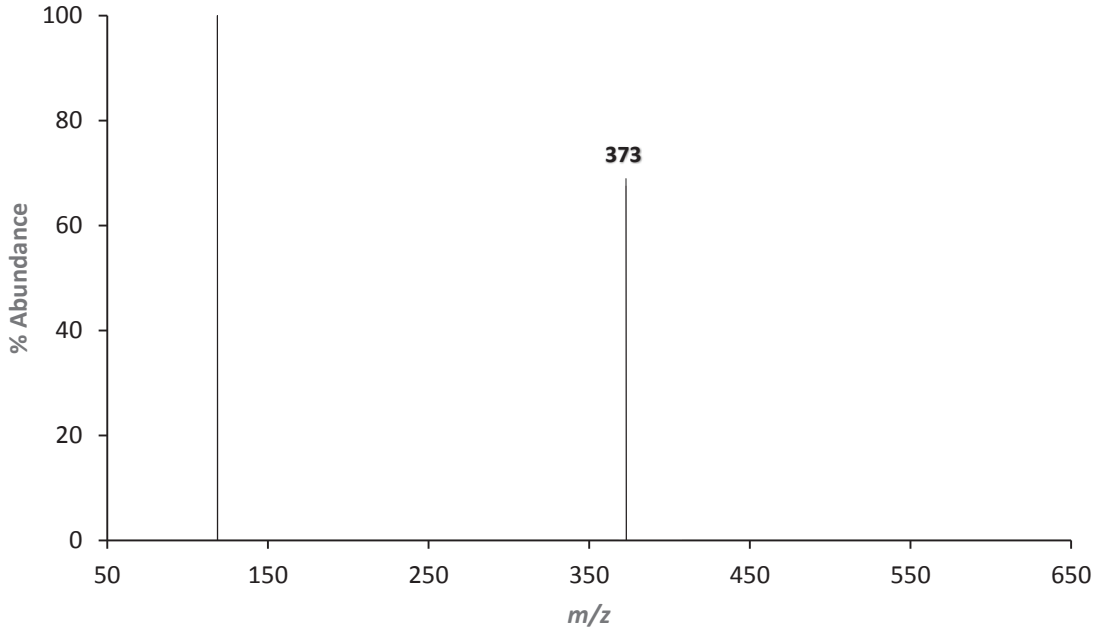

Figure 4.35: The 70eV positive EI mass spectrum obtained by scanning the third quadrupole after the selective reaction of *m/z* 162 ($[Cu(acac)]^+$) with neutral $Fe(tmtm)_3$ to produce the product at *m/z* 373 ($[Cu(tmtm)(tmtm\text{-}t\text{Bu})]^+$).

The mechanism proposed in Equation (4.33) incorporates both complete ligand exchange and *tert*-butyl fragmentation to account for the formation of $[Cu(tmtm)(tmtm\text{-}t\text{Bu})]^+$.

$$[Cu^{II}(acac)]^+ + Fe^{III}(tmtm)_3 \rightarrow$$

$$[Cu^{II}(tmtm)(tmtm\text{-}t\text{Bu})]^+ + Fe^{II}(acac)(tmtm) + t\text{Bu}^{\bullet} \qquad \text{(Eqn 4.33)}$$

The peak displayed in Figure 4.36 at *m/z* 346 indicates the formation of the mixed ligand product $[Cu(acac)(tmtm)]^+$ from the reaction between mass-selected $[Cu(acac)]^+$ at *m/z* 162 and neutral $Fe(tmtm)_3$. Generation of the mixed ligand product occurs at one mass unit higher than expected.

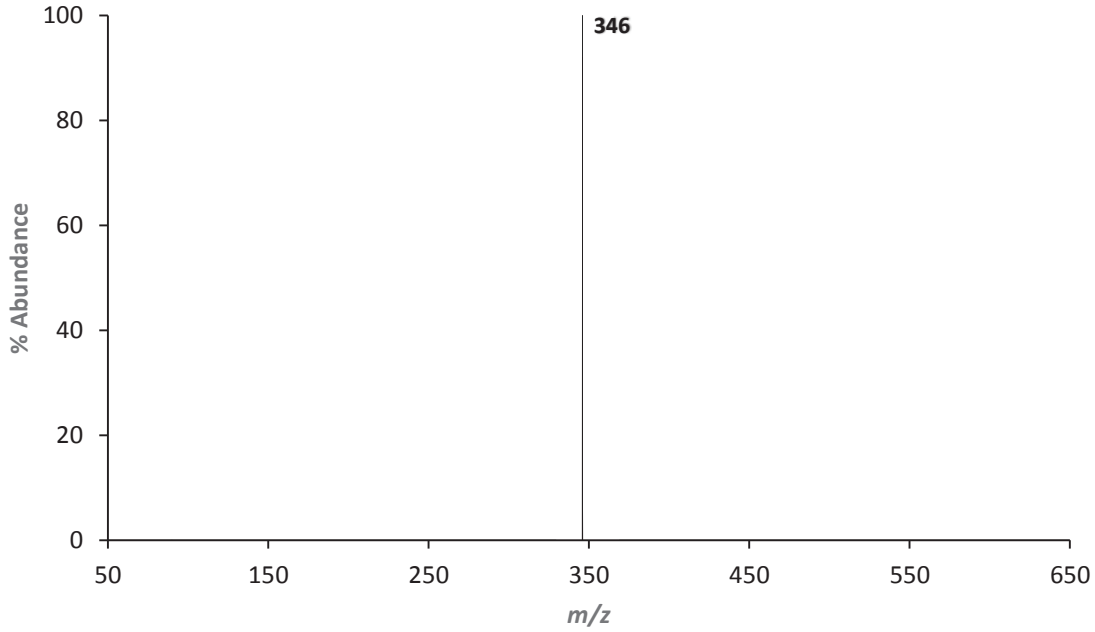

Figure 4.36: The 70eV positive EI mass spectrum obtained by scanning the third quadrupole after the selective reaction of *m/z* 162 ($[Cu(acac)]^+$) with neutral $Fe(tmtm)_3$ to produce the mixed ligand product at *m/z* 346 ($[Cu(acac)(tmtm)]^+$).

Based on this observation, the mixed ligand product appears to be formed from the donation of (tmtm) from $Fe(tmtm)_3$ to the cupric complex as shown in Equation (4.34).

$$[Cu^{II}(acac)]^+ + Fe^{III}(tmtm)_3 \rightarrow$$

$$[Cu^{II}(acac)(tmtm)]^{+\bullet} + Fe^{II}(tmtm)_2 \qquad \text{(Eqn 4.34)}$$

An additional ligand exchange product produced from reacting mass-selected $[Cu(acac)]^+$ at *m/z* 162 with neutral $Fe(tmtm)_3$ corresponds to the cuprous complex $[Cu(tmtm\text{-}t\text{Bu})_2]^+$ at *m/z* 316 in Figure 4.37. Product formation occurs at one mass unit higher than expected.

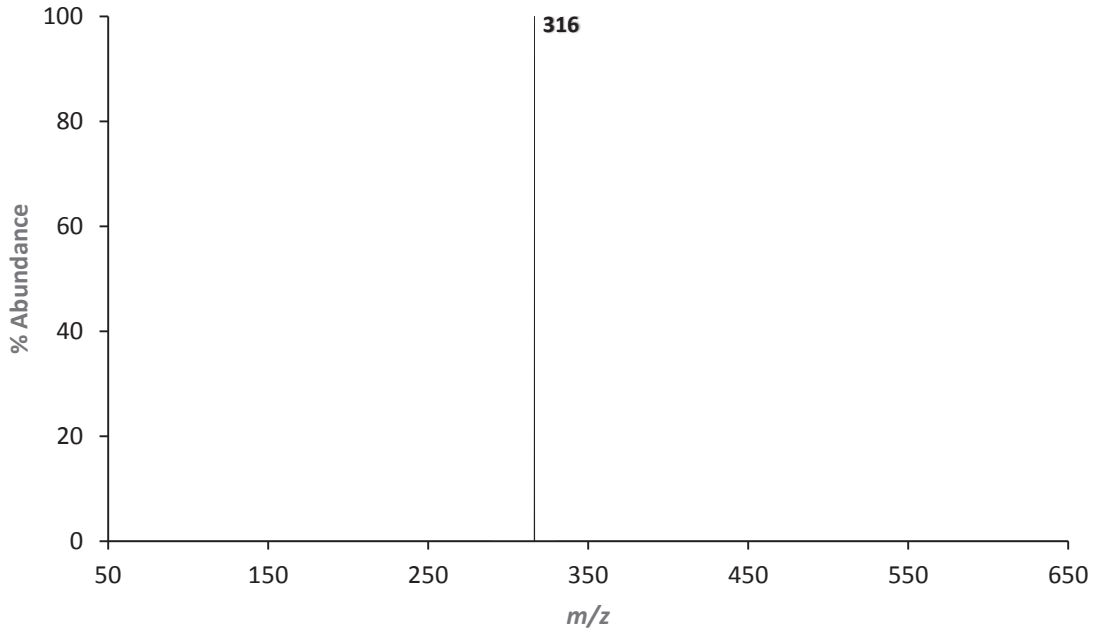

Figure 4.37: The 70eV positive EI mass spectrum obtained by scanning the third quadrupole after the selective reaction of *m/z* 162 ($[Cu(acac)]^+$) with neutral $Fe(tmtm)_3$ to produce the product at *m/z* 316 ($[Cu(tmtm\text{-}t\text{Bu})_2]^+$).

The corresponding reaction pathway likely incorporates complete ligand exchange, reductive rearrangement, and *tert*-butyl fragmentation to generate the product in a manner consistent with the mechanism proposed in Equation (4.35).

$$[Cu^{II}(acac)]^+ + Fe^{III}(tmtm)_3 \rightarrow$$

$$[Cu^{I}(tmtm\text{-}t\text{Bu})_2]^+ + Fe^{II}(acac)(tmtm) + 2t\text{Bu}^{\bullet} \qquad \text{(Eqn 4.35)}$$

The ion signal observed in Figure 4.38 at *m/z* 288 is indicative of the generation of the mixed ligand product $[Cu(acac)(tmtm\text{-}t\text{Bu})]^+$ from the collision-induced reaction between mass-selected $[Cu(acac)]^+$ at *m/z* 162 and neutral $Fe(tmtm)_3$.

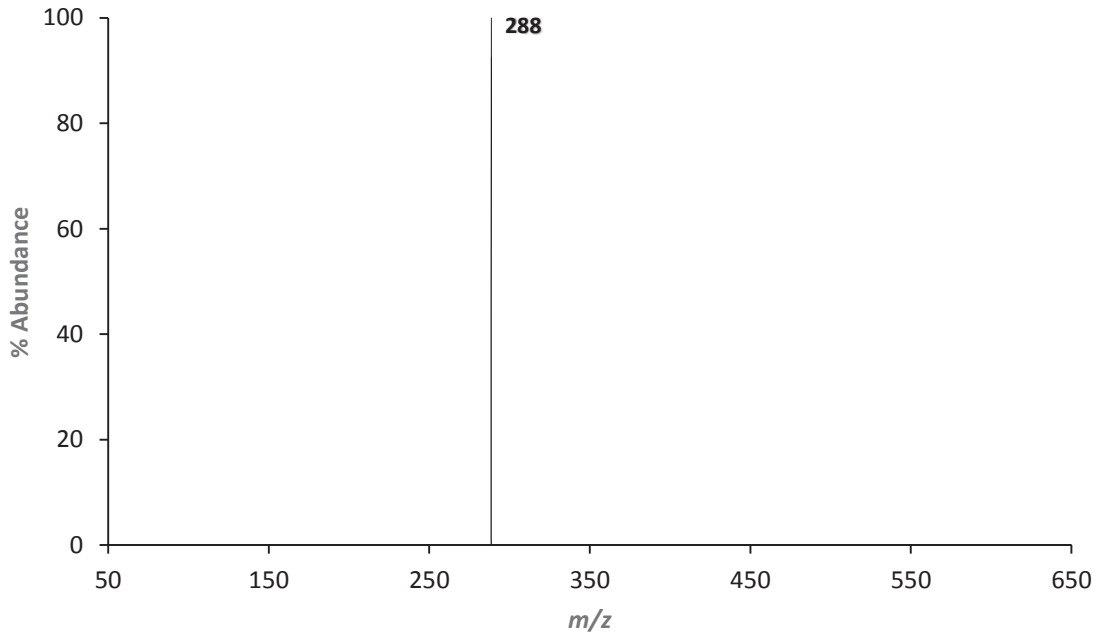

Figure 4.38: The 70eV positive EI mass spectrum obtained by scanning the third quadrupole after the selective reaction of *m/z* 162 ($[Cu(acac)]^+$) with neutral $Fe(tmtm)_3$ to produce the mixed ligand product at *m/z* 288 ($[Cu(acac)(tmtm\text{-}t\text{Bu})]^+$).

The reaction pathway potentially involves ligand donation and *tert*-butyl fragmentation to produce the mixed ligand fragment, and thus is consistent with the mechanism proposed in Equation (4.36).

$$[Cu^{II}(acac)]^+ + Fe^{III}(tmtm)_3 \rightarrow$$

$$[Cu^{II}(acac)(tmtm\text{-}t\text{Bu})]^+ + Fe^{II}(tmtm)_2 + t\text{Bu}^{\bullet} \qquad \text{(Eqn 4.36)}$$

The appearance of a peak at *m/z* 246 in Figure 4.39 suggests the formation $[Cu(tmtm)]^+$ from the reaction of mass-selected $[Cu(acac)]^+$ at *m/z* 162 and neutral $Fe(tmtm)_3$.

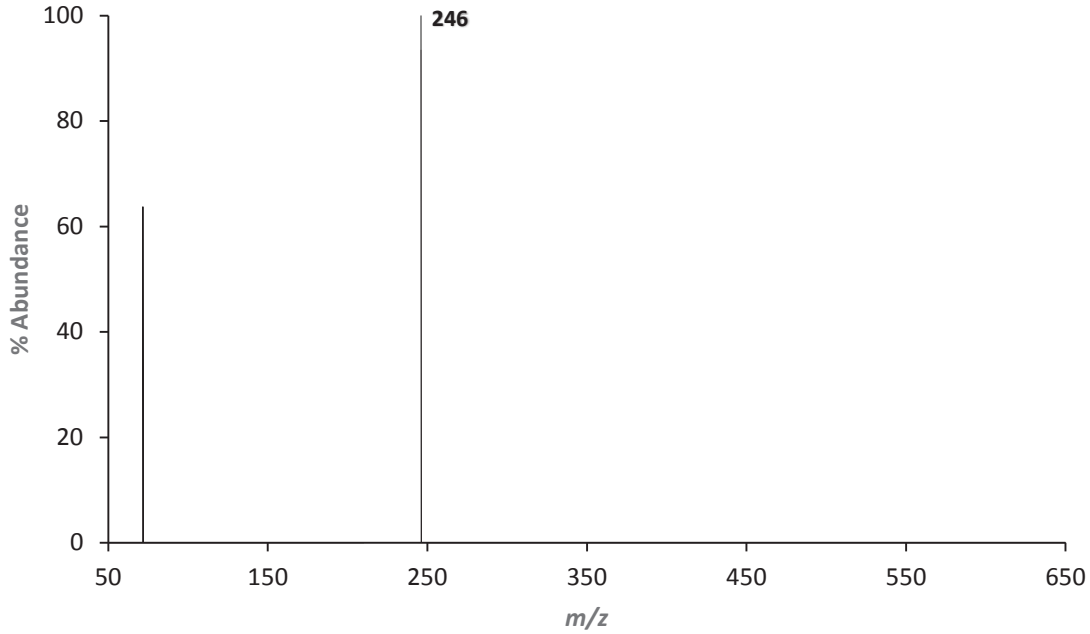

Figure 4.39: The 70eV positive EI mass spectrum obtained by scanning the third quadrupole after the selective reaction of *m/z* 162 ($[Cu(acac)]^+$) with neutral $Fe(tmtm)_3$ to produce the product at *m/z* 246 ($[Cu(tmtm)]^+$).

The formation of the singly-ligated product likely results from the partial ligand exchange between $[Cu(acac)]^+$ and $Fe(tmtm)_3$ as shown in Equation (4.37).

$$[Cu^{II}(acac)]^+ + Fe^{III}(tmtm)_3 \rightarrow$$

$$[Cu^{II}(tmtm)]^+ + Fe^{III}(acac)(tmtm)_2 \qquad \text{(Eqn 4.37)}$$

The peak appearing at *m/z* 154 in Figure 4.40 suggests the formation of $[Fe(acac)]^+$ from the collision-induced reaction between mass-selected $[Cu(acac)]^+$ at *m/z* 162 and neutral $Fe(tmtm)_3$. Production of $[Fe(acac)]^+$ occurs at one mass unit lower than expected. The additional ion signal appearing at *m/z* 225 does not correspond to a product of interest and was not further investigated.

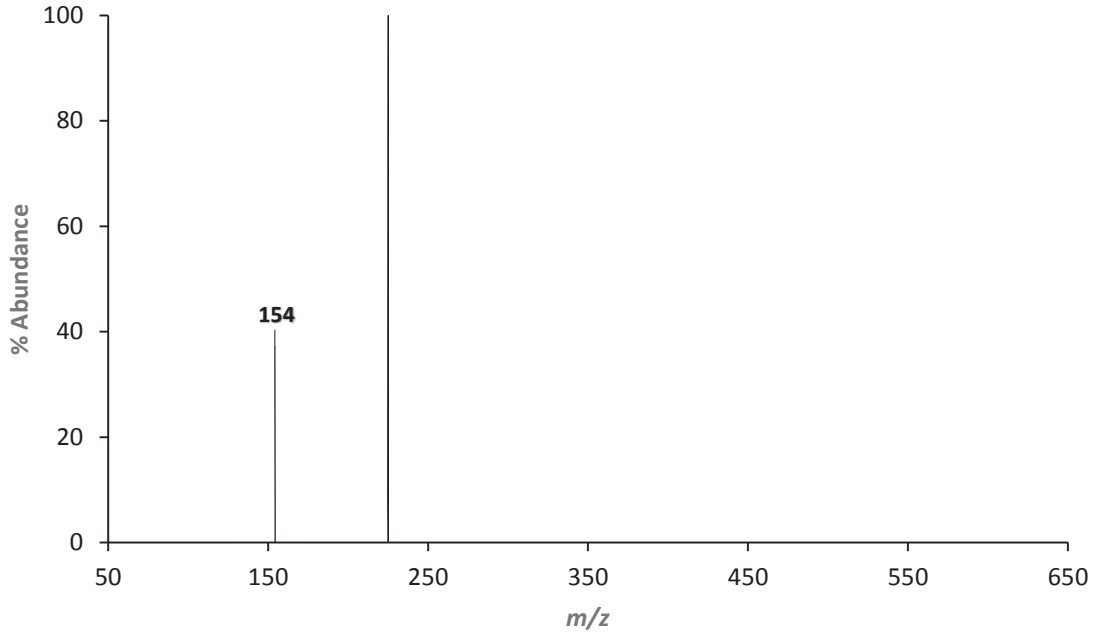

Figure 4.40: The 70eV positive EI mass spectrum obtained by scanning the third quadrupole after the selective reaction of *m/z* 162 ($[Cu(acac)]^+$) with neutral $Fe(tmtm)_3$ to produce the product at *m/z* 154 ($[Fe(acac)]^+$).

In a mechanistic proposal consistent with this result, complete ligand exchange between the reacting complexes yields the product in accordance to Equation (4.38).

$$[Cu^{II}(acac)]^+ + Fe^{III}(tmtm)_3 \rightarrow$$

$$[Fe^{II}(acac)]^+ + Cu^{II}(tmtm)_2 + tmtm^{\bullet} \qquad \text{(Eqn 4.38)}$$

Shown in Figure 4.41 are four peaks resulting from the collision-induced reactions of mass-selected $[Cu(acac\text{-}CH_3)]^+$ at *m/z* 147 and neutral $Fe(tmtm)_3$. The peak appearing at *m/z* 429 is indicative of the formation of $[Cu(tmtm)_2]^+$ while the ion signal displayed at *m/z* 146 corresponds to the mass-selected parent ion at one mass unit lower than expected. The remaining peaks at *m/z* 347 and *m/z* 143 do not correspond to any products of interest.

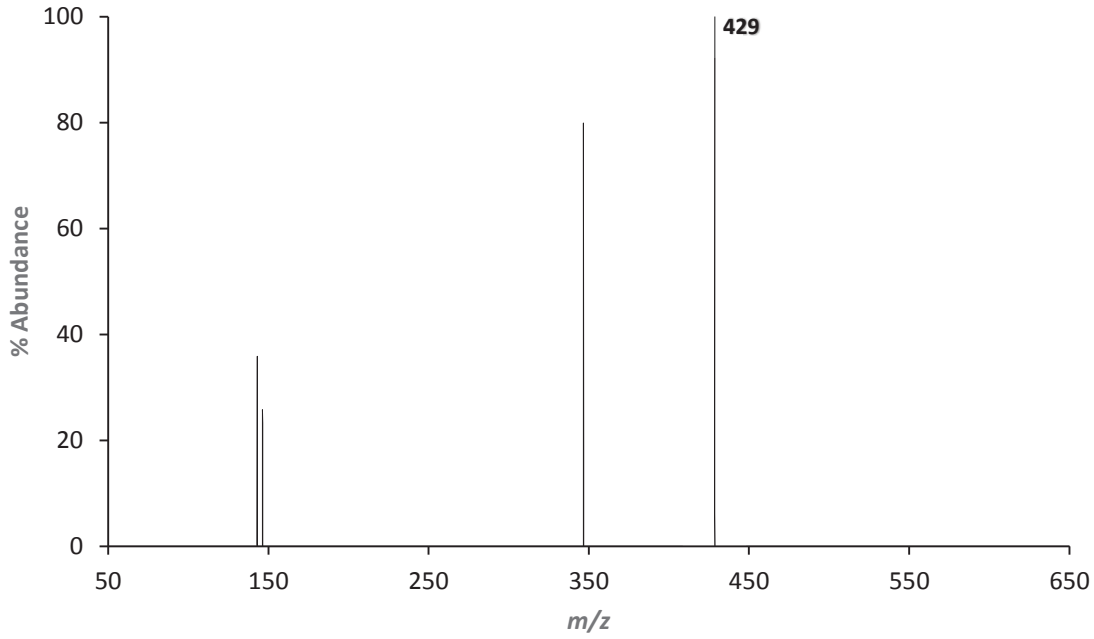

Figure 4.41: The 70eV positive EI mass spectrum obtained by scanning the third quadrupole after the selective reaction of *m/z* 147 ($[Cu(acac\text{-}CH_3)]^+$) with neutral $Fe(tmtm)_3$ to produce the product at *m/z* 429 ($[Cu(tmtm)_2]^+$).

Equation (4.39) presents a mechanistic proposal to account for product formation wherein the mass-selected ion undergoes complete ligand exchange with $Fe(tmtm)_3$ to acquire two equivalents of (tmtm) to form $[Cu(tmtm)_2]^+$.

$$[Cu^{I}(acac\text{-}CH_3)]^+ + Fe^{III}(tmtm)_3 \rightarrow$$

$$[Cu^{II}(tmtm)_2]^{+\bullet} + Fe^{I}(acac\text{-}CH_3)(tmtm) \qquad \text{(Eqn 4.39)}$$

The peak shown at *m/z* 371 in Figure 4.42 suggests the formation of $[Cu(tmtm)(tmtm\text{-}tBu)]^+$ from the reaction between mass-selected $[Cu(acac\text{-}CH_3)]^+$ at *m/z* 147 and neutral $Fe(tmtm)_3$. Formation of the product occurs at one mass unit lower than expected.

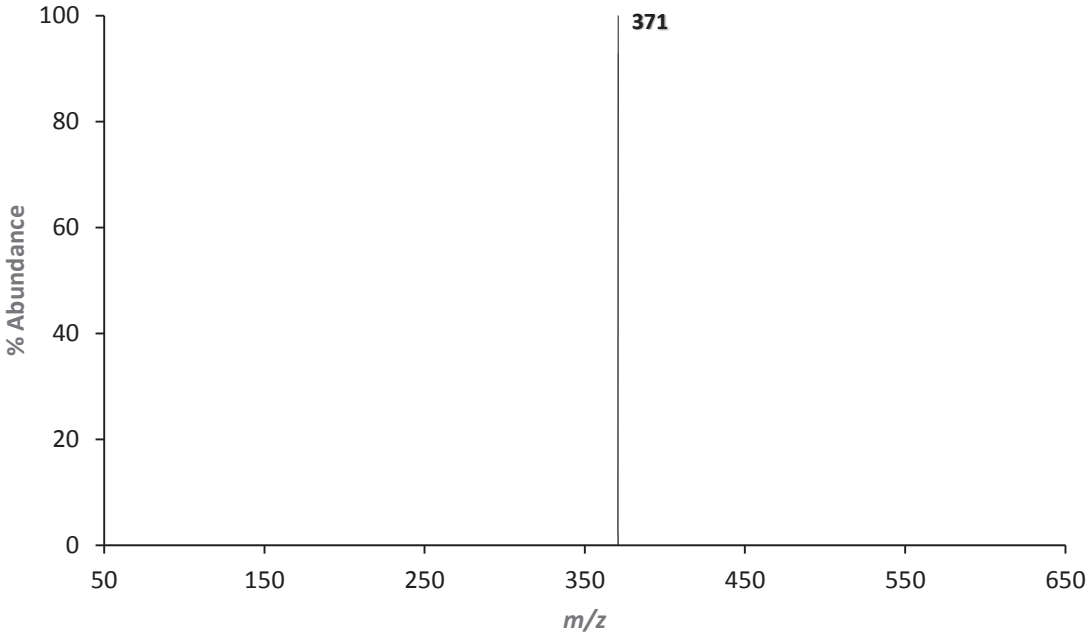

Figure 4.42: The 70eV positive EI mass spectrum obtained by scanning the third quadrupole after the selective reaction of *m/z* 147 ($[Cu(acac\text{-}CH_3)]^+$) with neutral $Fe(tmtm)_3$ to produce the product at *m/z* 371 ($[Cu(tmtm)(tmtm\text{-}tBu)]^+$).

The mechanism proposed in Equation (4.40) incorporates both complete ligand exchange and *tert*-butyl fragmentation to account for the formation of $[Cu(tmtm)(tmtm\text{-}tBu)]^+$.

$$[Cu^{I}(acac\text{-}CH_3)]^+ + Fe^{III}(tmtm)_3 \rightarrow$$

$$[Cu^{II}(tmtm)(tmtm\text{-}tBu)]^+ + Fe^{I}(acac\text{-}CH_3)(tmtm) + tBu^{\bullet} \qquad \text{(Eqn 4.40)}$$

In total, 40 ligand exchange products were generated from the collision-induced reactions of $Fe(tmtm)_3$ and $Cu(acac)_2$. All products shown to form are consistent with those formed during co-sublimation. Ten products were generated from the selective-reactions of $[Fe(tmtm)_2]^+$ at *m/z* 422 with neutral $Cu(acac)_2$. The fragment $[Fe(tmtm)(tmtm\text{-}t\text{Bu})]^+$ at *m/z* 365 was shown to form five products upon exposure to neutral $Cu(acac)_2$ while the mass-selection of $[Fe(tmtm)]^+$ at *m/z* 239 led to the formation of three products. Interestingly, the number of products generated from each fragment reflects the corresponding relative ratio change discussed in the previous section, and thus lends support to the use of relative ratios as a feasible method for mechanistic analysis in later sections.

Since the relative ratios of $Cu(acac)_2$ fragments were not particularly informative in regards to fragment reactivity, it was envisioned that the collision-induced reactions could help resolve this ambiguity. Indeed, a difference in productivity is observed amongst the $Cu(acac)_2$ fragments investigated. The singly-ligated fragment $[Cu(acac)]^+$ at *m/z* 162 was shown to be the most conducive towards the gas-phase formation of ligand exchange products following a reaction with neutral $Fe(tmtm)_3$ since the reaction of $[Cu(acac)]^+$ with $Fe(tmtm)_3$ led to the production of eight products. The second-most reactive fragment corresponds to $[Cu(acac)(acac\text{-}CH_3)]^+$ at *m/z* 246 which was shown to generate a total of six products. Mass-selection of $[Cu(acac)_2]^+$ at *m/z* 261 and $[Cu(acac\text{-}CH_3)_2]^+$ at *m/z* 231 both resulted in the formation of three products following reaction with $Fe(tmtm)_3$, whereas only two products stem from reactions incorporating $[Cu(acac\text{-}CH_3)]^+$.

Chapter 5

The Gas-Phase Ligand Exchange Reactions of Iron (III) Trimethyltrimethylacetylacetonate ($Fe(tmtm)_3$) with Copper Trifluorotrimethylacetylacetonate ($Cu(tftm)_2$)

5.1 Introduction

The data presented herein continues the discussion on the gas-phase ligand exchange reactions between $Fe(tmtm)_3$ and copper β-diketonates; namely, copper triflurotrimethylacetylacetonate ($Cu(tftm)_2$). The co-sublimation data is analyzed and interpreted to validate product formation. Moreover, relative ratios of the parent ions are calculated and analyzed to make sensible inferences on the relative reactivity of parent ions. In order to gather insight into the mechanistic framework of the reactions of interest, selective reactions between $Fe(tmtm)_3$ and $Cu(tftm)_2$ are investigated by means of tandem mass spectrometry.

5.2 Copper (II) Trifluorotrimethylacetylacetonate ($Cu(tftm)_2$)

For more information regarding $Cu(tftm)_2$ and its fragmentation behavior please refer back to Chapter 1, Lerach, or Hunter.[11,12] The base spectrum of $Cu(tftm)_2$ is displayed in Figure 5.1a and Figure 5.2a while the corresponding tabulated data may be found in Table 5.1 and 5.2.

5.3 The Co-sublimation of $Fe(tmtm)_3$ & $Cu(tftm)_2$

Displayed in Figure 5.1c and Figure 5.2c are the co-sublimation spectra of $Cu(tftm)_2$ and $Fe(tmtm)_3$ at an earlier and later time period of mass spectrometric analysis, respectively. Two separate co-sublimation spectra are shown since unique peaks appear during different timeframes. The baseline spectrum of $Cu(tftm)_2$ and $Fe(tmtm)_3$ are stacked above the co-sublimation spectrum in Figure 5.1 and Figure 5.2 to help highlight the gas-phase formation of novel copper and iron products observed herein for the first time. The corresponding masses with their respective abundances for the earlier scan are provided in Table 5.1 while the tabulated information for the later scan can be found in Table 5.2.

Complete ligand exchange products containing copper are observed in fairly low abundances during both periods. Two such peaks are observed at *m/z* 315 and *m/z* 189 which indicate the gas-phase formation of $[Cu(tmtm\text{-}t\text{Bu})_2]^+$ and $[Cu(tmtm\text{-}tBu)]^+$, respectively. Conversely, ion signals corresponding to mixed ligand products were observed in more considerable abundances during the earlier portion of mass analysis. The formation of the mixed ligand product $[Cu(tmtm)(tftm)]^+$, for instance, is apparent from the peak at *m/*z 441 while the peak corresponding to the mixed ligand fragment $[Cu(tmtm)(tftm)\text{-}t\text{Bu}]^+$ appears at *m/z* 384. Loss of a second equivalent of *tert*-butyl yields the mixed ligand fragment $[Cu(tmtm\text{-}t\text{Bu})(tftm\text{-}t\text{Bu})]^+$ at *m/z* 327.

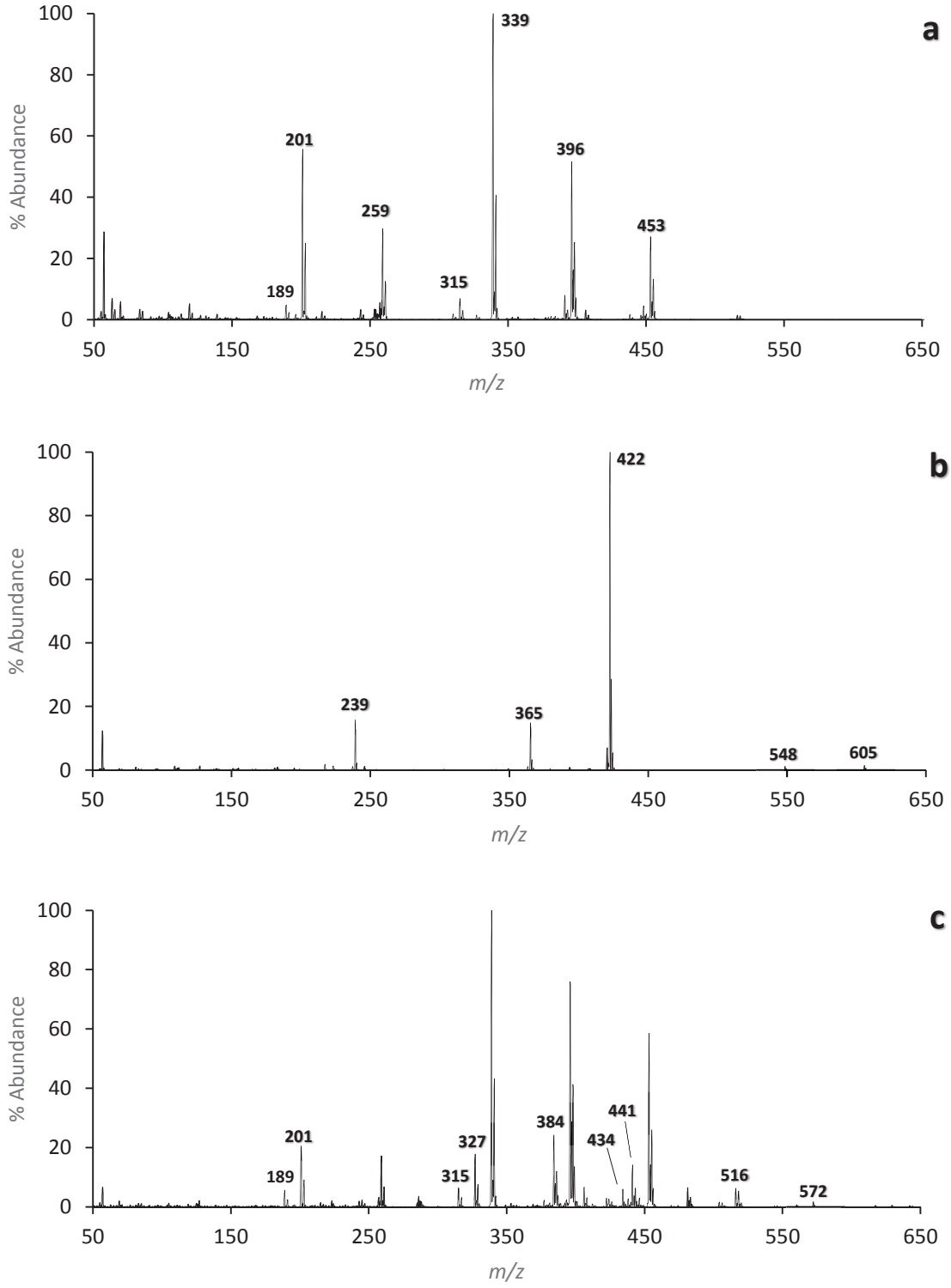

Figure 5.1: The 70eV positive EI mass spectra for a) $Cu(tftm)_2$, b) $Fe(tmtm)_3$, and c) the gas-phase reactions of $Cu(tftm)_2$ and $Fe(tmtm)_3$ at an earlier time of mass spectrometric analysis.

	Mass	Mass	FeL'_3	CuL'_2	FeL''_3	CuL''_2	FeL'_3 & CuL''_2	
Species	Fe	Cu	Fe	Cu	Fe	Cu	Fe	Cu
$[ML'_3]^+$	605	612	1	<1			<1	<1
$[ML'_3$-*t*Bu$]^+$	548	555	1	<1			<1	<1
$[ML'_2]^+$	422	429	100	26			3	1
$[ML'_2$-*t*Bu$]^+$	365	372	15	59			<1	1
$[ML'_2$-2*t*Bu$]^+$	308	315	<1	100			<1	***7***
$[ML']^+$	239	246	16	9*			<1	1*
$[ML'$-*t*Bu$]^+$	182	189	<1	28			<1	***6***
$[ML''_3]^+$	641	648			1	<1	<1	<1
$[ML''_3$-*t*Bu$]^+$	584	591			1	<1	<1	<1
$[ML''_2]^+$	446	453			69	27 (1.00)	**3**	59 (1.00)
$[ML''_2$-43$]^+$	403	410			17	<1	<1	<1
$[ML''_2$-*t*Bu$]^+$	389	396			46	50 (1.85)	<1	75 (1.27)
$[ML''_2$-$CF_3]^+$	377	384			4	1 (0.04)	***2***	*24* (0.41)
$[ML''_2$-2*t*Bu$]^+$	332	339			<1	100 (3.70)	<1	100 (1.70)
$[ML''_2$-2$CF_3]^+$	308	315			1	7 (0.26)	<1	*7* (0.12)
$[ML''$+42$]^+$	293	300			7	<1	<1	<1
$[ML'']^+$	251	258			20	30* (1.11)	<1	17* (0.29)
$[ML''$-$CF_2]^+$	201	208			38	<1	***21***	1 (0.02)
$[ML''$-*t*Bu$]^+$	194	201			8	56 (2.07)	<1	*21* (0.36)
$[ML''$-$CF_3]^+$	182	189			<1	4 (0.15)	<1	*6* (0.10)
$[ML'L''_2]^+$	629	636					1	<1
$[ML'L''_2$-*t*Bu$]^+$	572	579					**2**	<1
$[ML'L''_2$-2*t*Bu$]^+$	515	522					**6***	<1
$[ML'L'']^+$	434	441					**6**	**14**
$[ML'L''$-*t*Bu$]^+$	377	384					***2***	***24***
$[ML'L''$-2*t*Bu$]^+$	320	327					<1	**18**

Table 5.1 Relative positive ion intensities (% abundance) of hetero-metal species to their respective base peaks at an earlier time of mass spectrometric analysis as presented in Figure 5.1. L' = (tmtm), L'' = (tftm), *Protonated: observed at one mass unit higher than expected, *Italics:* Isobaric, **Bold**: Ligand exchange product, (Parentheses): Relative Ratio

As was the case for copper-containing complete ligand exchange products, those consisting of iron are typically observed in fairly low abundances during both timeframes. One such ion signal, corresponding to the complete ligand exchange product $[Fe(tftm)_2]^+$, is detected during both portions of mass analysis at *m/z* 446. The mixed ligand species $[Fe(tmtm)(tftm)_2$-*t*Bu$)]^+$ and $[Fe(H)(tmtm)(tftm)_2$-2*t*Bu$]^+$, on the other hand, are only observed during the earlier period of mass analysis at *m/z* 572 and *m/*z 516, respectively.

During the latter segment of mass analysis, the formation of the mixed ligand product $[Fe(tmtm)(tftm)]^+$ becomes increasingly evident based on the peak observed at

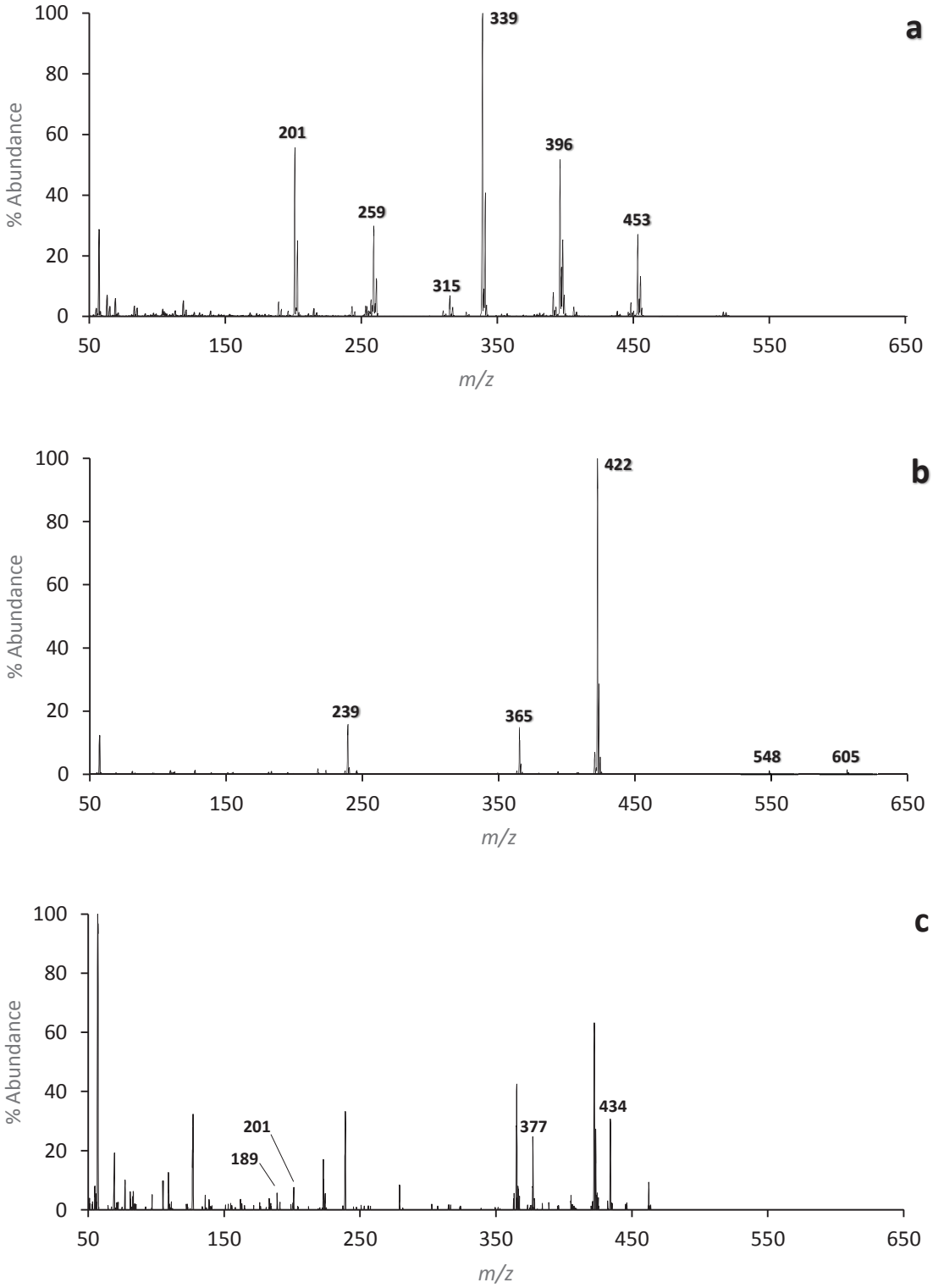

Figure 5.2: The 70eV positive EI mass spectra for a) $Cu(tftm)_2$, b) $Fe(tmtm)_3$, and c) the gas-phase reactions of $Cu(tftm)_2$ and $Fe(tmtm)_3$ at a later time of mass spectrometric analysis.

	Mass	Mass	FeL'_3	CuL'_2	FeL''_3	CuL''_2	FeL'_3 & CuL''_2	
Species	Fe	Cu	Fe	Cu	Fe	Cu	Fe	Cu
$[ML'_3]^+$	605	612	1 (0.07)	<1			<1	<1
$[ML'_3$-*t*Bu$]^+$	548	555	1 (0.07)	<1			<1	<1
$[ML'_2]^+$	422	429	100 (6.67)	26			63 (1.47)	<1
$[ML'_2$-*t*Bu$]^+$	365	372	15 (1)	59			43 (1)	<1
$[ML'_2$-2*t*Bu$]^+$	308	315	<1	100			<1	***2***
$[ML']^+$	239	246	16 (1.07)	9*			33 (0.77)	<1
$[ML'$-*t*Bu$]^+$	182	189	<1	28			<1	***6***
$[ML''_3]^+$	641	648			1	<1	<1	<1
$[ML''_3$-*t*Bu$]^+$	584	591			1	<1	<1	<1
$[ML''_2]^+$	446	453			69	27	**2**	<1
$[ML''_2$-43$]^+$	403	410			17	<1	<1	<1
$[ML''_2$-*t*Bu$]^+$	389	396			46	50	**2**	1
$[ML''_2$-$CF_3]^+$	377	384			4	1	***25***	*2*
$[ML''_2$-2*t*Bu$]^+$	332	339			0	100	<1	<1
$[ML''_2$-2$CF_3]^+$	308	315			1	7	<1	*2*
$[ML''$+42$]^+$	293	300			7	<1	<1	<1
$[ML'']^+$	251	258			20	30*	**2**	<1
$[ML''$-$CF_2]^+$	201	208			38	0	***8***	1
$[ML''$-*t*Bu$]^+$	194	201			8	56	<1	*8*
$[ML''$-$CF_3]^+$	182	189			0	4	<1	*6*
$[ML'L''_2]^+$	629	636					<1	<1
$[ML'L''_2$-*t*Bu$]^+$	572	579					<1	<1
$[ML'L''_2$-2*t*Bu$]^+$	515	522					<1	<1
$[ML'L'']^+$	434	441					**31**	<1
$[ML'L''$-*t*Bu$]^+$	377	384					***25***	***2***
$[ML'L''$-2*t*Bu$]^+$	320	327					<1	<1

Table 5.2 Relative positive ion intensities (% abundance) of hetero-metal species to their respective base peaks at a later time of mass spectrometric analysis as presented in Figure 5.2. L' = (tmtm), L'' = (tftm), *Protonated: observed at one mass unit higher than expected, *Italics:* Isobaric, **Bold**: Ligand exchange product, (Parentheses): Relative Ratio

m/z 434. Likewise, the production of the mixed ligand fragment [Fe(tmtm)(tftm)-*t*Bu]$^+$ is made apparent by the ion signal at *m/z* 377. The isobaric species [Fe(tftm)(tftm-CF_3)]$^+$ is unlikely to contribute to peak formation at *m/z* 377 considering its low abundance in the baseline spectrum of $Fe(tftm)_3$. Preferential loss of *tert*-butyl over CF_3 is consistent with prior experimentation and literature, and can be attributed to the resultant radical stability of the neutral fragment.[11-13, 19]

The fragmentation pathway accounting for the mixed ligand product [Fe(H)(tmtm)$(tftm)_2$-2*t*Bu]$^+$ could resemble the reductive rearrangement pathway discussed in Chapter 1 and depicted in Figure 1.3. The proposed mechanism in Figure

5.3 commences with the loss of *tert*-butyl followed by reductive rearrangement to generate the β-keto ester complex. The resulting intermediate can then undergo a second round of *tert*-butyl fragmentation to generate $[Fe(tmtm)(tftm)_2\text{-}2tBu]^+$. Alternatively, the formation of $[Fe(tmtm)(tftm\text{-}tBu)_2]^+$ could result from the acquisition of a fragmented β-keto ester ligand by neutral $Fe(tmtm)_3$ in a ligand exchange process with $[Cu(tftm\text{-}tBu)_2]^+$.

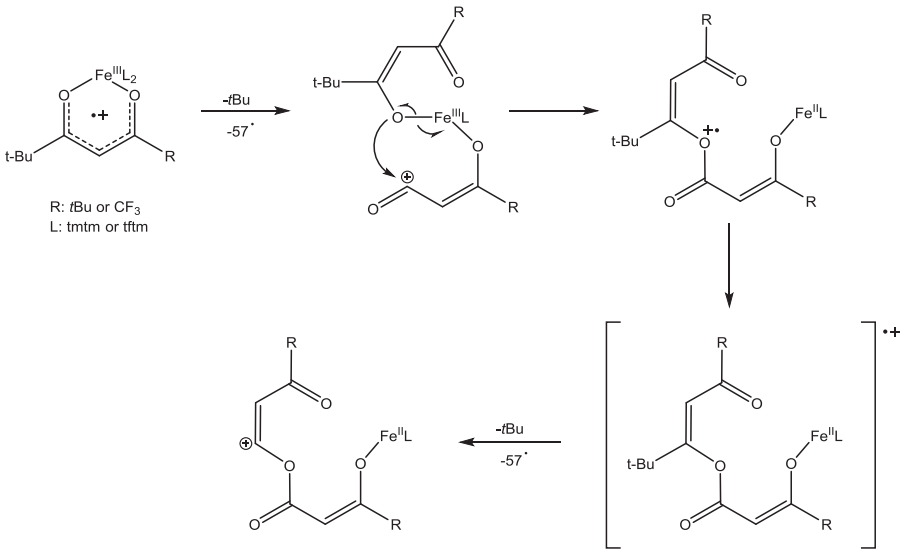

Figure 5.3: Fragmentation pathway of $[Fe(tmtm)(tftm)_2]^+$.

Using the same methodology from Chapter 4, the relative ratios of parent ion abundances were determined to probe the fragment reactivity of $Fe(tmtm)_3$ and $Cu(tftm)_2$. In this case, $[Cu(tftm)_2]^+$ at *m/z* 453 and $[Fe(tmtm)(tmtm\text{-}tBu)]^+$ at *m/z* 365 were selected as the reference species for the calculation of the relative ratios of the corresponding parent ions. The resulting values are placed in parentheses next to the corresponding normalized abundance in Table 5.1 and Table 5.2**.** By taking into account the observed differences between the relative ratios in the baseline and co-sublimation

spectrum, the mechanistic framework of the ligand exchange process becomes increasingly apparent.

Consider the gas-phase reaction of an ionic $Cu(tftm)_2$ fragment with neutral $Fe(tmtm)_3$. As shown in Table 5.1, significant peak attenuation is exhibited by $[Cu(tftm\text{-}t\text{Bu})_2]^+$ at *m/z* 339 as made evident by the decrease from a baseline relative ratio of 3.70 to a value of 1.70 in the co-sublimation spectrum. The decreasing abundance of $[Cu(tftm\text{-}t\text{Bu})_2]^+$ reflects a relatively high degree of fragment consumption in a reaction with neutral $Fe(tmtm)_3$. Another fairly reactive $Cu(tftm)_2$ fragment corresponds to $[Cu(tftm\text{-}t\text{Bu})]^+$ at *m/z* 201 which has a baseline relative ratio of 2.07 that decreases to a value of 0.36 in the co-sublimation spectrum. The parent ion $[Cu(H)(tftm)]^+$ at *m/z* 259 appears to be only moderately reactive considering that the baseline relative ratio decreases from 1.11 to a value of 0.29 following co-sublimation. Moderate reactivity is also demonstrated by $[Cu(tftm)(tftm\text{-}t\text{Bu})]^+$ at *m/z* 396 which decreases from a baseline relative ratio of 1.85 to a value of 1.27 in the co-sublimation spectrum

In considering the gas-phase reaction of an ionic $Fe(tmtm)_3$ fragment with neutral $Cu(tftm)_2$, further insight into the reaction pathways can be gained. Reference back to Table 5.2 reveals that the peak corresponding to $[Fe(tmtm)_2]^+$ at *m/z* 422 undergoes the most extensive degree of attenuation among the $Fe(tmtm)_3$ fragments; decreasing from a relative ratio of 6.67 in the baseline spectrum to a relative ratio of 1.47 in the co-sublimation spectrum. This would suggest that reaction pathways incorporating $[Fe(tmtm)_2]^+$ with neutral $Cu(tftm)_2$ are among the most prominent to

generate the ligand exchange products. In addition, the relative ratio of $[Fe(tmtm)]^+$ at *m/z* 239 decreases from 1.07 in the baseline spectrum to a value of 0.77 in the co-sublimation spectrum. The lesser degree of peak attenuation suggests that reaction pathways incorporating $[Fe(tmtm)]^+$ are less frequent, and provide minor contributions towards product formation. The collision-induced reactions of $Fe(tmtm)_3$ and $Cu(tftm)_2$ presented herein attempt to support these inferences, and in addition, are utilized to formulate reaction pathways to account for product formation.

5.4 Selective Reactions of $Fe(tmtm)_3$ & $Cu(tftm)_2$

Tandem mass spectrometry was utilized to investigate the selective reactions between $Fe(tmtm)_3$ and $Cu(tftm)_2$ in an effort to gain mechanistic insight into the ligand exchange processes apparent in the co-sublimation spectra. This was accomplished by scanning the mass range *m/z* 50 to *m/z* 650, selecting for the specified cation of interest, and allowing for its exclusive passage into the collision chamber to react with the neutral gas species. This particular section will examine the reactions between a neutral counter species and the following parent ions: $[Fe(tmtm)_2]^+$, $[Fe(tmtm)(tmtm\text{-}t\text{Bu})]^+$, $[Fe(tmtm)]^+$, $[Cu(tftm)_2]^+$, $[Cu(tftm)(tftm\text{-}t\text{Bu})]^+$, $[Cu(tftm\text{-}t\text{Bu})_2]^+$, and $[Cu(H)(tftm)]^+$. The selective reactions were performed over a span of ten minutes with a source temperature of 160 °C, manifold temperature of 80 °C, electron energy of 70 eV, and the electron multiplier held at 1200 V.

Beginning with the mass-selection of $[Fe(tmtm)_2]^+$ at *m/z* 422, the resulting collision-induced reaction with neutral $Cu(tftm)_2$ generates a peak at *m/z* 640 in Figure 5.4 and corresponds to $[Fe(tftm)_3]^+$, albeit at one mass unit lower than expected.

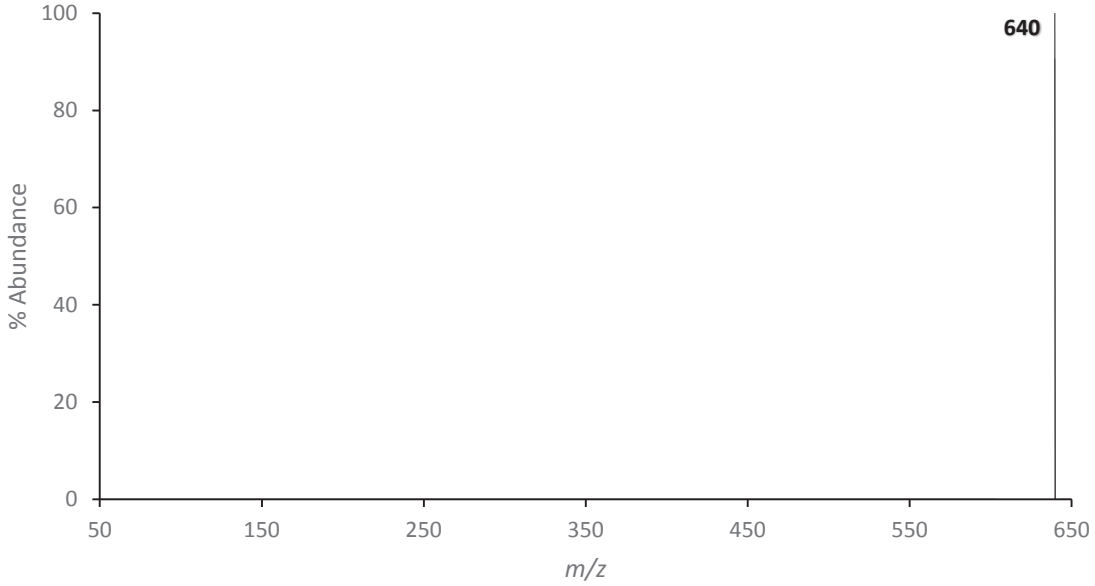

Figure 5.4: The 70eV positive EI mass spectrum obtained by scanning the third quadrupole after the selective reaction of *m/z* 422 ($[Fe(tmtm)_2]^+$) with neutral $Cu(tftm)_2$ to produce the product at *m/z* 640 ($[Fe(tftm)_3]^+$).

Equation (5.1) provides a corresponding mechanism to account for this observation wherein the product is generated through a complete ligand exchange process that incorporates two molecules of $Cu(tftm)_2$.

$$[Fe^{III}(tmtm)_2]^+ + 2Cu^{II}(tftm)_2 \rightarrow$$

$$[Fe^{III}(tftm)_3]^{+\bullet} + Cu^{II}(tmtm)_2 + Cu^{I}(tftm) \qquad \text{(Eqn 5.1)}$$

Figure 5.5 displays two peaks at *m/z* 572 and *m/z* 365 which signifies the formation of $[Fe(tmtm)(tftm)_2\text{-}t\text{Bu}]^+$ and $[Fe(tmtm)(tmtm\text{-}t\text{Bu})]^+$, respectively, from the collision-induced reaction between mass-selected $[Fe(tmtm)_2]^+$ at *m/z* 422 and neutral $Cu(tftm)_2$.

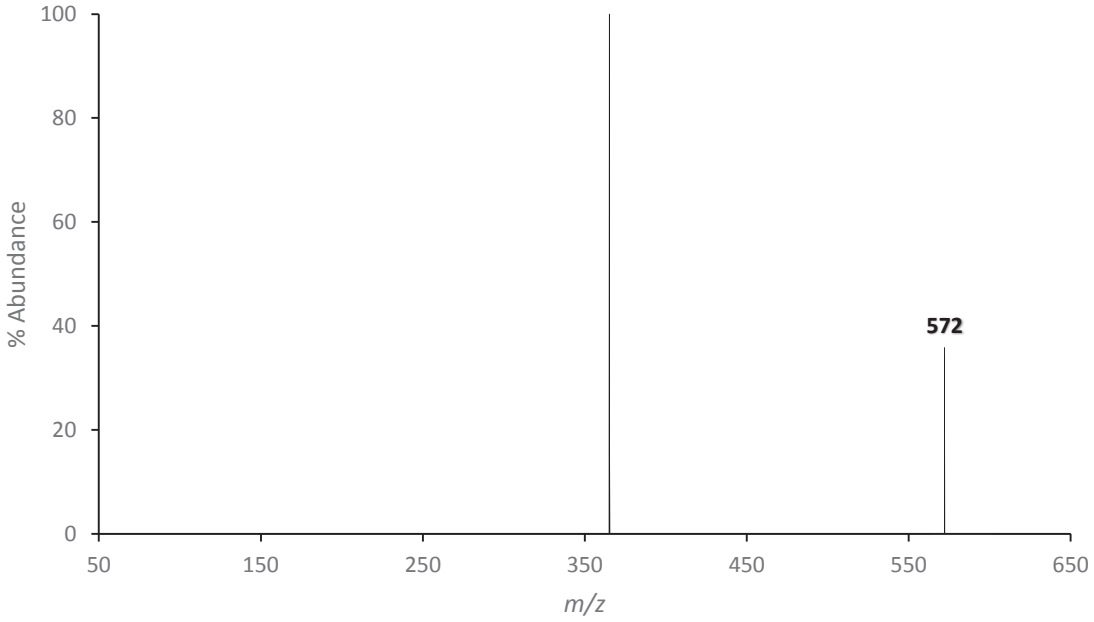

Figure 5.5: The 70eV positive EI mass spectrum obtained by scanning the third quadrupole after the selective reaction of *m/z* 422 ($[Fe(tmtm)_2]^+$) with neutral $Cu(tftm)_2$ to produce the mixed ligand fragment at *m/z* 572 ($[Fe(tmtm)(tftm)_2\text{-}tBu]^+$).

The mixed ligand fragment is likely generated through a process of partial ligand exchange and *tert*-butyl fragmentation as shown in Equation (5.2).

$$[Fe^{III}(tmtm)_2]^+ + Cu^{II}(tftm)_2 \rightarrow$$

$$[Fe^{III}(tmtm)(tftm)_2\text{-}t\text{Bu}]^+ + Cu^{I}(tmtm) + t\text{Bu}^{\bullet} \qquad \text{(Eqn 5.2)}$$

The peak at *m/z* 447 in Figure 5.6 is indicative of the gas-phase formation of $[Fe(tftfm)_2]^+$ resulting from the reaction between mass-selected $[Fe(tmtm)_2]^+$ at *m/z* 422 and neutral $Cu(tftfm)_2$. Product formation occurs at one mass unit higher than expected. The remaining peaks at *m/z* 422 and 209 represent the fragments $[Fe(tmtm)_2]^+$ and $[Cu(tftfm\text{-}CF_2)]^+$, respectively.

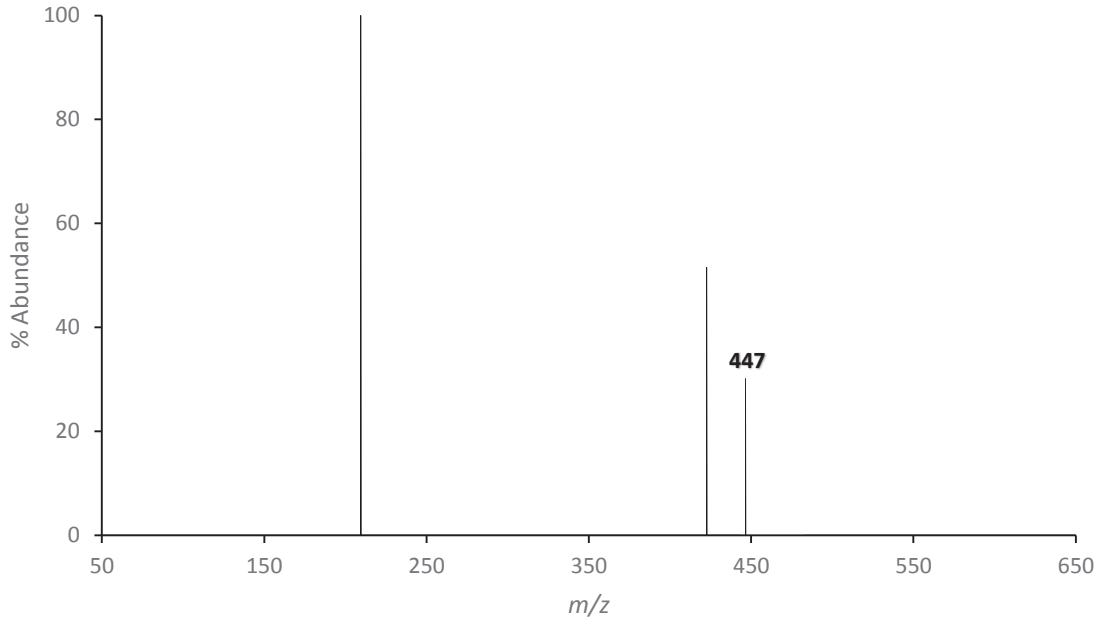

Figure 5.6: The 70eV positive EI mass spectrum obtained by scanning the third quadrupole after the selective reaction of *m/z* 422 ($[Fe(tmtm)_2]^+$) with neutral $Cu(tftfm)_2$ to produce the product at *m/z* 447 ($[Fe(tftfm)_2]^+$).

The formation of $[Fe(tftfm)_2]^+$ likely results from a complete ligand exchange process between the reactants, $[Fe(tmtm)_2]^+$ and $Cu(tftfm)_2$, as outlined in Equation (5.3).

$$[Fe^{III}(tmtm)_2]^+ + Cu^{II}(tftfm)_2 \rightarrow$$

$$[Fe^{III}(tftfm)_2]^+ + Cu^{II}(tmtm)_2 \qquad \text{(Eqn 5.3)}$$

The generation of the mixed ligand product $[Cu(tmtm)(tftm)]^+$ can be inferred from the presence of a peak at *m/z* 440 in Figure 5.7. Product formation occurs at one mass unit lower than expected.

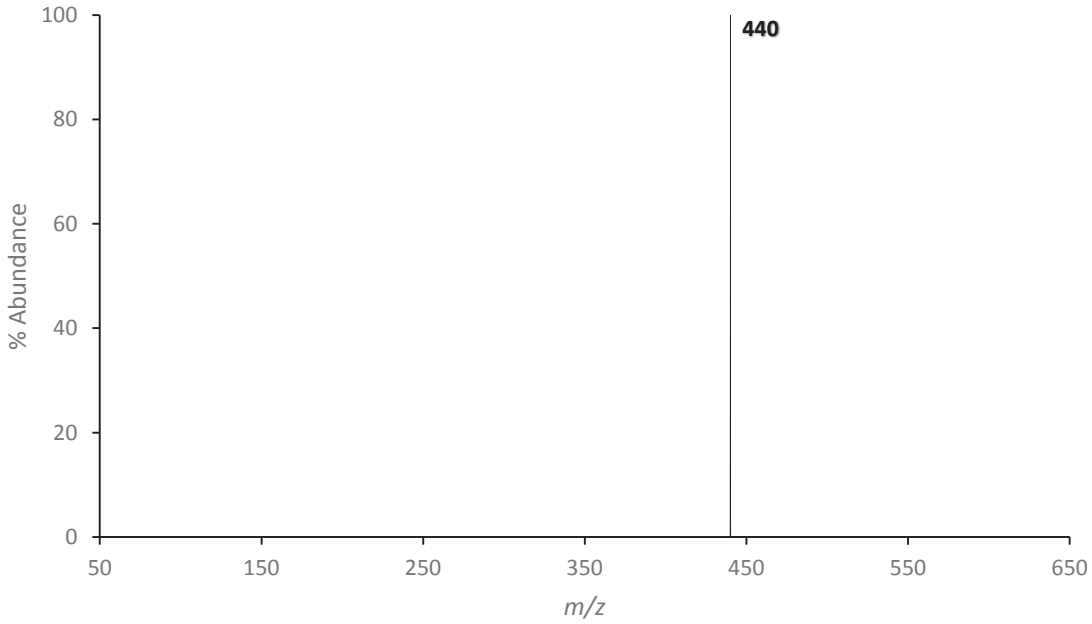

Figure 5.7: The 70eV positive EI mass spectrum obtained by scanning the third quadrupole after the selective reaction of *m/z* 422 ($[Fe(tmtm)_2]^+$) with neutral $Cu(tftm)_2$ to produce the mixed ligand product at *m/z* 440 ($[Cu(tmtm)(tftm)]^+$).

The mechanism proposed in Equation (5.4) is consistent with this observation and features a partial exchange process to generate the copper product.

$$[Fe^{III}(tmtm)_2]^+ + Cu^{II}(tftm)_2 \rightarrow$$

$$[Cu^{II}(tmtm)(tftm)]^{+\bullet} + Fe^{II}(tmtm)(tftm) \qquad \text{(Eqn 5.4)}$$

The spectrum below in Figure 5.8 contains a single peak at *m/z* 434 which correspond to the formation of the mixed ligand product $[Fe(tmtm)(tftm)]^+$ from the reaction of mass-selected $[Fe(tmtm)_2]^+$ at *m/z* 422 and neutral $Cu(tftm)_2$.

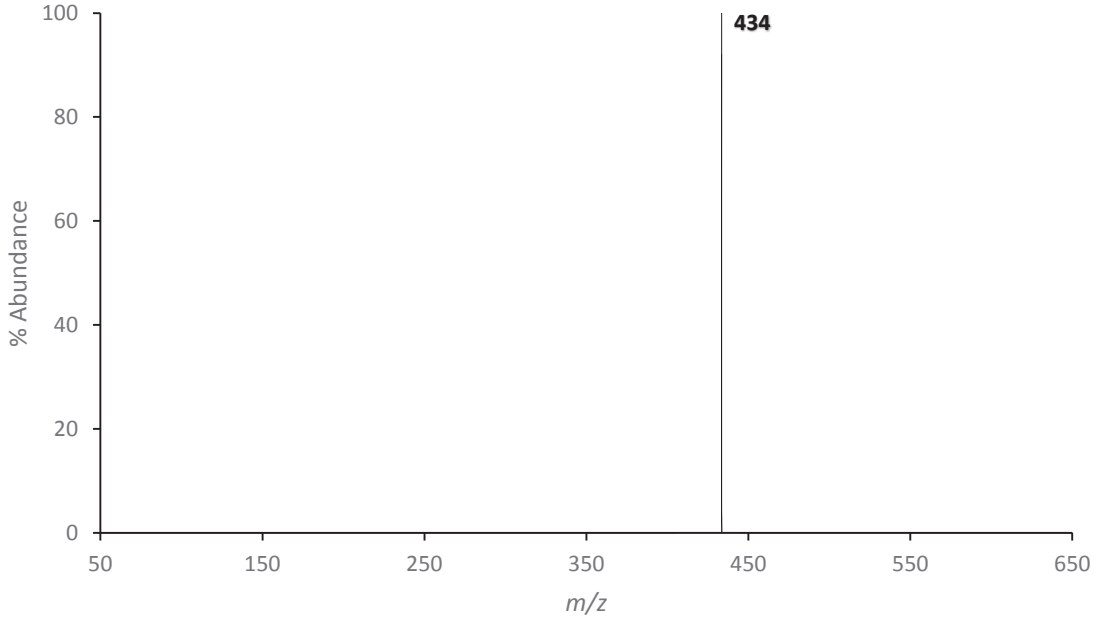

Figure 5.8: The 70eV positive EI mass spectrum obtained by scanning the third quadrupole after the selective reaction of *m/z* 422 ($[Fe(tmtm)_2]^+$) with neutral $Cu(tftm)_2$ to produce the mixed ligand product at *m/z* 434 ($[Fe(tmtm)(tftm)]^+$).

The proposed mechanism representative of this finding is provided in Equation (5.5) which entails partial ligand exchange to generate $[Fe(tmtm)(tftm)]^+$.

$$[Fe^{III}(tmtm)_2]^+ + Cu^{II}(tftm)_2 \rightarrow$$

$$[Fe^{III}(tmtm)(tftm)]^+ + Cu^{II}(tmtm)(tftm) \qquad \text{(Eqn 5.5)}$$

Two peaks at *m/z* 225 and *m/z* 378 are found in Figure 5.9 from the reaction between mass-selected $[Fe(tmtm)_2]^+$ at *m/z* 422 and neutral $Cu(tftm)_2$. The latter peak corresponds to the mixed ligand fragment $[Fe(tmtm)(tftm)\text{-}t\text{Bu}]^+$ at one mass unit higher than expected. The former peak does not correspond to any species of interest, and was not further investigated.

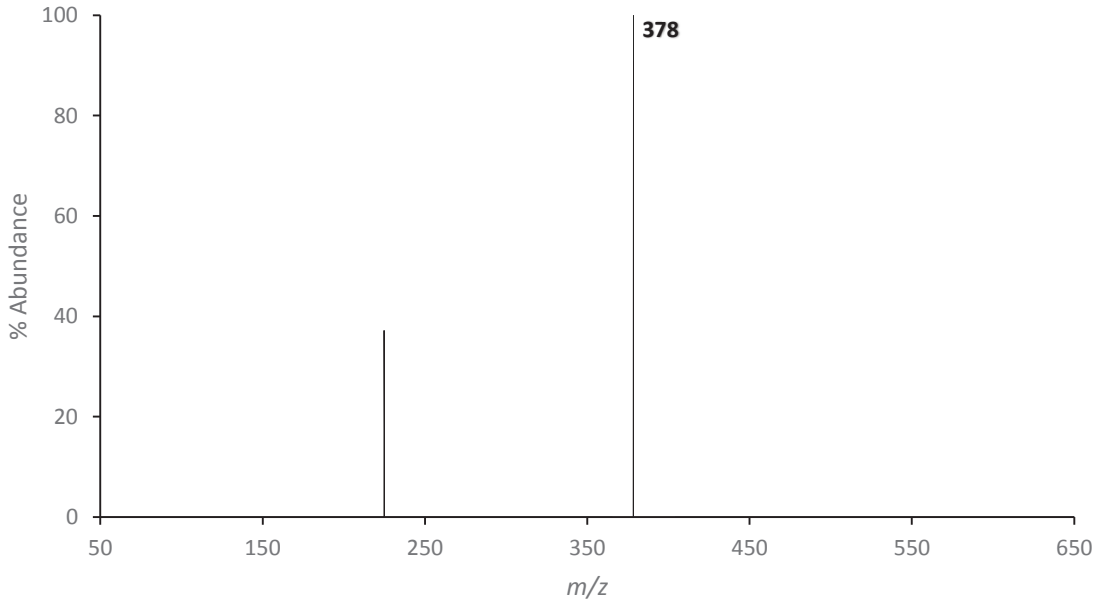

Figure 5.9: The 70eV positive EI mass spectrum obtained by scanning the third quadrupole after the selective reaction of *m/z* 422 ($[Fe(tmtm)_2]^+$) with neutral $Cu(tftm)_2$ to produce the mixed ligand fragment at *m/z* 378 ($[Fe(tmtm)(tftm)\text{-}tBu]^+$).

The production of the mixed ligand fragment is consistent with the proposed mechanism expressed in Equation (5.6).

$$[Fe^{III}(tmtm)_2]^+ + Cu^{II}(tftm)_2 \rightarrow$$

$$[Fe^{II}(tmtm)(tftm)\text{-}t\text{Bu}]^+ + Cu^{II}(tmtm)(tftm) + t\text{Bu}^{\bullet} \qquad \text{(Eqn 5.6)}$$

The formation of the mixed ligand fragment $[Cu(tmtm\text{-}tBu)(tftm\text{-}tBu)]^+$ can be inferred from the peak displayed at *m/z* 326 in Figure 5.10 which was produced upon reacting mass-selected $[Fe(tmtm)_2]^+$ at *m/z* 422 with neutral $Cu(tftm)_2$. Production of the mixed ligand fragment occurs at one mass unit lower than expected.

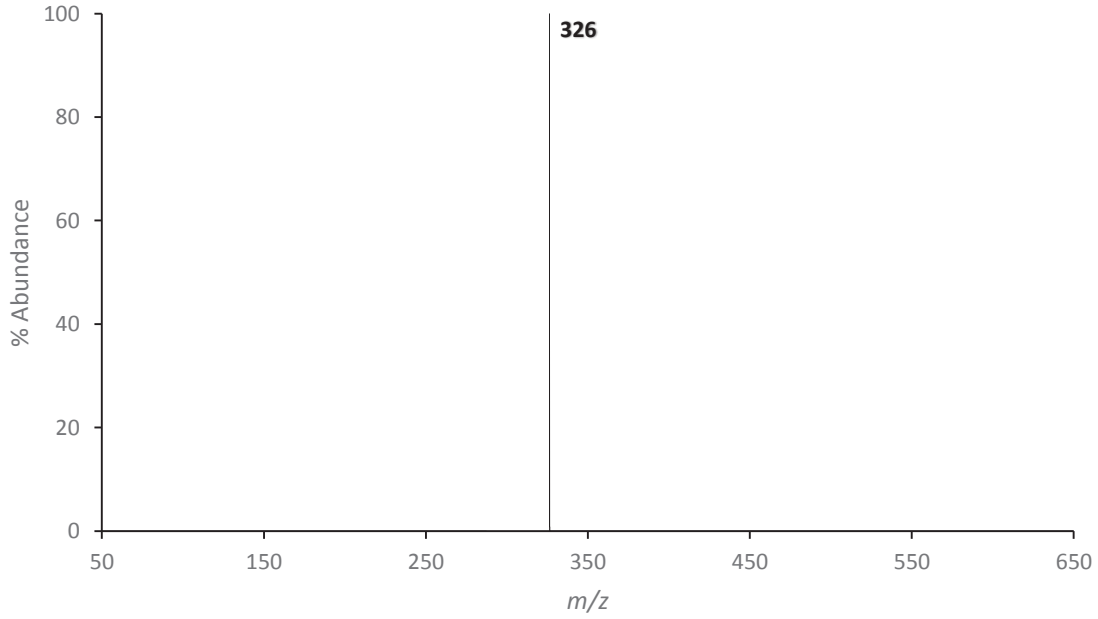

Figure 5.10: The 70eV positive EI mass spectrum obtained by scanning the third quadrupole after the selective reaction of *m/z* 422 ($[Fe(tmtm)_2]^+$) with neutral $Cu(tftm)_2$ to produce the mixed ligand fragment at *m/z* 326 ($[Cu(tmtm\text{-}tBu)(tftm\text{-}tBu)]^+$).

Product formation likely results from successive rounds of fragmentation and partial ligand exchange as shown in Equation (5.7).

$$[Fe^{III}(tmtm)_2]^+ + Cu^{II}(tftm)_2 \rightarrow$$

$$[Cu^{I}(tmtm\text{-}tBu)(tftm\text{-}tBu)]^+ + Fe^{II}(tmtm)(tftm) + 2tBu^{\bullet} \qquad \text{(Eqn 5.7)}$$

The next set of selective reactions involves the mass-selection of $[Fe(tmtm)(tmtm\text{-}t\text{Bu})]^+$ at *m/z* 365 while keeping $Cu(tftm)_2$ as the neutral gas-phase complex in the collision chamber. Starting with Figure 5.11, the peak shown at *m/z* 441 corresponds to the formation of the mixed ligand product $[Cu(tmtm)(tftm)]^+$.

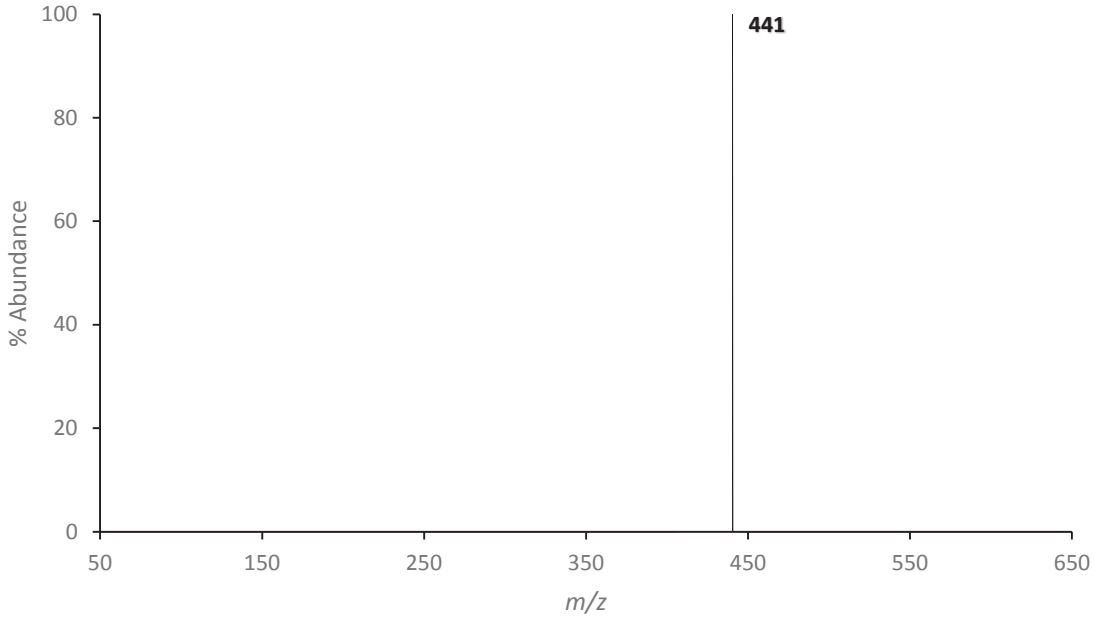

Figure 5.11: The 70eV positive EI mass spectrum obtained by scanning the third quadrupole after the selective reaction of *m/z* 365 ($[Fe(tmtm)(tmtm\text{-}tBu)]^+$) with neutral $Cu(tftm)_2$ to produce the mixed ligand product at *m/z* 441 ($[Cu(tmtm)(tftm)]^+$).

Equation (5.8) depicts a reaction pathway that incorporates partial ligand exchange between the positively charged iron complex and neutral copper complex to produce the mixed ligand product.

$$[Fe^{II}(tmtm)(tmtm\text{-}t\text{Bu})]^+ + Cu^{II}(tftm)_2 \rightarrow$$

$$[Cu^{II}(tmtm)(tftm)]^{+\bullet} + Fe^{I}(tmtm\text{-}t\text{Bu})(tftm) \qquad \text{(Eqn 5.8)}$$

An additional product observed from the reaction between mass-selected $[Fe(tmtm)(tmtm\text{-}t\text{Bu})]^+$ at *m/z* 365 and neutral $Cu(tftm)_2$ includes the complete ligand exchange product $[Cu(tmtm)_2]^+$ as indicated by the peak at *m/z* 428 in Figure 5.12. Formation of the product occurs at one mass unit lower than expected.

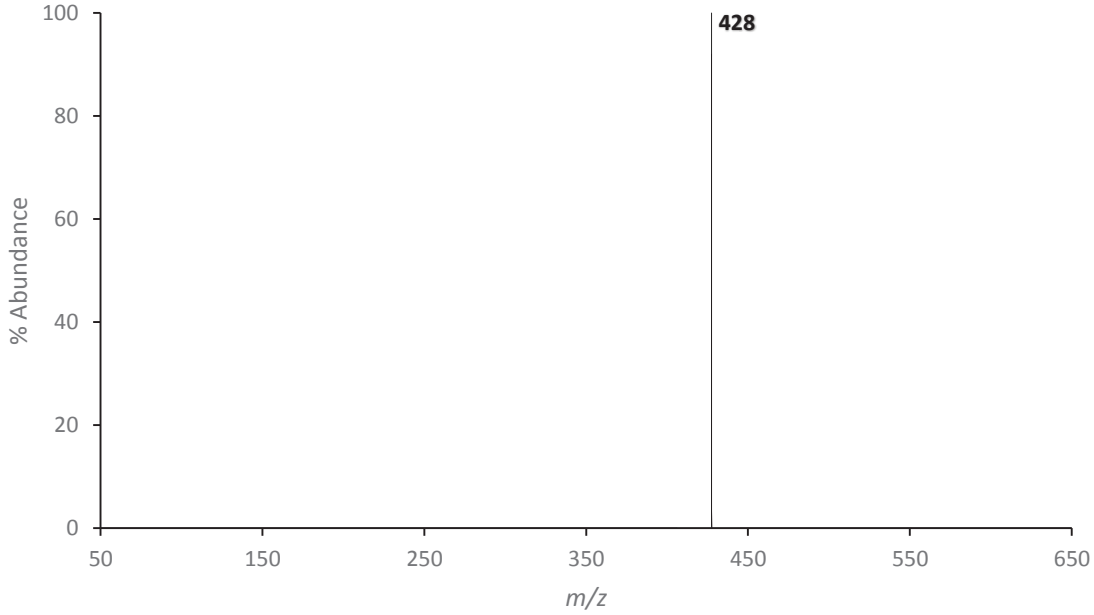

Figure 5.12: The 70eV positive EI mass spectrum obtained by scanning the third quadrupole after the selective reaction of *m/z* 365 ($[Fe(tmtm)(tmtm\text{-}tBu)]^+$) with neutral $Cu(tftm)_2$ to produce the product at *m/z* 428 ($[Cu(tmtm)_2]^+$).

The reaction pathway provided in Equation (5.9) entails a partial ligand exchange process between $Cu(tftm)_2$ and two equivalents of the mass-selected parent ion.

$$2[Fe^{II}(tmtm)(tmtm\text{-}t\text{Bu})]^+ + Cu^{II}(tftm)_2 \rightarrow$$

$$[Cu^{II}(tmtm)_2]^{+\bullet} + [Fe^{II}(tmtm\text{-}t\text{Bu})(tftm)]^+$$

$$+ Fe^{I}(tmtm\text{-}t\text{Bu})(tftm) \qquad \text{(Eqn 5.9)}$$

The spectrum displayed below in Figure 5.13 contains two peaks at *m/z* 388 and *m/z* 365. The former signifies the formation of $[Fe(tftm)(tftm\text{-}t\text{Bu})]^+$ from the collision-induced reaction between mass-selected $[Fe(tmtm)(tmtm\text{-}t\text{Bu})]^+$ at *m/z* 365 and neutral $Cu(tftm)_2$ while the latter indicates the detection of the mass-selected parent ion. Product formation occurs at one mass unit lower than expected.

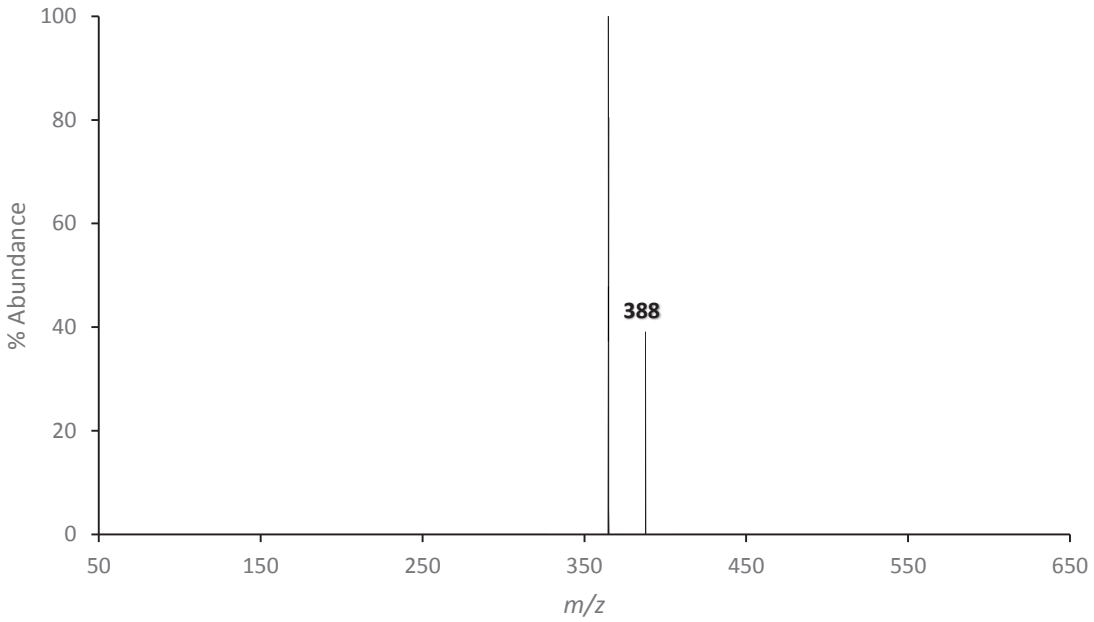

Figure 5.13: The 70eV positive EI mass spectrum obtained by scanning the third quadrupole after the selective reaction of *m/z* 365 ($[Fe(tmtm)(tmtm\text{-}tBu)]^+$) with neutral $Cu(tftm)_2$ to produce the product at *m/z* 388 ($[Fe(tftm)(tftm\text{-}tBu)]^+$).

This finding is consistent with the proposed mechanism shown in Equation (5.10) wherein a complete ligand exchange process is coupled with *tert*-butyl fragmentation to produce $[Fe(tftm)(tftm\text{-}tBu)]^+$.

$$[Fe^{II}(tmtm)(tmtm\text{-}t\text{Bu})]^+ + Cu^{II}(tftm)_2 \rightarrow$$

$$[Fe^{II}(tftm)(tftm\text{-}t\text{Bu})]^+ + Cu^{I}(tmtm)(tmtm\text{-}t\text{Bu}) + t\text{Bu}^{\bullet} \qquad \text{(Eqn 5.10)}$$

Shown in Figure 5.14 are three peaks at *m/z* 508, *m/z* 384, and *m/z* 365. The peak at *m/z* 365 corresponds to the parent ion $[Fe(tmtm)(tmtm\text{-}t\text{Bu})]^+$ while the peak at *m/z* 508 could not be identified. The peak at *m/z* 384 is consistent with the formation of $[Cu(tmtm\text{-}t\text{Bu})(tftm)]^+$ from reacting mass-selected $[Fe(tmtm)(tmtm\text{-}t\text{Bu})]^+$ at *m/z* 365 with neutral $Cu(tftm)_2$.

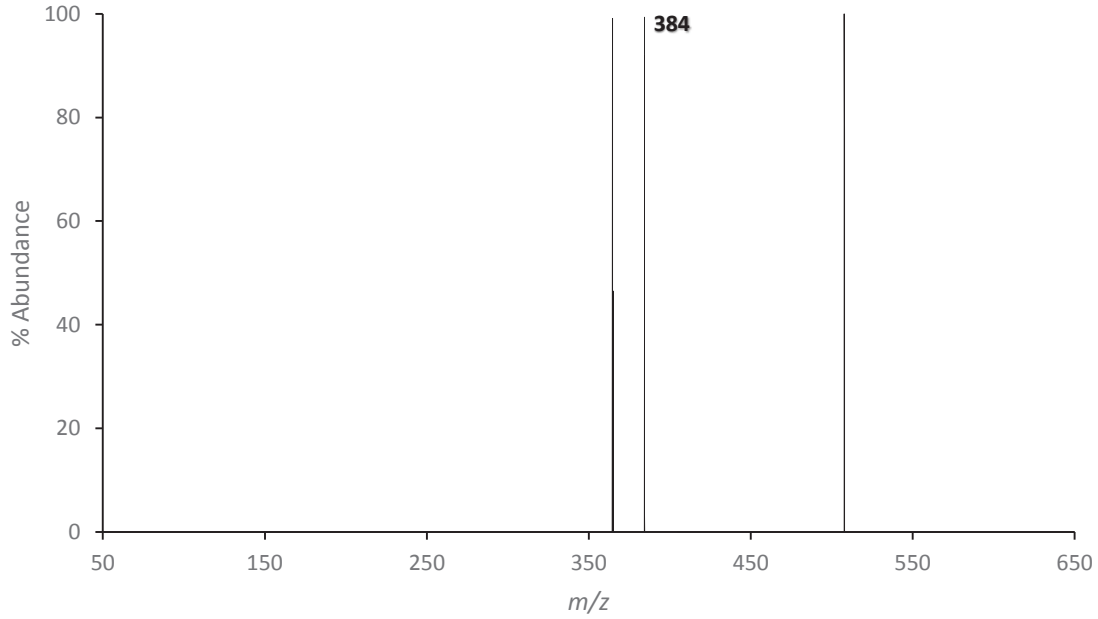

Figure 5.14: The 70eV positive EI mass spectrum obtained by scanning the third quadrupole after the selective reaction of *m/z* 365 ($[Fe(tmtm)(tmtm\text{-}tBu)]^+$) with neutral $Cu(tftm)_2$ to produce the mixed ligand fragment at *m/z* 384 ($[Cu(tmtm\text{-}tBu)(tftm)]^+$).

Production of the fragmented mixed ligand product would likely result from partial ligand exchange between $[Fe(tmtm)(tmtm\text{-}t\text{Bu})]^+$ and $Cu(tftm)_2$ as outlined in Equation (5.11).

$$[Fe^{II}(tmtm)(tmtm\text{-}t\text{Bu})]^+ + Cu^{II}(tftm)_2 \rightarrow$$

$$[Cu^{II}(tmtm\text{-}t\text{Bu})(tftm)]^+ + Fe^{II}(tmtm)(tftm) \qquad \text{(Eqn 5.11)}$$

Similar to the previous spectrum, Figure 5.15 features three peaks. However, only the peak *m/z* 326 relates to a ligand exchange product, and specifically indicates the formation of $[Cu(tmtm\text{-}t\text{Bu})(tftm\text{-}t\text{Bu})]^+$. The other two peaks at *m/z* 218 and *m/z* 229 do not correspond any of the species of interest. Product formation occurs at one mass unit lower than expected.

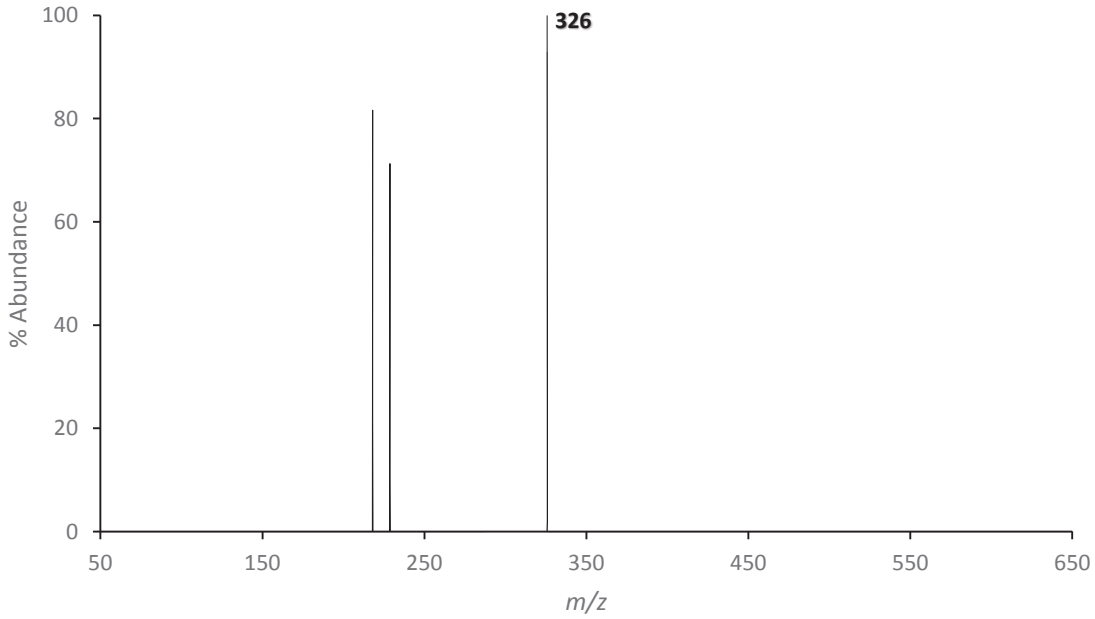

Figure 5.15: The 70eV positive EI mass spectrum obtained by scanning the third quadrupole after the selective reaction of *m/z* 365 ($[Fe(tmtm)(tmtm\text{-}tBu)]^+$) with neutral $Cu(tftm)_2$ to produce the mixed ligand fragment at *m/z* 326 ($[Cu(tmtm\text{-}tBu)(tftm\text{-}t\text{Bu})]^+$).

This observation is consistent with the mechanism displayed in Equation (5.12) which incorporates partial ligand exchange, reductive rearrangement, and *tert*-butyl fragmentation to generate the mixed ligand fragment.

$$[Fe^{II}(tmtm)(tmtm\text{-}t\text{Bu})]^+ + Cu^{II}(tftm)_2 \rightarrow$$

$$[Cu^{I}(tmtm\text{-}t\text{Bu})(tftm\text{-}t\text{Bu})]^+ + Fe^{II}(tmtm)(tftm) + t\text{Bu}^{\bullet} \qquad \text{(Eqn 5.12)}$$

The peak appearing at *m/z* 245 in Figure 5.16 suggests the formation of the singly-ligated product $[Cu(tmtm)]^+$ from the collision-induced reaction of mass-selected $[Fe(tmtm)(tmtm\text{-}t\text{Bu})]^+$ at *m/z* 365 and neutral $Cu(tftm)_2$. Product formation occurs at one mass unit lower than expected. The ion signals observed at *m/z* 365 and *m/z* 239 indicate the detection of the mass-selected parent ion and the fragment $[Fe(tmtm)]^+$.

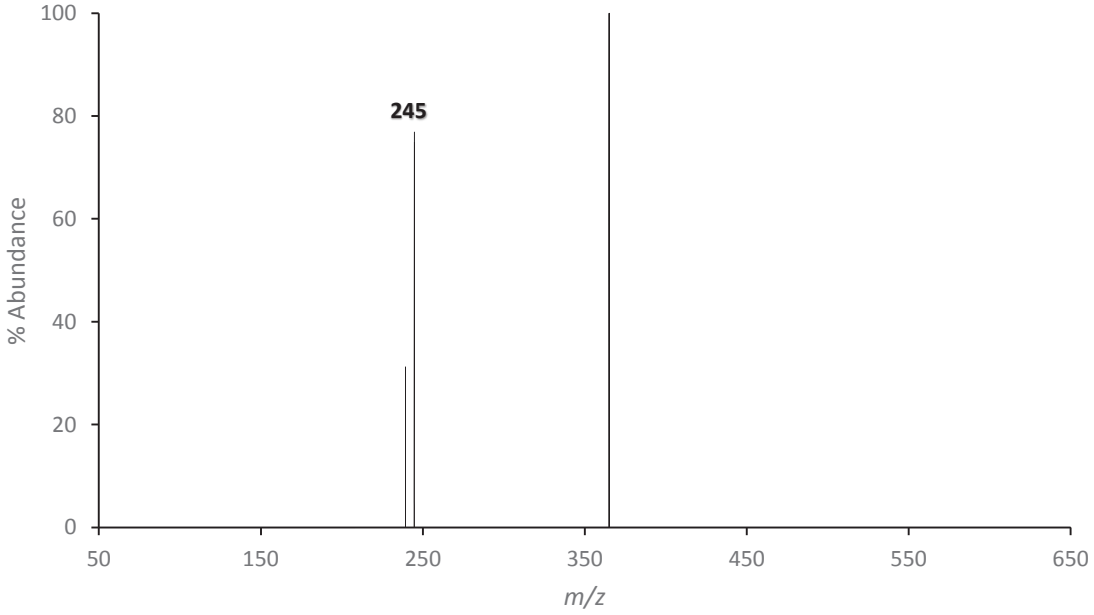

Figure 5.16: The 70eV positive EI mass spectrum obtained by scanning the third quadrupole after the selective reaction of *m/z* 365 ($[Fe(tmtm)(tmtm\text{-}t\text{Bu})]^+$) with neutral $Cu(tftm)_2$ to produce the product at *m/z* 245 ($[Cu(tmtm)]^+$).

Product formation likely results from an exchange process in which the copper complex donates two equivalents of (tftm) to $[Fe(tmtm)(tmtm\text{-}t\text{Bu})]^+$ in exchange for one equivalent of (tmtm) as depicted in Equation (5.13).

$$[Fe^{II}(tmtm)(tmtm\text{-}t\text{Bu})]^+ + Cu^{II}(tftm)_2 \rightarrow$$

$$[Cu^{II}(tmtm)]^+ + Fe^{II}(tmtm\text{-}t\text{Bu})(tftm)_2 \qquad \text{(Eqn 5.13)}$$

To investigate potential gas-phase reactions between $[Fe(tmtm)]^+$ and $Cu(tftm)_2$, the first quadrupole was setup to selectively introduce $[Fe(tmtm)]^+$ at *m/z* 239 to the collision chamber. The first product observed to form from the ensuing reactions corresponds to the peak at *m/z* 640 in Figure 5.17 which can be identified as $[Fe(tftm)_3]^+$. Formation of the product occurs at one mass unit lower than expected. The remaining peaks at *m/z* 181 and *m/z* 239 correspond to an unidentified ion and the parent ion, respectively.

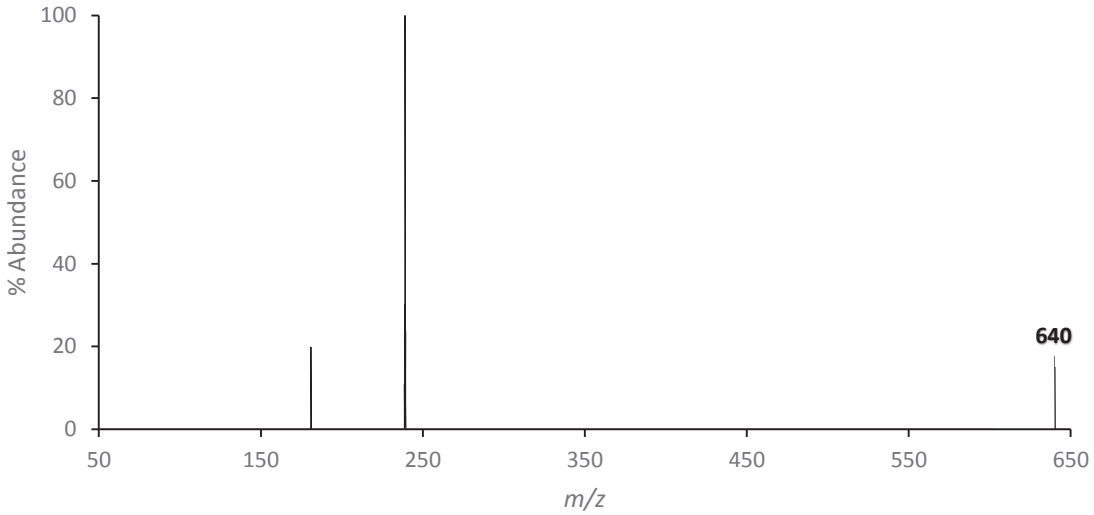

Figure 5.17: The 70eV positive EI mass spectrum obtained by scanning the third quadrupole after the selective reaction of *m/z* 239 ($[Fe(tmtm)]^+$) with neutral $Cu(tftm)_2$ to produce the product at *m/z* 640 ($[Fe(tftm)_3]^+$).

The triply-ligated product would seemingly result from the collision between $[Fe(tmtm)]^+$ and two equivalents of $Cu(tftm)_2$ as shown in Equation (5.14). Such a process entails both complete ligand exchange and donation to successfully generate $[Fe(tftm)_3]^+$.

$$[Fe^{II}(tmtm)]^+ + 2Cu^{II}(tftm)_2 \rightarrow$$

$$[Fe^{III}(tftm)_3]^{+\bullet} + Cu^{I}(tmtm) + Cu^{I}(tftm) \qquad \text{(Eqn 5.14)}$$

The spectrum in Figure 5.18 suggests the formation of the product $[Fe(tftm)_2(tftm\text{-}t\text{Bu})]^+$ at *m/z* 585 from reacting mass-selected $[Fe(tmtm)]^+$ at *m/z* 239 with neutral $Cu(tftm)_2$. Product formation occurs at one mass unit higher than expected.

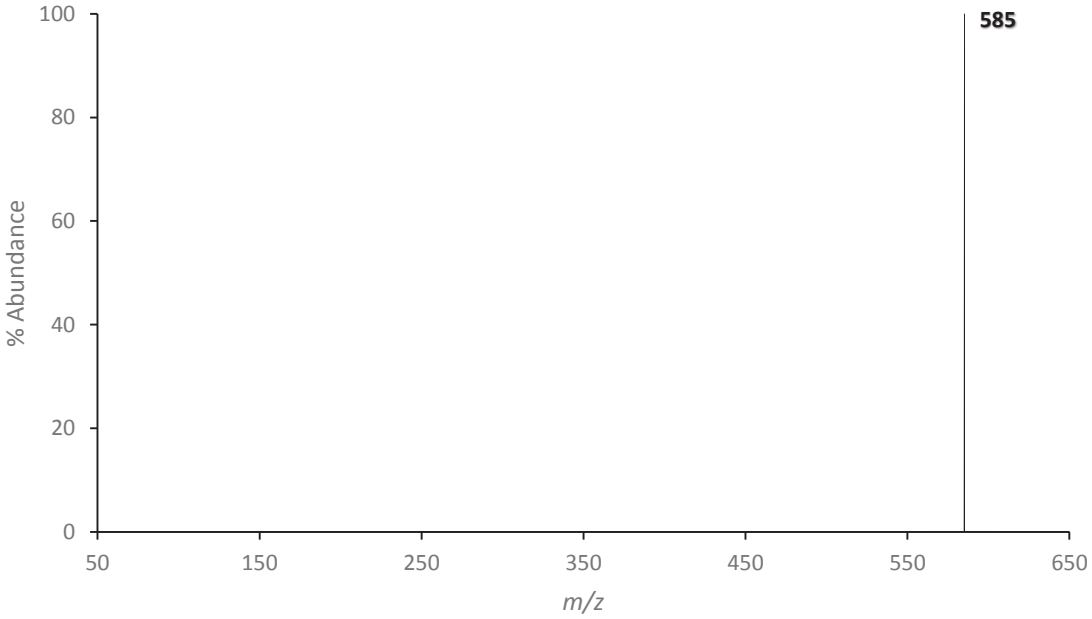

Figure 5.18: The 70eV positive EI mass spectrum obtained by scanning the third quadrupole after the selective reaction of *m/z* 239 ($[Fe(tmtm)]^+$) with neutral $Cu(tftm)_2$ to produce the product at *m/z* 585 ($[Fe(tftm)_2(tftm\text{-}tBu)]^+$).

The generation of the product likely results from complete and partial ligand exchange with two equivalents of $Cu(tftm)_2$ as outlined in Equation (5.15).

$$[Fe^{II}(tmtm)]^+ + 2Cu^{II}(tftm)_2 \rightarrow$$

$$[Fe^{III}(tftm)_2(tftm\text{-}t\text{Bu})]^+ + Cu^{I}(tmtm) + Cu^{I}(tftm) + t\text{Bu}^{\bullet} \qquad \text{(Eqn 5.15)}$$

Following the reaction of mass-selected $[Fe(tmtm)]^+$ at *m/z* 239 with neutral $Cu(tftm)_2$, a peak corresponding to $[Fe(tmtm)(tftm)_2\text{-}t\text{Bu}]^+$ at *m/z* 572 is generated in the spectrum in Figure 5.19.

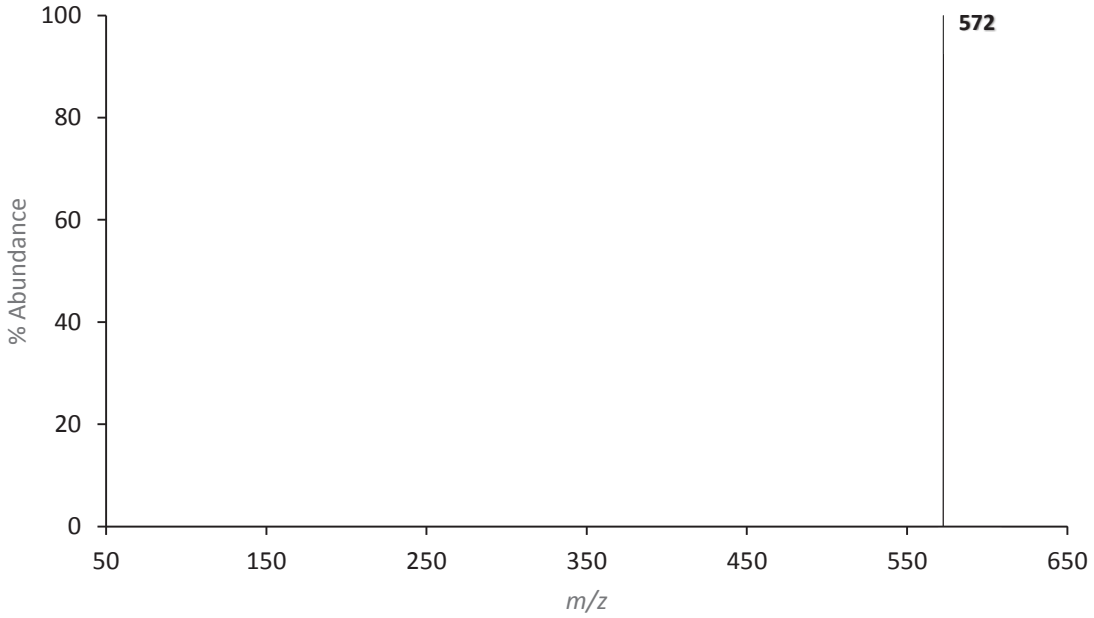

Figure 5.19: The 70eV positive EI mass spectrum obtained by scanning the third quadrupole after the selective reaction of *m/z* 239 ($[Fe(tmtm)]^+$) with neutral $Cu(tftm)_2$ to produce the mixed ligand fragment at *m/z* 572 ($[Fe(tmtm)(tftm)_2\text{-}tBu]^+$).

The mixed ligand fragment may be formed in accordance to Equation (5.16) wherein $Cu(tftm)_2$ donates both ligands to $[Fe(tmtm)]^+$ in a redox process coupled with *tert*-butyl fragmentation.

$$[Fe^{II}(tmtm)]^+ + Cu^{II}(tftm)_2 \rightarrow$$

$$[Fe^{III}(tmtm)(tftm)_2\text{-}t\text{Bu}]^+ + Cu^0 + t\text{Bu}^\bullet \qquad \text{(Eqn 5.16)}$$

Another ligand exchange product generated from the reaction of mass-selected $[Fe(tmtm)]^+$ at *m/z* 239 with neutral $Cu(tftm)_2$ appears to be $[Fe(tftm)_2]^+$ based on the ion signal at *m/z* 445 in Figure 5.20. Product formation occurs at one mass unit lower than expected.

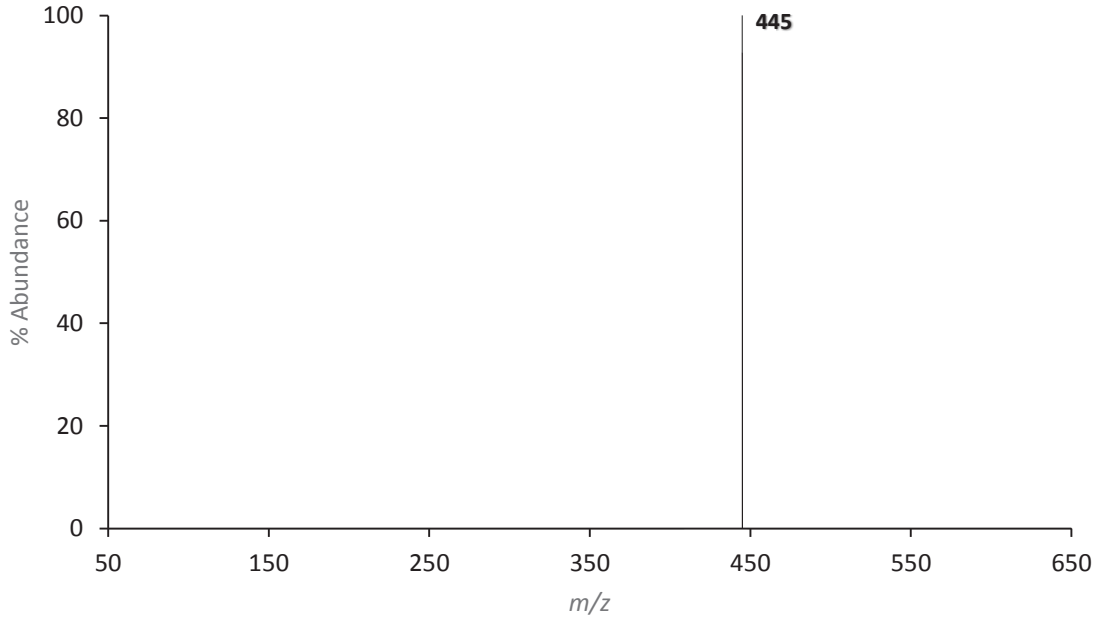

Figure 5.20: The 70eV positive EI mass spectrum obtained by scanning the third quadrupole after the selective reaction of *m/z* 239 ($[Fe(tmtm)]^+$) with neutral $Cu(tftm)_2$ to produce the product at *m/z* 445 ($[Fe(tftm)_2]^+$).

The gas-phase formation of $[Fe(tftm)_2]^+$ is proposed in Equation (5.17) which features a complete ligand exchange process to form the product.

$$[Fe^{II}(tmtm)]^+ + Cu^{II}(tftm)_2 \rightarrow$$

$$[Fe^{III}(tftm)_2]^+ + Cu^{I}(tmtm) \qquad \text{(Eqn 5.17)}$$

The final product to form from the collision-induced reaction of mass-selected $[Fe(tmtm)]^+$ at *m/z* 239 and neutral $Cu(tftm)_2$ corresponds to the mixed ligand fragment $[Cu(tmtm)(tftm)\text{-}t\text{Bu}]^+$ which is consistent with the peak observed at *m/z* 385 in Figure 5.21. The mixed ligand fragment is generated at one mass unit higher than expected.

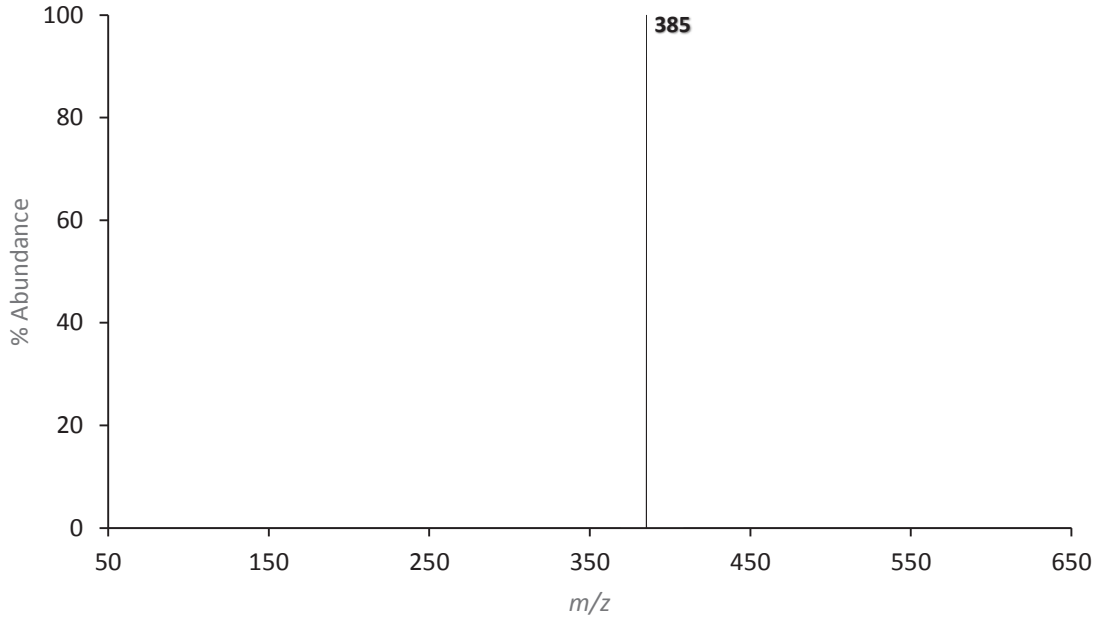

Figure 5.21: The 70eV positive EI mass spectrum obtained by scanning the third quadrupole after the selective reaction of *m/z* 239 ($[Fe(tmtm)]^+$) with neutral $Cu(tftm)_2$ to produce the mixed ligand fragment at *m/z* 385 ($[Cu(tmtm)(tftm)\text{-}tBu]^+$).

The proposed mechanism in Equation (5.18) incorporates partial ligand exchange and *tert*-butyl fragmentation to form the mixed ligand fragment.

$$[Fe^{II}(tmtm)]^+ + Cu^{II}(tftm)_2 \rightarrow$$

$$[Cu^{II}(tmtm)(tftm)\text{-}t\text{Bu}]^+ + Fe^{I}(tftm) + t\text{Bu}^{\bullet} \qquad \text{(Eqn 5.18)}$$

The following series of reactions incorporates neutral $Fe(tmtm)_3$ gas and mass-selected parent ions of $Cu(tftm)_2$. Only two products were shown to form from the collision-induced reactions of mass-selected $[Cu(tftm)_2]^+$ at *m/z* 453 with neutral $Fe(tmtm)_3$. The peak displayed at *m/z* 388 in Figure 5.22 corresponds to the first product $[Fe(tftm)(tftm\text{-}t\text{Bu})]^+$ at one mass unit lower than expected.

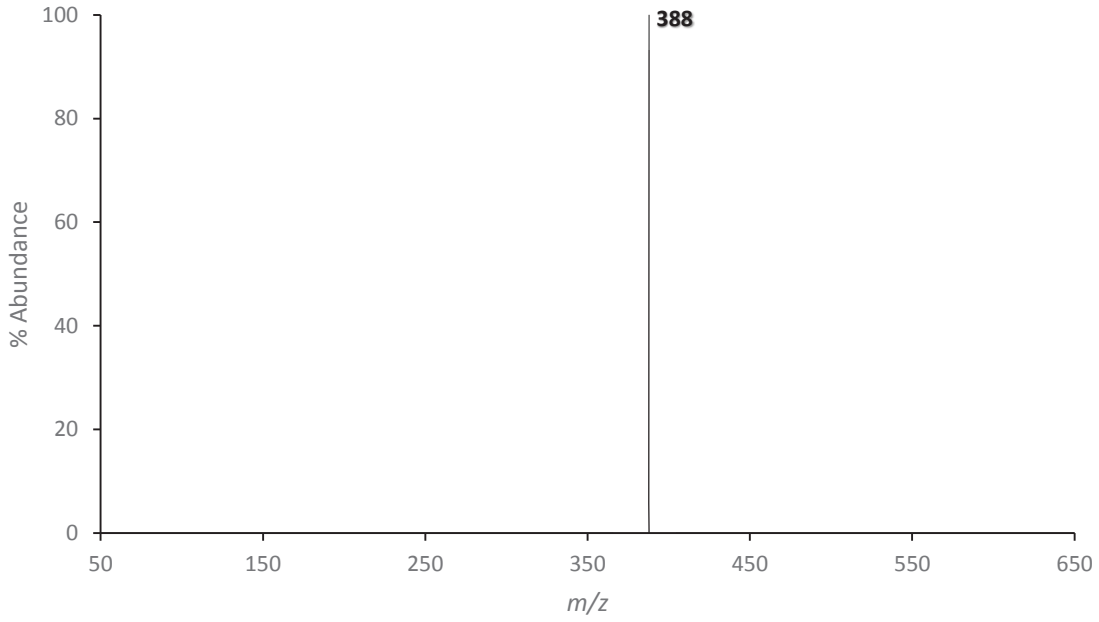

Figure 5.22: The 70eV positive EI mass spectrum obtained by scanning the third quadrupole after the selective reaction of *m/z* 453 ($[Cu(tftm)_2]^+$) with neutral $Fe(tmtm)_3$ to produce the product at *m/z* 388 ($[Fe(tftm)(tftm\text{-}tBu)]^+$).

Expressed in Equation (5.19) is a mechanistic proposal consistent with this observation in which the mass-selected parent ion undergoes complete ligand exchange with neutral $Fe(tmtm)_3$ to produce the product.

$$[Cu^{II}(tftm)_2]^{+\bullet} + Fe^{III}(tmtm)_3 \rightarrow$$

$$[Fe^{II}(tftm)(tftm\text{-}t\text{Bu})]^+ + Cu^{II}(tmtm)_2 + tmtm^{\bullet} + t\text{Bu}^{\bullet} \qquad \text{(Eqn 5.19)}$$

The second product resulting from a reaction between mass-selected $[Cu(tftm)_2]^+$ at *m/z* 453 and neutral $Fe(tmtm)_3$ is shown in Figure 5.23 at *m/z* 384, and specifically corresponds to the formation of the mixed ligand fragment $[Cu(tmtm)(tftm)\text{-}t\text{Bu}]^+$. The remaining ion signals at *m/z* 466 and *m/z* 453 correspond to an unidentifiable species and the mass-selected parent ion, respectively.

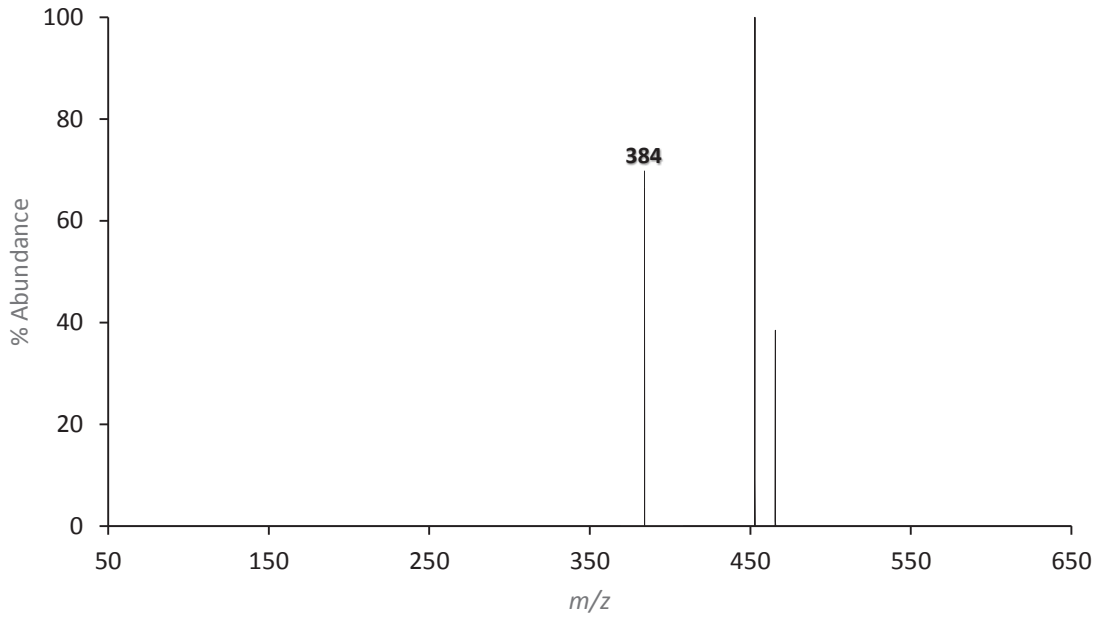

Figure 5.23: The 70eV positive EI mass spectrum obtained by scanning the third quadrupole after the selective reaction of *m/z* 453 ($[Cu(tftm)_2]^+$) with neutral $Fe(tmtm)_3$ to produce the mixed ligand fragment at *m/z* 384 ($[Cu(tmtm)(tftm)\text{-}t\text{Bu}]^+$).

Equation (5.20) provides a mechanistic proposal wherein the mixed ligand fragment is generated through a process of partial ligand exchange and *tert*-butyl fragmentation.

$$[Cu^{II}(tftm)_2]^{+\bullet} + Fe^{III}(tmtm)_3 \rightarrow$$

$$[Cu^{II}(tmtm)(tftm)\text{-}t\text{Bu}]^+ + Fe^{III}(tmtm)_2(tftm) + t\text{Bu}^{\bullet} \qquad \text{(Eqn 5.20)}$$

To investigate the collision-induced reactions between $[Cu(tftm)(tftm\text{-}t\text{Bu})]^+$ and neutral $Fe(tmtm)_3$, the first quadrupole was configured to selectively introduce $[Cu(tftm)(tftm\text{-}t\text{Bu})]^+$ at *m/z* 396 to the collision chamber containing the neutral ferric complex. In examining the resulting scan in Figure 5.24, a single species appears to have been detected at *m/z* 516 which corresponds to $[Fe(tmtm)(tftm)(tftm\text{-}t\text{Bu})\text{-}t\text{Bu}]^+$ at one mass unit higher than expected.

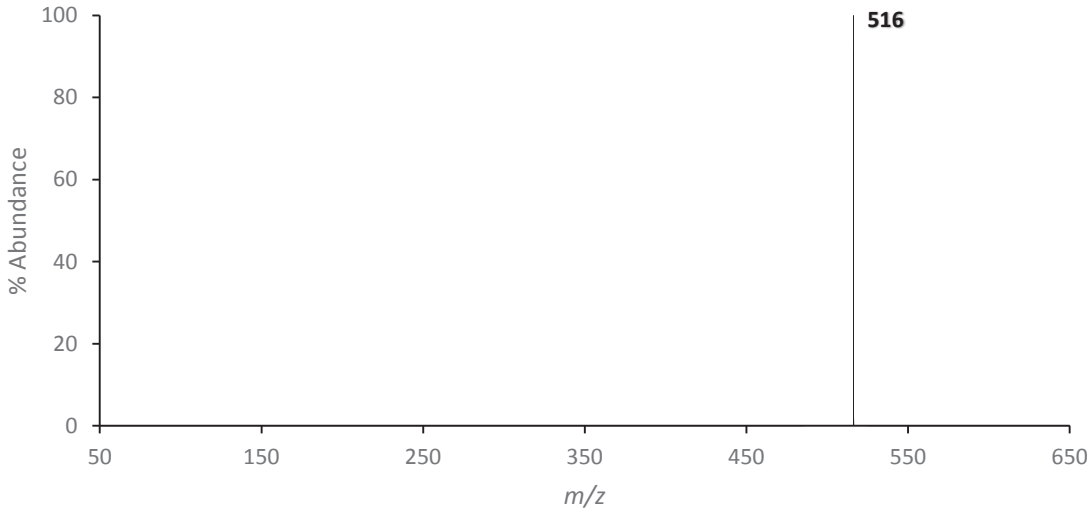

Figure 5.24: The 70eV positive EI mass spectrum obtained by scanning the third quadrupole after the selective reaction of *m/z* 396 ($[Cu(tftm)(tftm\text{-}tBu)]^+$) with neutral $Fe(tmtm)_3$ to produce the mixed ligand fragment at *m/z* 516 ($[Fe(tmtm)(tftm)(tftm\text{-}tBu)\text{-}t\text{Bu}]^+$).

A mechanism consistent with the gas-phase formation of the mixed ligand fragment is proposed in Equation (5.21) which entails a complete ligand exchange process, reductive rearrangement, and *tert*-butyl fragmentation. Successive ligand exchange processes with two equivalents of $[Cu(tftm)(tftm\text{-}t\text{Bu})]^+$ is a less likely alternative considering the low pressure conditions of the mass spectrometer.

$$[Cu^{II}(tftm)(tftm\text{-}t\text{Bu})]^+ + Fe^{III}(tmtm)_3 \rightarrow$$

$$[Fe^{II}(tmtm)(tftm)(tftm\text{-}t\text{Bu})\text{-}t\text{Bu}]^+ + Cu^{II}(tmtm)_2 + t\text{Bu}^{\bullet} \qquad \text{(Eqn 5.21)}$$

An additional product observed for the reaction of mass-selected $[Cu(tftm)(tftm\text{-}t\text{Bu})]^+$ at *m/z* 396 and neutral $Fe(tmtm)_3$ corresponds to the peak at *m/z* 447 in Figure 5.25 which can be identified as $[Fe(tftm)_2]^+$. Product formation occurs at one mass unit higher than expected.

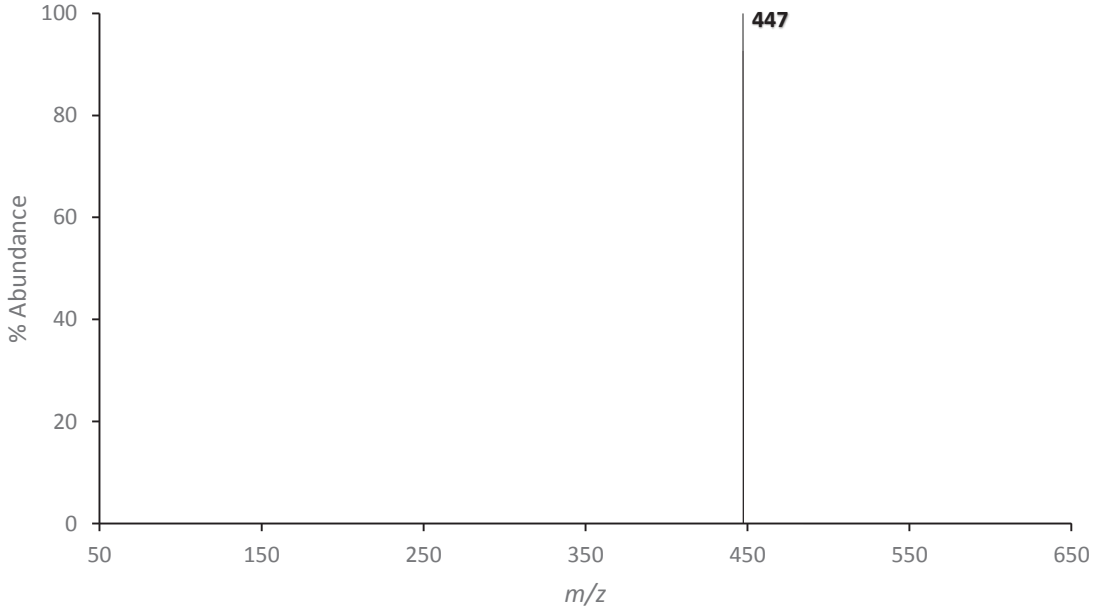

Figure 5.25: The 70eV positive EI mass spectrum obtained by scanning the third quadrupole after the selective reaction of *m/z* 396 ($[Cu(tftm)(tftm\text{-}tBu)]^+$) with neutral $Fe(tmtm)_3$ to produce the product at *m/z* 447 ($[Fe(tftm)_2]^+$).

In the proposed mechanism listed in Equation (5.22), two equivalents of the mass-selected parent ion are required to undergo consecutive rounds of partial ligand exchange with a single equivalent of $Fe(tmtm)_3$ to produce the ligand exchange product.

$$2[Cu^{II}(tftm)(tftm\text{-}t\text{Bu})]^+ + Fe^{III}(tmtm)_3 \rightarrow$$

$$[Fe^{III}(tftm)_2]^+ + [Cu^{II}(tmtm)(tftm\text{-}t\text{Bu})]^+$$

$$+ Cu^{I}(tmtm)(tftm\text{-}t\text{Bu}) + tmtm^{\bullet} \qquad \text{(Eqn 5.22)}$$

The mixed ligand product $[Cu(tmtm)(tftm)]^+$ is shown to form in Figure 5.26 at *m/z* 440 from reacting mass-selected $[Cu(tftm)(tftm\text{-}t\text{Bu})]^+$ at *m/z* 396 with neutral $Fe(tmtm)_3$. Production of the mixed ligand species occurs at one mass unit lower than expected.

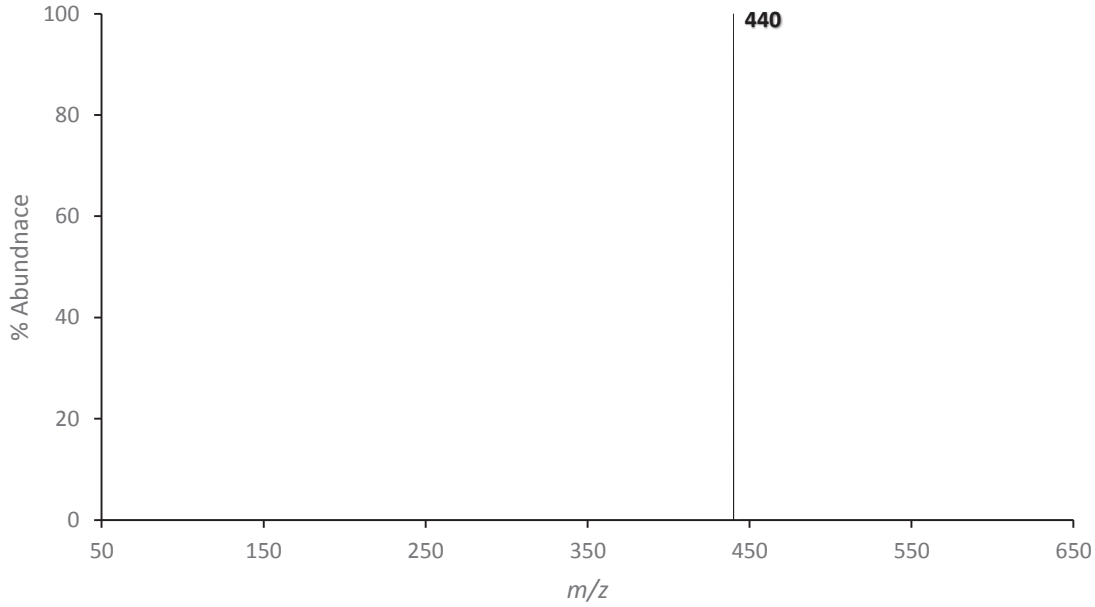

Figure 5.26: The 70eV positive EI mass spectrum obtained by scanning the third quadrupole after the selective reaction of *m/z* 396 ($[Cu(tftm)(tftm\text{-}tBu)]^+$) with neutral $Fe(tmtm)_3$ to produce the mixed ligand product at *m/z* 440 ($[Cu(tmtm)(tftm)]^+$).

Product formation likely results from a process of partial ligand exchange between the mass-selected ion and neutral $Fe(tmtm)_3$ as outlined in Equation (5.23).

$$[Cu^{II}(tftm)(tftm\text{-}t\text{Bu})]^+ + Fe^{III}(tmtm)_3 \rightarrow$$

$$[Cu^{II}(tmtm)(tftm)]^{+\bullet} + Fe^{II}(tmtm)_2(tftm\text{-}t\text{Bu}) \qquad \text{(Eqn 5.23)}$$

The ion signal observed below at *m/z* 430 in Figure 5.27 results from a reaction between mass-selected $[Cu(tftm)(tftm\text{-}t\text{Bu})]^+$ at *m/z* 396 with neutral $Fe(tmtm)_3$, and indicates the formation of the ligand exchange product $[Cu(tmtm)_2]^+$ at *m/z* 430. Product formation occurs at one mass unit higher than expected.

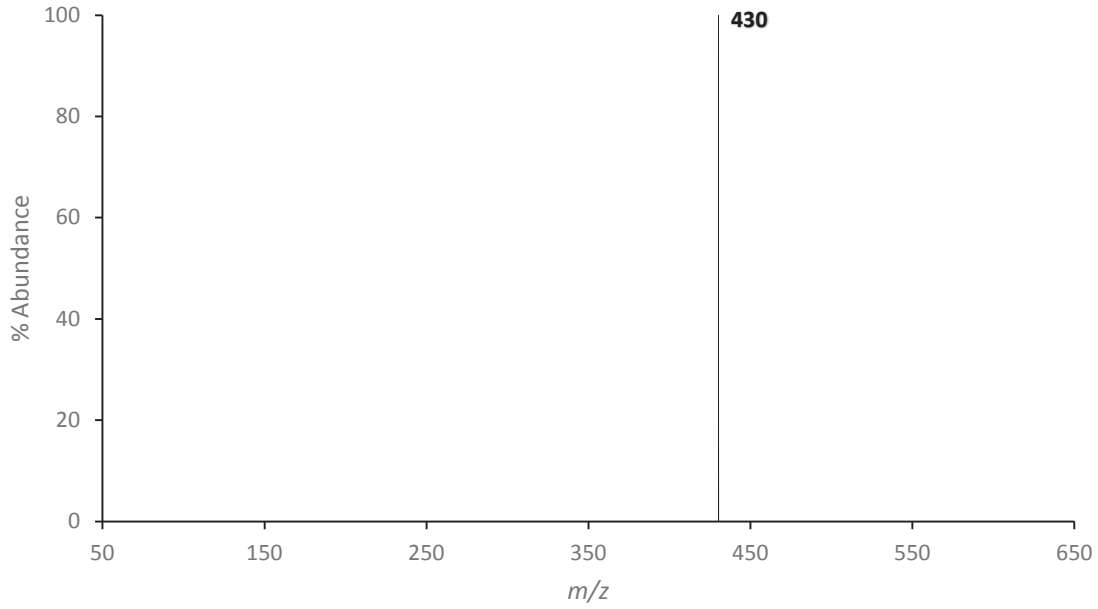

Figure 5.27: The 70eV positive EI mass spectrum obtained by scanning the third quadrupole after the selective reaction of *m/z* 396 ($[Cu(tftm)(tftm\text{-}tBu)]^+$) with neutral $Fe(tmtm)_3$ to produce the product at *m/z* 430 ($[Cu(tmtm)_2]^+$).

Generation of the cupric product is proposed to occur through a process of complete ligand exchange as expressed in Equation (5.24).

$$[Cu^{II}(tftm)(tftm\text{-}t\text{Bu})]^+ + Fe^{III}(tmtm)_3 \rightarrow$$

$$[Cu^{II}(tmtm)_2]^{+\bullet} + Fe^{II}(tmtm)(tftm)(tftm\text{-}t\text{Bu}) \qquad \text{(Eqn 5.24)}$$

Another product observed from the reaction between the mass-selected $[Cu(tftm)(tftm\text{-}t\text{Bu})]^+$ at *m/z* 396 with neutral $Fe(tmtm)_3$ includes the product $[Fe(tftm)(tftm\text{-}t\text{Bu})]^+$ as indicated by the peak at *m/z* 388 in Figure 5.28. Formation of the product occurs at one mass unit lower than expected.

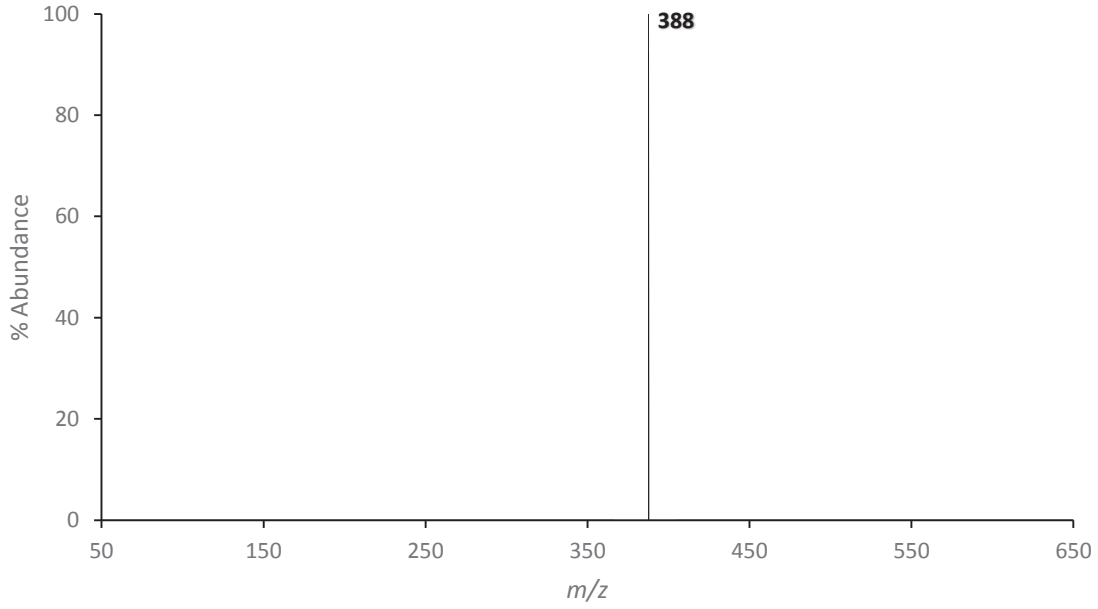

Figure 5.28: The 70eV positive EI mass spectrum obtained by scanning the third quadrupole after the selective reaction of *m/z* 396 ($[Cu(tftm)(tftm\text{-}tBu)]^+$) with neutral $Fe(tmtm)_3$ to produce the product at *m/z* 388 ($[Fe(tftm)(tftm\text{-}tBu)]^+$).

Given this finding, it was possible to propose the following mechanism in Equation (5.25) which features complete ligand exchange to form the ferrous product.

$$[Cu^{II}(tftm)(tftm\text{-}t\text{Bu})]^+ + Fe^{III}(tmtm)_3 \rightarrow$$

$$[Fe^{II}(tftm)(tftm\text{-}t\text{Bu})]^+ + Cu^{II}(tmtm)_2 + tmtm^{\bullet} \qquad \text{(Eqn 5.25)}$$

The spectrum presented in Figure 5.29 contains a peak at *m/z* 384, thus suggesting the formation of $[Cu(tmtm)(tftm\text{-}t\text{Bu})]^+$ from the reaction between neutral $Fe(tmtm)_3$ and mass-selected $[Cu(tftm)(tftm\text{-}t\text{Bu})]^+$ at *m/z* 396.

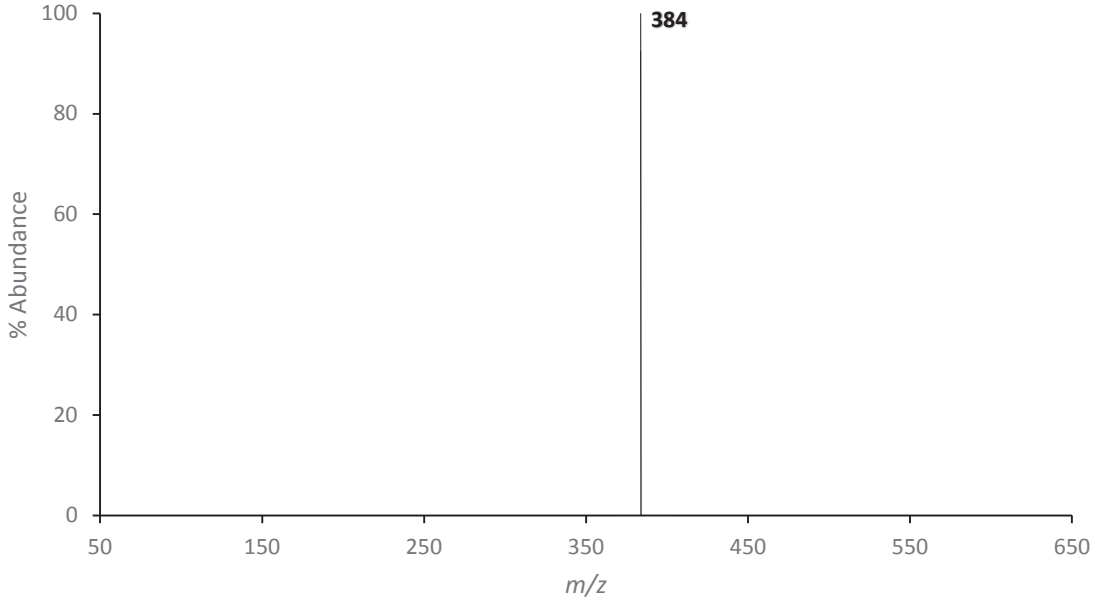

Figure 5.29: The 70eV positive EI mass spectrum obtained by scanning the third quadrupole after the selective reaction of *m/z* 396 ($[Cu(tftm)(tftm\text{-}tBu)]^+$) with neutral $Fe(tmtm)_3$ to produce the mixed ligand product at *m/z* 384 ($[Cu(tmtm)(tftm\text{-}tBu)]^+$).

The reaction pathway likely involves partial ligand exchange to produce the mixed ligand fragment, and thus is consistent with the mechanism proposed in Equation (5.26).

$$[Cu^{II}(tftm)(tftm\text{-}t\text{Bu})]^+ + Fe^{III}(tmtm)_3 \rightarrow$$

$$[Cu^{II}(tmtm)(tftm\text{-}t\text{Bu})]^+ + Fe^{III}(tmtm)_2(tftm) \qquad \text{(Eqn 5.26)}$$

Shown in Figure 5.30 are four peaks resulting from the collision-induced reaction of mass-selected $[Cu(tftm)(tftm\text{-}t\text{Bu})]^+$ at *m/z* 396 with neutral $Fe(tmtm)_3$. The peak at *m/z* 396 corresponds to the mass-selected parent ion $[Cu(tftm)(tftm\text{-}t\text{Bu})]^+$ while the peak at *m/z* 371 suggests the generation of the cupric product $[Cu(tmtm)(tmtm\text{-}t\text{Bu})]^+$. The species at *m/z* 290 does not correspond to any product of interest. Lastly, the ion signal observed at *m/z* 199 corresponds to the ferrous species $[Fe(tftm\text{-}CF_2)]^+$ at two mass units lower than expected.

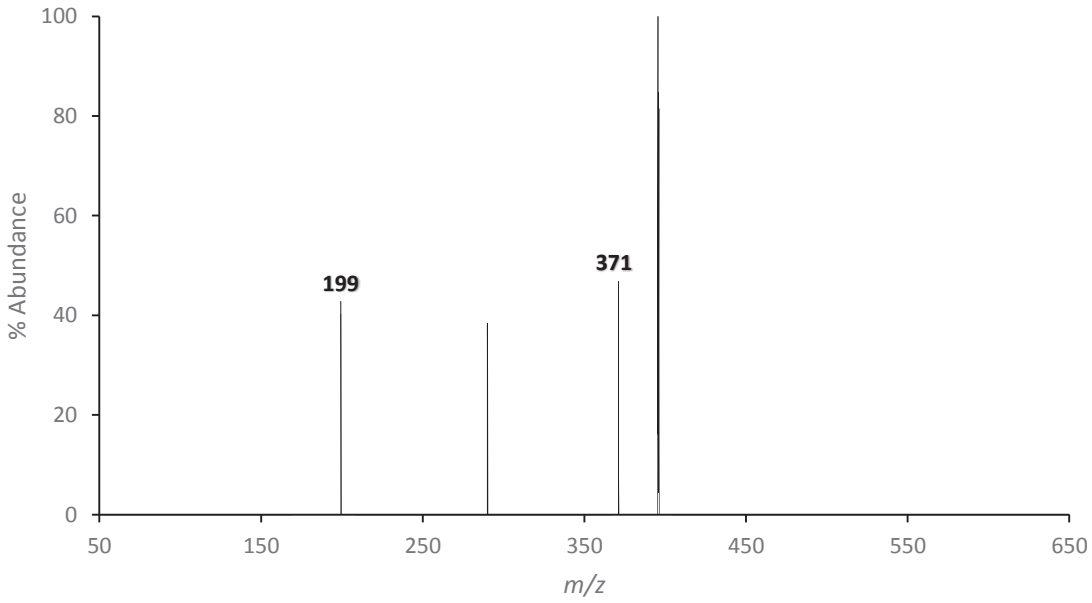

Figure 5.30: The 70eV positive EI mass spectrum obtained by scanning the third quadrupole after the selective reaction of *m/z* 396 ($[Cu(tftm)(tftm\text{-}tBu)]^+$) with neutral $Fe(tmtm)_3$ to produce the product at *m/z* 371 and *m/z* 199 ($[Cu(tmtm)(tmtm\text{-}tBu)]^+$ and $[Fe(tftm\text{-}CF_2)]^+$).

The mechanistic proposal accounting for the formation of the cupric product is expressed in Equation (5.27) which incorporates partial ligand exchange and *tert*-butyl fragmentation. Formation of the ferrous species would likely occur via ligand exchange and fluorine migration as shown in Equation (5.28).

$$[Cu^{II}(tftm)(tftm\text{-}t\text{Bu})]^{+} + Fe^{III}(tmtm)_3 \rightarrow$$

$$[Cu^{II}(tmtm)(tmtm\text{-}t\text{Bu})]^{+} + Fe^{II}(tmtm)(tftm)(tftm\text{-}t\text{Bu}) + t\text{Bu}^{\bullet} \qquad \text{(Eqn 5.27)}$$

$$[Cu^{II}(tftm)(tftm\text{-}t\text{Bu})]^{+} + Fe^{III}(tmtm)_3 \rightarrow$$

$$[Fe^{II}(tftm\text{-}CF_2)]^{+} + Cu^{I}(tmtm)(tftm\text{-}t\text{Bu}) + 2tmtm^{\bullet} + CF_2 \qquad \text{(Eqn 5.28)}$$

To investigate potential gas-phase reactions between $[Cu(tftm\text{-}tBu)_2]^+$ and $Fe(tmtm)_3$, the first quadrupole was setup to selectively introduce $[Cu(tftm\text{-}tBu)_2]^+$ at *m/z* 339 to the collision chamber. Shown in Figure 5.31 are three resulting ion signals from the ensuing collisions. The peak at *m/z* 514 is indicative of $[Fe(tmtm)(tftm\text{-}tBu)_2]^+$ while the peak at *m/z* 339 is representative of the mass-selected parent ion. The third peak at *m/z* 233 does not correspond to any product of interest.

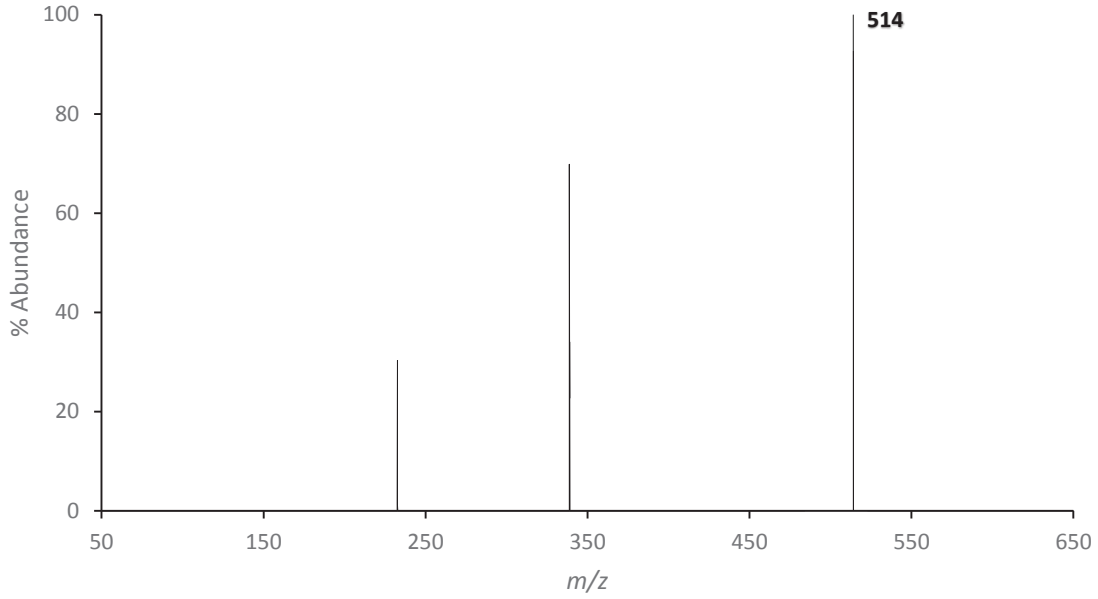

Figure 5.31: The 70eV positive EI mass spectrum obtained by scanning the third quadrupole after the selective reaction of *m/z* 339 ($[Cu(tftm\text{-}tBu)_2]^+$) with neutral $Fe(tmtm)_3$ to mixed ligand fragment at *m/z* 514 ($[Fe(tmtm)(tftm\text{-}tBu)_2]^+$).

Equation (5.29) provides a mechanistic interpretation accounting for the production of the mixed ligand fragment wherein the iron complex acquires the β-keto ester fragment in a ligand exchange process.

$$[Cu^{I}(tftm\text{-}tBu)_2]^+ + Fe^{III}(tmtm)_3 \rightarrow$$

$$[Fe^{II}(tmtm)(tftm\text{-}tBu)_2]^+ + Cu^{II}(tmtm)_2 \qquad \text{(Eqn 5.29)}$$

Another product observed from the reaction between the mass-selected $[Cu(tftm\text{-}tBu)_2]^+$ at *m/z* 339 and neutral $Fe(tmtm)_3$ includes the mixed ligand fragment $[Fe(tmtm)(tftm\text{-}tBu)]^+$ as indicated by the peak at *m/z* 376 in Figure 5.32. The mixed ligand fragment is generated at one mass unit lower than expected.

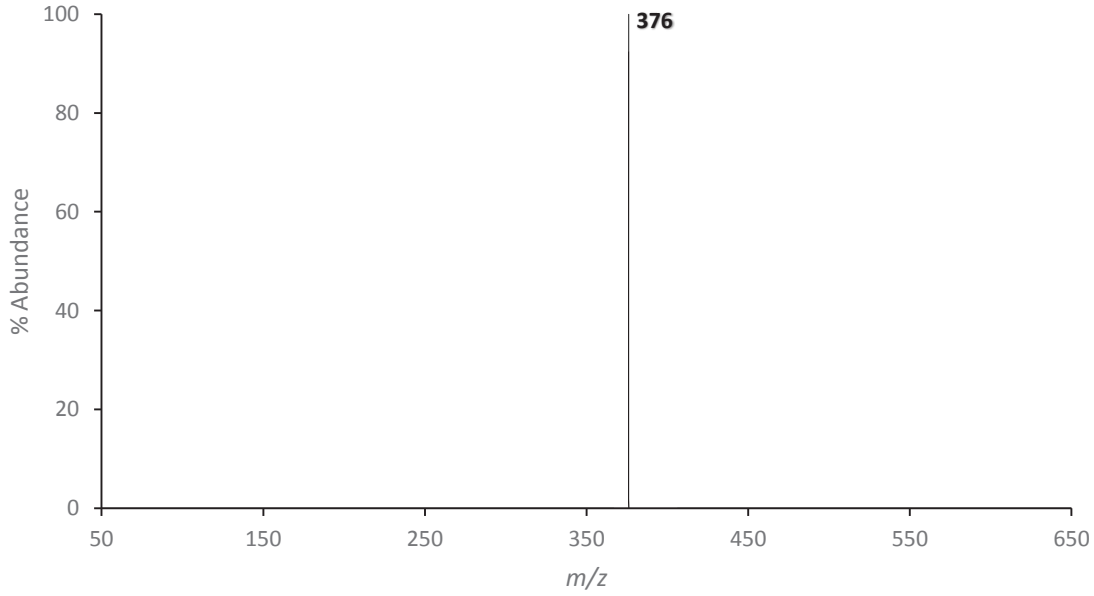

Figure 5.32: The 70eV positive EI mass spectrum obtained by scanning the third quadrupole after the selective reaction of *m/z* 339 ($[Cu(tftm\text{-}tBu)_2]^+$) with neutral $Fe(tmtm)_3$ to produce the mixed ligand fragment at *m/z* 376 ($[Fe(tmtm)(tftm\text{-}tBu)]^+$).

The cation and neutral species undergo partial ligand exchange following the cleavage of the β-keto ester fragment as shown in Equation (5.30) to generate the mixed ligand fragment.

$$[Cu^{I}(tftm\text{-}tBu)_2]^+ + Fe^{III}(tmtm)_3 \rightarrow$$

$$[Fe^{II}(tmtm)(tftm\text{-}tBu)]^+ + Cu^{I}(tmtm)(tftm\text{-}tBu) + tmtm^{\bullet} \qquad \text{(Eqn 5.30)}$$

In continuing the investigation on the collision-induced reactions between cationic copper fragments and neutral $Fe(tmtm)_3$, the first quadrupole was configured to allow $[Cu(H)(tftm)]^+$ at *m/z* 259 to enter the collision cell for reaction. One resulting peak presented in Figure 5.33 at *m/z* 640 corresponds to the formation of the complete ligand exchange product $[Fe(tftm)_3]^+$, but is one mass unit lower than the expected value. The ion signal observed at *m/z* 171 does not correspond to a product of interest and could not be identified.

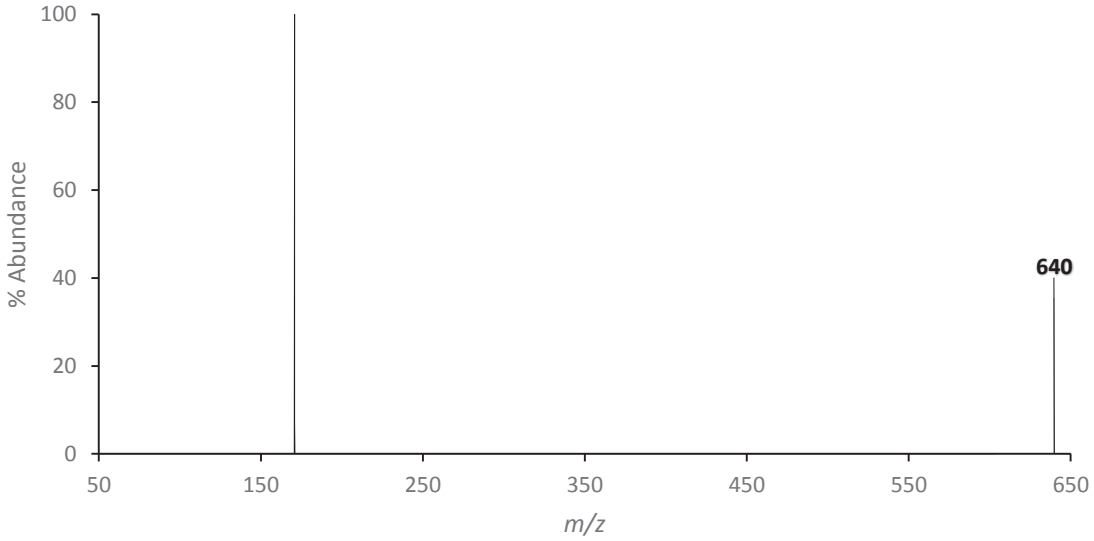

Figure 5.33: The 70eV positive EI mass spectrum obtained by scanning the third quadrupole after the selective reaction of *m/z* 259 ($[Cu(H)(tftm)]^+$) with neutral $Fe(tmtm)_3$ to produce the product at *m/z* 640 ($[Fe(tftm)_3]^+$).

Presented in Equation (5.31) is a mechanistic proposal accounting for the gas-phase formation of $[Fe(tftm)_3]^+$. The formation of the triply-ligated product from $[Cu(H)(tftm)]^+$ requires three equivalents of the mass-selected ion to react with a single equivalent of the neutral ferric species.

$$3[Cu^{II}(H)(tftm)]^{+\bullet} + Fe^{III}(tmtm)_3 \rightarrow$$

$$[Fe^{III}(tftm)_3]^{+\bullet} + 2[Cu^{II}(H)(tmtm)]^{+\bullet} + Cu^{II}(H)(tmtm) \qquad \text{(Eqn 5.31)}$$

Displayed in Figure 5.34 is a peak at *m/z* 572 which is indicative of the generation of $[Fe(tmtm)(tftm)_2\text{-}tBu]^+$ from the reaction between mass-selected $[Cu(H)(tftm)]^+$ at *m/z* 259 and neutral $Fe(tmtm)_3$.

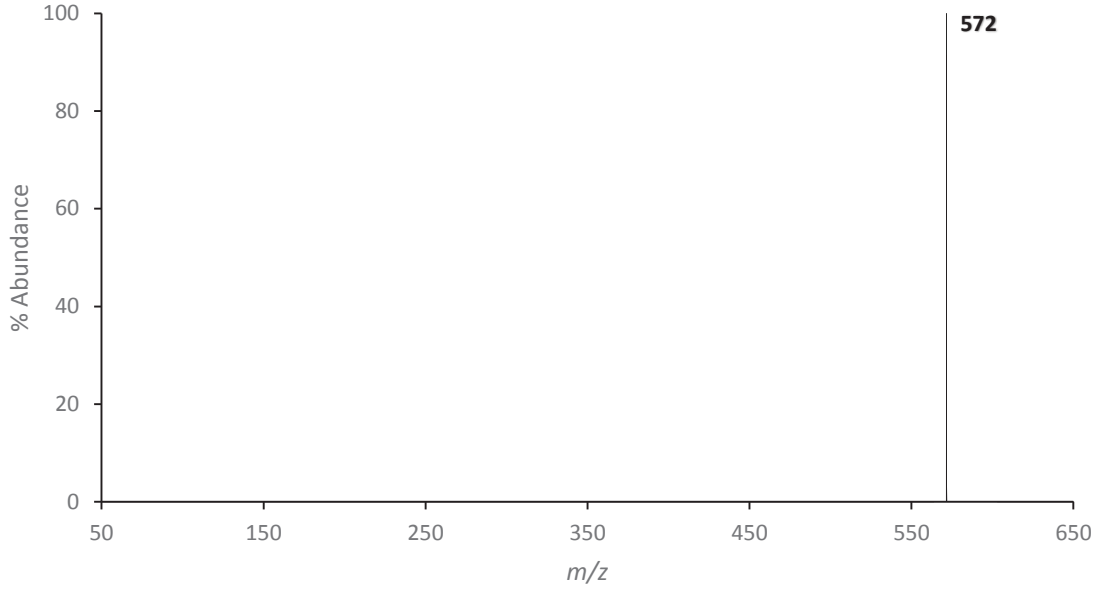

Figure 5.34: The 70eV positive EI mass spectrum obtained by scanning the third quadrupole after the selective reaction of *m/z* 259 ($[Cu(H)(tftm)]^+$) with neutral $Fe(tmtm)_3$ to produce the mixed ligand fragment at *m/z* 572 ($[Fe(tmtm)(tftm)_2\text{-}tBu]^+$).

A mechanistic interpretation of this outcome is given in Equation (5.32) wherein two equivalents of $[Cu(H)(tftm)]^+$ are required to produce the ferric product from one equivalent of $Fe(tmtm)_3$.

$$2[Cu^{II}(H)(tftm)]^{+\bullet} + Fe^{III}(tmtm)_3 \rightarrow$$

$$[Fe^{III}(tmtm)(tftm)_2\text{-}tBu]^+ + [Cu^{II}(H)(tmtm)]^{+\bullet}$$

$$+ Cu^{II}(H)(tmtm) + tBu^{\bullet} \qquad \text{(Eqn 5.32)}$$

Three peaks are generated in Figure 5.35 from the collision-induced reaction of mass-selected $[Cu(H)(tftm)]^+$ at *m/z* 259 and neutral $Fe(tmtm)_3$. The first peak shown at *m/z* 527 corresponds to the ligand exchange product $[Fe(tftm)(tftm\text{-}t\text{Bu})_2]^+$ while the second and third peaks at *m/z* 447 and *m/z* 441 can be identified as $[Fe(H)(tftm)_2]^+$ and the mixed ligand product $[Cu(tmtm)(tftm)]^+$, respectively.

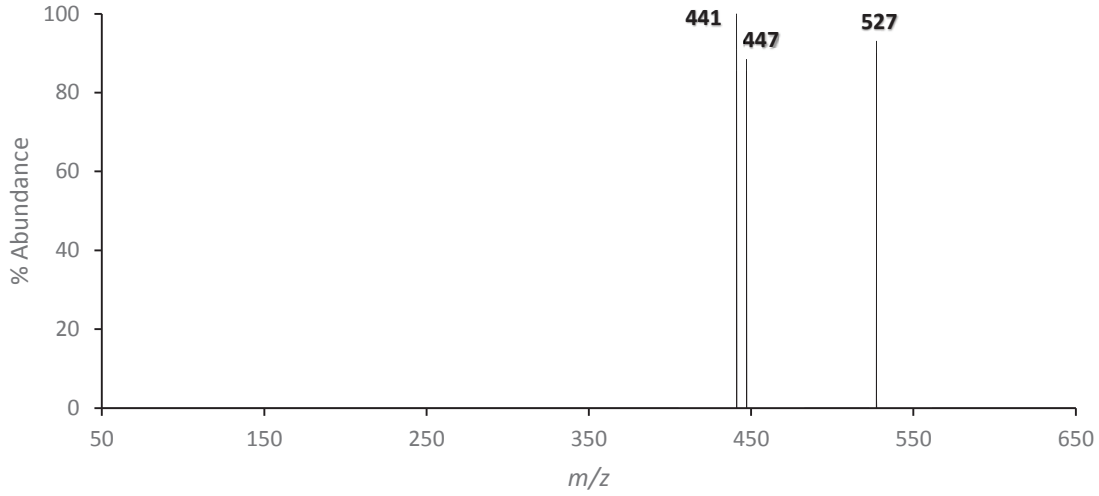

Figure 5.35: The 70eV positive EI mass spectrum obtained by scanning the third quadrupole after the selective reaction of *m/z* 259 ($[Cu(H)(tftm)]^+$) with neutral $Fe(tmtm)_3$ to produce the products at *m/z* 572, *m/z* 447, and *m/z* 441 ($[Fe(tmtm)(tftm)_2\text{-}tBu]^+$, $[Fe(H)(tftm)_2]^+$, and $[Cu(tmtm)(tftm)]^+$).

Three separate equations are outlined below to account for the gas-phase formation of the observed products. In Equation (5.33), three equivalents of $[Cu(H)(tftm)]^+$ react with one equivalent of $Fe(tmtm)_3$ to produce $[Fe(tftm)(tftm\text{-}t\text{Bu})_2]^+$ following reductive rearrangement and *tert*-butyl fragmentation. Equations (5.34) and (5.35) entail the ligand exchange between neutral $Fe(tmtm)_3$ and two equivalents of $[Cu(H)(tftm)]^+$ to generate $[Fe(H)(tftm)_2]^+$. Finally, the mechanistic proposal presented in Equation (5.36) expresses a partial ligand exchange process between the mass-selected

parent ion and the neutral ferric species to produce the mixed ligand product $[Cu(tmtm)(tftm)]^{+}$.

$$3[Cu^{II}(H)(tftm)]^{+\bullet} + Fe^{III}(tmtm)_3 \rightarrow$$

$$[Fe^{II}(tftm)(tftm\text{-}t\text{Bu})_2]^{+} + 2[Cu^{II}(H)(tmtm)]^{+\bullet} + Cu^{II}(H)(tmtm)$$

$$+ 2t\text{Bu}^{\bullet} \qquad \text{(Eqn 5.33)}$$

$$2[Cu^{II}(H)(tftm)]^{+\bullet} + Fe^{III}(tmtm)_3 \rightarrow$$

$$[Fe^{III}(H)(tftm)_2]^{+} + [Cu^{II}(H)(tmtm)]^{+\bullet} + Cu^{II}(tmtm)_2 \qquad \text{(Eqn 5.34)}$$

$$2[Cu^{II}(H)(tftm)]^{+\bullet} + Fe^{III}(tmtm)_3 \rightarrow$$

$$[Fe^{III}(H)(tftm)_2]^{+} + [Cu^{II}(tmtm)_2]^{+\bullet} + Cu^{II}(H)(tmtm) \qquad \text{(Eqn 5.35)}$$

$$[Cu^{II}(H)(tftm)]^{+\bullet} + Fe^{III}(tmtm)_3 \rightarrow$$

$$[Cu^{II}(tmtm)(tftm)]^{+\bullet} + Fe^{III}(H)(tmtm)_2 \qquad \text{(Eqn 5.36)}$$

Featured in Figure 5.36 is a peak at *m/z* 389 which is indicative of the formation of $[Fe(tftm)(tftm\text{-}t\text{Bu})]^+$ from the collision-induced reaction between mass-selected $[Cu(H)(tftm)]^+$ at *m/z* 259 and neutral $Fe(tmtm)_3$.

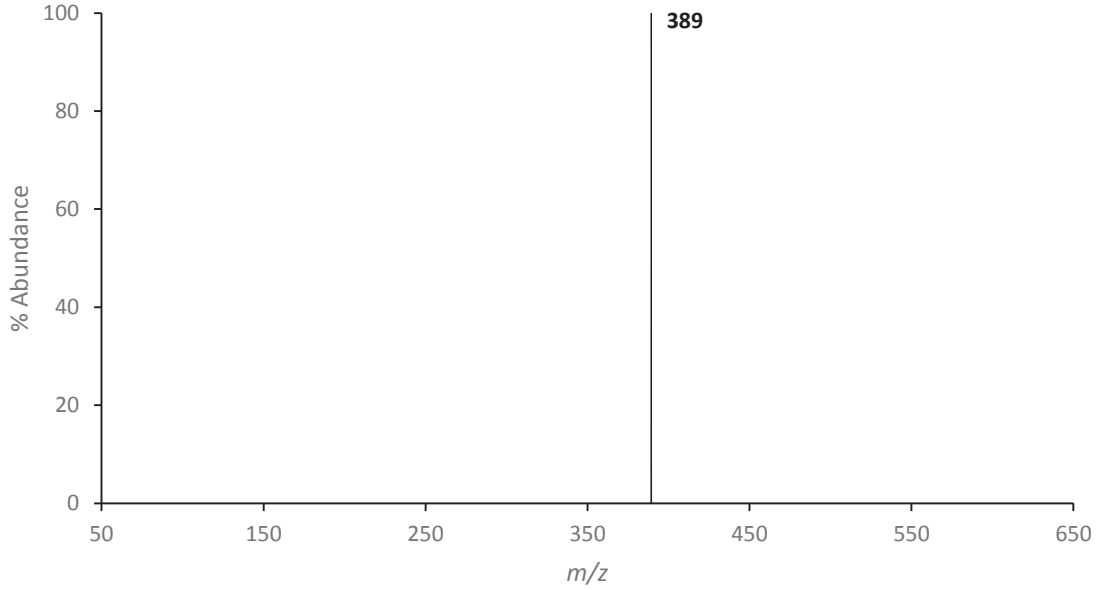

Figure 5.36: The 70eV positive EI mass spectrum obtained by scanning the third quadrupole after the selective reaction of *m/z* 259 ($[Cu(H)(tftm)]^+$) with neutral $Fe(tmtm)_3$ to produce the product at *m/z* 389 ($[Fe(tftm)(tftm\text{-}tBu)^+]$).

As shown in Equation (5.37), two equivalents of the mass-selected ion undergo successive rounds of partial ligand exchange with a single equivalent of $Fe(tmtm)_3$ to generate $[Fe(tftm)(tftm\text{-}t\text{Bu})]^+$.

$$2[Cu^{II}(H)(tftm)]^{+\bullet} + Fe^{III}(tmtm)_3 \rightarrow$$

$$[Fe^{II}(tftm)(tftm\text{-}t\text{Bu})]^+ + [Cu^{II}(H)(tmtm)]^{+\bullet} + Cu^{II}(H)(tmtm)$$

$$+ tmtm^{\bullet} + t\text{Bu}^{\bullet} \qquad \text{(Eqn 5.37)}$$

The appearance of a peak at *m/z* 327 in Figure 5.37 suggests the formation of the cuprous mixed ligand fragment $[Cu(tmtm\text{-}t\text{Bu})(tftm\text{-}t\text{Bu})]^+$ as a result of reacting mass-selected $[Cu(H)(tftm)]^+$ at *m/z* 259 with neutral $Fe(tmtm)_3$. An additional peak is observed at *m/z* 259 which corresponds to the mass-selected parent ion.

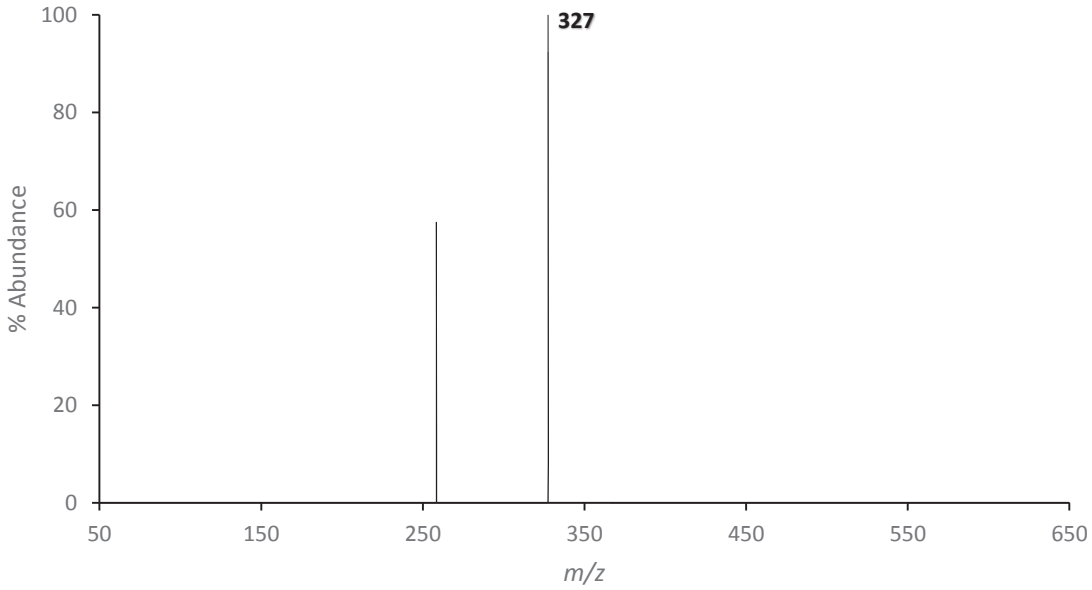

Figure 5.37: The 70eV positive EI mass spectrum obtained by scanning the third quadrupole after the selective reaction of *m/z* 259 ($[Cu(H)(tftm)]^+$) with neutral $Fe(tmtm)_3$ to produce the mixed ligand fragment at *m/z* 327 ($[Cu(tmtm\text{-}tBu)(tftm\text{-}tBu)]^+$).

Mechanistically, the generation of $[Cu(tmtm\text{-}t\text{Bu})(tftm\text{-}t\text{Bu})]^+$ is proposed to occur according to Equation (5.38) which includes partial ligand exchange, reductive rearrangement, and *tert*-butyl fragmentation.

$$[Cu^{II}(H)(tftm)]^{+\bullet} + Fe^{III}(tmtm)_3 \rightarrow$$

$$[Cu^{I}(tmtm\text{-}t\text{Bu})(tftm\text{-}t\text{Bu})]^+ + Fe^{III}(H)(tmtm)_2 + 2t\text{Bu}^{\bullet} \qquad \text{(Eqn 5.38)}$$

The discussion on the selective reactions of $Fe(tmtm)_3$ and $Cu(tftm)_2$ closes with the examination of the spectrum shown in Figure 5.38. The final product observed from reacting mass-selected $[Cu(H)(tftm)]^+$ at *m/z* 259 and neutral $Fe(tmtm)_3$ corresponds to the ion signal at *m/z* 189, which suggests the formation of the cuprous product $[Cu(tmtm\text{-}t\text{Bu})]^+$. The ion signal observed at *m/z* 259 corresponds to the mass-selected parent ion while the peak at *m/z* 612 does not correspond to any species of interest.

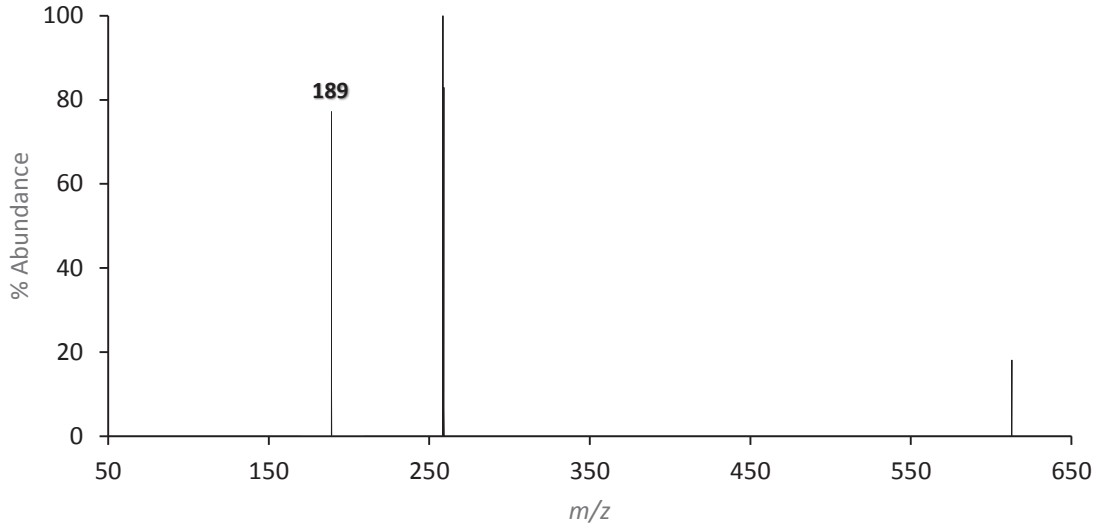

Figure 5.38: The 70eV positive EI mass spectrum obtained by scanning the third quadrupole after the selective reaction of *m/z* 259 ($[Cu(H)(tftm)]^+$) with neutral $Fe(tmtm)_3$ to produce the product at *m/z* 189 ($[Cu(tftm\text{-}t\text{Bu})]^+$).

The proposed mechanisms in Equations (5.39) and (5.40) incorporate a combination of ligand exchange and *tert*-butyl fragmentation to yield $[Cu(tftm\text{-}t\text{Bu})]^+$.

$$[Cu^{II}(H)(tftm)]^{+\bullet} + Fe^{III}(tmtm)_3 \rightarrow$$

$$[Cu^{I}(tmtm\text{-}t\text{Bu})]^+ + Fe^{III}(H)(tmtm)_2 + (tftm^{\bullet}) + t\text{Bu}^{\bullet} \qquad \text{(Eqn 5.39)}$$

$$[Cu^{II}(H)(tftm)]^{+\bullet} + Fe^{III}(tmtm)_3 \rightarrow$$

$$[Cu^{I}(tmtm\text{-}t\text{Bu})]^+ + Fe^{III}(H)(tmtm)(tftm) + (tmtm^{\bullet}) + t\text{Bu}^{\bullet} \qquad \text{(Eqn 5.40)}$$

In total, 38 ligand exchange products were generated from the selective reactions of $Fe(tmtm)_3$ and $Cu(tftm)_2$. All products shown to form are consistent with those formed during co-sublimation. A total of seven products were produced from the collision-induced reactions of $[Fe(tmtm)_2]^+$ at *m/z* 422 with neutral $Cu(tftm)_2$. Mass-selection of $[Fe(tmtm)(tmtm\text{-}t\text{Bu})]^+$ at *m/z* 365 resulted in the formation of six products upon exposure to neutral $Cu(tftm)_2$ while the fragment $[Fe(tmtm)]^+$ at *m/z* 239 generated five products. Similar to Chapter 4, the mass-selection of $[Fe(tmtm)_2]^+$ was shown to be the most conducive towards product generation, but only by a marginal amount. Nevertheless, the results of the collision-induced reactions of cationic $Fe(tmtm)_3$ and neutral $Cu(tftm)_2$ reflect those obtained from the relative ratio analysis.

A weaker correlation is determined when comparing the results of the relative ratio analysis and collision-induced reactions of $Cu(tftm)_2$ parent ions. The mass-selection of $[Cu(tftm)(tftm\text{-}t\text{Bu})]^+$ at *m/z* 396 and $[Cu(tftm)(H)]^+$ at *m/z* 259 each resulted in the formation of eight products following reaction with neutral $Fe(tmtm)_3$. Conversely, only two products were shown to form from the selective reactions of both $[Cu(tftm)_2]^+$ at *m/z* 453 and $[Cu(tftm\text{-}t\text{Bu})_2]^+$ at *m/z* 339 with neutral $Fe(tmtm)_3$. In the previous section, opposing conclusions were prompted from the relative ratio analysis where $[Cu(tftm\text{-}t\text{Bu})_2]^+$ and $[Cu(tftm)(tftm\text{-}t\text{Bu})]^+$ exhibited a high and low degree of reactivity, respectively. Despite these discrepancies, the number of products generated from the collision-induced reactions of $[Cu(tftm)_2]^+$ and $[Cu(tftm)(H)]^+$ with $Fe(tmtm)_3$ demonstrate some consistency with the conclusions presented in the previous section.

Chapter 6

The Gas-Phase Ligand Exchange Reactions of Iron (III) Trimethyltrimethylacetylacetonate ($Fe(tmtm)_3$) with Metal Acetylacetonates ($M(acac)_n$, n = 2, 3) and Metal Trifluorotrimethylacetylacetonates ($M(tftm)_2$)

6.1 Introduction

The data presented herein supplements the previous chapters by continuing the investigation into the gas-phase ligand exchange reactions between $Fe(tmtm)_3$ and various other metal β-diketonates. Like the prior chapters, the metal complexes of interest contain either acetylacetonate (acac) or trifluorotrimethylacetylacetonate (tftm). In the following sections, the co-sublimation data is analyzed and interpreted to validate product formation. In addition, relative ratios of the parent ions are calculated and analyzed to gain mechanistic insight and elucidate possible reaction pathways that account for the gas-phase formation of the mixed ligand species.

6.2 Aluminum Acetylacetonate ($Al(acac)_3$)

For more information regarding $Al(acac)_3$ and its fragmentation behavior please refer back to Chapter 1, Lerach, or Shannon.[11,13] The base spectrum and corresponding tabulated data of $Al(acac)_3$ may be found in Figure 6.1a and Table 6.1.

6.3 The Co-sublimation of $Fe(tmtm)_3$ & $Al(acac)_3$

The co-sublimation mass spectrum of $Fe(tmtm)_3$ and $Al(acac)_3$ is presented in Figure 6.1c, wherein a series of gas-phase iron and aluminum product species are observed for the first time. The baseline spectrum of $Al(acac)_3$ and $Fe(tmtm)_3$ are displayed above the co-sublimation spectrum in Figure 6.1a and Figure 6.1b, respectively, to emphasize the appearance of novel peaks in Figure 6.1c. The corresponding masses with their respective abundances are provided in Table 6.1.

In examining the co-sublimation spectrum, it becomes immediately evident that a majority of the products are not formed in significant quantities. The major product stemming from this particular reaction can be found at *m/z* 309 which corresponds to the mixed ligand product $[Al(acac)(tmtm)]^+$. In addition, the formation of the complete ligand exchange product $[Al(tmtm)_2]^+$ can be inferred from the peak at *m/z* 393. In comparison to iron complexes, those of aluminum favor the formation of the intact doubly-ligated species. As stated in Chapter 4, the relatively high abundance of $[Al(acac)(tmtm)]^+$ and $[Al(tmtm)_2]^+$ is due to the stability acquired from the localization of positive charge onto the metal center.[19]

The ion signal at *m/z* 239 corresponds to the complete exchange product, $[Fe(acac)(acac\text{-}CH_3)]^+$, which is isobaric with the $Fe(tmtm)_3$ fragment $[Fe(tmtm)]^+$. Formation of the singly-ligated product $[Fe(acac)]^+$ can be inferred from the peak

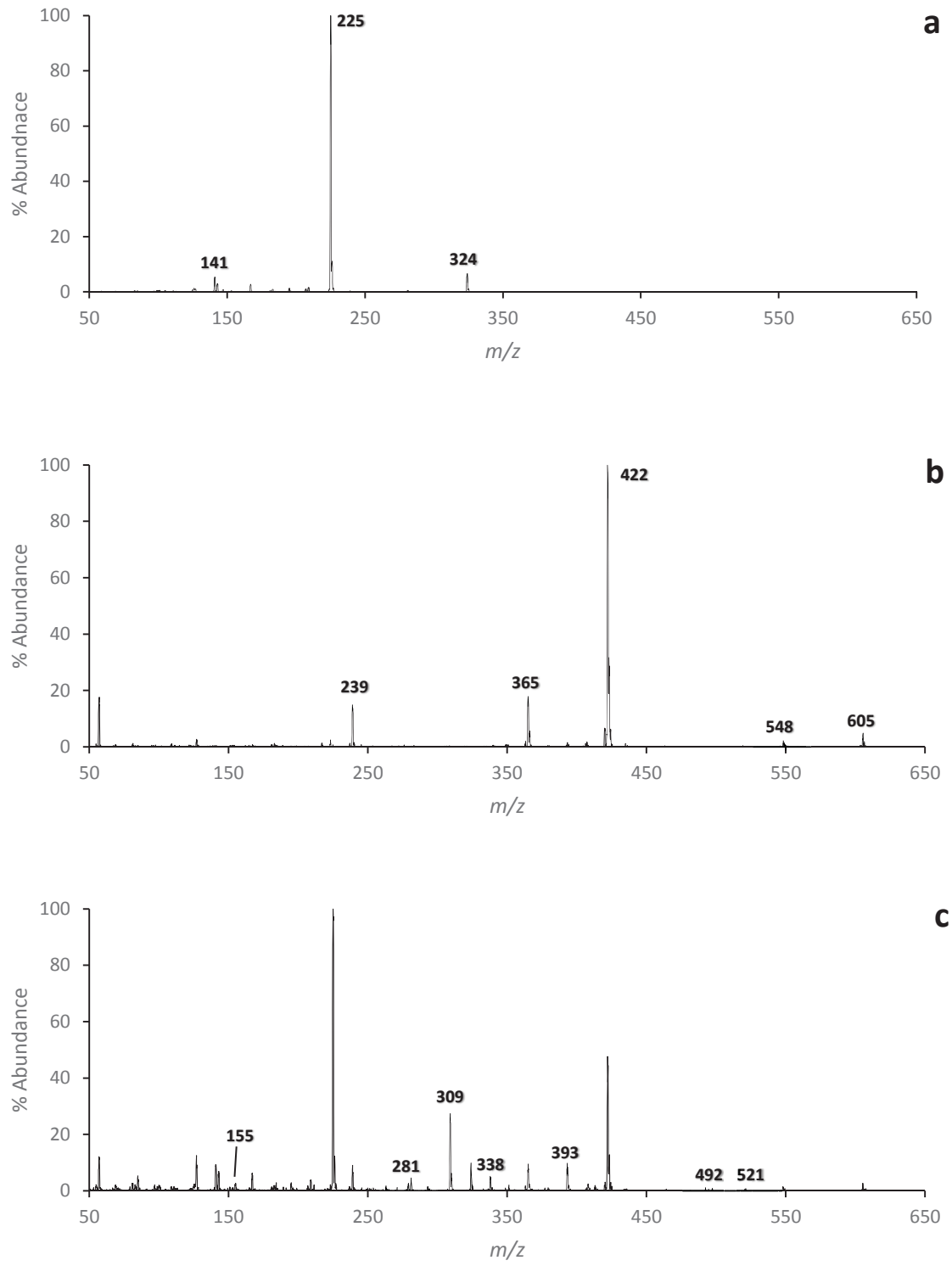

Figure 6.1: The 70eV positive EI mass spectra for a) $Al(acac)_3$, b) $Fe(tmtm)_3$, and c) the gas-phase reactions of $Al(acac)_3$ and $Fe(tmtm)_3$.

	Mass	Mass	AlL_3	FeL_3	AlL'_3	FeL'_3	AlL_3 & FeL'_3	
Species	Al	Fe	Al	Fe	Al	Fe	Al	Fe
$[ML_3]^+$	324	353	7 (1.40)	22			10 (1.11)	<1
$[ML_2]^+$	225	254	100 (20.0)	100			100 (11.1)	1
$[ML_2\text{-}CH_3]^+$	210	239	0	20			<1	***9***
$[ML\text{+}CH_3]^+$	141	170	5 (1.00)	0			9 (1.00)	<1
$[ML]^+$	126	155	0	21			<1	**3**
$[ML'_3]^+$	576	605			8	5 (0.28)	<1	3 (0.30)
$[ML'_3\text{-}t\text{Bu}]^+$	519	548			2	2 (0.11)	<1	2 (0.20)
$[ML'_2]^+$	393	422			100	100 (5.56)	**10**	41 (4.10)
$[ML'_2\text{-}t\text{Bu}]^+$	336	365			4*	18 (1.00)	<1	10 (1.00)
$[ML']^+$	210	239			<1	15 (0.83)	<1	*9* (0.90)
$[MLL'_2]^+$	492	521					1	1
$[ML_2L'\text{-}t\text{Bu}]^+$	435	464					1	1
$[MLL']^+$	309	338					**25**	**5**
$[MLL'\text{-}t\text{Bu}]^+$	252	281					1	**5**

Table 6.1 Relative positive ion intensities (% abundance) of hetero-metal species to their respective base peaks as presented in Figure 6.1. L = (acac), L' = (tmtm), *Protonated: observed at one mass unit higher than expected, *Italics:* Isobaric, **Bold**: Ligand exchange product, (Parenthesis): Relative ratio

found at *m/z* 155. Finally, the peak observed at *m/z* 338 is indicative of the mixed ligand product $[Fe(acac)(tmtm)]^+$ while the ion signal at *m/z* 281 results from *tert*-butyl fragmentation to generate $[Fe(acac)(tmtm\text{-}t\text{Bu})]^+$.

As was performed for the combination of $Fe(tmtm)_3$ and $Cu(acac)_2$, the relative ratios of the parent ion peaks were determined to gain mechanistic insight into the gas-phase formation of the ligand exchange products generated during mass analysis. In this case, $[Al(acac)(CH_3)]^+$ at *m/z* 141 was selected as the reference species to calculate the relative ratios of the $Al(acac)_3$ fragments. The resulting values are placed in parenthesis next to the corresponding normalized abundance in Table 6.1. Based on the differences observed between the relative ratios, the ensuing reactions of the investigated β-diketonate complexes are increasingly discernible.

Consider the gas-phase reaction of an ionic $Al(acac)_3$ fragment with neutral $Fe(tmtm)_3$. As shown in Table 6.1, the relative ratio of $[Al(acac)_2]^+$ at *m/z* 225 decreases

from 20.0 in the baseline spectrum to a value of 11.1 in the co-sublimation spectrum, thus amounting to a difference of 8.9. In contrast, the relative ratio of $[Al(acac)_3]^+$ at *m/z* 324 decreases from 1.40 to a relative ratio of 1.11 following co-sublimation which gives a significantly lower difference of 0.29. The greater degree of peak attenuation exhibited by $[Al(acac)_2]^+$ demonstrates that reaction pathways incorporating $[Al(acac)_2]^+$ are more prominent than those involving $[Al(acac)_3]^+$. The mechanistic proposal provided in Equation (6.1) features partial ligand exchange between $[Al(acac)_2]^+$ and neutral $Fe(tmtm)_3$ to yield the mixed ligand product $[Al(acac)(tmtm)]^+$ at *m/z* 309.

$$[Al^{III}(acac)_2]^+ + Fe^{III}(tmtm)_3 \rightarrow$$

$$[Al^{III}(acac)(tmtm)]^+ + Fe^{III}(acac)(tmtm)_2 \qquad \text{(Eqn 6.1)}$$

Additional insight can be gained by also considering the gas-phase reactions of ionic $Fe(tmtm)_3$ fragments with neutral $Al(acac)_3$. The relative ratios for $Fe(tmtm)_3$ fragments were calculated using $[Fe(tmtm)(tmtm\text{-}t\text{Bu})]^+$ at *m/z* 365 as the reference species. The resulting values are placed in parenthesis next to the corresponding normalized abundance in Table 6.1. Notably, the relative ratio of $[Fe(tmtm)_2]^+$ at *m/z* 422 in the baseline spectrum decreases from 5.56 to a value of 4.10 in the co-sublimation spectrum whereas the remaining $Fe(tmtm)_3$ fragments exhibit relative ratio differences less than 0.10.

Consequently, reaction pathways incorporating $[Fe(tmtm)_2]^+$ with neutral $Al(acac)_3$ are likely the most active in generating ligand exchange products. The

remaining $Fe(tmtm)_3$ fragments appear to be relatively inert, and at most, make minor contributions to product formation. Equation (6.2) presents a mechanistic proposal wherein $[Fe(tmtm)_2]^+$ and $Al(acac)_3$ undergo partial ligand exchange to form the mixed ligand product $[Fe(acac)(tmtm)]^+$ at *m/z* 338. In comparison, the generation of the mixed ligand fragment $[Fe(acac)(tmtm\text{-}t\text{Bu})]^+$ at *m/z* 281 likely incorporates partial ligand exchange, but with the addition of *tert*-butyl fragmentation as outlined in Equation (6.3).

$$[Fe^{III}(tmtm)_2]^+ + Al^{III}(acac)_3 \rightarrow$$
$$[Fe^{III}(acac)(tmtm)]^+ + Al^{III}(acac)(tmtm)_2 \qquad \text{(Eqn 6.2)}$$

$$[Fe^{III}(tmtm)_2]^+ + Al^{III}(acac)_3 \rightarrow$$
$$[Fe^{II}(acac)(tmtm\text{-}t\text{Bu})]^+ + Al^{III}(acac)(tmtm)_2 + t\text{Bu}^{\bullet} \qquad \text{(Eqn 6.3)}$$

6.4 Cobalt (II) Acetylacetonate ($Co(acac)_2$)

For more information regarding $Co(acac)_2$ and its fragmentation behavior please refer back to Chapter 1, Lerach, Hunter, or Shannon.[11-13] The base spectrum and corresponding tabulated data of $Co(acac)_2$ may be found in Figure 6.2a and Table 6.2.

6.5 The Co-sublimation of $Fe(tmtm)_3$ & $Co(acac)_2$

Shown in Figure 6.2c is the co-sublimation spectrum resulting from the gas-phase reaction between $Co(acac)_2$ and $Fe(tmtm)_3$ which displays a series of gas-phase iron and cobalt species for the first time. The baseline spectrum of $Co(acac)_2$ and $Fe(tmtm)_3$ are stacked above the co-sublimation spectrum in Figure 6.2a and Figure 6.2b, respectively, to accentuate the formation of ligand exchange products in Figure 6.2c. The corresponding masses with their respective abundances are provided in Table 6.2.

The results from the co-sublimation of $Co(acac)_2$ and $Fe(tmtm)_3$ present a diverse array of ligand exchange products for both metals at appreciable ion intensities. Formation of the complete ligand exchange product $[Fe(acac)_2]^+$ is evident from the appearance of the peak at *m/z* 254 while loss of a methyl group generates the fragmented species $[Fe(acac)(acac\text{-}CH_3)]^+$ at *m/z* 239. Furthermore, the ion signal appearing at *m/z* 155 suggests the generation of the singly-ligated product $[Fe(acac)]^+$. Mixed ligand products also seem to be generated from reacting $Fe(tmtm)_3$ with $Co(acac)_2$ such as $[Fe(acac)(tmtm)]^+$ at *m/z* 338. Loss of *tert*-butyl presumably leads to the formation of the mixed ligand fragment $[Fe(acac)(tmtm\text{-}t\text{Bu})]^+$ at *m/z* 281.

Unlike a majority of the product peaks in the co-sublimation spectrum, those corresponding to hexacoordinate mixed ligand products were not formed in considerable quantities. However, given their novelty the formation of such species should still be noted. The appearance of a peak at *m/z* 521 is indicative of

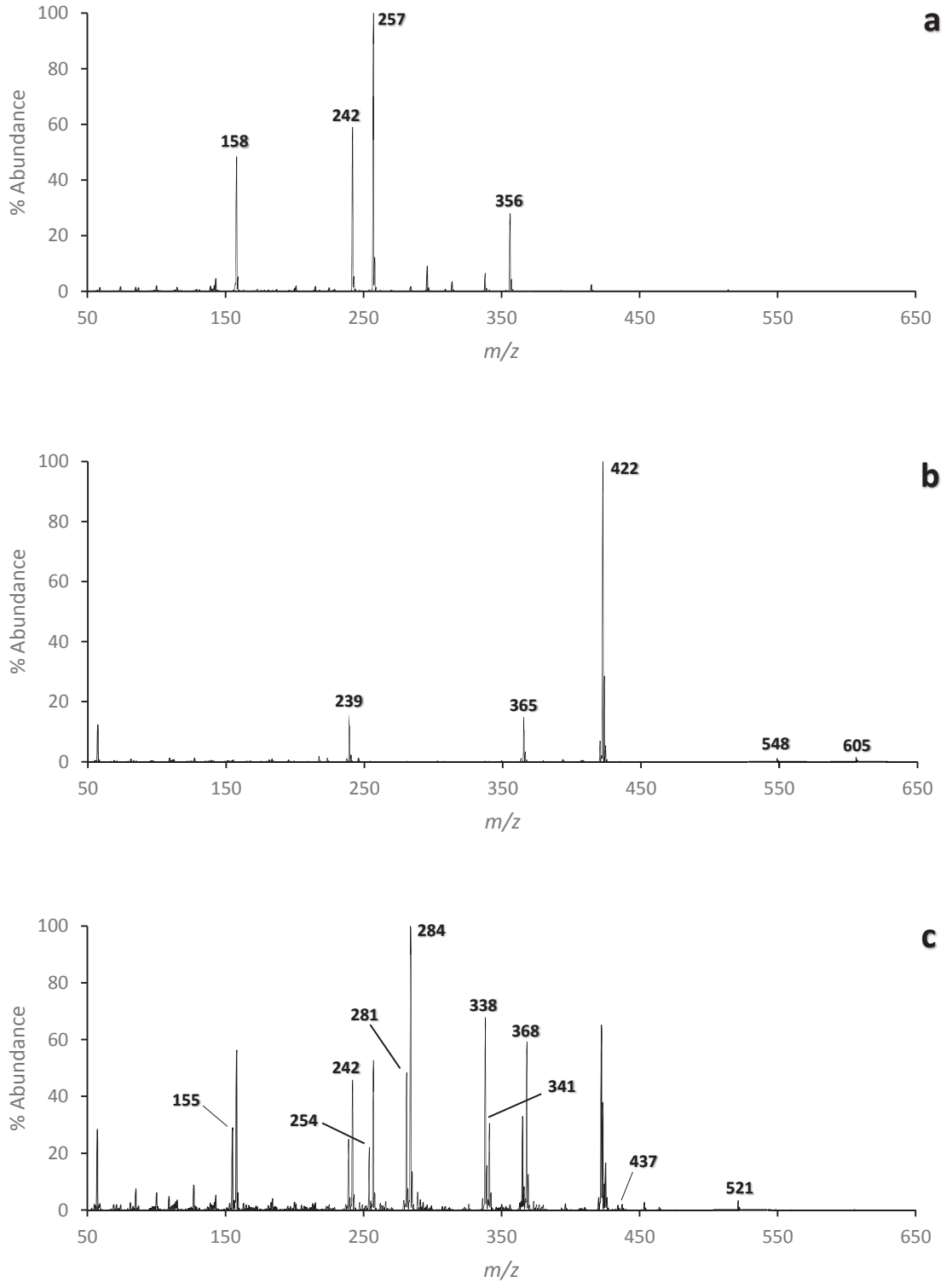

Figure 6.2: The 70eV positive EI mass spectra for a) $Co(acac)_2$, b) $Fe(tmtm)_3$, and c) the gas-phase reactions of $Co(acac)_2$ and $Fe(tmtm)_3$.

	Mass	Mass	FeL_3	CoL_3	FeL'_3	CoL'_2	FeL'_3 & CoL_2	
Species	Fe	Co	Fe	Co	Fe	Co	Fe	Co
$[ML_3]^+$	353	356	22	28 (0.58)			1	2 (0.04)
$[ML_2]^+$	254	257	100	100 (2.08)			**22**	53 (0.95)
$[ML_2\text{-}CH_3]^+$	239	242	20	59 (1.23)			***25***	*46* (0.82)
$[ML]^+$	155	158	21	48 (1.00)			**29**	56 (1.00)
$[ML'_3]^+$	605	608			1 (0.07)	1	<1	<1
$[ML'_3\text{-}t\text{Bu}]^+$	548	551			1 (0.07)	<1	<1	<1
$[ML'_2]^+$	422	425			100 (6.67)	29	65 (1.97)	**17**
$[ML'_2\text{-}t\text{Bu}]^+$	365	368			15 (1.00)	100	33 (1.00)	**59**
$[ML']^+$	239	242			16 (1.07)	17	*25* (0.76)	***46***
$[MLL'_2]^+$	521	524					**3**	<1
$[ML_2L']^+$	437	440					**2**	<1
$[MLL']^+$	338	341					**68**	**31**
$[MLL'\text{-}t\text{Bu}]^+$	281	284					**48**	**100**

Table 6.2 Relative positive ion intensities (% abundance) of hetero-metal species to their respective base peaks as presented in Figure 6.2. L = (acac), L' = (tmtm) *Italics:* Isobaric, **Bold**: Ligand exchange product, (Parenthesis): Relative ratio

$[Fe(acac)(tmtm)_2]^+$ whereas the ion signal at *m/z* 437 is consistent with the formation of $[Fe(acac)_2(tmtm)]^+$.

In examining the cobalt ligand exchange products, it can be seen that a peak corresponding to the complete ligand exchange product $[Co(tmtm)_2]^+$ appears at *m/z* 425. In addition, the peak shown at *m/z* 368 is representative of the fragmented species $[Co(tmtm)(tmtm\text{-}t\text{Bu})]^+$ while the peak at *m/z* 242 corresponds to the singly-ligated species $[Co(tmtm)]^+$. Detection of the mixed ligand product $[Co(acac)(tmtm)]^+$ can also be inferred from the peak at *m/z* 341. Loss of *tert*-butyl results in the gas-phase formation of $[Co(acac)(tmtm\text{-}t\text{Bu})]^+$ at *m/z* 284 which also corresponds to the base peak of the co-sublimation spectrum. The high abundance of fragmented cobalt products is consistent with prior experimentation and literature, and is likely associated with the delocalization of positive charge across the conjugated π system of the ligand which thereby facilitates the loss of an odd electron neutral fragment.[11-13,19]

Relative ratios of the parent ion abundances were determined in a manner consistent with Chapter 4 to acquire mechanistic insight into the reaction pathways responsible for the gas-phase formation of ligand exchange products. For this data set, $[Co(acac)]^+$ at *m/z* 158 and $[Fe(tmtm)(tmtm\text{-}t\text{Bu})]^+$ at *m/z* 365 were selected as the reference species to calculate the relative ratios of the corresponding parent ions. The resulting values are placed in parenthesis next to the corresponding normalized abundance in Table 6.2**.** Fragment reactivity can be assessed by comparing the baseline and co-sublimation relative ratio values determined for each parent ion.

The first set of gas-phase reactions to be considered are those that incorporate an ionic $Co(acac)_2$ fragment and neutral $Fe(tmtm)_3$. As shown in Table 6.2, the ion signal corresponding to $[Co(acac)_2]^+$ at *m/z* 257 appears to undergo significant peak attenuation as a result of co-sublimation; decreasing from a relative ratio of 2.08 in the baseline spectrum to a relative ratio of 0.95 in the co-sublimation spectrum. The triply-ligated species $[Co(acac)_3]^+$ at *m/z* 356 also appears to undergo peak attenuation, but to a lesser extent; decreasing from a relative ratio of 0.58 in the baseline spectrum to a relative ratio of 0.04 in the co-sublimation spectrum. A similar drop in relative peak intensity is observed for $[Co(acac)(acac\text{-}CH_3)]^+$ at *m/z* 242 which decreases from a relative ratio of 1.23 in the baseline spectrum to a relative ratio of 0.82 following co-sublimation.

Thus, $[Co(acac)_2]^+$ appears to be the most reactive fragment contributing to the gas-phase formation of ligand exchange products. The fragments $[Co(acac)_3]^+$ and $[Co(acac)(acac\text{-}CH_3)]^+$ likely make lesser contributions to the observed product

distribution. Consequently, a probable reaction pathway leading to the production of the mixed ligand product $[Co(acac)(tmtm)]^+$ at *m/z* 341 features partial ligand exchange between $[Co(acac)_2]^+$ and neutral $Fe(tmtm)_3$, as shown in Equation (6.4). An additional mechanistic proposal accounting for the generation of the mixed ligand fragment $[Co(acac)(tmtm\text{-}t\text{Bu})]^+$ at *m/z* 284 is presented in Equation (6.5).

$$[Co^{III}(acac)_2]^+ + Fe^{III}(tmtm)_3 \rightarrow$$

$$[Co^{III}(acac)(tmtm)]^+ + Fe^{III}(acac)(tmtm)_2 \qquad \text{(Eqn 6.4)}$$

$$[Co^{III}(tmtm)_2]^+ + Fe^{II}(acac)_3 \rightarrow$$

$$[Co^{II}(acac)(tmtm\text{-}t\text{Bu})]^+ + Fe^{III}(acac)(tmtm)_2 + t\text{Bu}^{\bullet} \qquad \text{(Eqn 6.5)}$$

Further understanding of the gas-phase formation of mixed ligand products can be acquired by assessing the reactions of ionic $Fe(tmtm)_3$ fragments with neutral $Co(acac)_2$. The relative ratio of $[Fe(tmtm)_2]^+$ at *m/z* 422 decreases from 6.67 in the baseline spectrum to 1.97 in the co-sublimation spectrum resulting in a difference of 4.70. In contrast, the species $[Fe(tmtm)]^+$ at *m/z* 239 exhibits a relative ratio difference of 0.31 between the baseline and co-sublimation spectrum.

As a result, the data presented seems to suggest that the reaction pathway combining $[Fe(tmtm)_2]^+$ with neutral $Co(acac)_2$ is the most prevalent for the generation of ligand exchange products. The remaining $Fe(tmtm)_3$ fragments, on the other hand, exhibit a low degree of change in relative peak abundance, and therefore are less likely

to make a significant contribution to product generation. Equation (6.6) outlines a reaction pathway wherein $[Fe(tmtm)_2]^+$ undergoes partial ligand exchange with neutral $Co(acac)_2$ to generate the mixed ligand product $[Fe(acac)(tmtm)]^+$ at *m/z* 338. Loss of *tert*-butyl yields the mixed ligand fragment $[Fe(acac)(tmtm\text{-}t\text{Bu})]^+$ at *m/z* 281 as shown in Equation (6.7).

$$[Fe^{III}(tmtm)_2]^+ + Co^{II}(acac)_2 \rightarrow$$

$$[Fe^{III}(acac)(tmtm)]^+ + Co^{II}(acac)(tmtm) \qquad \text{(Eqn 6.6)}$$

$$[Fe^{III}(tmtm)_2]^+ + Co^{II}(acac)_2 \rightarrow$$

$$[Fe^{II}(acac)(tmtm\text{-}t\text{Bu})]^+ + Co^{II}(acac)(tmtm) + t\text{Bu}^{\bullet} \qquad \text{(Eqn 6.7)}$$

6.6 Cobalt (II) Trifluorotrimethylacetylacetonate ($Co(tftm)_2$)

For more information regarding $Co(tftm)_2$ and its fragmentation behavior please refer back to Chapter 1, Lerach, or Hunter.[11,12] The base spectrum and corresponding tabulated data of $Co(tftm)_2$ may be found in Figure 6.3a and Table 6.3.

6.7 The Co-sublimation of $Fe(tmtm)_3$ & $Co(tftm)_2$

The co-sublimation spectrum of $Co(tftm)_2$ and $Fe(tmtm)_3$ is displayed in Figure 6.3c wherein a series of gas-phase iron and cobalt products are observed for the first time. The co-sublimation spectrum is positioned directly beneath the baseline spectrum

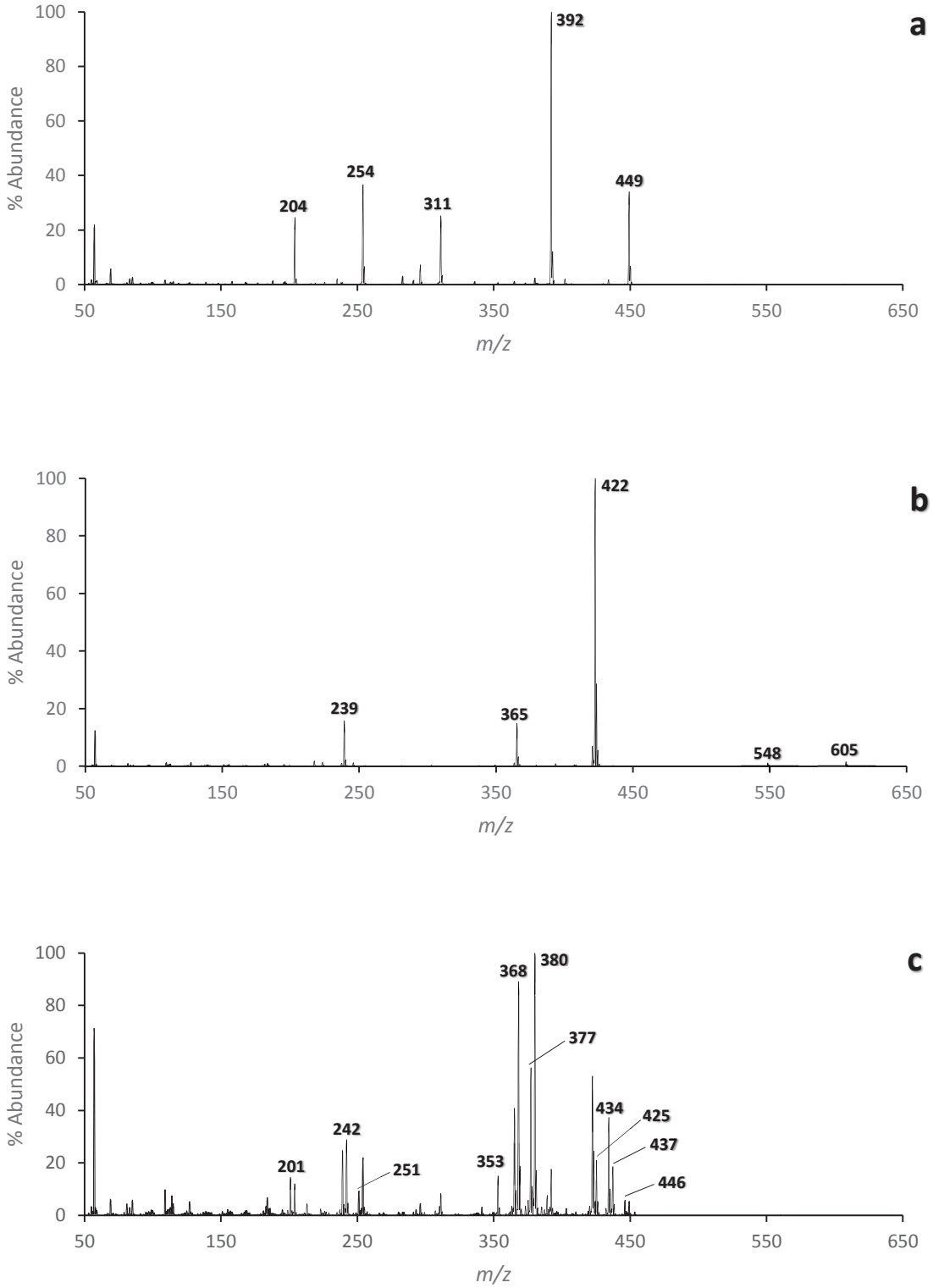

Figure 6.3: The 70eV positive EI mass spectra for a) $Co(tftm)_2$, b) $Fe(tmtm)_3$, and c) the gas-phase reactions of $Co(tftm)_2$ and $Fe(tmtm)_3$.

	Mass	Mass	FeL'_3	CoL'_2	FeL''_3	CoL''_2	FeL'_3 & CoL''_2	
Species	Fe	Co	Fe	Co	Fe	Co	Fe	Co
$[ML'_3]^+$	605	608	1 (0.07)	1			<1	<1
$[ML'_3$-*t*Bu$]^+$	548	551	1 (0.07)	<1			<1	<1
$[ML'_2]^+$	422	425	100 (6.67)	29			53 (1.29)	**21**
$[ML'_2$-*t*Bu$]^+$	365	368	15 (1.00)	100			41 (1.00)	**89**
$[ML']^+$	239	242	16 (1.07)	17			25 (0.61)	**29**
$[ML''_3]^+$	641	644			1	<1	<1	<1
$[ML''_3$-*t*Bu$]^+$	584	587			1	<1	<1	<1
$[ML''_2]^+$	446	449			69	34 (4.86)	**6**	5 (1.00)
$[ML''_2$-43$]^+$	403	406			17	<1	**3**	<1
$[ML''_2$-*t*Bu$]^+$	389	392			46	100 (14.3)	**8**	18 (3.60)
$[ML''_2$-$CF_3]^+$	377	380			4	2 (0.29)	***56***	*100* (20)
$[ML''_2$-$2CF_3]^+$	308	311			0	25 (3.57)	1	8 (1.60)
$[ML''$+42$]^+$	293	296			7	7 (1.00)	**2**	5 (1.00)
$[ML'']^+$	251	254			20	37 (5.29)	**9**	24 (4.80)
$[ML''$-$CF_2]^+$	201	204			38	25 (3.57)	**15**	12 (2.40)
$[ML''$-*t*Bu$]^+$	194	197			8	1 (0.14)	**2**	1 (0.20)
$[ML'L'']^+$	434	437					**37**	**19**
$[ML'L''$-*t*Bu$]^+$	377	380					**56**	**100**
$[ML'L''$-CO*t*Bu$]^+$	349	352					1	**15***

Table 6.3 Relative positive ion intensities (% abundance) of hetero-metal species to their respective base peaks as presented in Figure 6.3. L' = (tmtm), L'' = (tftm), *Protonated; observed at one mass unit higher than expected *Italics:* Isobaric, **Bold**: Ligand exchange product, (Parenthesis): Relative ratio

of $Co(tftm)_2$ and $Fe(tmtm)_3$ which are presented in Figure 6.3a and Figure 6.3b, respectively. By stacking the spectra, the appearance of novel peaks generated from a gas-phase reaction is emphasized. The corresponding masses with their respective abundances are provided in Table 6.3.

Similar to the previous section, a variety of ligand exchange products are observed for both metals in appreciable abundances. One such product is observed at *m/z* 425 which corresponds to the complete ligand exchange product $[Co(tmtm)_2]^+$. Additionally, the formation of the fragmented product $[Co(tmtm)(tmtm\text{-}t\text{Bu})]^+$ can be inferred from the peak at *m/z* 368 while the singly-ligated species $[Co(tmtm)]^+$ makes an appearance at *m/z* 242. The peak observed at *m/z* 437 signifies the gas-phase formation of the mixed ligand product $[Co(tmtm)(tftm)]^+$. Loss of *tert*-butyl generates the mixed

ligand fragment $[Co(tmtm)(tftm)\text{-}t\text{Bu}]^+$ at *m/z* 380. Notably, there also appears to be a peak at *m/z* 353 that suggests the loss of CO*t*Bu to form $[Co(H)(tmtm)(tftm)\text{-}CO t\text{Bu}]^+$. The high abundance of fragmented cobalt products is consistent with the results presented in the previous section.

Unlike the cobalt complete exchange products, those of iron appear in relatively lower abundances with the exception of two peaks corresponding to mixed ligand products. The ion signal displayed at *m/z* 434 indicates the gas-phase formation of the mixed ligand product $[Fe(tmtm)(tftm)]^+$ while the peak appearing at *m/z* 377 either represents $[Fe(tftm)(tftm\text{-}CF_3)]^+$ or $[Fe(tmtm)(tftm)\text{-}t\text{Bu}]^+$. However, as was established during Chapters 1 and 5, the loss of CF_3 from (tftm) is not as favorable as *tert*-butyl fragmentation; thus suggesting the preferential formation of the mixed ligand fragment.

Unexpectedly, the ion signal corresponding to the mixed ligand fragment is observed in greater abundance than the intact mixed ligand product. As observed in prior sections, ferric complexes do not typically favor redox dependent fragmentation events. However, as made evident in the baseline spectrum of $Fe(tftm)_3$, redox dependent fragmentations become more tolerable when iron is ligated to the electron withdrawing (tftm) ligand. As shown by the co-sublimation spectrum, this degree of tolerance is also extended to the formation of tftm-containing ferrous products via ligand exchange.

Additional iron-containing products appear in lower abundances such as the peak at *m/z* 446 which is consistent with the generation of $[Fe(tftm)_2]^+$. Formation of the

fragmented product $[Fe(tftm)(tftm\text{-}t\text{Bu})]^+$ can also be inferred from the peak displayed at *m/z* 389. Finally, the singly-ligated product $[Fe(tftm)]^+$ appears to form at *m/z* 251 while the ion signal at *m/z* 201 suggests loss of CF_2 via fluorine migration to form $[Fe(tftm\text{-}CF_2)]^+$.

Relative ratios of the parent ion signals were ascertained using the method outlined in Chapter 4 to obtain a mechanistic understanding of the reaction pathways accountable for the gas-phase formation of ligand exchange products. For this particular reaction, $[Co(tftm)+42]^+$ at *m/z* 296 and $[Fe(tmtm)(tmtm\text{-}t\text{Bu})]^+$ at *m/z* 365 were designated as the reference ions to assess the relative ratios of the corresponding parent species. The resulting values are placed in parenthesis next to the corresponding normalized abundance in Table 6.3**.** Based on the observed differences between the relative ratios, the mechanistic framework of the reactions of interest becomes more apparent.

The gas-phase reactions between ionic $Co(tftm)_2$ fragments and neutral $Fe(tmtm)_3$ will be the first to be considered. In referring to Table 6.3, the fragment that appears to demonstrate a high degree of reactivity is $[Co(tftm)(tftm\text{-}t\text{Bu})]^+$ at *m/z* 392 which is made apparent from the corresponding relative ratio decreasing from 14.3 in the baseline spectrum to a relative ratio of 3.60 in the co-sublimation spectrum. The remaining $Co(tftm)_2$ fragments have markedly lower differences in relative ratios between baseline and co-sublimation spectrum. For example, the second-most reactive $Co(tftm)_2$ fragment of seems to be $[Co(tftm)_2]^+$ at *m/z* 449 which has a relative ratio decreasing from 4.86 in the baseline spectrum to a relative ratio of 1.00 in the co-

sublimation spectrum. All remaining $Co(tftm)_2$ have relative ratio differences that range from 1.97 to 0.06 when the reference species is not included, and therefore are unlikely to make significant contributions to the observed product distribution.

Therefore, reaction pathways incorporating the combination of $[Co(tftm)(tftm\text{-}t\text{Bu})]^+$ with neutral $Fe(tmtm)_3$ are likely more prominent in the gas-phase formation of ligand exchange products. In as such, a mechanistic proposal accounting for the generation of the mixed ligand product $[Co(tmtm)(tftm)]^+$ at *m/z* 437 is expressed in Equation (6.8). The mechanisms responsible for the formation of the mixed ligand fragments $[Co(tmtm)(tftm\text{-}t\text{Bu})]^+$ at *m/z* 380 and $[Co(tmtm)(tftm\text{-}COt\text{Bu})]^+$ at *m/z* 353 are provided in Equation (6.9) and Equation (6.10), respectively.

$$[Co^{II}(tftm)(tftm\text{-}t\text{Bu})]^+ + Fe^{III}(tmtm)_3 \rightarrow$$

$$[Co^{III}(tmtm)(tftm)]^+ + Fe^{II}(tmtm)_2(tftm\text{-}t\text{Bu}) \qquad \text{(Eqn 6.8)}$$

$$[Co^{II}(tftm)(tftm\text{-}t\text{Bu})]^+ + Fe^{III}(tmtm)_3 \rightarrow$$

$$[Co^{II}(tmtm)(tftm\text{-}t\text{Bu})]^+ + Fe^{III}(tmtm)_2(tftm) \qquad \text{(Eqn 6.9)}$$

$$[Co^{II}(tftm)(tftm\text{-}t\text{Bu})]^+ + Fe^{III}(tmtm)_3 \rightarrow$$

$$[Co^{II}(tmtm)(tftm\text{-}COt\text{Bu})]^+ + Fe^{II}(tmtm)_2(tftm\text{-}t\text{Bu}) + CO \qquad \text{(Eqn 6.10)}$$

Additional mechanistic insight can be gained by also considering the reactions of ionic $Fe(tmtm)_3$ fragments with neutral $Co(tftm)_2$. Take for instance the relative ratio of $[Fe(tmtm)_2]^+$ at *m/z* 422 which decreases from 6.67 in the baseline spectrum to a value of 1.29 in the co-sublimation spectrum, thus amounting to a difference of 5.38. This degree of difference is quite substantial in comparison to that determined for the remaining fragments which exhibit relative ratio differences less than 0.50.

Accordingly, the data appears to suggest that reactions between ionic $Fe(tmtm)_3$ fragments and neutral $Co(tftm)_2$ predominantly include $[Fe(tmtm)_2]^+$ to the generate ligand exchange products. Since a low degree of peak attenuation was demonstrated by $[Fe(tmtm)(tmtm\text{-}t\text{Bu})]^+$ at *m/z* 365 and $[Fe(tmtm)]^+$ at *m/z* 239, these fragments appear to be significantly less engaged in the reaction. Equation (6.11) provides a mechanistic proposal to account for the formation of the mixed ligand product $[Fe(tmtm)(tftm)]^+$ at *m/z* 434 while Equation (6.12) outlines a reaction pathway leading to the generation of the mixed ligand fragment $[Fe(tmtm)(tftm)\text{-}t\text{Bu})]^+$ at *m/z* 377. Both expressions imply partial ligand exchange while only the latter incorporates *tert*-butyl fragmentation.

$$[Fe^{III}(tmtm)_2]^+ + Co^{II}(tftm)_2 \rightarrow$$

$$[Fe^{III}(tmtm)(tftm)]^+ + Co^{II}(tmtm)(tftm) \qquad \text{(Eqn 6.11)}$$

$$[Fe^{III}(tmtm)_2]^+ + Co^{II}(tftm)_2 \rightarrow$$

$$[Fe^{II}(tmtm)(tftm)\text{-}t\text{Bu})]^+ + Co^{II}(tmtm)(tftm) + t\text{Bu}^{\bullet} \qquad \text{(Eqn 6.12)}$$

6.8 Zinc Acetylacetonate ($Zn(acac)_2$)

For more information regarding $Zn(acac)_2$ and its fragmentation behavior please refer back to Chapter 1, Lerach, Hunter, or Shannon.[11-13] The base spectrum and corresponding tabulated data of $Zn(acac)_2$ may be found in Figure 6.4a and Table 6.4.

6.9 The Co-sublimation of $Fe(tmtm)_3$ & $Zn(acac)_2$

Presented in Figure 6.4c is the co-sublimation spectrum of $Zn(acac)_2$ and $Fe(tmtm)_3$ wherein a series of gas-phase iron and zinc products are observed for the first time. In order to highlight novel product formations, the baseline spectrum of $Zn(acac)_2$ and $Fe(tmtm)_3$ are stacked above the co-sublimation spectrum and are shown in Figure 6.4a and Figure 6.4b, respectively. The corresponding masses with their respective abundances are provided in Table 6.4.

As shown in Figure 6.4c, an assortment of both iron and zinc ligand exchange products are observed to form. The complete ligand exchange product $[Zn(tmtm)_2]^+$ does appear to form at *m/z* 430, but is in low abundance. Additionally, the fragmented product $[Zn(tmtm)(tmtm\text{-}t\text{Bu})]^+$ makes an appearance at *m/z* 373 while the ion signal at *m/z* 247 signifies the gas-phase formation of $[Zn(tmtm)]^+$. Mixed ligand products are also observed to form such as $[Zn(acac)(tmtm)]^+$ at *m/z* 346 and its fragmented analog $[Zn(acac)(tmtm\text{-}t\text{Bu})]^+$ at *m/z* 289. Preferential loss of *tert*-butyl to form fragmented products is consistent with prior experimentation and literature, and likely results from a destabilized molecular ion that cannot delocalize positive charge across the zinc center.[11-13,19]

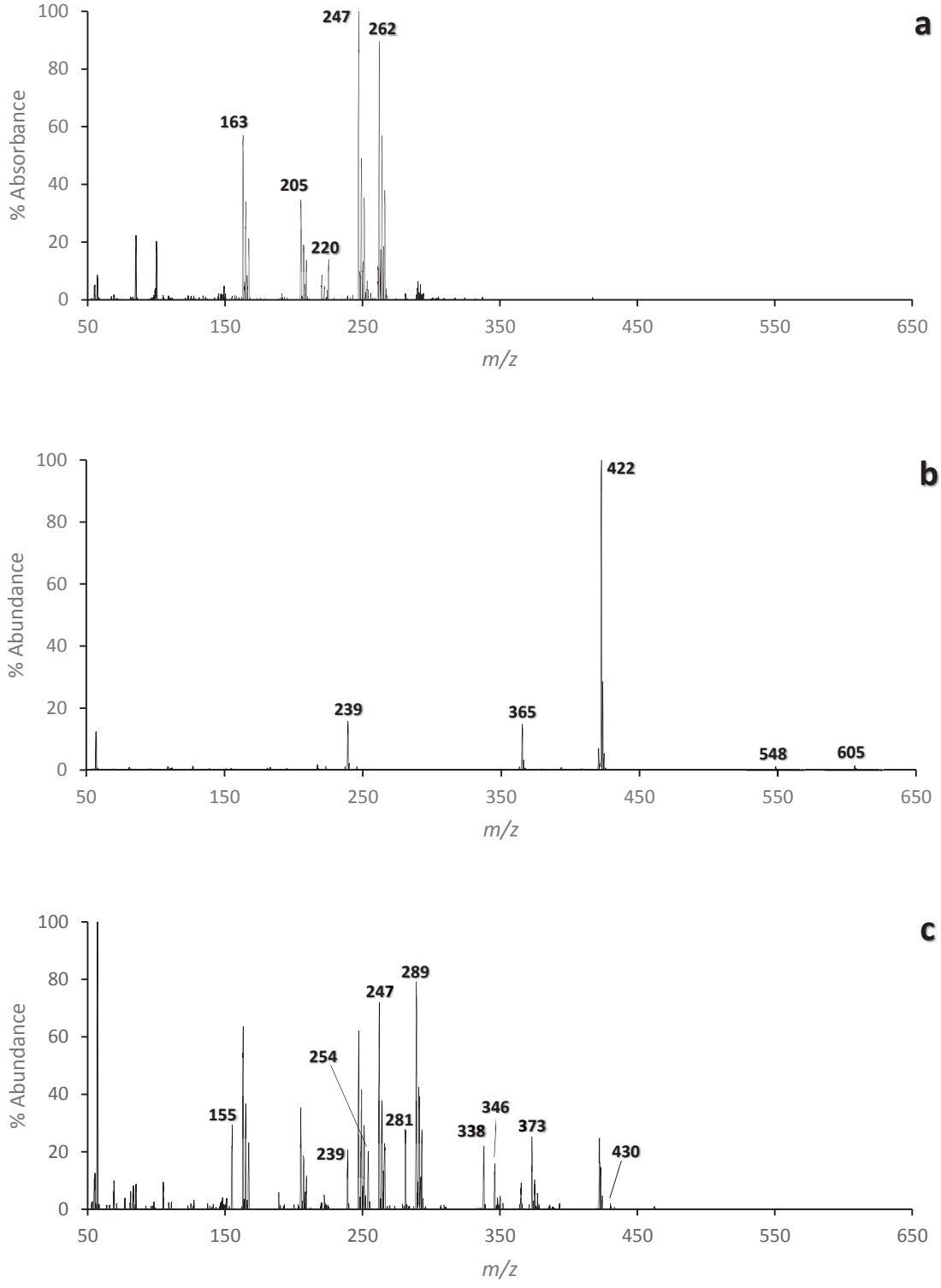

Figure 6.4: The 70eV positive EI mass spectra for a) $Zn(acac)_2$, b) $Fe(tmtm)_3$, and c) the gas-phase reactions of $Zn(acac)_2$ and $Fe(tmtm)_3$.

	Mass	Mass	FeL_3	ZnL_2	FeL'_3	ZnL'_2	FeL'_3 & ZnL_2	
Species	Fe	Zn	Fe	Zn	Fe	Zn	Fe	Zn
$[ML_3]^+$	353	361	22	<1			<1	<1
$[ML_2]^+$	254	262	100	90 (1.58)			**20**	72 (1.13)
$[ML_2\text{-}CH_3]^+$	239	247	20	100 (2.85)			***21***	*62* (0.97)
$[ML_2\text{-}CH_2CO]^+$	211	220	0	9 (0.16)			<1	2 (0.03)
$[ML+CH_2CO]^+$	198	205	0	35 (0.61)			<1	35 (0.55)
$[ML]^+$	155	163	21	57 (1.00)			**29**	64 (1.00)
$[ML'_3]^+$	605	612			1 (0.07)	<1	<1	<1
$[ML'_3\text{-}t\text{Bu}]^+$	548	556			1 (0.07)	<1	<1	<1
$[ML'_2]^+$	422	430			100 (6.67)	12	25 (2.78)	**2**
$[ML'_2\text{-}t\text{Bu}]^+$	365	373			15 (1.00)	100	9 (1.00)	**25**
$[ML']^+$	239	247			16 (1.07)	8	*21* (2.33)	***62***
$[MLL']^+$	338	346					**22**	**16**
$[MLL'\text{-}t\text{Bu}]^+$	281	289					**28**	**79**

Table 6.4 Relative positive ion intensities (% abundance) of hetero-metal species to their respective base peaks as presented in Figure 6.4. L = (acac), L' = (tmtm), *Italics:* Isobaric, **Bold**: Ligand exchange product, (Parenthesis): Relative ratio

Focusing now on iron-containing product ions, appearing at *m/z* 254 in Figure 6.4c is an ion signal corresponding to the complete exchange product $[Fe(acac)_2]^+$. A loss of a methyl group produces the fragmented product $[Fe(acac)(acac\text{-}CH_3)]^+$ at *m/z* 239 while the loss of (acac) results in the production of the singly-ligated species $[Fe(acac)]^+$ at *m/z* 155. Generation of the mixed ligand product $[Fe(acac)(tmtm)]^+$ is evident based on the peak at *m/z* 338 while loss of *tert*-butyl results in the formation of $[Fe(acac)(tmtm\text{-}t\text{Bu})]^+$ at *m/z* 281.

To gain mechanistic insight into the gas-phase formation of the aforementioned products, it was necessary to calculate and compare the relative ratios of the parent ions using the method described in Chapter 4. The fragments $[Zn(acac)]^+$ at *m/z* 163 and $[Fe(tmtm)(tmtm\text{-}t\text{Bu})]^+$ at *m/z* 365 were chosen as the reference species to evaluate the relative ratios of the corresponding parent ions. The resulting values are placed in parenthesis next to the corresponding normalized abundance in Table 6.4**.** As shown by

the differences between the relative ratios, some reaction mechanisms are likely more prominent than others in regards to the formation of ligand exchange products.

The reaction between ionic $Zn(acac)_2$ fragments and neutral $Fe(tmtm)_3$ will be the first to be assessed. Based on Table 6.4, the fragment that exhibits the greatest degree of peak attenuation as a result of co-sublimation is $[Zn(acac)(acac\text{-}CH_3)]^+$ at *m/z* 247; as made apparent by the decrease from a relative ratio of 2.85 in the baseline spectrum to a relative ratio of 0.97 in the co-sublimation spectrum. The peak demonstrating the second-most significant drop in relative peak height is $[Zn(acac)_2]^+$ at *m/z* 262; decreasing from a relative ratio of 1.58 in the baseline spectrum to a relative ratio of 1.13 in the co-sublimation spectrum. The remaining $Zn(acac)_2$ fragments $[Zn(acac)(acac\text{-}CH_2CO)]^+$ at *m/z* 220 and $[Zn(acac)(CH_2CO)]^+$ at *m/z* 205 have relative ratio differences of 0.13 and 0.06, respectively.

Consequently, the gas-phase reaction between $[Zn(acac)(acac\text{-}CH_3)]^+$ and neutral $Fe(tmtm)_3$ appears to be the most productive combination to generate ligand exchange products. Accordingly, the mixed ligand product $[Zn(acac)(tmtm)]^+$ at *m/z* 346 would predominantly be generated via partial ligand exchange according to Equation (6.13). Loss of *tert*-butyl to generate $[Zn(acac)(tmtm\text{-}t\text{Bu})]^+$ at *m/z* 289 is consistent with the mechanistic proposal outlined in Equation (6.14).

$$[Zn^{II}(acac)(acac\text{-}CH_3)]^+ + Fe^{III}(tmtm)_3 \rightarrow$$

$$[Zn^{II}(acac)(tmtm)]^{+\bullet} + Fe^{II}(acac\text{-}CH_3)(tmtm)_2 \qquad \text{(Eqn 6.13)}$$

$$[Zn^{II}(acac)(acac\text{-}CH_3)]^+ + Fe^{III}(tmtm)_3 \rightarrow$$

$$[Zn^{II}(acac)(tmtm\text{-}t\text{Bu})]^+ + Fe^{II}(acac\text{-}CH_3)(tmtm)_2 + t\text{Bu}^\bullet \qquad \text{(Eqn 6.14)}$$

Furthermore, if the reaction of an ionic $Fe(tmtm)_3$ fragment with neutral $Zn(acac)_2$ is considered, additional insight into the reaction pathways can be gained. Again, reference to Table 6.4 reveals that the peak corresponding to $[Fe(tmtm)_2]^+$ at *m/z* 422 decreases from a relative ratio of 6.67 in the baseline spectrum to 2.78 in the co-sublimation spectrum. The singly-ligated species $[Fe(tmtm)]^+$ at *m/z* 239 exhibits peaks growth; increasing from a relative ratio of 1.07 in the baseline spectrum to 2.33 in the co-sublimation spectrum. Such an increase not only reflects the relative decrease of $[Fe(tmtm)_2]^+$, but also is indicative of peak summation with the isobaric product $[Fe(acac)(acac\text{-}CH_3)]^+$.

Considering that the doubly-ligated species $[Fe(tmtm)_2]^+$ was the only species to demonstrate a relative ratio decrease, it would seem that the same fragment is also widely responsible for the formation of ligand exchange products upon reaction with neutral $Zn(acac)_2$. The mechanistic proposal presented in Equation (6.15) is consistent with the observed results and accounts for the formation of the mixed ligand product $[Fe(acac)(tmtm)]^+$ at *m/z* 338. Equation (6.16) outlines a similar reaction pathway that leads to the production of the mixed ligand fragment $[Fe(acac)(tmtm\text{-}t\text{Bu})]^+$ at *m/z* 281. Both mechanisms operate via partial ligand exchange while only the latter features *tert*-butyl fragmentation.

$$[Fe^{III}(tmtm)_2]^+ + Zn^{II}(acac)_2 \rightarrow$$

$$[Fe^{III}(acac)(tmtm)]^+ + Zn^{II}(acac)(tmtm) \qquad \text{(Eqn 6.15)}$$

$$[Fe^{III}(tmtm)_2]^+ + Zn^{II}(acac)_2 \rightarrow$$

$$[Fe^{II}(acac)(tmtm\text{-}t\text{Bu})]^+ + Zn^{II}(acac)(tmtm) + t\text{Bu}^{\bullet} \qquad \text{(Eqn 6.16)}$$

6.10 Zinc Trifluorotrimethylacetylacetonate ($Zn(tftm)_2$)

For more information regarding $Zn(tftm)_2$ and its fragmentation behavior please refer back to Chapter 1, Lerach, or Hunter.[11,12] The base spectrum and corresponding tabulated data of $Zn(tftm)_2$ may be found in Figure 6.5 and Table 6.5.

6.11 The Co-sublimation of $Fe(tmtm)_3$ & $Zn(tftm)_2$

The co-sublimation spectrum of $Fe(tmtm)_3$ and $Zn(tftm)_2$ is displayed in Figure 6.5c which illustrates, for the first time, the gas-phase formation of novel iron and zinc products. To accentuate the generation of product ions, the co-sublimation spectrum is positioned directly underneath the baseline spectrum of $Zn(tftm)_2$ and $Fe(tmtm)_3$ which are presented in Figure 6.5a and Figure 6.5b, respectively. The corresponding masses with their respective abundances are provided in Table 6.5.

As presented in Figure 6.5c, a variety of both iron and zinc-containing products are shown to form in low to moderate abundances. Displayed at *m/z* 373 is an ion signal corresponding to the fragmented product $[Zn(tmtm)(tmtm\text{-}t\text{Bu})]^+$. The singly-ligated product $[Zn(tmtm)]^+$ is also observed at *m/z* 247 but in fairly low abundance. Finally, a

peak corresponding to the mixed ligand fragment $[Zn(tmtm)(tftm)\text{-}t\text{Bu}]^+$ appears at *m/z* 385. Preferential formation of fragmented zinc products is a feature consistent with the results presented in the previous section.

Additionally, a variety of iron products were also shown to form such as the complete exchange product $[Fe(tftm)_2]^+$ at *m/z* 446. Loss of *tert*-butyl results in the formation of $[Fe(tftm)(tftm\text{-}t\text{Bu})]^+$ as indicated by the ion signal at *m/z* 389. The peak displayed at *m/z* 251 is indicative of the presence of the ferrous species $[Fe(tftm)]^+$ while the peak displayed at *m/z* 201 suggests the formation of $[Fe(tftm\text{-}CF_2)]^+$ via fluorine migration.

Furthermore, the gas-phase formation of the mixed ligand product $[Fe(tmtm)(tftm)]^+$ is made evident by the appearance of a peak at *m/z* 434. Generation of the mixed ligand fragment $[Fe(tmtm)(tftm)\text{-}t\text{Bu}]^+$ can also be inferred from the ion signal displayed at *m/z* 377. As was observed for the co-sublimation spectrum of $Fe(tmtm)_3$ and $Co(tftm)_2$ in Figure 6.3c, the mixed ligand fragment in Figure 6.5c is generated in greater abundance than its intact counterpart. This observation further demonstrates how redox dependent fragmentations become more tolerable when the metal is ligated to the electron-withdrawing (tftm) ligand.

Relative ratios of the parent ion abundances were determined using the procedure explained in Chapter 4 to attain mechanistic insight into the reaction pathways responsible for the gas-phase formation of ligand exchange products. As shown in Table 6.5, $[Zn(tftm)_2]^+$ at *m/z* 454 and $[Fe(tmtm)(tmtm\text{-}t\text{Bu})]^+$ at *m/z* 365 were

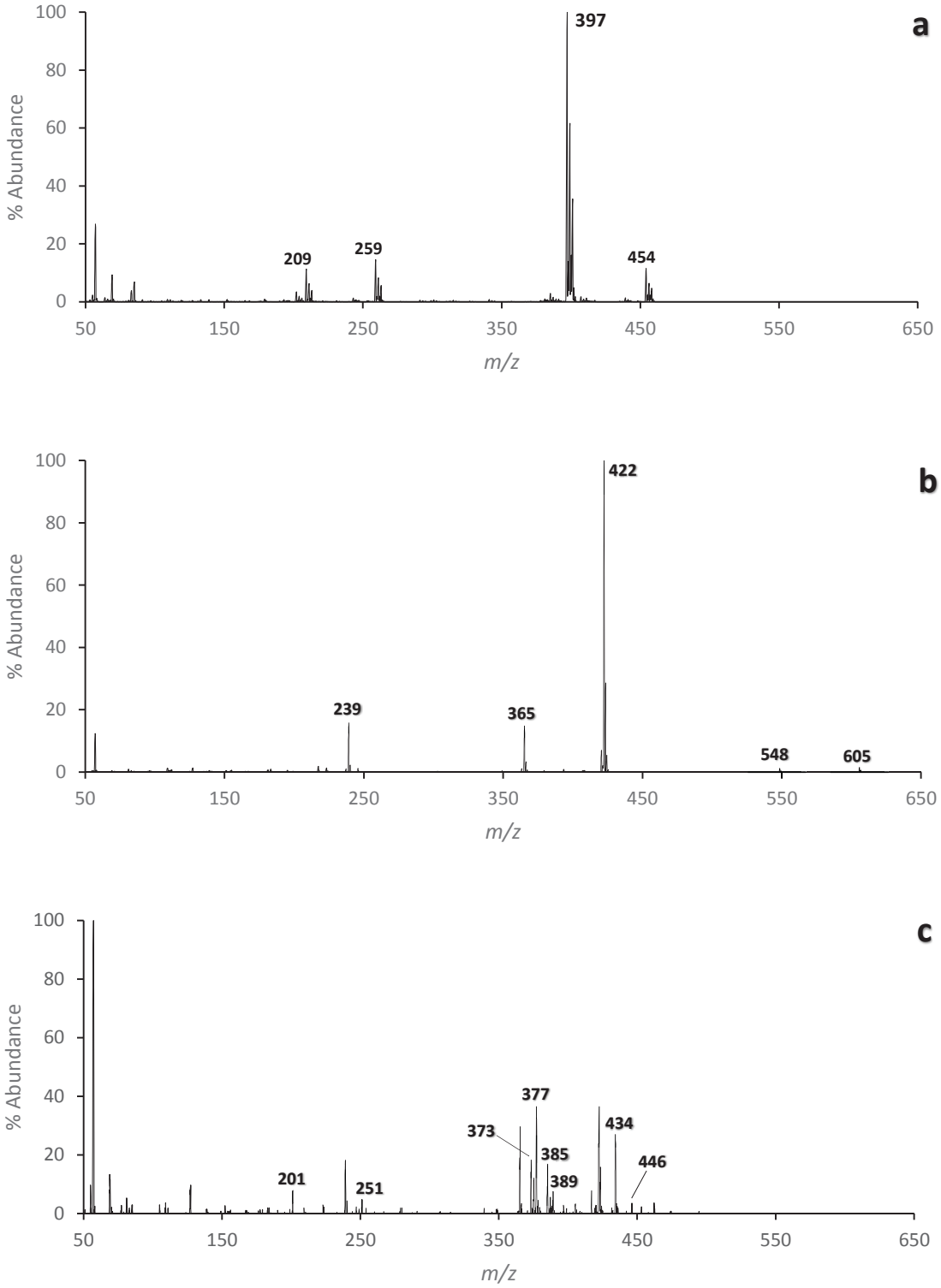

Figure 6.5: The 70eV positive EI mass spectra for a) $Zn(tftm)_2$, b) $Fe(tmtm)_3$, and c) the gas-phase reactions of $Zn(tftm)_2$ and $Fe(tmtm)_3$.

	Mass	Mass	FeL'_3	ZnL'_2	FeL''_3	ZnL''_2	FeL'_3 & ZnL''_2	
Species	Fe	Zn	Fe	Zn	Fe	Zn	Fe	Zn
$[ML'_3]^+$	605	613	1 (0.07)	<1			<1	<1
$[ML'_3$-*t*Bu$]^+$	548	556	1 (0.07)	<1			<1	<1
$[ML'_2]^+$	422	430	100 (6.67)	12			36 (1.20)	<1
$[ML'_2$-*t*Bu$]^+$	365	373	15 (1.00)	100			30 (1.00)	**18**
$[ML']^+$	239	247	16 (1.07)	8			18 (0.60)	**2**
$ML''_2]^+$	446	454			69	11 (1.00)	**4**	15 (1.00)
$[ML''_2$-43$]^+$	403	411			17	<1	**1**	<1
$[ML''_2$-*t*Bu$]^+$	389	397			46	100 (9.09)	**8**	2 (0.13)
$[ML''_2$-$CF_3]^+$	377	385			4	3 (0.27)	***36***	*17* (1.13)
$[ML''$+$CH_2CO]^+$	293	301			7	<1	<1	<1
$[ML'']^+$	251	259			20	15 (1.36)	**5**	<1
$[ML''$-$CF_2]^+$	201	209			38	11 (1.00)	**8**	2 (0.13)
$[ML''$-*t*Bu$]^+$	194	202			8	3 (0.27)	<1	<1
$[ML'L'']^+$	434	442					**27**	1
$[ML'L''$-*t*Bu$]^+$	377	385					**36**	**17**

Table 6.5 Relative positive ion intensities (% abundance) of hetero-metal species to their respective base peaks as presented in Figure 6.5. L' = (tmtm), L'' = (tftm), *Italics:* Isobaric, **Bold**: Ligand exchange product, (Parenthesis): Relative ratio

selected as the reference species to calculate the relative ratios of the corresponding parent ions. The resulting values are placed in parenthesis next to the corresponding normalized abundance in Table 6.5**.** The differences between the relative ratios allow for a more detailed scheme of the reaction pathways to become established.

First consider the gas-phase reactions between ionic $Zn(tftm)_2$ fragments and neutral $Fe(tmtm)_3$. After reviewing Table 6.5, it becomes apparent that the fragment demonstrating the greatest relative ratio difference is $[Zn(tftm)(tftm\text{-}t\text{Bu})]^+$ at *m/z* 397; decreasing from a relative ratio of 9.09 in the baseline spectrum to a relative ratio of 0.13 in the co-sublimation spectrum. The second-most attenuated peak corresponds to the species $[Zn(tftm)]^+$ at *m/z* 259 which has a relative ratio of 1.36 in the baseline spectrum, but lacks a corresponding peak in the co-sublimation spectrum. Additionally, it can be seen that the relative ratio of $[Zn(tftm)(tftm\text{-}CF_3)]^+$ at *m/z* 385 increases from a relative ratio of 0.27 to a relative ratio of 1.13 following co-sublimation. As previously

discussed, relative peak growth may reflect the attenuation of the reference species, but can also result from the detection of an isobaric species such as the mixed ligand fragment $[Zn(tmtm)(tftm\text{-}t\text{Bu})]^+$. The remaining $Zn(tftm)_2$ fragment $[Zn(tftm\text{-}CF_2)]^+$ at *m/z* 209 demonstrates a relatively small degree of peak attenuation as made evident by the relative ratio difference of 0.87.

Based on the information presented, it would seem that reactions between $[Zn(tftm)(tftm\text{-}t\text{Bu})]^+$ with neutral $Fe(tmtm)_3$ are the most productive towards the generation of ligand exchange products. In a mechanistic proposal consistent with these results, $[Zn(tftm)(tftm\text{-}t\text{Bu})]^+$ and neutral $Fe(tmtm)_3$ undergo partial ligand exchange to generate the mixed ligand fragment $[Zn(tmtm)(tftm\text{-}t\text{Bu})]^+$ at *m/z* 385, as shown in Equation (6.17).

$$[Zn^{II}(tftm)(tftm\text{-}t\text{Bu})]^+ + Fe^{III}(tmtm)_3 \rightarrow$$

$$[Zn^{II}(tmtm)(tftm\text{-}t\text{Bu})]^+ + Fe^{III}(tmtm)_2(tftm) \qquad \text{(Eqn 6.17)}$$

Additional reaction pathways can be determined by considering the reactions of ionic $Fe(tmtm)_3$ fragments with neutral $Zn(tftm)_2$. Referring back to Table 6.5, it becomes apparent that the peak corresponding to $[Fe(tmtm)_2]^+$ at *m/z* 422 undergoes a substantial degree of attenuation; decreasing from a relative ratio of 6.67 in the baseline spectrum to a relative ratio of 1.20 in the co-sublimation spectrum. The observed difference suggests $[Fe(tmtm)_2]^+$ assumes a very active role in the reaction

whereas the relative ratio difference of 0.47 exhibited by $[Fe(tmtm)]^+$ at *m/z* 239 implies a less active role.

Accordingly, the mixed ligand product $[Fe(tmtm)(tftm)]^+$ at *m/z* 434 would predominantly be generated via partial ligand exchange according to Equation (6.18). Loss of *tert*-butyl to generate $[Fe(tmtm)(tftm)\text{-}t\text{Bu})]^+$ at *m/z* 281 is consistent with the mechanistic proposal outlined in Equation (6.19).

$$[Fe^{III}(tmtm)_2]^+ + Zn^{II}(tftm)_2 \rightarrow$$

$$[Fe^{III}(tmtm)(tftm)]^+ + Zn^{II}(tmtm)(tftm) \qquad \text{(Eqn 6.18)}$$

$$[Fe^{III}(tmtm)_2]^+ + Zn^{II}(tftm)_2 \rightarrow$$

$$[Fe^{II}(tmtm)(tftm)\text{-}t\text{Bu})]^+ + Zn^{II}(tmtm)(tftm) + t\text{Bu}^{\bullet} \qquad \text{(Eqn 6.19)}$$

Chapter 7

The Co-Sublimation and Gas-Phase Ligand Exchange Reactions of Aluminum Trimethyltrimethylacetylacetonate ($Al(tmtm)_3$) with Metal Acetylacetonates ($M(acac)_n$, n = 2, 3)

7.1 Introduction

The information presented herein pertains to the investigation of gas-phase ligand exchange reactions between $Al(tmtm)_3$ and various other metal acetylacetonates. Like the prior chapter, one of the primary objectives is to interpret the products of gas-phase ligand exchange reactions. Additionally, relative ratios are calculated and analyzed to make sensible inferences on the gas-phase mechanisms contributing to the formation of the mixed ligand species.

7.2 Aluminum Trimethyltrimethylacetylacetonate ($Al(tmtm)_3$)

$Al(tmtm)_3$ is a twelve-electron complex composed of three equivalents of (tmtm) chelated to aluminum. The synthesis of this complex is outlined in Chapter 3. The EI mass spectrum is displayed in Figure 7.1 with tabulated data describing the relative abundance featured in Table 7.1. A mass range of *m/z* 325 to 580 was selected to accentuate the natural isotopic pattern of aluminum, and to allow for a closer inspection of the fragmentation pattern specific for $Al(tmtm)_3$. The base peak of the spectrum, shown at *m/z* 393, corresponds to the fragment $[Al(tmtm)_2]^+$. Deprotonation and loss of *tert*-butyl leads to the production of $[Al(tmtm)(tmtm\text{-}t\text{BuH})]^+$ at *m/z* 335. The

peak appearing at *m/z* 576 correspond to the molecular ion $[Al(tmtm)_3]^+$. Normalization of the spectrum was accomplished using the ion signal of $[Al(tmtm)_2]^+$ as the reference peak.

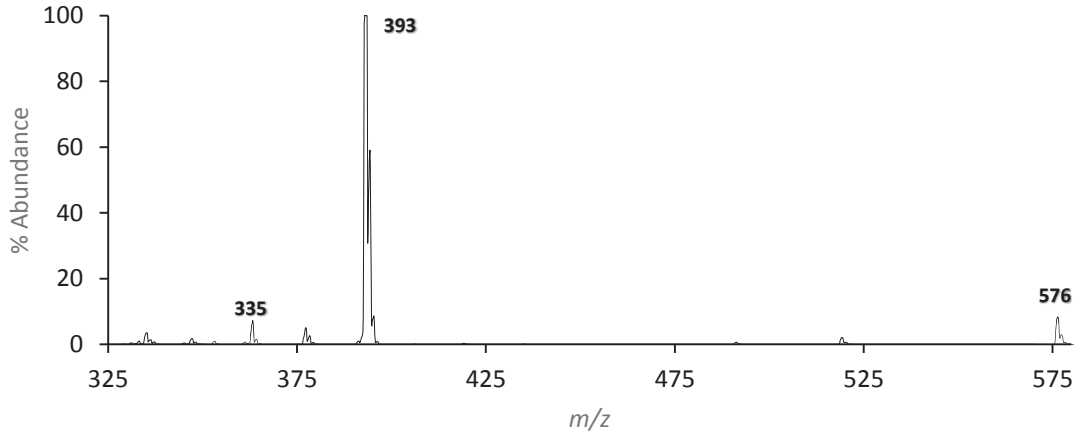

Figure 7.1: The 70 eV positive EI mass spectrum of $Al(tmtm)_3$.

Species	*m/z*	Relative Abundances
$[Al(tmtm)_3]^+$	576	8
$[Al(tmtm)_2]^+$	393	100
$[Al(tmtm)(tmtm\text{-}tBuH)]^+$	335	4

Table 7.1 The fragmentation species and corresponding relative abundances of the mass spectral analysis of $Al(tmtm)_3$ as presented in Figure 7.1.

7.3 Iron (III) Acetylacetonate ($Fe(acac)_3$)

For more information regarding the general fragmentation behavior of $Fe(acac)_3$ please refer back to Chapter 1. The base spectrum and corresponding tabulated data of $Fe(acac)_3$ may be found in Figure 7.2a and Table 7.2.

7.4 The Co-sublimation of $Al(tmtm)_3$ & $Fe(acac)_3$

The co-sublimation mass spectrum of $Al(tmtm)_3$ and $Fe(acac)_3$ is presented in Figure 7.2c. In addition, the baseline spectrum of $Fe(acac)_3$ and $Al(tmtm)_3$ are displayed above the co-sublimation spectrum in Figure 7.2a and Figure 7.2b, respectively, for comparison. The corresponding masses with their respective abundances are provided in Table 7.2.

Following a review of the co-sublimation spectrum, it becomes apparent that the combination of $Al(tmtm)_3$ and $Fe(acac)_3$ is not conducive towards the gas-phase production of ligand exchange products. At first glance, the ion signal observed at *m/z* 239 seemingly points towards the production of $[Fe(tmtm)]^+$. However, considering the absence of iron-containing products, the generally high abundance of $Fe(acac)_3$ fragments, and the relatively low abundance of $[Fe(tmtm)]^+$ in the $Fe(tmtm)_3$ baseline spectrum, it is more probable that the peak of interest reflects the detection of the isobaric parent fragment $[Fe(acac)(acac\text{-}CH_3)]^+$ with comparatively negligible detection of $[Fe(tmtm)]^+$. The only other products that appear to form in marginally substantial abundances are the mixed ligand fragments $[Al(acac\text{-}CH_4)(tmtm)]^+$ at *m/z* 293 and $[Al(acac)(tmtm\text{-}t\text{BuH})]^+$ at *m/z* 251. However, the ion signal corresponding to $[Al(acac)(tmtm\text{-}t\text{BuH})]^+$ is difficult to resolve due to its proximity to $[^{54}Fe(acac)_2]^+$ at *m/z* 252.

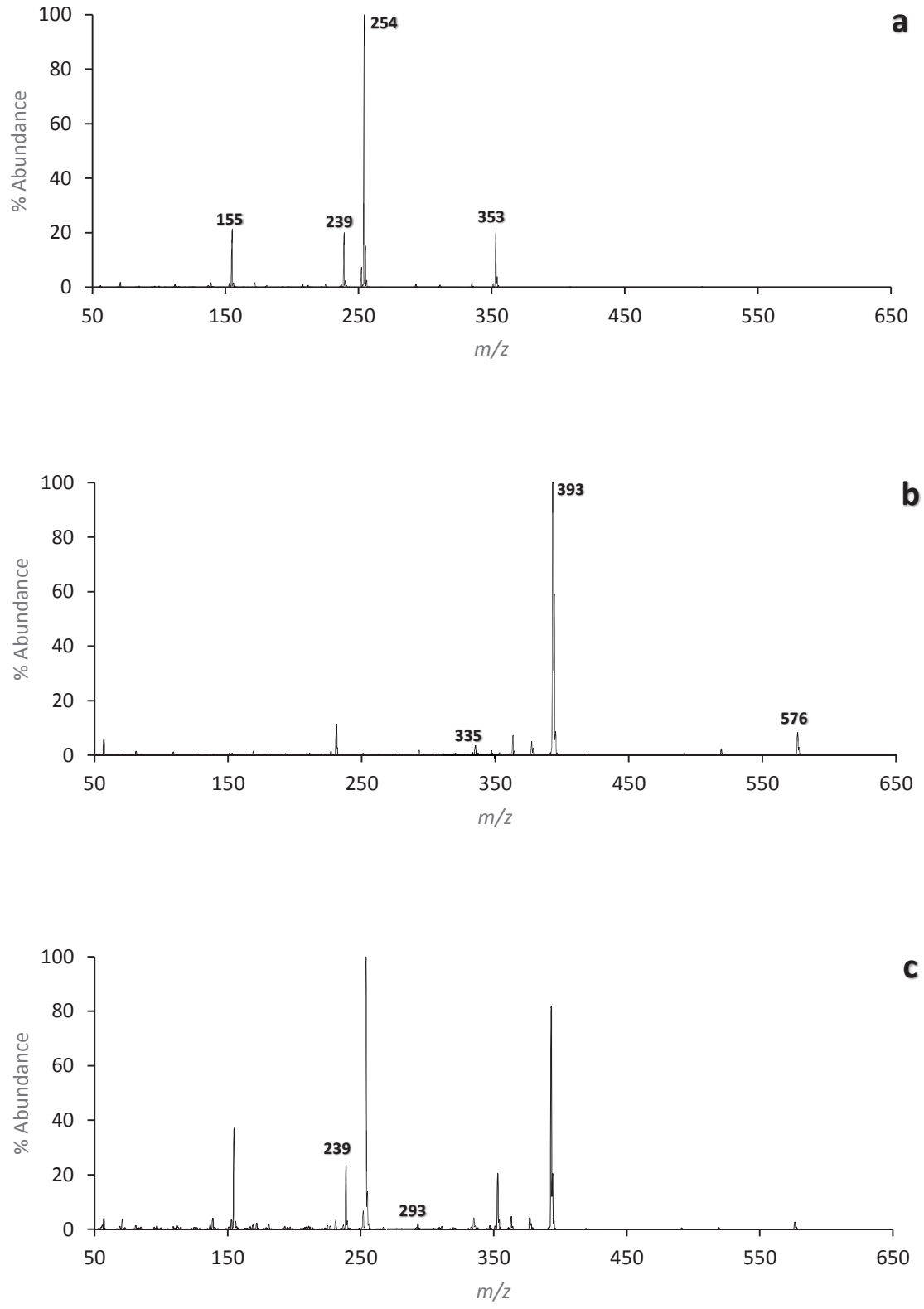

Figure 7.2: The 70eV positive EI mass spectra for a) $Fe(acac)_3$, b) $Al(tmtm)_3$, and c) the gas-phase reactions of $Fe(acac)_3$ and $Al(tmtm)_3$.

	Mass	Mass	AlL_3	FeL_3	AlL'_3	FeL'_3	AlL'_3 & FeL_3	
Species	Al	Fe	Al	Fe	Al	Fe	Al	Fe
$[ML_3]^+$	324	353	7	28			<1	21
$[ML_2]^+$	225	254	100	100			1	100
$[ML_2\text{-}CH_3]^+$	210	239	<1	59			*1*	*24*
$[ML\text{+}CH_3]^+$	141	170	5	<1			<1	<1
$[ML]^+$	126	155	<1	48			<1	37
$[ML'_3]^+$	576	605			8	1	3	<1
$[ML'_2]^+$	393	422			100	100	82	<1
$[ML'_2\text{-}tBu]^+$	336	365			4**	15	4**	<1
$[ML']^+$	210	239			<1	16	*1*	***24***
$[MLL']^+$	309	338					<1	<1
$[MLL'\text{-}CH_3]^+$	294	323					**5****	<1
$[MLL'\text{-}tBu]^+$	252	281					**7****	<1

Table 7.2 Relative positive ion intensities (% abundance) of hetero-metal species to their respective base peaks as presented in Figure 7.2. L = (acac), L' = (tmtm), **Deprotonated; observed at one mass unit lower than expected, *Italics*: Isobaric, **Bold**: Ligand exchange product

7.5 Cobalt (II) Acetylacetonate ($Co(acac)_2$)

For more information regarding $Co(acac)_2$ and its fragmentation behavior please refer back to Chapter 1, Lerach, Hunter, or Shannon.[11-13] The base spectrum and corresponding tabulated data of $Co(acac)_2$ may be found in Figure 7.3a and Table 7.3.

7.6 The Co-sublimation of $Al(tmtm)_3$ & $Co(acac)_2$

The co-sublimation spectrum of $Al(tmtm)_3$ and $Co(acac)_2$ is displayed in Figure 7.3c which illustrates, for the first time, the gas-phase formation of novel aluminum and cobalt products. To accentuate the generation of product ions, the co-sublimation spectrum is displayed directly beneath the baseline spectrum of $Co(acac)_2$ and $Al(tmtm)_3$ which are presented in Figure 7.3a and Figure 7.3b, respectively. The corresponding masses with their respective abundances are provided in Table 7.3.

As shown in Figure 7.3c, a variety of products are formed from the reaction between $Al(tmtm)_3$ and $Co(acac)_2$. The singly-ligated product $[Co(tmtm)]^+$ appears to

form at *m/z* 242, but is noted to be isobaric with the parent fragment $[Co(acac)(acac\text{-}CH_3)]^+$. The relatively high abundance associated with *m/z* 242 is more consistent with the detection of the parent fragment, but evidence supporting the formation of other ligand exchange products in appreciable abundances warrants the potential for $[Co(tmtm)]^+$ to be generated. Further support for the formation of $[Co(tmtm)]^+$ is given by the relative peak growth of $[Co(acac)(acac\text{-}CH_3)]^+$ with respect to $[Co(acac)_2]^+$ which is consistent with the peak summation of reactant and product species.

Moreover, the mixed ligand product $[Co(acac)(tmtm)]^+$ also appears to form based on the peak found at *m/z* 341 while the formation of the mixed ligand fragment $[Co(acac)(tmtm\text{-}t\text{Bu})]^+$ is indicated by the peak at *m/z* 284. The high abundance of the mixed ligand fragment is consistent with prior experimentation and literature, and is likely associated with the delocalization of positive charge across the conjugated π system of the ligand which thereby facilitates the loss of an odd electron neutral fragment.[11-13,19] Additionally, the mixed ligand product $[Al(acac)(tmtm)]^+$ appears to form at *m/z* 309.

Relative ratios of the parent ion abundances were determined using the procedure explained in Chapter 4 to attain mechanistic insight into the reaction pathways responsible for the gas-phase formation of ligand exchange products. As shown in Table 7.3, $[Co(acac\text{-}CH_3)]^+$ at *m/z* 143 and $[Al(tmtm)_2]^+$ at *m/z* 393 were

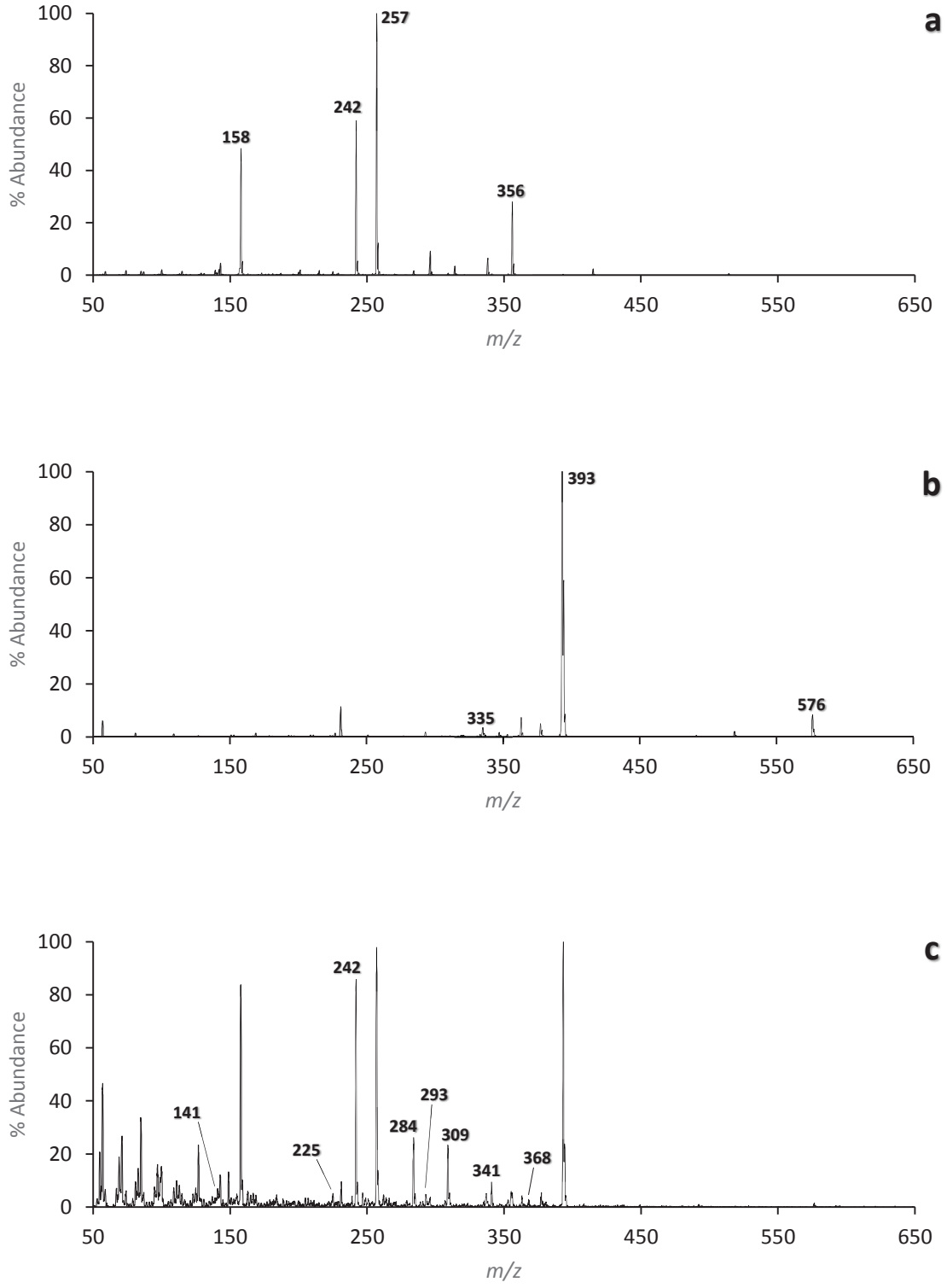

Figure 7.3: The 70eV positive EI mass spectra for a) $Co(acac)_2$, b) $Al(tmtm)_3$, and c) the gas-phase reactions of $Co(acac)_2$ and $Al(tmtm)_3$.

	Mass	Mass	AlL_3	CoL_2	AlL'_3	CoL'_2	AlL'_3 & CoL_2	
Species	Al	Co	Al	Co	Al	Co	Al	Co
$[ML_3]^+$	324	356	7	28 (5.60)			<1	5 (0.45)
$[ML_2]^+$	225	257	100	100 (20.0)			**5**	98 (8.91)
$[ML_2\text{-}CH_3]^+$	210	242	<1	59 (11.8)			*2*	*86* (7.82)
$[ML+CH_3]^+$	141	173	5	<1			**7**	1
$[ML]^+$	126	158	<1	48 (9.60)			*23*	84 (7.64)
$[ML\text{-}CH_3]^+$	111	143	<1	5 (1.00)			10	11 (1.00)
$[ML'_3]^+$	576	608			8 (0.08)	1	2 (0.02)	<1
$[ML'_2]^+$	393	425			100 (1)	29	100 (1)	1
$[ML'_2\text{-}tBu]^+$	336	368			4** (0.04)	100	2** (0.02)	**3**
$[ML']^+$	210	242			<1	17	*2*	***86***
$[MLL']^+$	309	341					**23**	**10**
$[MLL'\text{-}CH_3]^+$	294	326					**5****	<1
$[MLL'\text{-}tBu]^+$	252	284					**3****	**26**

Table 7.3 Relative positive ion intensities (% abundance) of hetero-metal species to their respective base peaks as presented in Figure 7.3. L = (acac), L' = (tmtm), **Deprotonated; observed at one mass unit lower than expected, *Italics:* Isobaric, **Bold**: Ligand exchange product, (Parenthesis): Relative ratio

selected as the reference species to calculate the relative ratios of the corresponding parent ions. The resulting values are placed in parenthesis next to the corresponding normalized abundance in Table 7.3**.** The differences between the relative ratios allow for a more detailed scheme of the reaction pathways to become established.

First consider the gas-phase reactions between ionic $Co(acac)_2$ fragments and neutral $Al(tmtm)_3$. After reviewing Table 7.3, it becomes clear that the fragment demonstrating the most substantial relative ratio decrease is $[Co(acac)_2]^+$ at *m/z* 257; decreasing from a relative ratio of 20.0 in the baseline spectrum to a relative ratio of 8.91 in the co-sublimation spectrum. The second-most attenuated relative ratio corresponds to the species $[Co(acac)_3]^+$ at *m/z* 356 which has a relative ratio of 5.60 in the baseline spectrum and decreases to a relative ratio of 0.45 upon reaction with $Al(tmtm)_3$. Additionally, the relative ratio of $[Co(acac)(acac\text{-}CH_3)]^+$ at *m/z* 242 decreases from a relative ratio of 11.8 to a relative ratio of 7.82 following co-sublimation. The remaining $Co(acac)_2$ fragment $[Co(acac)]^+$ at *m/z* 158 begins with a relative ratio of 9.60

in the baseline spectrum which then decreases to a relative ratio of 7.64 following co-sublimation.

Based on the information presented, it would seem that reactions between $[Co(acac)_2]^+$ with neutral $Al(tmtm)_3$ are the most productive towards the generation of ligand exchange products. In a mechanistic proposal consistent with these findings, $[Co(acac)_2]^+$ and neutral $Al(tmtm)_3$ undergo partial ligand exchange to generate either the mixed ligand product $[Co(acac)(tmtm)]^+$ at *m/z* 341 or the mixed ligand fragment $[Co(acac)(tmtm\text{-}t\text{Bu})]^+$ at *m/z* 284 as shown in Equation (7.1) and Equation (7.2), respectively.

$$[Co^{III}(acac)_2]^+ + Al^{III}(tmtm)_3 \rightarrow$$
$$[Co^{III}(acac)(tmtm)]^+ + Al^{III}(acac)(tmtm)_2 \qquad \text{(Eqn 7.1)}$$

$$[Co^{III}(acac)_2]^+ + Al^{III}(tmtm)_3 \rightarrow$$
$$[Co^{II}(acac)(tmtm\text{-}t\text{Bu})]^+ + Al^{III}(acac)(tmtm)_2 + t\text{Bu}^{\bullet} \qquad \text{(Eqn 7.2)}$$

A similar analysis for cationic $Al(tmtm)_3$ fragments reveals little information in regards to relative fragment reactivity. Referring back to Table 7.3, it is apparent that the relative peak heights of the parent ions in the co-sublimation spectrum are almost identical to those in the baseline spectrum. Consequently, a clear preference for one fragment to react over another is not particularly evident. However, the high abundance of $[Al(tmtm)_2]^+$ relative to all other $Al(tmtm)_3$ makes it statistically relevant in regards to

the production of ligand exchange products. In the following mechanistic proposal outlined in Equation (7.3), the mixed ligand product $[Al(acac)(tmtm)]^+$ at *m/z* 309 is generated through a process of partial ligand exchange between $[Al(tmtm)_2]^+$ and neutral $Co(acac)_2$.

$$[Al^{III}(tmtm)_2]^+ + Co^{II}(acac)_2 \rightarrow$$

$$[Al^{III}(acac)(tmtm)]^+ + Co^{II}(acac)(tmtm) \qquad \text{(Eqn 7.3)}$$

7.7 Nickel (II) Acetylacetonate ($Ni(acac)_2$)

For more information regarding $Ni(acac)_2$ and its fragmentation behavior please refer back to Chapter 1, Lerach, Hunter, or Shannon.[11-13] The base spectrum and corresponding tabulated data of $Ni(acac)_2$ may be found in Figure 7.4a and Table 7.4.

7.8 The Co-sublimation of $Al(tmtm)_3$ & $Ni(acac)_2$

Presented in Figure 7.4c is the co-sublimation spectrum resulting from the gas-phase reaction between $Al(tmtm)_3$ and $Ni(acac)_2$ which displays a series of gas-phase aluminum and nickel species for the first time. The co-sublimation spectrum is positioned directly beneath the baseline spectrum of $Ni(acac)_2$ and $Al(tmtm)_3$ which are presented in Figure 7.4a and Figure 7.4b, respectively. By stacking the spectra, the appearance of novel peaks generated from a gas-phase reaction is emphasized. The corresponding masses with their respective abundances are provided in Table 7.4.

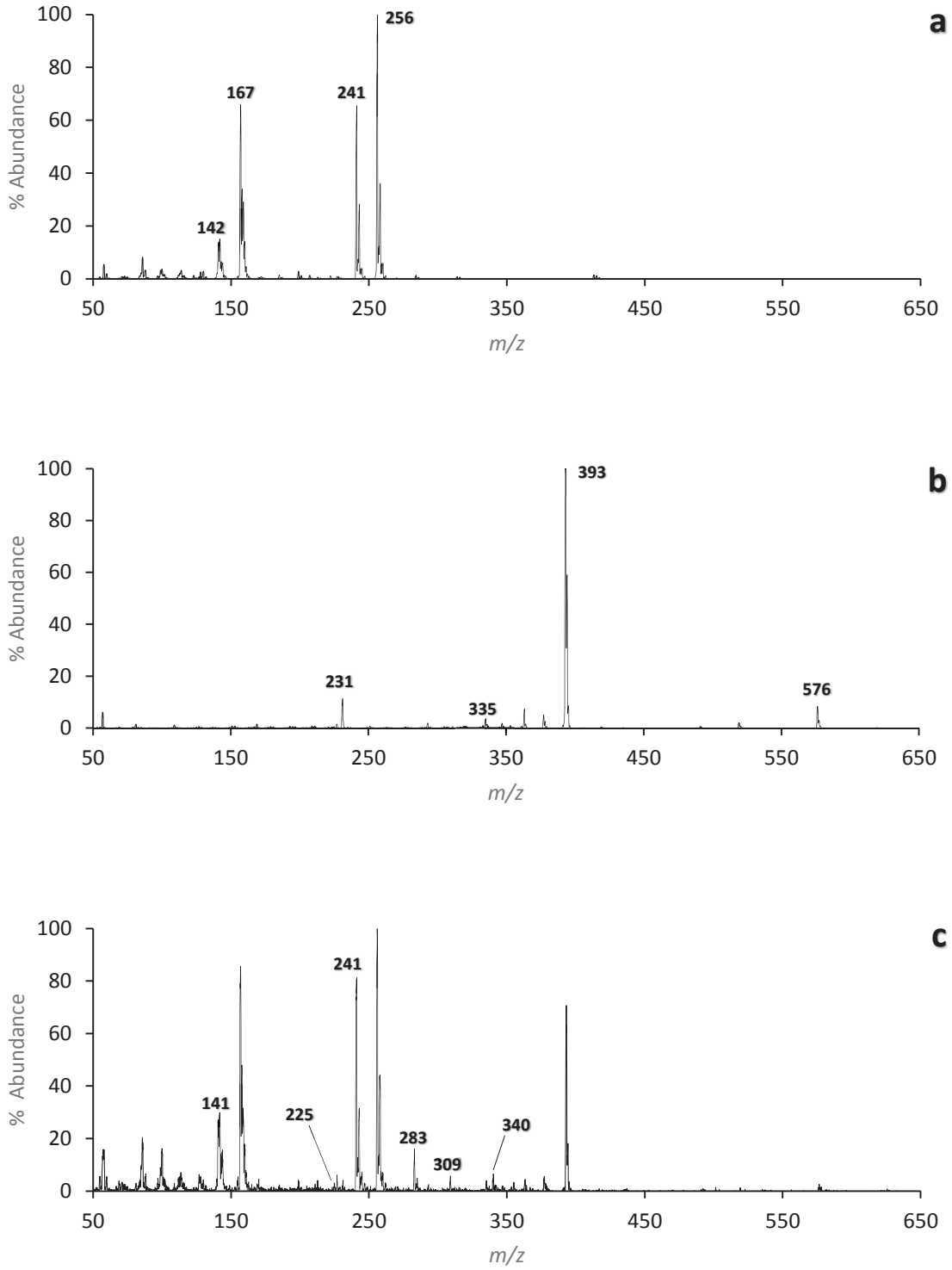

Figure 7.4: The 70eV positive EI mass spectra for a) $Ni(acac)_2$, b) $Al(tmtm)_3$, and c) the gas-phase reactions of $Ni(acac)_2$ and $Al(tmtm)_3$.

	Mass	Mass	AlL_3	NiL_2	AlL'_3	NiL'_2	AlL'_3 & NiL_2	
Species	Al	Ni	Al	Ni	Al	Ni	Al	Ni
$[ML_3]^+$	324	355	7	<1			<1	3
$[ML_2]^+$	225	256	100	100 (6.67)			**3**	100 (3.70)
$[ML_2\text{-}CH_3]^+$	210	241	<1	66 (4.40)			*1*	*81* (3.00)
$[ML\text{+}CH_3]^+$	141	172	5	1			**30**	2
$[ML]^+$	126	157	<1	66 (4.40)			*4*	85 (3.15)
$[ML\text{-}CH_3]^+$	111	142	<1	15 (1.00)			2	27 (1.00)
$[ML'_3]^+$	576	607			8 (2.00)	0	3 (0.75)	<1
$[ML'_2]^+$	393	424			100 (25.0)	48	71 (17.8)	<1
$[ML'_2\text{-}t\text{Bu}]^+$	336	367			4**(1.00)	96	4**(1.00)	1
$[ML']^+$	210	241			<1	13	*1*	***81***
$[MLL']^+$	309	340					**6**	**6**
$[MLL'\text{-}t\text{Bu}]^+$	252	283					**2****	**16**

Table 7.4 Relative positive ion intensities (% abundance) of hetero-metal species to their respective base peaks as presented in Figure 7.4. L = (acac), L' = (tmtm), **Deprotonated; observed at one mass unit lower than expected, *Italics:* Isobaric, **Bold**: Ligand exchange product, (Parenthesis): Relative ratio

The co-sublimation mass spectrum of $Al(tmtm)_3$ and $Ni(acac)_2$ present multiple examples of ligand exchange products that contain both aluminum and nickel. The apparent formation of $[Al(acac)(CH_3)]^+$ at *m/z* 141 is difficult to discern from the parent ion $[Ni(acac\text{-}CH_3)]^+$ at *m/z* 142 due to close proximity. The peak displayed at *m/z* 241 appears to indicate the formation of $[Ni(tmtm)]^+$, but also corresponds to the isobaric parent ion $[Ni(acac)(acac\text{-}CH_3)]^+$. The high abundance of other prominent $Ni(acac)_2$ fragments in the co-sublimation spectrum suggests that $[Ni(acac)(acac\text{-}CH_3)]^+$ is predominantly responsible for the peak intensity corresponding to *m/z* 241. On the other hand, the ion signal for $[Ni(acac)(acac\text{-}CH_3)]^+$ also appears to increase relative to $[Ni(acac)_2]^+$ which is consistent with the peak summation of $[Ni(acac)(acac\text{-}CH_3)]^+$ and $[Ni(tmtm)]^+$.

Additionally, the mixed ligand product $[Al(acac)(tmtm)]^+$ is generated according to the peak at *m/z* 309. Likewise, nickel-containing mixed ligand products were observed to form from a gas-phase ligand exchange reaction between $Al(tmtm)_3$ and

$Ni(acac)_2$. One such product is detected at *m/z* 340 and corresponds to the formation of $[Ni(acac)(tmtm)]^+$. Loss of *tert*-butyl leads to the production of the mixed ligand fragment $[Ni(acac)(tmtm\text{-}tBu)]^+$ at *m/z* 283. The preferential *tert*-butyl fragmentation shown to occur for the nickel mixed ligand product is consistent with prior experimentation and literature, and likely results from a destabilized molecular ion that cannot delocalize positive charge across the nickel center.[11-13,19]

As demonstrated in Chapter 4, the relative ratios of the parent ion signals were calculated to elucidate the mechanistic framework of the reactions contributing to the gas-phase formation of mixed ligand products. In this case, $[Ni(acac\text{-}CH_3)]^+$ at *m/z* 142 was selected as the reference species to calculate the relative ratios of the $Ni(acac)_2$ fragments. The resulting values are placed in parenthesis next to the corresponding normalized abundance in Table 7.4. Based on the differences observed between the relative ratios, the reaction pathways leading to the formation of mixed ligand products are increasingly discernible.

First consider the gas-phase reaction of an ionic $Ni(acac)_2$ fragment with neutral $Al(tmtm)_3$. The peak corresponding to $[Ni(acac)_2]^+$ at *m/z* 256 undergoes substantial peak attenuation; decreasing from a relative ratio of 6.67 in the baseline spectrum to a relative ratio of 3.70 in the co-sublimation spectrum. A lesser degree of peak attenuation was observed for $[Ni(acac)(acac\text{-}CH_3)]^+$ at *m/z* 241 which exhibited a relative ratio decrease from 4.40 in the baseline spectrum to a value of 3.00 following a reaction with $Al(tmtm)_3$. A similar drop in relative peak intensity is observed for $[Ni(acac)]^+$ at *m/z*

157; decreasing from a relative ratio of 4.40 in the baseline spectrum to a value of 3.15 following co-sublimation.

Consequently, reaction pathways incorporating the parent fragment $[Ni(acac)_2]^+$ with neutral $Al(tmtm)_3$ are the most prominent in regards to the production of ligand exchange products. Based on this inference, a mechanistic proposal for the gas-phase formation of the mixed ligand product $[Ni(acac)(tmtm)]^+$ at *m/z* 340 is provided in Equation (7.4) which features partial ligand exchange between neutral $Al(tmtm)_3$ and ionic $[Ni(acac)_2]^+$. Loss of *tert*-butyl to generate the mixed ligand fragment $[Ni(acac)(tmtm\text{-}t\text{Bu})]^+$ at *m/z* 283 is outlined in Equation (7.5).

$$[Ni^{II}(acac)_2]^{+\bullet} + Al^{III}(tmtm)_3 \rightarrow$$

$$[Ni^{II}(acac)(tmtm)]^{+\bullet} + Al^{III}(acac)(tmtm)_2 \qquad \text{(Eqn 7.4)}$$

$$[Ni^{II}(acac)_2]^{+\bullet} + Al^{III}(tmtm)_3 \rightarrow$$

$$[Ni^{II}(acac)(tmtm\text{-}t\text{Bu})]^{+} + Al^{III}(acac)(tmtm)_2 + t\text{Bu}^{\bullet} \qquad \text{(Eqn 7.5)}$$

Furthermore, if the reaction of an ionic $Al(tmtm)_3$ fragment with neutral $Ni(acac)_2$ is considered, additional insight into the reaction pathways can be obtained. The relative ratios for $Al(tmtm)_3$ fragments were determined using $[Al(tmtm)(tmtm\text{-}t\text{BuH})]^+$ at *m/z* 335 as the reference species. The resulting values are placed in parenthesis next to the corresponding normalized abundance in Table 7.4. A marked drop in relative intensity is observed for $[Al(tmtm)_2]^+$ at *m/z* 393 which

decreases from a relative ratio of 25.0 in the baseline spectrum to a relative ratio of 17.8 in the co-sublimation spectrum. In contrast, the relative ratio of the triply-ligated species $[Al(tmtm)_3]^+$ at *m/z* 576 only decreases by 1.25.

Based on these observations, the reactions between $[Al(tmtm)_2]^+$ and neutral $Ni(acac)_2$ are the most conducive towards the generation of ligand exchange products. The remaining $Al(tmtm)_3$ fragments, on the other hand, appear to be relatively inert and are unlikely to make significant contributions to product formation. Equation (7.6) presents a mechanistic proposal wherein $[Al(tmtm)_2]^+$ and $Ni(acac)_2$ undergo partial ligand exchange to form mixed ligand product $[Al(acac)(tmtm)]^+$ at *m/z* 309.

$$[Al^{III}(tmtm)_2]^+ + Ni^{II}(acac)_2 \rightarrow$$

$$[Al^{III}(acac)(tmtm)]^+ + Ni^{II}(acac)(tmtm) \qquad \text{(Eqn 7.6)}$$

7.9 Copper (II) Acetylacetonate ($Cu(acac)_2$)

For more information regarding $Cu(acac)_2$ and its fragmentation behavior please refer back to Chapter 1, Lerach, Hunter, or Shannon.[11-13] The base spectrum and corresponding tabulated data of $Cu(acac)_2$ may be found in Figure 7.5a and Table 7.5.

7.10 The Co-sublimation of $Al(tmtm)_3$ & $Cu(acac)_2$

Presented in Figure 7.5c is the co-sublimation spectrum of $Cu(acac)_2$ and $Al(tmtm)_3$ wherein a series of gas-phase aluminum and copper products are observed

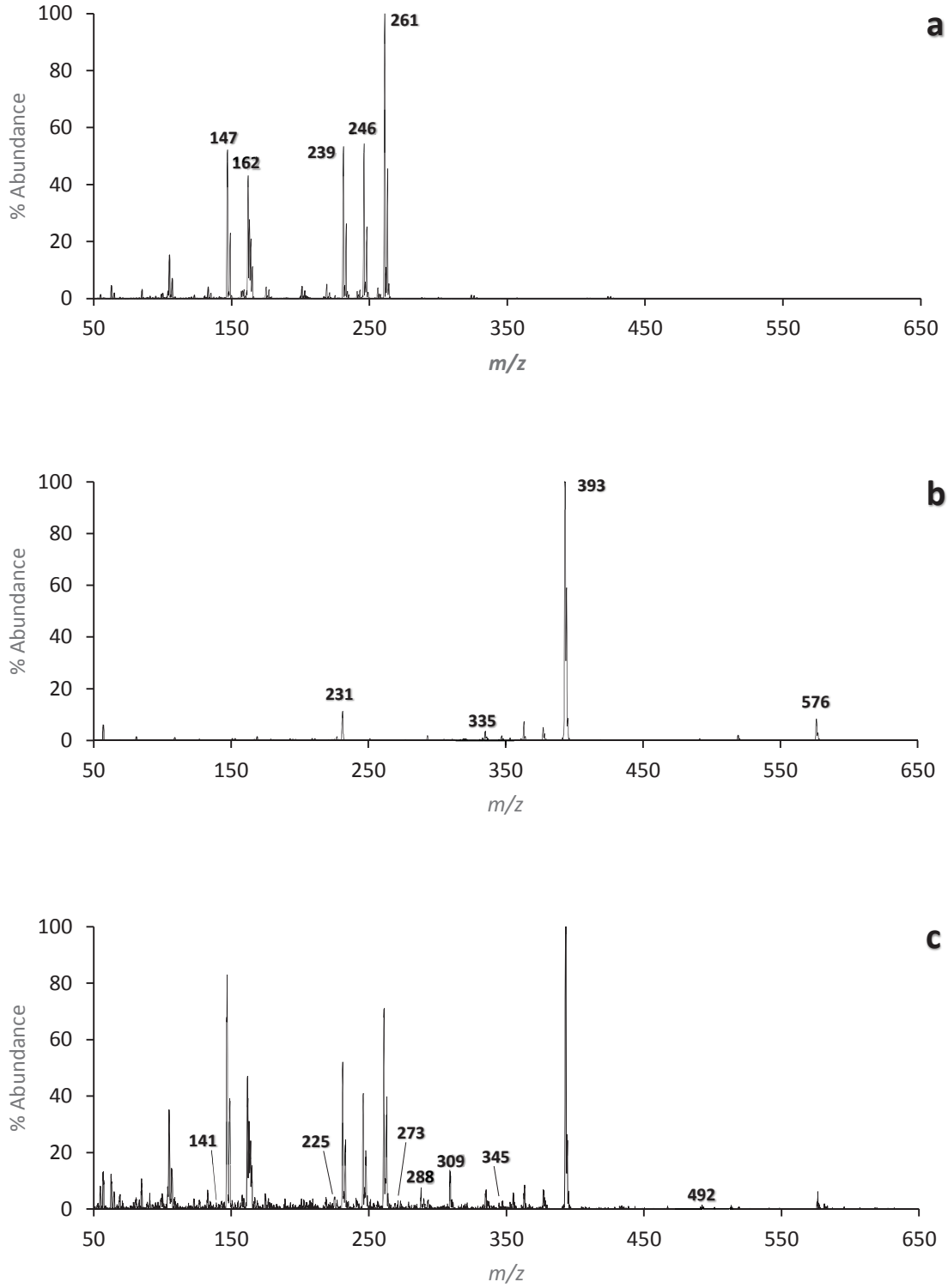

Figure 7.5: The 70eV positive EI mass spectra for a) $Cu(acac)_2$, b) $Al(tmtm)_3$, and c) the gas-phase reactions of $Cu(acac)_2$ and $Al(tmtm)_3$.

	Mass	Mass	AlL_3	CuL_2	AlL'_3	CuL'_2	AlL'_3 & CuL_2	
Species	Al	Cu	Al	Cu	Al	Cu	Al	Cu
$[ML_3]^+$	324	360	7	>1			>1	>1
$[ML_2]^+$	225	261	100	100 (1.92)			**4**	71 (0.87)
$[ML_2\text{-}CH_3]^+$	210	246	>1	54 (1.04)			*1*	*41* (0.50)
$[ML_2\text{-}2CH_3]^+$	195	231	1	53 (1.02)			2	*52* (0.63)
$[ML+CH_3]^+$	141	177	5	>1			**2**	4
$[ML]^+$	126	162	>1	43 (0.83)			*3*	47 (0.57)
$[ML\text{-}CH_3]^+$	111	147	>1	52 (1.00)			>1	82 (1.00)
$[ML'_3]^+$	576	612			8 (2.00)	>1	6 (0.86)	>1
$[ML'_2]^+$	393	429			100 (25.0)	26	100 (14.3)	>1
$[ML'_2\text{-}t\text{Bu}]^+$	336	372			4** (1.00)	59	7** (1.00)	>1
$[ML'_2\text{-}2t\text{Bu}]^+$	279	315			>1	100	3	1
$[ML']^+$	210	246			>1	9*	*1*	**8***
$[ML'\text{-}t\text{Bu}]^+$	182	189			>1	28	>1	**4**
$[MLL'_2]^+$	492	528					**2**	>1
$[MLL']^+$	309	345					**14**	**2**
$[MLL'\text{-}t\text{Bu}]^+$	252	288					**3****	**8**
$[MLL'\text{-}CH_3\text{-}t\text{Bu}]^+$	237	273					1	**3**

Table 7.5 Relative positive ion intensities (% abundance) of hetero-metal species to their respective base peaks as presented in Figure 7.5. L = (acac), L' = (tmtm), **Deprotonated; observed at one mass unit lower than expected, *Italics:* Isobaric, **Bold**: Ligand exchange product, (Parenthesis): Relative ratio

for the first time. In order to highlight novel product formation, the baseline spectrum of $Cu(acac)_2$ and $Al(tmtm)_3$ are stacked above the co-sublimation spectrum and are shown in Figure 7.5a and Figure 7.5b, respectively. The corresponding masses with their respective abundances are provided in Table 7.5.

As shown in Figure 7.5c, few examples of ligand exchange products are observed to form in substantial abundances. The peak displayed at *m/z* 492 suggests the detection of the triply-ligated product $[Al(acac)(tmtm)_2]^+$ while the peak at *m/z* 309 indicates the formation of the mixed ligand product $[Al(acac)(tmtm)]^+$. In addition, the ligand exchange product $[Cu(tmtm)H]^+$ appears to form at *m/z* 247, while the ion signal appearing at *m/z* 189 indicates the production of $[Cu(tmtm\text{-}t\text{Bu})]^+$. The mixed ligand product $[Cu(acac)(tmtm)]^+$ also appears to form such as at *m/z* 345, but only in fairly low abundance, while formation of the mixed ligand fragment $[Cu(acac)(tmtm\text{-}t\text{Bu})]^+$ can be inferred from the peak at *m/z* 288.

To gain mechanistic insight into the gas-phase formation of the aforementioned products, it was necessary to calculate and compare the relative ratios of the parent ions using the method described in Chapter 4. The fragments $[Cu(acac\text{-}CH_3)]^+$ at *m/z* 147 and $[Al(tmtm)(tmtm\text{-}t\text{BuH})]^+$ at *m/z* 335 were chosen as the reference species to evaluate the relative ratios of the corresponding parent ions. The resulting values are placed in parenthesis next to the corresponding normalized abundance in Table 7.5**.** As shown by the differences between the relative ratios, some reaction mechanisms are likely more prominent than others in regards to the formation of ligand exchange products.

The reaction between ionic $Cu(acac)_2$ fragments and neutral $Al(tmtm)_3$ will be the first to be evaluated. Based on Table 7.5, the fragment that exhibits the greatest degree of peak attenuation as a result of co-sublimation is $[Cu(acac)_2]^+$ at *m/z* 261, as made apparent by the decrease from a relative ratio of 1.92 in the baseline spectrum to a relative ratio of 0.87 in the co-sublimation spectrum. The peak demonstrating the second-most substantial decrease in relative peak height is $[Cu(acac)(acac\text{-}CH_3)]^+$ at *m/z* 246; decreasing from a relative ratio of 1.04 in the baseline spectrum to a relative ratio of 0.50 in the co-sublimation spectrum. The remaining $Cu(acac)_2$ fragments $[Cu(acac\text{-}CH_3)_2]^+$ at *m/z* 231 and $[Cu(acac)]^+$ at *m/z* 162 have relative ratio differences of 0.39 and 0.26, respectively.

Consequently, the gas-phase reaction between $[Cu(acac)_2]^+$ and neutral $Al(tmtm)_3$ appears to be the most productive reaction to generate ligand exchange products. As a result, the mixed ligand product $[Cu(acac)(tmtm)]^+$ at *m/z* 345 would

predominantly be generated through a process of partial ligand exchange as shown Equation (7.7). Loss of *tert*-butyl to generate $[Cu(acac)(tmtm\text{-}t\text{Bu})]^+$ at *m/z* 288 is consistent with the mechanistic proposal provided in Equation (7.8).

$$[Cu^{II}(acac)_2]^{+\bullet} + Al^{III}(tmtm)_3 \rightarrow$$

$$[Cu^{II}(acac)(tmtm)]^{+\bullet} + Al^{III}(acac)(tmtm)_2 \qquad \text{(Eqn 7.7)}$$

$$[Cu^{II}(acac)_2]^{+\bullet} + Al^{III}(tmtm)_3 \rightarrow$$

$$[Cu^{II}(acac)(tmtm\text{-}t\text{Bu})]^{+} + Al^{III}(acac)(tmtm)_2 + t\text{Bu}^{\bullet} \qquad \text{(Eqn 7.8)}$$

Additional insight into the reaction pathways can be gained if the reaction of an ionic $Al(tmtm)_3$ fragment with neutral $Cu(acac)_2$ is considered. Again by referring to Table 7.5, it becomes apparent that the peak corresponding to $[Al(tmtm)_2]^+$ at *m/z* 393 decreases from a relative ratio of 25.0 in the baseline spectrum to a relative ratio of 14.3 in the co-sublimation spectrum. A smaller degree of difference is observed for the fragment $[Al(tmtm)_3]^+$ at *m/z* 576 which decreases from a relative ratio of 2.00 to a relative ratio of 0.86 upon reaction with $Cu(acac)_2$.

The high degree of peak attenuation for the species $[Al(tmtm)_2]^+$ suggests that this fragment is most conducive towards the generation of ligand exchange products following reaction with neutral $Cu(acac)_2$. The mechanistic proposal presented in Equation (7.9) is consistent with the observed results and accounts for the formation of the mixed ligand product $[Al(acac)(tmtm)]^+$ at *m/z* 309.

$$[Al^{III}(tmtm)_2]^+ + Cu^{II}(acac)_2 \rightarrow$$

$$[Al^{III}(acac)(tmtm)]^+ + Cu^{II}(acac)(tmtm) \qquad \text{(Eqn 7.9)}$$

7.11 Zinc Acetylacetonate ($Zn(acac)_2$)

For more information regarding $Zn(acac)_2$ and its fragmentation behavior please refer back to Chapter 1, Lerach, Hunter, or Shannon.[11-13] The base spectrum and corresponding tabulated data of $Zn(acac)_2$ may be found in Figure 7.6a and Table 7.6.

7.12 The Co-sublimation of $Al(tmtm)_3$ & $Zn(acac)_2$

Shown in Figure 7.6c is the co-sublimation spectrum resulting from the gas-phase reaction between $Zn(acac)_2$ and $Al(tmtm)_3$ which displays a series of gas-phase aluminum and zinc species for the first time. The baseline spectrum of $Zn(acac)_2$ and $Al(tmtm)_3$ are stacked above the co-sublimation spectrum in Figure 7.6a and Figure 7.6b, respectively, to accentuate the formation of ligand exchange products in Figure 7.6c. The corresponding masses with their respective abundances are provided in Table 7.6.

As made evident in Figure 7.6c, the co-sublimation of $Zn(acac)_2$ and $Al(tmtm)_3$ is fairly unconducive towards the gas-phase production of ligand exchange products. The ion signal appearing in low abundance at *m/z* 309 suggests the generation of the mixed ligand product $[Al(acac)(tmtm)]^+$ while the mixed ligand fragment $[Al(acac)(tmtm\text{-}t\text{BuH})]^+$ at *m/z* 251 seems to be generated from deprotonation coupled with a loss of *tert*-butyl. However, the markedly high abundance associated with

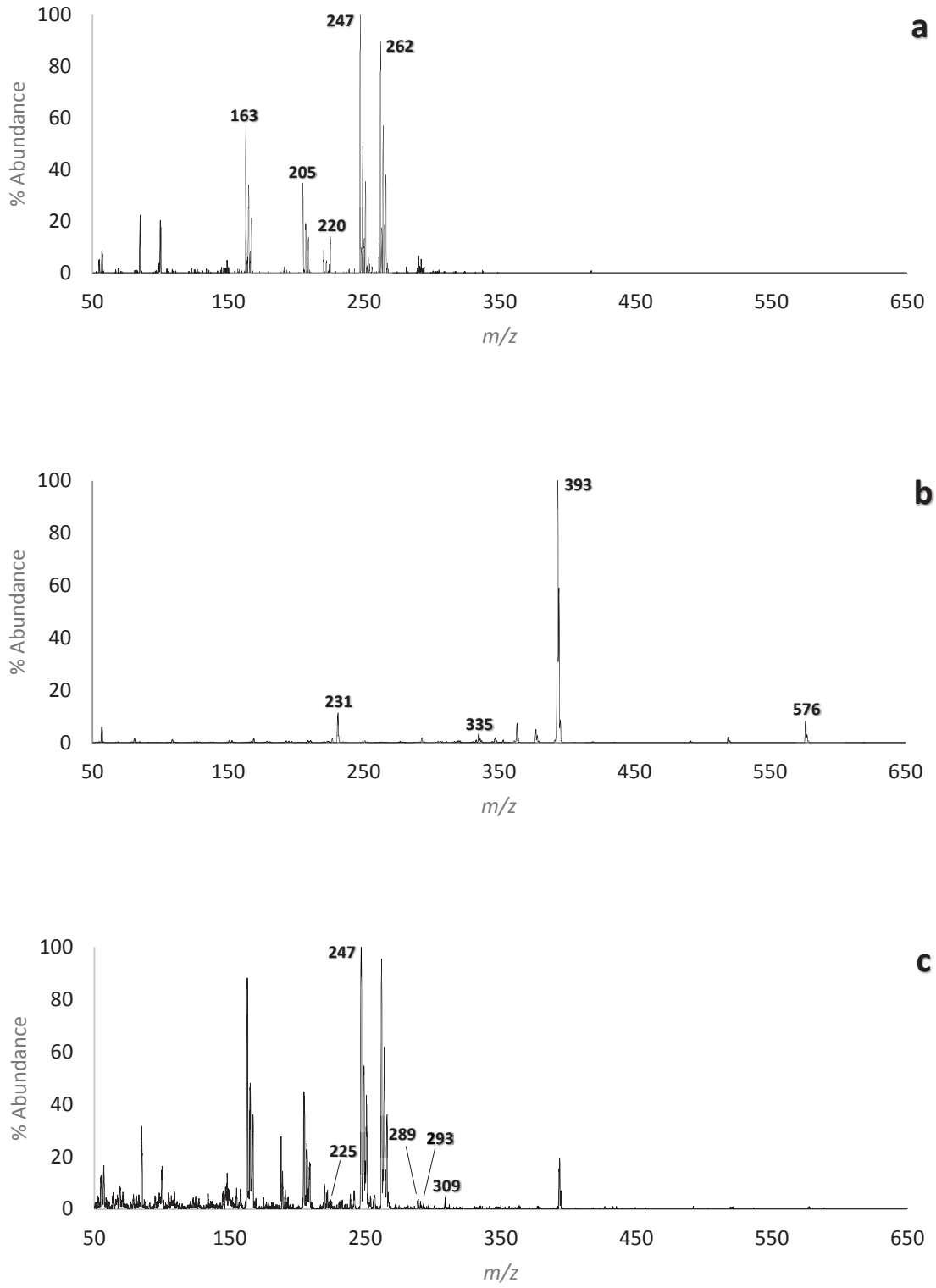

Figure 7.6: The 70eV positive EI mass spectra for a) $Zn(acac)_2$, b) $Al(tmtm)_3$, and c) the gas-phase reactions of $Zn(acac)_2$ and $Al(tmtm)_3$.

	Mass	Mass	AlL_3	ZnL_2	AlL'_3	ZnL'_2	AlL'_3 & ZnL_2	
Species	Al	Zn	Al	Zn	Al	Zn	Al	Zn
$[ML_3]^+$	324	361	7	>1			>1	>1
$[ML_2]^+$	225	262	100	90			**3**	96
$[ML_2\text{-}CH_3]^+$	210	247	>1	100			*2*	*100*
$[ML_2\text{-}CH_2CO]^+$	183	220	1	9			1	10
$[ML+CH_2CO]^+$	168	205	>1	35			3	45
$[ML+CH_3]^+$	141	178	5	>1			1	2
$[ML]^+$	126	163	>1	57			4	88
$[ML'_3]^+$	576	612			8 (1.60)	>1	>1 (0.00)	>1
$[ML'_2]^+$	393	430			100 (20.0)	12	19 (19.0)	>1
$[ML'_2\text{-}t\text{Bu}]^+$	336	373			5** (1)	2	1** (1)	>1
$[ML']^+$	210	247			>1	8	*2*	***100***
$[MLL']^+$	309	346					**5**	1
$[MLL'\text{-}CH_3]^+$	294	331					**3****	1
$[MLL'\text{-}t\text{Bu}]^+$	252	289					***43****	**4**

Table 7.6 Relative positive ion intensities (% abundance) of hetero-metal species to their respective base peaks as presented in Figure 7.6. L = (acac), L' = (tmtm), **Deprotonated; observed at one mass unit lower than expected, *Italics:* Isobaric, **Bold**: Ligand exchange product

$Al(acac)(tmtm\text{-}t\text{BuH})]^+$ is more likely attributed to the isotopic zinc fragment $[^{68}Zn(acac)(acac\text{-}CH_3)]^+$ at *m/z* 251.

Among the ion signals associated with zinc-containing complexes, only two correspond to potential ligand exchange products. The first corresponds to the singly-ligated species $[Zn(tmtm)]^+$ at *m/z* 247 while the second peak at *m/z* 289 is indicative of the mixed ligand fragment $[Zn(acac)(tmtm\text{-}t\text{Bu})]^+$. However, the formation of $[Zn(tmtm)]^+$ is considerably uncertain due to its isobaric nature with the parent fragment $[Zn(acac)(acac\text{-}CH_3)]^+$, the generally high abundance of $Zn(acac)_2$ fragments, lack of zinc-containing products, and low abundance of $[Zn(tmtm)]^+$ in the $Zn(tmtm)_2$ baseline spectrum. As a result, the mixed ligand fragment $[Zn(acac)(tmtm\text{-}t\text{Bu})]^+$ appears to be the only zinc-containing product formed from the gas-phase reaction between $Al(tmtm)_3$ and $Zn(acac)_2$, albeit in low abundance.

Chapter 8

Computational Analysis of the Gas-Phase Ligand Exchange Reactions Between Copper (II) Acetylacetonate ($Cu(acac)_2$) and Copper (II) Ethylethylacetylacetonate ($Cu(eeac)_2$)

The computational work presented herein attempts to account for the gas-phase formation of mixed ligand products under the reaction conditions of mass spectrometric analysis. All intermediates and transition states were modeled using the PM3 semi-empirical method with Spartan '04 Computational Software. In order to reduce computational cost and complexity, a homo-metal system was selected to model the partial ligand exchange mechanism; namely, the reaction between copper (II) acetylacetonate ($Cu(acac)_2$) and copper (II) ethylethylacetylacetonate ($Cu(eeac)_2$) as shown in Figure 8.1. While not entirely representative of the previously discussed gas-phase reactions, the reaction model highlights general features thought to be employed during ligand exchange processes.

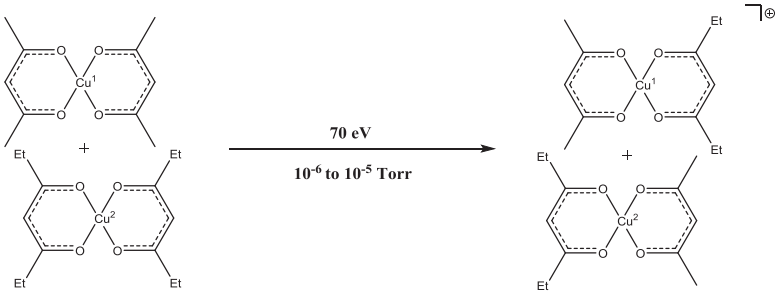

Figure 8.1: Partial ligand exchange reaction between $Cu(acac)_2$ and $Cu(eeac)_2$ following ionization as conducted during EI mass spectrometry.

Two different possibilities were considered for the mechanism of partial ligand exchange between homo-metal chelates. One possibility is that the reaction occurs via a concerted process wherein ligand exchange occurs in a single step to produce the mixed ligand product. The second possibility is that the reaction occurs via a multistep pathway that incorporates sequential bond forming and breaking events to ultimately produce the mixed ligand products. If the reaction is indeed occurring through a concerted exchange process, the transition state would be cyclic in nature which is more prevalent in synthetic organic chemistry and biosynthetic processes. According to the Woodward-Hoffman Rules, in order for a pericyclic reaction to occur under thermal conditions, the phases of the molecular orbitals (MOs) must overlap and satisfy the conservation of orbital symmetry. However, under photochemical conditions, some symmetry forbidden reactions can be achieved by promoting π electrons of conjugated π systems to the next highest energy level which may have the appropriate symmetry for reaction.

To satisfy the conservation of orbital symmetry, the transition state of concerted partial ligand exchange should resemble the model shown in Figure 8.2 where orbital

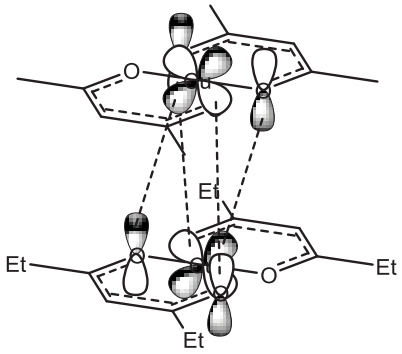

Figure 8.2: Proposed transition state for a pericyclic reaction between neutral and cationic cupric chelates.

overlap occurs between the metal d orbitals and ligand orbitals of the opposing complex. To predict the viability of a concerted transition state, the HOMO of $Cu(acac)_2$ and the LUMO of $[Cu(eeac)_2]^+$ were determined and then compared. As shown in Figure B1, the frontier orbitals do not exhibit the appropriate symmetry to allow for a pericyclic reaction. Photoexcitation of the HOMO would not likely resolve orbital incompatibility since higher energy orbitals lack d orbital character.

In any case, an energy profile was constructed to map energy as a function of bridging Cu-O bond distance, as shown in Figure B2. The energy maximum corresponding to 2.640 Å provided an appropriate bond length to be incorporated into the concerted transition state calculation. The resulting structure shown in Figure B3 reveals an unlikely transition state with four inequivalent bond lengths for the bridging Cu-O bonds, ranging from 2.67 Å to 4.77 Å, and one imaginary frequency at i269.31 cm^{-1} that corresponds to a single Cu-O bond stretch at the shortest Cu-O bond. Consequently, it would appear another mechanistic pathway could more accurately represent the gas-phase ligand exchange process.

Another possibility to be considered is a stepwise mechanism that features sequential bond formation and cleavage. In fact, a very common form of ligand

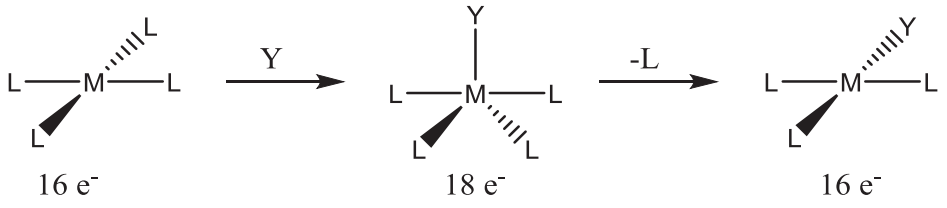

Figure 8.3: General mechanism of associative ligand substitution.[33]

substitution in both coordination and organometallic chemistry is known as associative ligand substitution and features sequential bond formation and cleavage, as shown in Figure 8.3.[33] This type of substitution commonly occurs with 16-electron square planar complexes wherein the incoming ligand binds to the metal center to form a relatively stable 18-electron trigonal bipyramidal intermediate. The resulting intermediate then undergoes the loss of a previously bound ligand to form a new 16-electron square planar complex.

Cationic cupric chelates are square planar complexes, as shown in Figure B1, and have 16-electron configurations owing to two XL-type ligands, a d^9 electron configuration, and the loss of a valence electron. Consequently, both $[Cu(acac)_2]^+$ and $[Cu(eeac)_2]^+$ are suitable candidates for associative ligand substitution. For each step of the mechanistic pathway, an equilibrium or transition state geometry optimization was performed to determine a local energy minimum or saddle point, respectively, on the potential energy surface as shown in Table 8.1 and Figure B4 to B20. Energy profiles of bond formations and cleavages were constructed to determine appropriate constraints for each Cu-O bond formed or broken during the reaction. For each transition state optimization, only one imaginary vibrational mode was calculated, and all were shown to correspond to Cu-O bond stretching. The associated bond lengths were consistently determined to be between the range of 2.700 Å and 2.800 Å.

With the above information in hand, a complete reaction mechanism was assembled in Figure 8.4 to model the partial ligand exchange between $Cu^a(acac)_2$ and

	Energy (kcal/mol)	v (cm^{-1})	Bond Length* (Å)
1	-353.4		
TS1	-345.1	i342.89	2.740
2	-382.0		
TS2	-324.1	i327.29	2.736
3	-347.0		
TS3	-325.5	i328.18	2.792
4	-351.2		
TS4	-318.9	i310.51	2.800
5	-363.3		
TS5	-349.7	i276.00	2.715
6	-372.1		
TS6	-323.2	i233.13	2.762
7	-338.7		
TS7	-310.7	i334.78	2.700
8	-382.0		
TS8	-346.3	i280.91	2.761
9	-359.9		

Table 8.1 Heats of formation, imaginary frequencies, and bond lengths for calculated reaction intermediates and transition states.
*Bond length of the Cu-O bond either forming or breaking in the corresponding transition state.

$Cu^b(eeac)_2$ with the corresponding reaction coordinate presented in Figure 8.5. Following ionization, the reaction commences with the ligation of an (acac) oxygen from $Cu(acac)_2$ to Cu^b to form **2** from **1** via **TS1**. Bond cleavage of one of four Cu^b-O bond ensues through **TS2** to produce intermediate **3**. The dissociated carbonyl oxygen then binds to Cu^a as illustrated by **TS3** to generate **4**. Bond cleavage between the bridging oxygen atom and Cu^a produces intermediate **5** via **TS4** which subsequently enters **TS5** wherein the bridging (acac) ligand becomes fully chelated to Cu^b to form **6**. Intermediate **6** then undergoes Cu^b-O bond cleavage through **TS6** which results in the complete dissociation of (eeac) from Cu^b to form **7**. The dissociated carbonyl oxygen of (eeac) becomes ligated to Cu^a, as shown in **TS7,** and results in the formation of intermediate **8**. To complete the mechanistic pathway, the bridging (acac) completely dissociates from Cu^a via **TS8** to produce the mixed ligand exchange product $[Cu(acac)(eeac)]^+$ and its neutral counterpart.

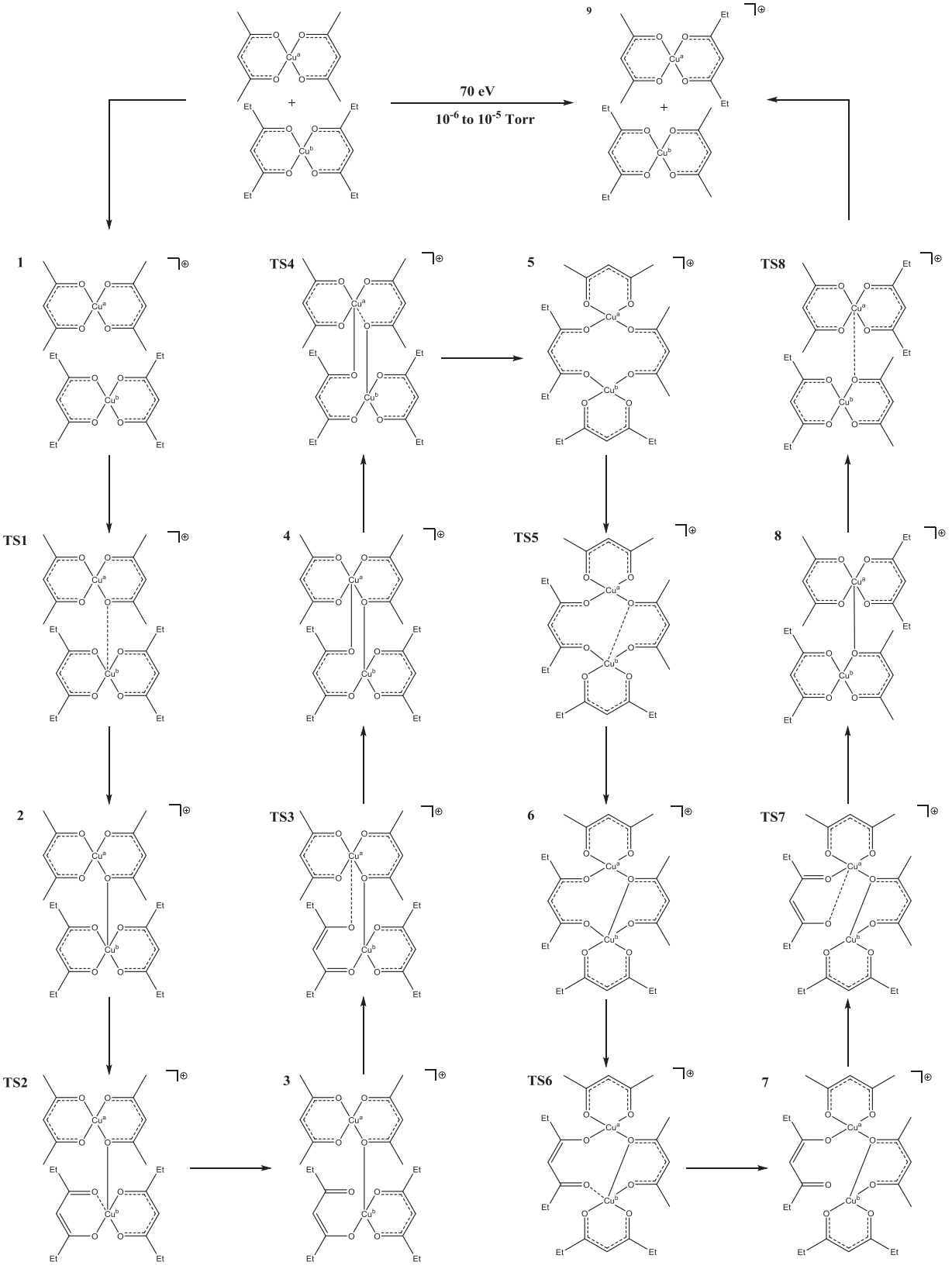

Figure 8.4: Mechanistic proposal for the gas-phase reaction of $Cu(acac)_2$ and $Cu(eeac)_2$.

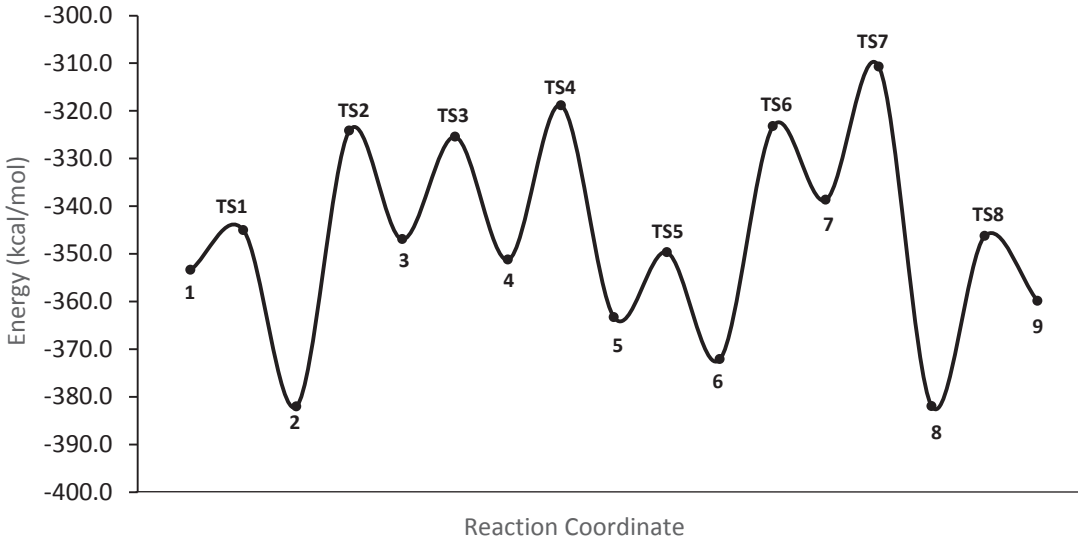

Figure 8.5: Reaction coordinate for the gas-phase reaction of $Cu(acac)_2$ and $Cu(eeac)_2$.

The relative stability associated with intermediates **2** and **8** is likely associated with the electron configuration associated with Cu^a and Cu^b in the encounter complex. In both **2** and **8**, one of two copper centers is pentacoordinate; bound to two XL-type ligands and one L-type ligand. In a neutral cupric complex, the ligand orbitals contribute ten electrons while the atomic orbitals of copper provide nine electrons for a total of 19 electrons. However, in a cationic complex, one of the electrons from the ligand orbitals is ejected, bringing the electron count down to a noble gas configuration of 18 electrons. Despite also having pentacoordinate centers, intermediates **4** and **6** are relatively unstable in comparison to **2** and **8** which can possibly be associated with geometrical distortions.

The relatively high stability of intermediates **2** and **8** does not necessarily contradict the absence of dimer detection from experimental work since the system employs very low pressures and a high abundance of energy. With an energy excess,

reaction progress is not inhibited by high energy barriers. Consequently, the lifetime of any enthalpically favored intermediates under the reaction conditions would be too fleeting for detection. Furthermore, following product formation and encounter complex dissociation, the resulting products will unlikely be given the opportunity to undergo a reverse exchange process due to low collisional frequency which eliminates the possibility of thermodynamic equilibration.

Conclusions

In closing, the production of ligand exchange products via the co-sublimation of hetero-metal chelates has clearly been established from the results and discussions presented in prior chapters. In fact, almost every combination of metal β-diketonate employed was conducive towards gas-phase ligand exchange and resulted in the generation of mixed ligand products and other various ligand exchange products. The reaction between $Al(tmtm)_3$ and $Fe(acac)_3$ was the only exception which lacked experimental evidence for gas-phase ligand exchange. In addition, the production of hexacoordinate mixed ligand species from trivalent reactants was shown to be a fairly rare event; only occurring to a small degree for the reactions between $Fe(tmtm)_3$ and $Cu(acac)_2$, $Fe(tmtm)_3$ and $Cu(tftm)_2$, $Fe(tmtm)_3$ and $Co(acac)_2$, and lastly, $Al(tmtm)_3$ and $Cu(acac)_2$.

Relative ratios of parent ions were calculated and analyzed in Chapters 4 through 7 to evaluate fragment reactivity, and in Chapters 6 and 7 to construct mechanistic proposals to account for the formation of mixed ligand products. In Chapters 4 and 5, the mass-selected reactions of $Fe(tmtm)_3$ and copper chelates were investigated to elucidate the reaction pathways responsible for the production of ligand exchange products. The number of products generated from the mass-selected reactions between cationic iron fragments and neutral cupric fragments was shown to be consistent with the fragment reactivity inferred from relative ratio analyses. In addition, collision-

induced reactions between cationic $Cu(acac)_2$ fragments and neutral $Fe(tmtm)_3$ appear to resolve the ambiguity in fragment reactivity based on the corresponding relative ratio analysis. The mass-selected reactions between cationic $Cu(tftm)_2$, on the other hand, only partially reflected the findings from the corresponding relative ratio analysis.

Considering the results of all reactions investigated, it appears as though multiple factors contribute towards fragment reactivity. In most instances, the parent ion with the greatest baseline abundance was also the most reactive, as suggested by the relative ratio analyses and the mass-selected reactions of $Fe(tmtm)_3$ fragments. However, the importance of statistical relevance may decrease as the electron count of the complex increases, as suggested by the collision-induced reactions of $Cu(acac)_2$ where the molecular ion was shown to generate a lesser variety of products despite being the most abundant parent ion in the corresponding baseline spectrum. In this case, reactions appear to be more favorable for less coordinatively saturated fragments resulting from the loss of a ligand or branching substituent. Interestingly enough, despite having moderate to high baseline abundances and a low electron count, the Cu(I) complexes also exhibit a low degree of reactivity. Aside from the inherent inability to generate certain mixed ligand products, these complexes also lack denticity which would eliminate the possibility of π-π stacking which may prove useful for attaining an optimal orientation to allow ligand exchange to occur.

Finally, Chapter 8 presented a general mechanistic pathway, modeled by the PM3 semi-empirical method, to account for the gas-phase formation of mixed ligand

products via partial ligand exchange. The proposal outlines a process of sequential bond formations and dissociations consistent with associative ligand substitution. While seemingly appropriate for a Cu-Cu encounter complex, future investigations of hetero-metal systems may require modifications to construct a viable reaction pathway. In addition, future work could implement density functional theory to improve the credibility of the proposed mechanism.

References

1. Burtoloso, A.C. *Synlett* **2005** *18*, 2859-2860.
2. Zhang, C.; Feng, P.; Jiao, N. *J. Am. Chem. Soc.* **2013**, *135*, 15257.
3. Zhou, Z. *et al. J. Chem. Soc., Chem. Commun.* **1984**, 1038-1040.
4. O'Neill, P.M. *et al. Tetrahedron Lett.* **2003**, *44*, 8135-8138.
5. Sun, P.P., Duan, J.P., Shih, H.T., Cheng, C.H. *Appl. Phys. Lett.* **2002** *81*, 792.
6. Katok, K.V., Terttkh, V.A., Brichka, S.Y., Prikhod, G.P. *Journal of Thermal Analysis and Calorimetry* **2006** *86*, 109-114.
7. Condorelli, G. G., Malandrino, G., Fragalà, I. L. *Coordination Chemistry Reviews* **2007** *251*, 1931-1950.
8. Liguori, P.F. *et al*. *Dalton Transactions* **2010** *39*, 4205-4212.
9. Seršen, S. *et al*. *Journal of Medicinal Chemistry* **2015** *58*, 3984−3996.
10. Majer, J.R., Perry, R. *Chemical Communications* **1969** *9*, 454-455.
11. Lerach, J.O., Investigations into the Gas-Phase Rearrangements of Some Transition Metal β-Diketonate Complexes, MS Thesis, Youngstown State University, August 2008.
12. Hunter, G.O., The Examination of the Stability and Reactivity of Select Transition Metal β-Diketonate Complexes During Gas-Phase Ligand Exchange Reactions, MS Thesis, Youngstown State University, December 2009.
13. Macdonald, C. G., Shannon, J. S. *Australian Journal of Chemistry* **1966** *19*, 1454-1566.
14. Bancroft, G. M., Reichert, C., Westmore, J. B. *Inorg. Chem.* **1968** *7(5)*, 870-874.

15. Koob, R. D., Morris, M. L., Clobes, A. L. *Chemical Communications* **1969** *20*, 1177-1178.

16. Clobes, A. L., Morris, M. L., Koob, R. D. *Organic Mass Spectrometry* **1971** *5*, 633-649.

17. Clobes, A.L., Morris, M. L., Koob, R. D. *Journal of the American Chemical Society* **1969** *11*, 3087–3089.

18. Morris, M.L., Koob R.D. *Inorg. Chem.* **1981** *20*, 2731-2738.

19. Westmore, J. B., *Chemical Reviews* **1976** *6*, 695-715.

20. Fahlman, B. D., Barron, A. R. *Advanced Materials for Optics and Electronics* **2000** *10*, 223-232.

21. Croxtall, B., Fawcett, J. Hope, E. G., Stuart, A. M. *Journal of Fluorine Chemistry* **2003** *119*, 65-73.

22. Jones, M. M. *Journal of the American Chemical Society* **1959** *8*, 3188-3189.

23. Reid, J. C., Calvin, M. *Journal of the American Chemical Society* **1950** *72*, 2948-2952.

24. Skopenko, V. V., Amirkhanov, V. M., Yu Sliva, T., Vasilchenko, I. S., Anpilova, E. L., Garnoskii, A. D. *Russian Chemical Reviews* **2004** *73(8),* 737-752.

25. Pierce, J. L., Busch, K. L. Graham Cooks, R., Walton, R. A. *Inorganic Chemistry* **1982** *21*, 2597-2602.

26. Curtis, J. M., Derrick, P.J. *Inorganica Chimica Acta* **1992** *201*, 197-201.

27. Wyatt, M. F., Havard, S., Stien, B.K., Brenton, A.G., *Rapid Communications in Mass Spectrometry* **2008** *22*, 11-18.

28. Van Bramer, S.E. *An Introduction to Mass Spectrometry*. Widener University, Chester, PA, 1997.

29. Klein, D.R. *Organic Chemistry*, 2nd ed.; John Wiley & Sons, Inc., 2012.

30. Borisov, S.V. *et al*. *J. Struct. Chem.* **2011**, *52*, 1070-7077.

31. Watson, W.H., Lin, C. *Inorg. Chem.* **1966**, *5*, 1074-1077.

32. Bhanage, B.M., Tambade, P.J., Patil, Y.P. *Appl. Organometal. Chem.* **2009**, *23*, 235-240.

33. Hartwig, J.F. *Organotransition Metal Chemistry: From Bonding to Catalysis*, 1st ed.; University Science Books, 2009.

Appendix A:

Baseline Spectra of Synthesized Metal β-Diketonates

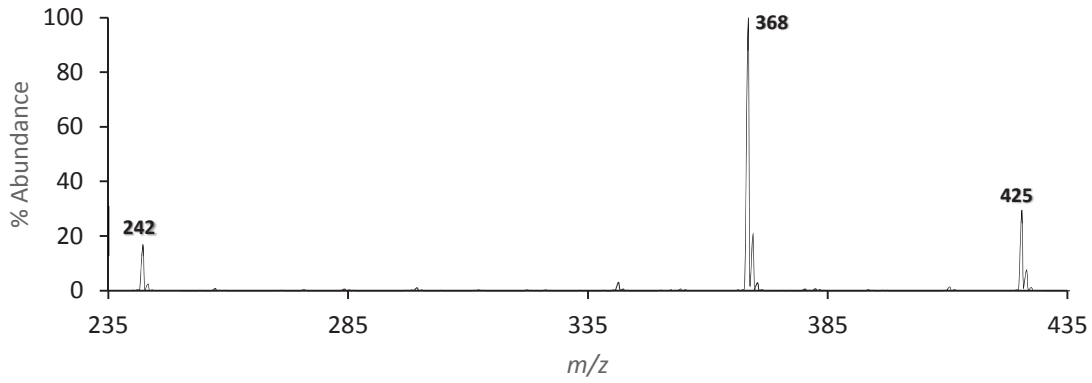

Figure A1: The 70 eV positive EI mass spectrum of $Co(tmtm)_2$.

Species	*m/z*	Relative Abundances
$[Co(tmtm)_2]^+$	425	29
$[Co(tmtm)(tmtm\text{-}tBu)]^+$	368	100
$[Co(tmtm)]^+$	242	17

Table A1 The fragmentation species and corresponding relative abundances of the mass spectrometric analysis of $Co(tmtm)_2$ as presented in Figure A1.

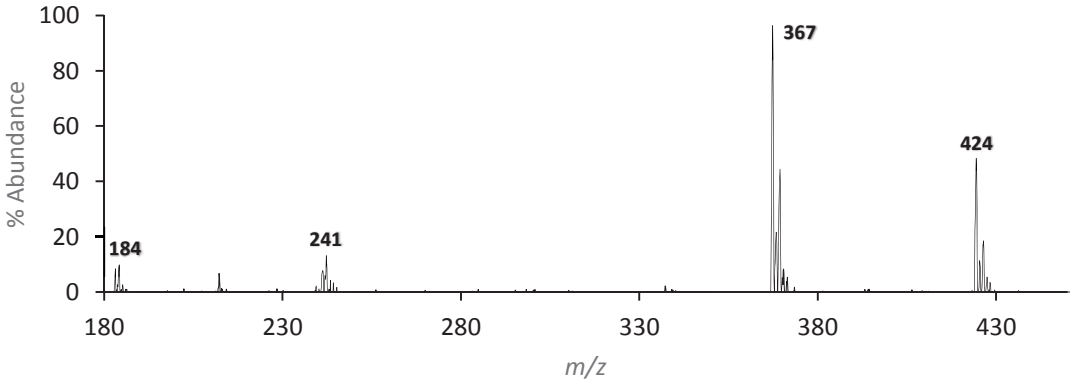

Figure A2: The 70 eV positive EI mass spectrum of $Ni(tmtm)_2$.

Species	*m/z*	Relative Abundances
$[Ni(tmtm)_2]^+$	424	48
$[Ni(tmtm)(tmtm\text{-}tBu)]^+$	367	96
$[Ni(tmtm)]^+$	241	14
$[Ni(tmtm\text{-}tBu)]^+$	184	10

Table A2 The fragmentation species and corresponding relative abundances of the mass spectrometric analysis of $Ni(tmtm)_2$ as presented in Figure A2.

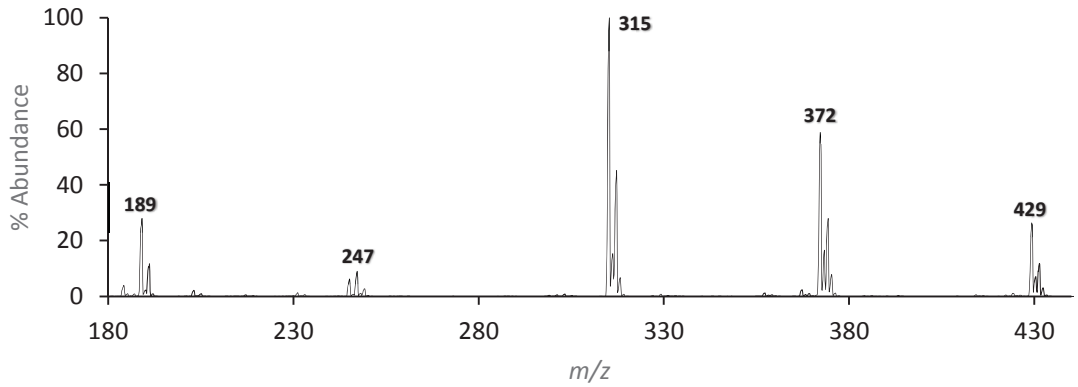

Figure A3: The 70 eV positive EI mass spectrum of $Cu(tmtm)_2$.

Species	*m/z*	Relative Abundances
$[Cu(tmtm)_2]^+$	429	26
$[Cu(tmtm)(tmtm\text{-}t\text{Bu})]^+$	372	59
$[Cu(tmtm\text{-}t\text{Bu})_2]^+$	315	100
$[Cu(tmtm)H]^+$	247	9
$[Cu(tmtm\text{-}t\text{Bu})]^+$	189	28

Table A3 The fragmentation species and corresponding relative abundances of the mass spectrometric analysis of $Cu(tmtm)_2$ as presented in Figure A3.

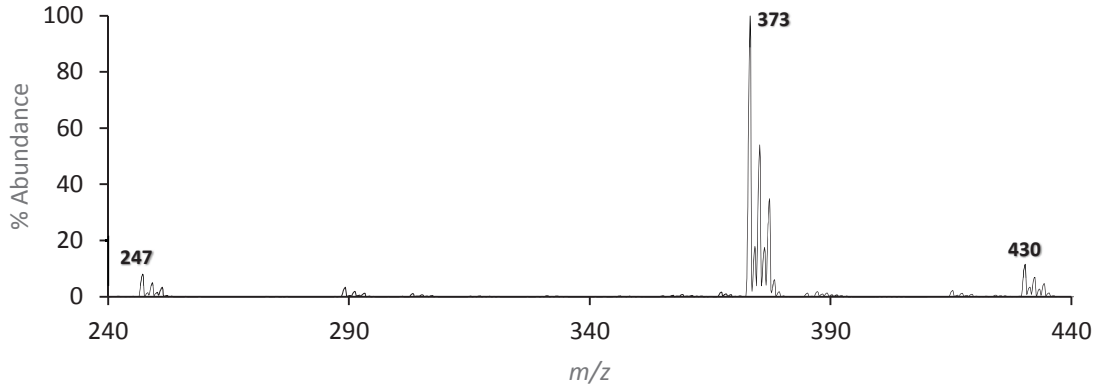

Figure A4: The 70 eV positive EI mass spectrum of $Zn(tmtm)_2$.

Species	*m/z*	Relative Abundances
$[Zn(tmtm)_2]^+$	430	12
$[Zn(tmtm)(tmtm\text{-}t\text{Bu})]^+$	373	100
$[Zn(tmtm)]^+$	247	8

Table A4 The fragmentation species and corresponding relative abundances of the mass spectrometric analysis of $Zn(tmtm)_2$ as presented in Figure A4.

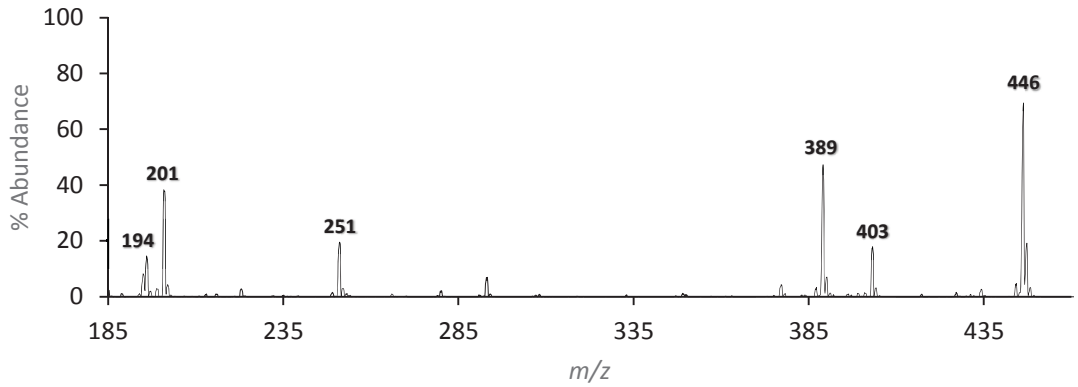

Figure A5: The 70 eV positive EI mass spectrum of $Fe(tftm)_3$.

Species	*m/z*	Relative Abundances
$[Fe(tftm)_2]^+$	446	69
$[Fe(tftm)_2\text{-}43]^+$	403	17
[Fe(tftm)(tftm-*t*Bu)]$^+$	389	46
[Fe(tftm)+42]$^+$	293	7
[Fe(tftm)]$^+$	251	20
$[Fe(tftm\text{-}CF_2)]^+$	201	38
[Fe(tftm-*t*Bu)]$^+$	194	8

Table A5 The fragmentation species and corresponding relative abundances of the mass spectrometric analysis of $Fe(tftm)_3$ as presented in Figure A5.

Appendix B:

Molecular Models from Computational Analysis

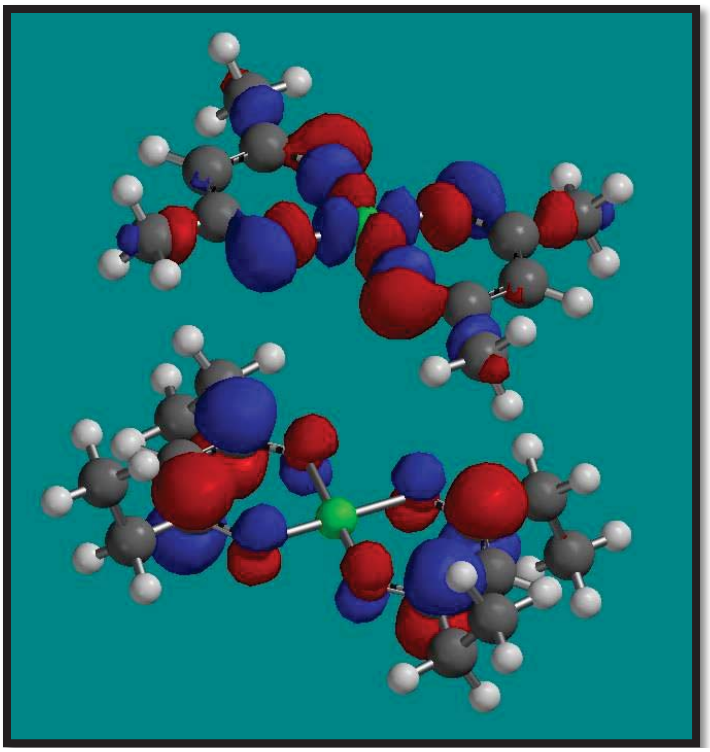

Figure B1: HOMO of $Cu(acac)_2$ positioned above LUMO of $Cu(eeac)_2$.

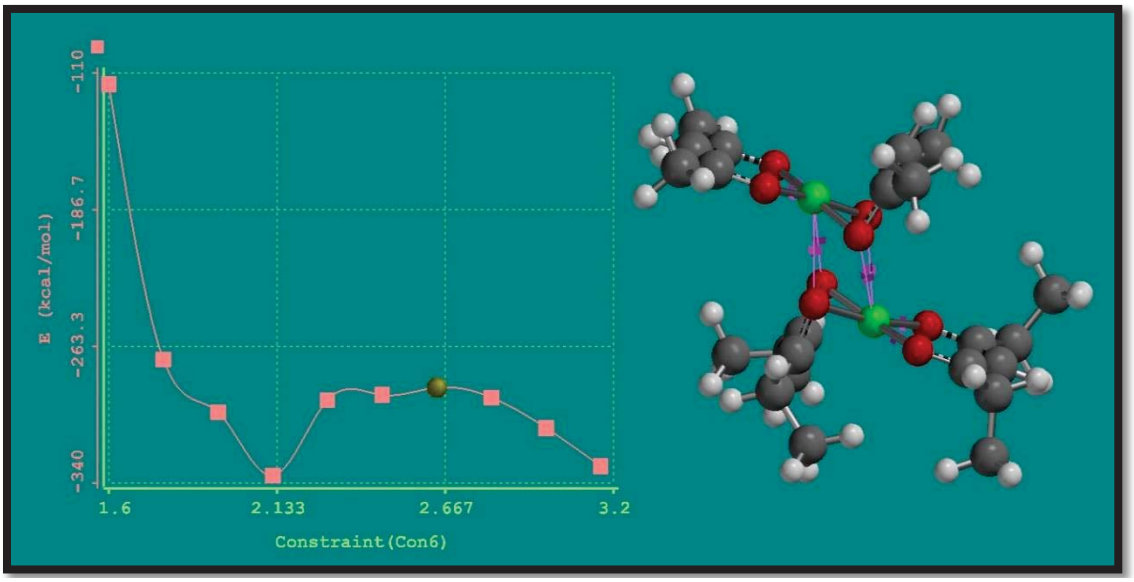

Figure B2: Energy profile of concerted partial ligand exchange between the $Cu(acac)_2$ and $Cu(eeac)_2$ cationic encounter complex. Local energy maximum shown at approximately 2.640 Å.

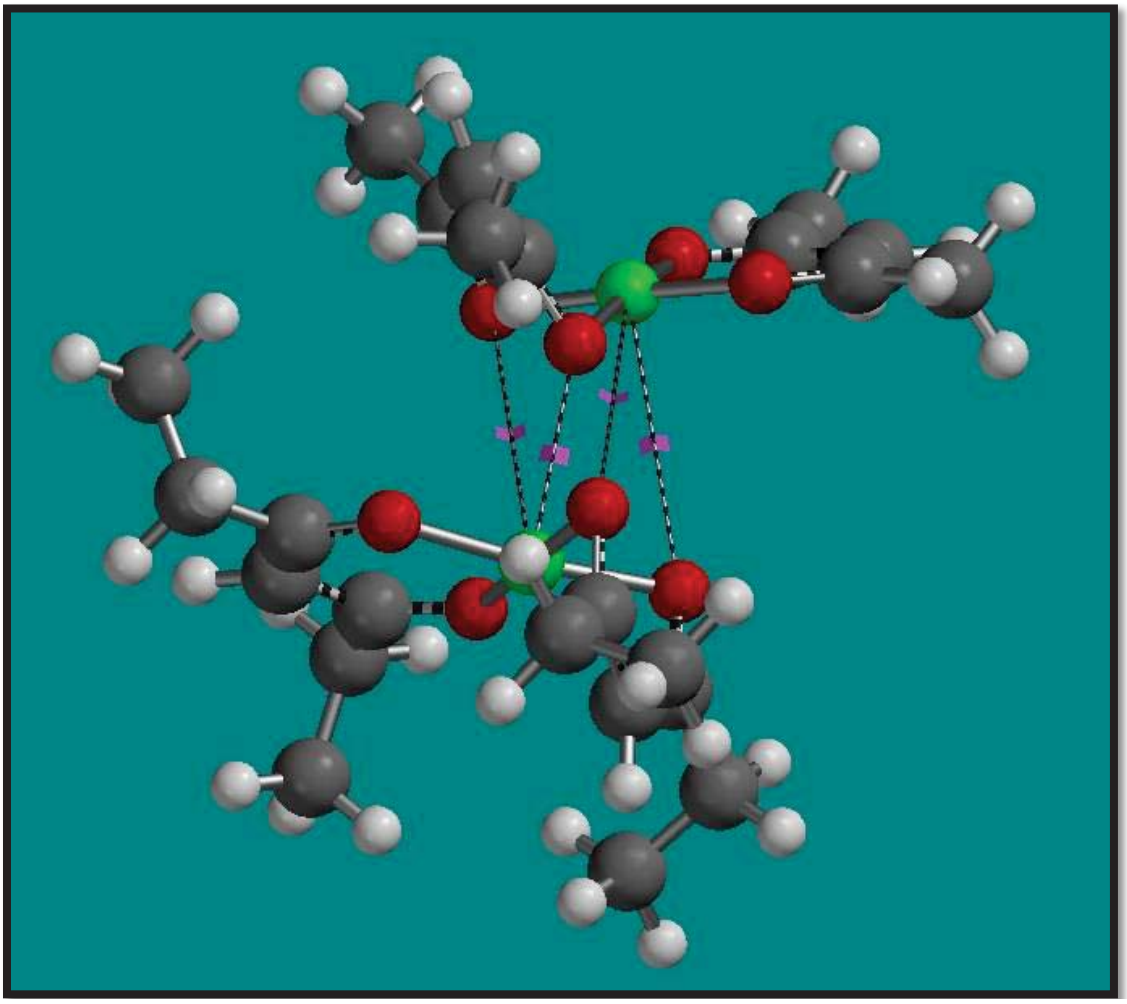

Figure B3: Structure of the optimized transition state for concerted partial ligand exchange between the $Cu(acac)_2$ and $Cu(eeac)_2$ cationic encounter complex.
Bond lengths (from left to right): 4.44 Å, 2.67 Å, 4.77 Å, 4.00 Å
Imaginary frequency: i269.31 cm^{-1}; single Cu-O bond stretch

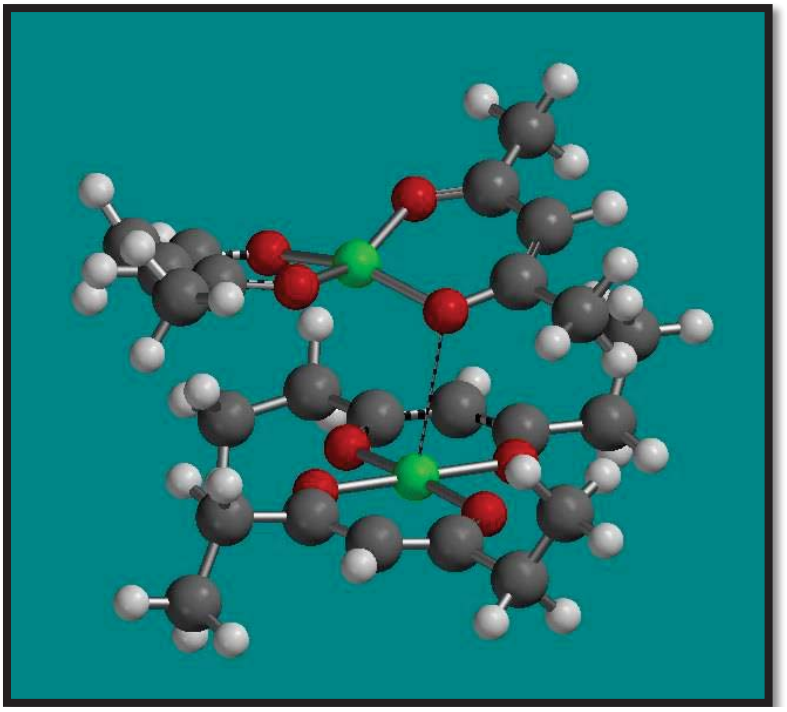

Figure B4: Intermediate 1 of $Cu(acac)_2$ & $Cu(eeac)_2$ Partial Ligand Exchange.

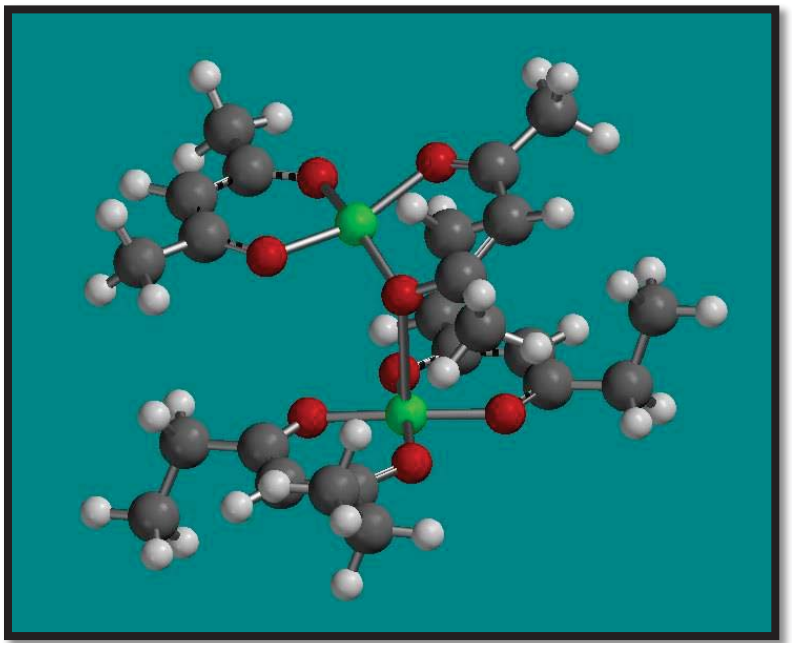

Figure B5: Transition State 1 of $Cu(acac)_2$ & $Cu(eeac)_2$ Partial Ligand Exchange.

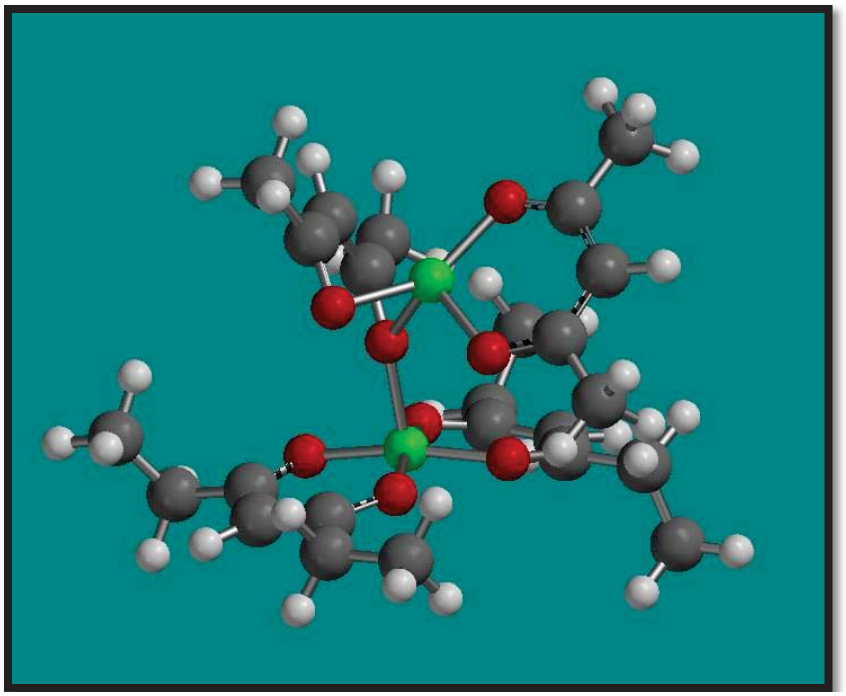

Figure B6: Intermediate 2 of $Cu(acac)_2$ & $Cu(eeac)_2$ Partial Ligand Exchange.

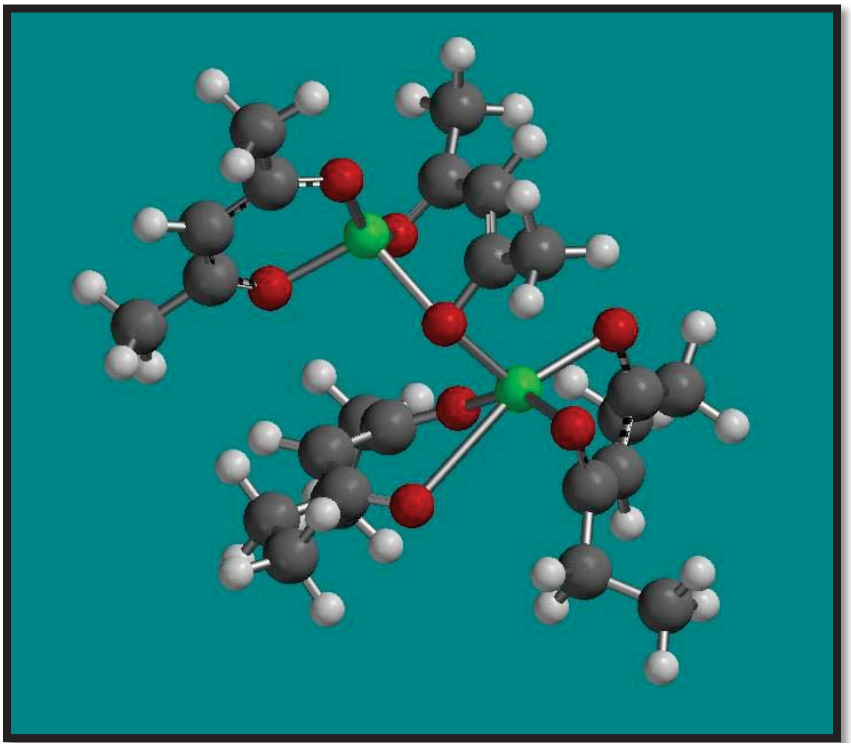

Figure B7: Transition State 2 of $Cu(acac)_2$ & $Cu(eeac)_2$ Partial Ligand Exchange.

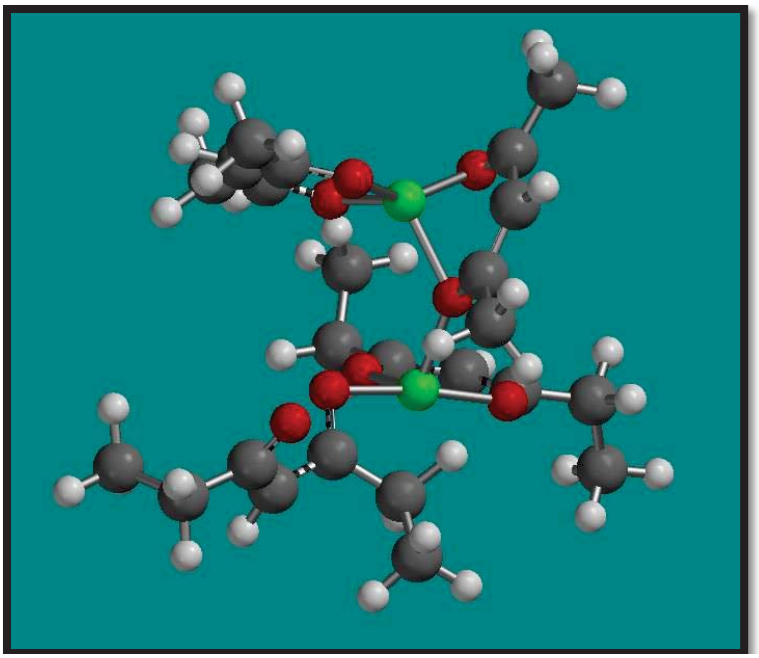

Figure B8: Intermediate 3 of $Cu(acac)_2$ & $Cu(eeac)_2$ Partial Ligand Exchange.

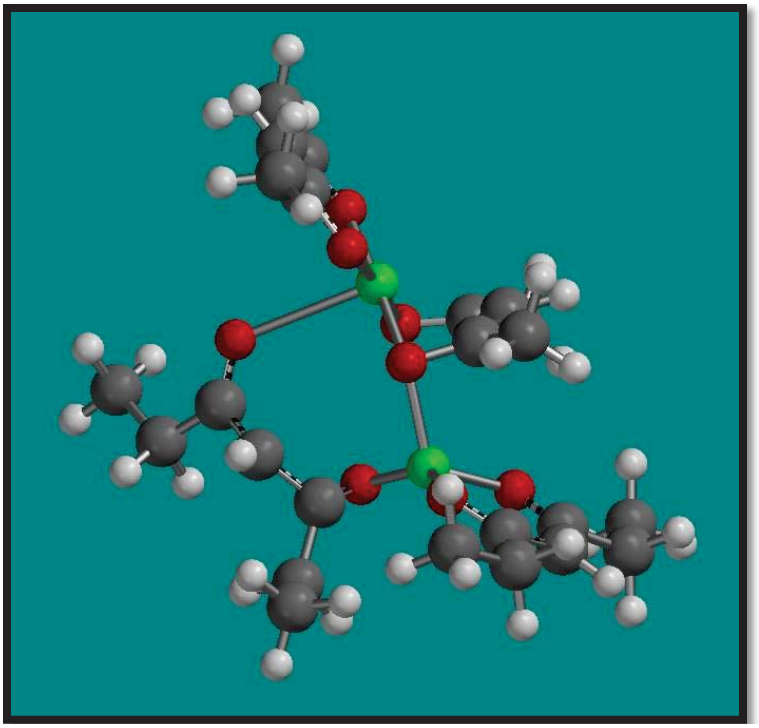

Figure B9: Transition State 3 of $Cu(acac)_2$ & $Cu(eeac)_2$ Partial Ligand Exchange.

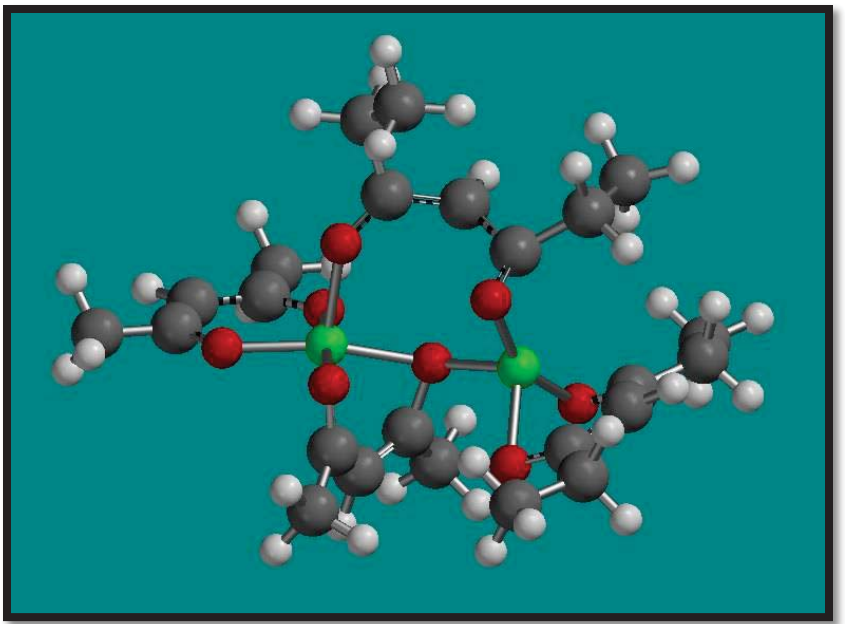

Figure B10: Intermediate 4 of $Cu(acac)_2$ & $Cu(eeac)_2$ Partial Ligand Exchange.

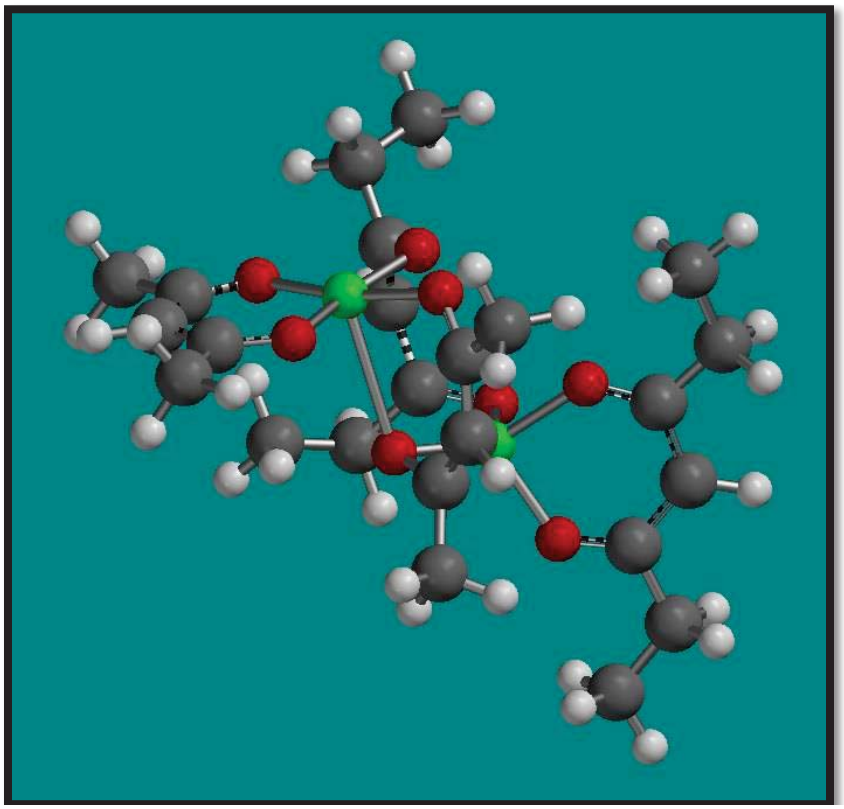

Figure B11: Transition State 4 of $Cu(acac)_2$ & $Cu(eeac)_2$ Partial Ligand Exchange.

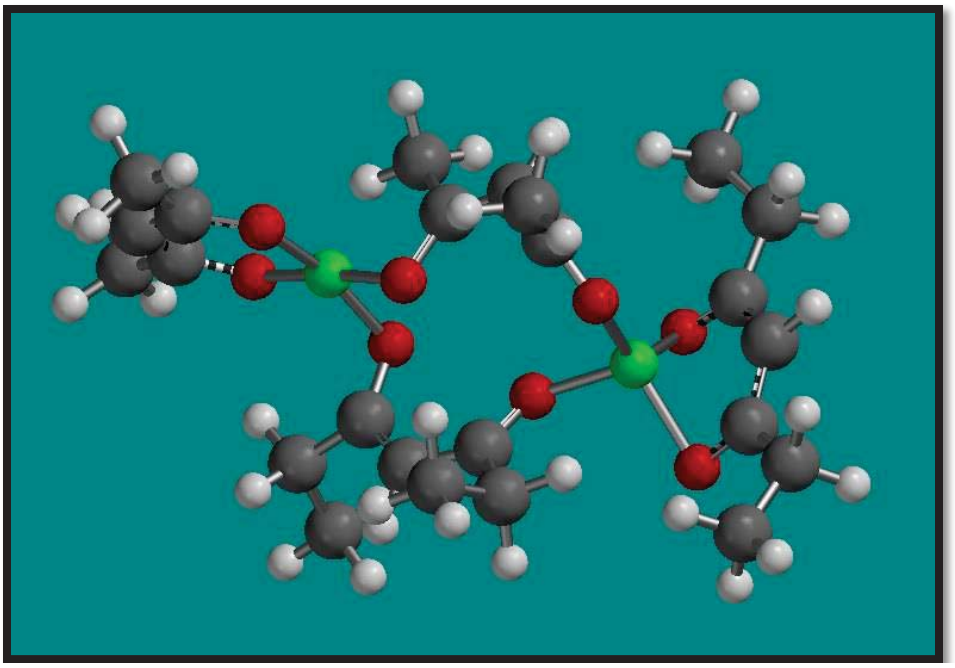

Figure B12: Intermediate 5 of $Cu(acac)_2$ & $Cu(eeac)_2$ Partial Ligand Exchange.

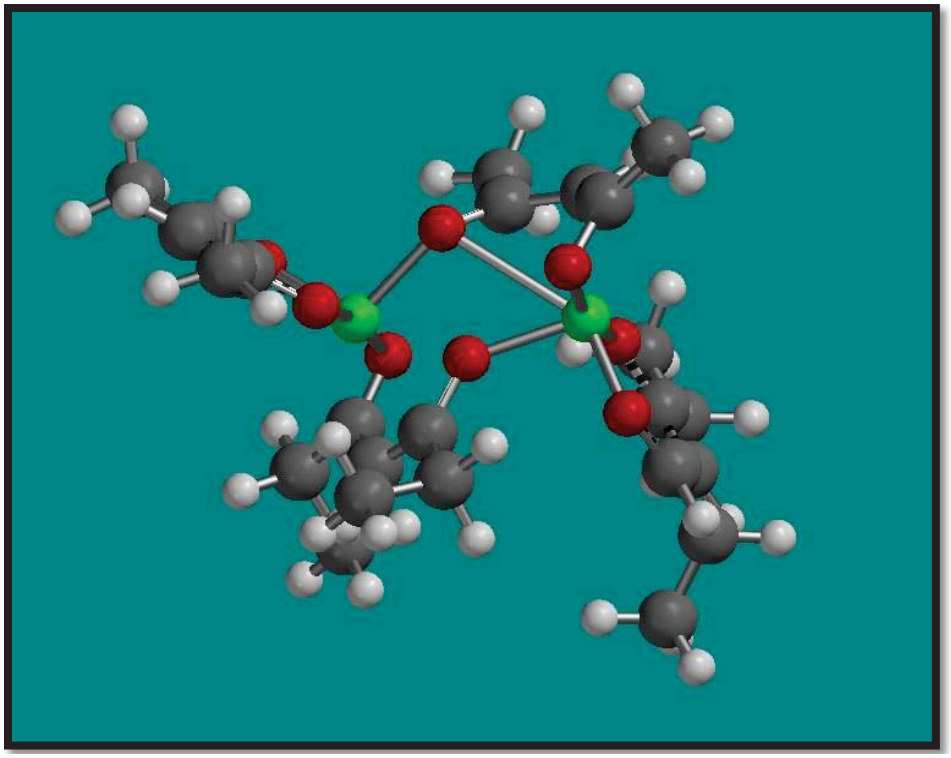

Figure B13: Transition State 5 of $Cu(acac)_2$ & $Cu(eeac)_2$ Partial Ligand Exchange.

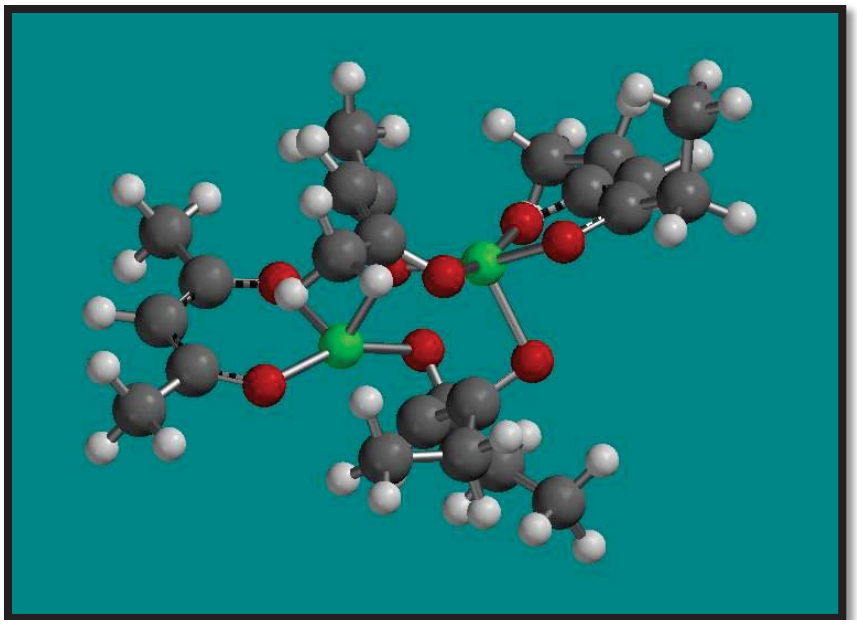

Figure B14: Intermediate 6 of $Cu(acac)_2$ & $Cu(eeac)_2$ Partial Ligand Exchange.

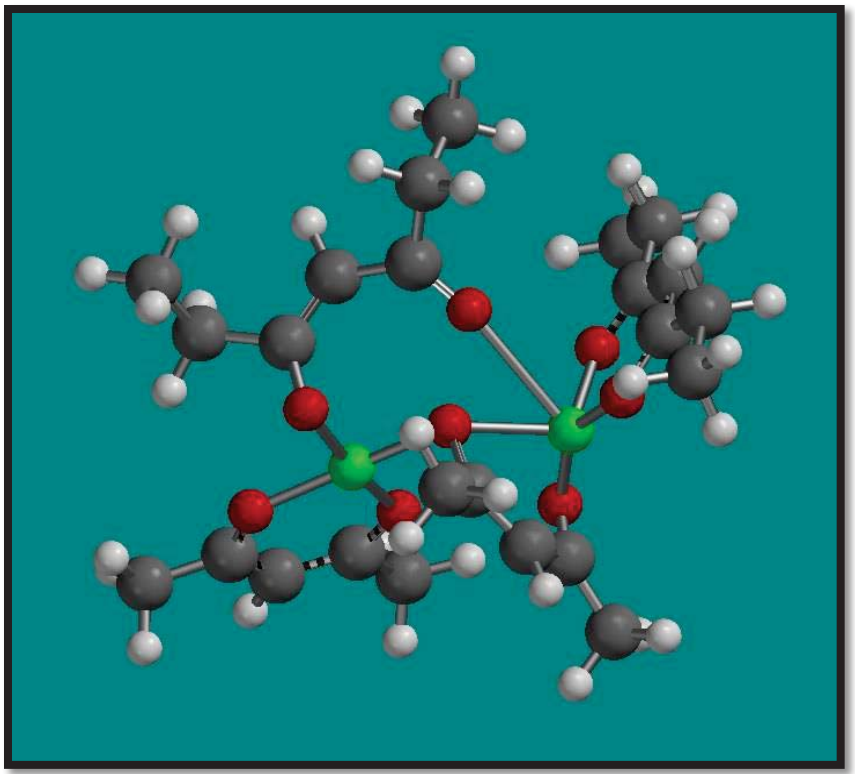

Figure B15: Transition State 6 of $Cu(acac)_2$ & $Cu(eeac)_2$ Partial Ligand Exchange.

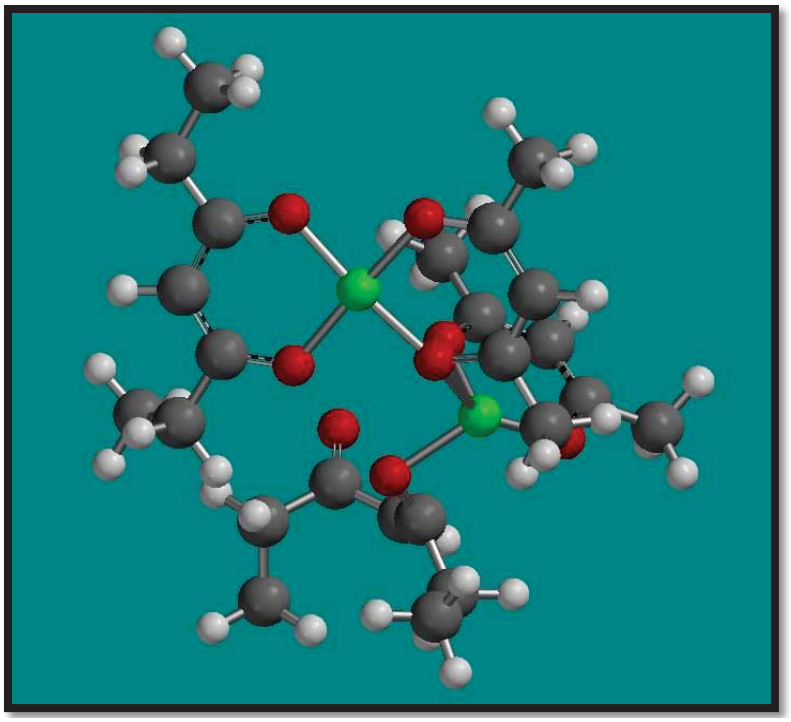

Figure B16: Intermediate 7 of $Cu(acac)_2$ & $Cu(eeac)_2$ Partial Ligand Exchange.

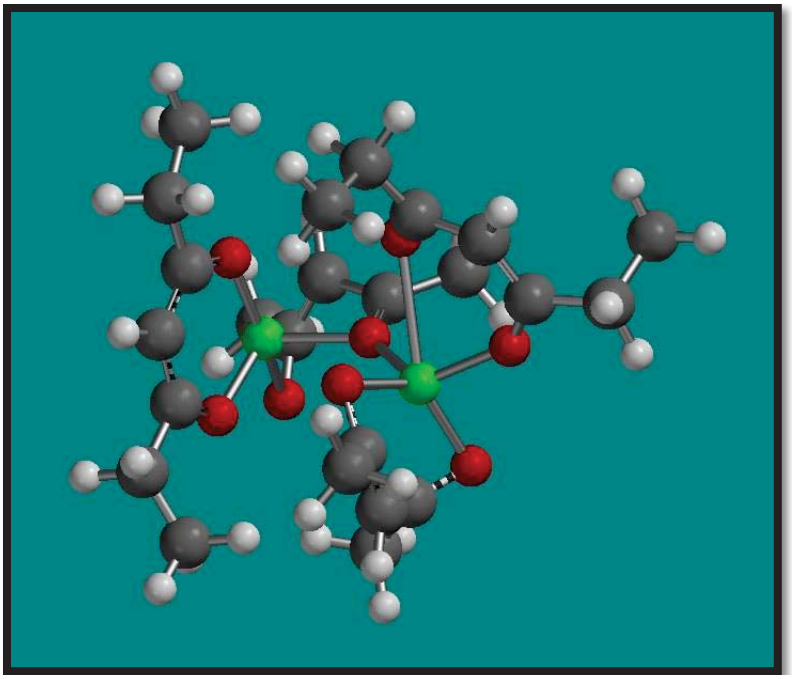

Figure B17: Transition State 7 of $Cu(acac)_2$ & $Cu(eeac)_2$ Partial Ligand Exchange.

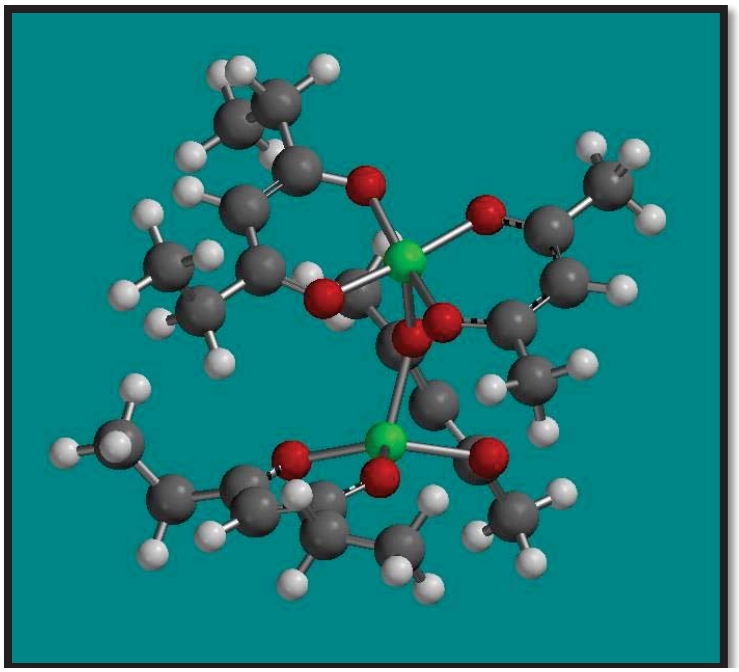

Figure B18: Intermediate 8 of $Cu(acac)_2$ & $Cu(eeac)_2$ Partial Ligand Exchange.

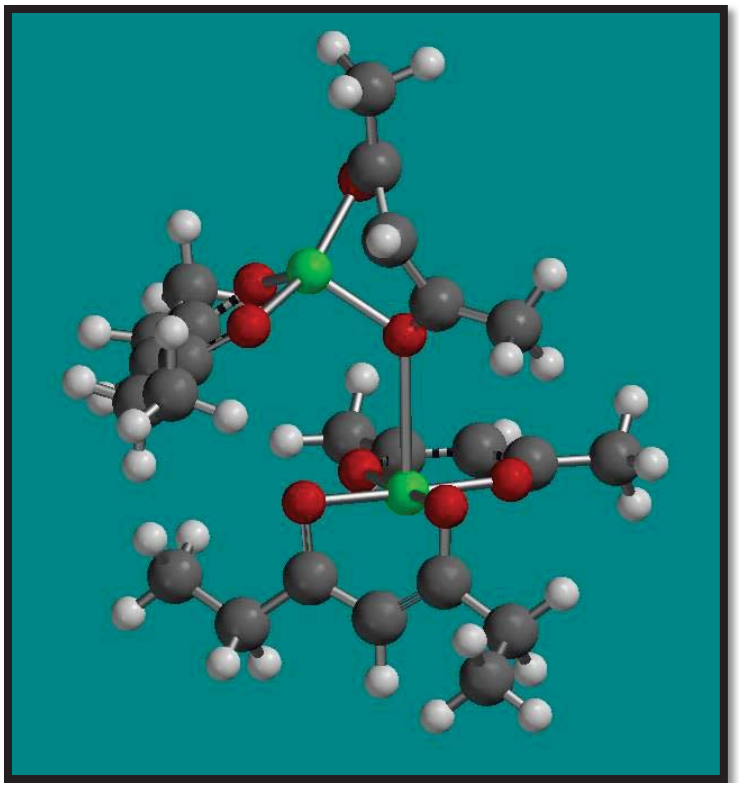

Figure B19: Transition State 8 of $Cu(acac)_2$ & $Cu(eeac)_2$ Partial Ligand Exchange.

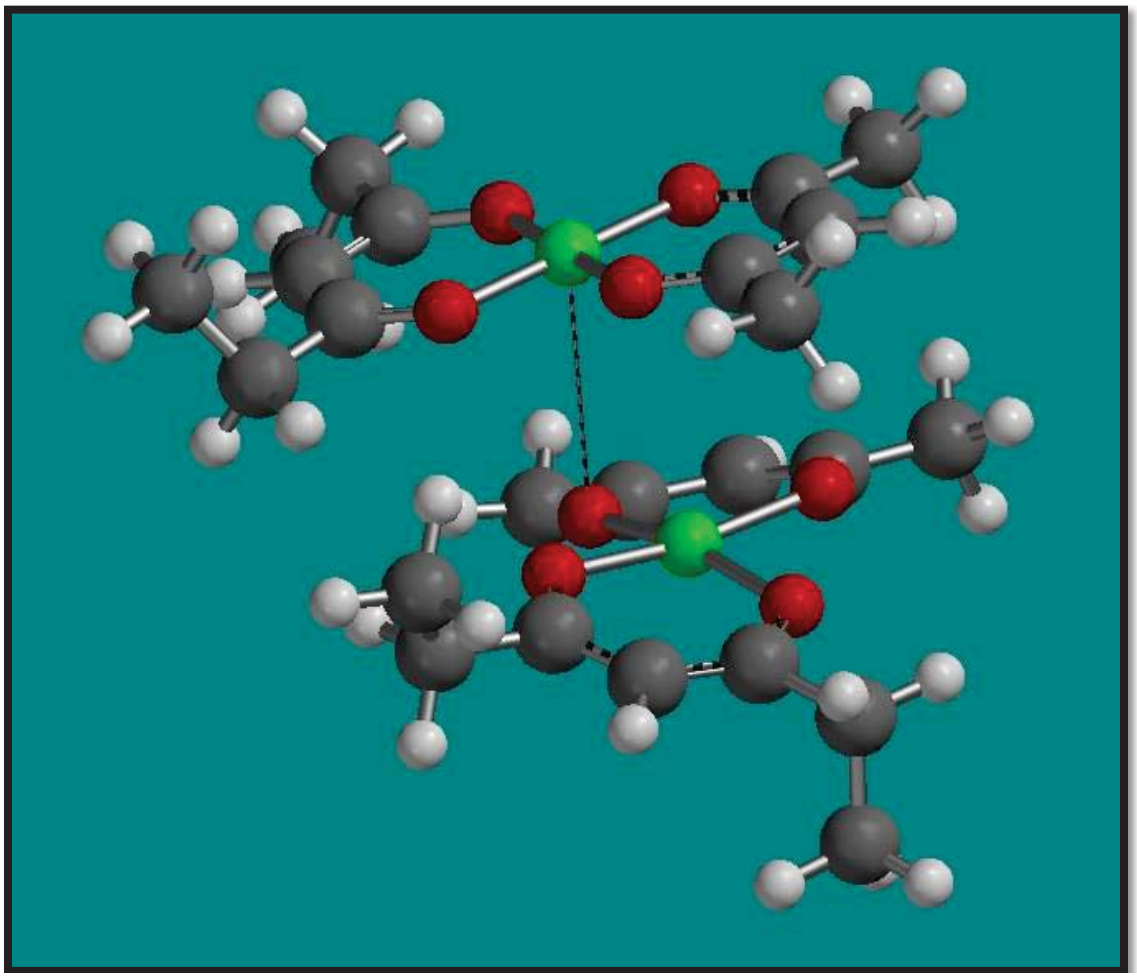

Figure B20: Intermediate 9 of $Cu(acac)_2$ & $Cu(eeac)_2$ Partial Ligand Exchange.